Technical University of Denmark

DTU

Magnetic Properties of Large-Scale Nanostructured Graphene Systems

Gregersen, Søren Schou; Jauho, Antti-Pekka; Power, Stephen

Publication date:
2017

Document Version
Publisher's PDF, also known as Version of record

[Link back to DTU Orbit](#)

DTU Library
Technical Information Center of Denmark

Magnetic Properties of Large-Scale Nanostructured Graphene Systems

Søren Schou Gregersen
PhD Thesis March 2017

DTU Nanotech
Department of Micro- and Nanotechnology

Magnetic Properties of Large-Scale Nanostructured Graphene Systems.
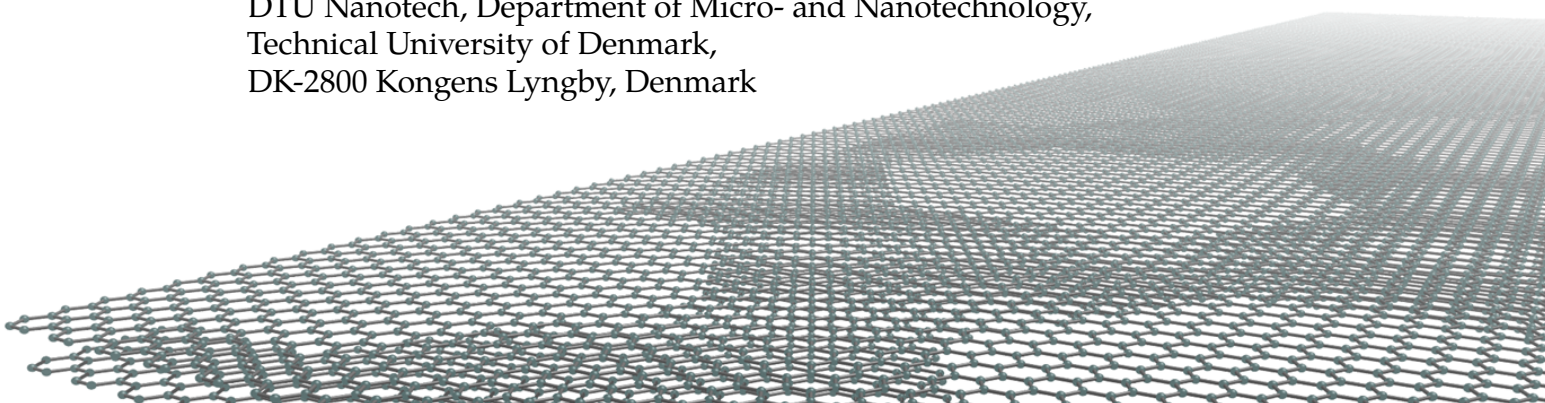
PhD Thesis

March 31, 2017

Author:

Søren Schou Gregersen

Email: sorgre@nanotech.dtu.dk
Supervisor: Antti-Pekka Jauho
Cosupervisor: Stephen R. Power

Center for Nanostructured Graphene (CNG),
DTU Nanotech, Department of Micro- and Nanotechnology,
Technical University of Denmark,
DK-2800 Kongens Lyngby, Denmark

Preface

This work is submitted in candidacy for the Ph.D. degree at the Technical University of Denmark (DTU). The work has been carried out at the Department of Micro and Nanotechnology (DTU Nanotech), from April 2014 to March 2017. The project is jointly funded by the Center for Nanostructured Graphene (CNG), which is sponsored by the Danish Research Foundation, Project DNRF103, and DTU Nanotech. This Ph.D. project was supervised by Prof. Antti-Pekka Jauho and co-supervised by Post. Doc. Stephen R. Power. I have written and implemented all presented simulation methods in C++/python, unless explicitly stated otherwise.

I would like to thank Antti and Stephen, who have both been very supportive throughout the entire project. I would also like to thank the groups of Prof. Antti-Pekka Jauho and Prof. Mads Brandbyge. It has been a pleasure working with them in the past three years. A special thanks to Prof. Stephan Roche at ICN2, Barcelona, and his group for taking me in, and not in the least for making my external stay a great experience.

Finally, I would like to thank my family and, in particular, my girlfriend Christina K. Larsen, for their support and encouragement.

Thank you,
Søren Schou Gregersen

Abstract

The on-going progress in two-dimensional (2D) materials and nanostructure fabrication motivates the study of *altered* and *combined* materials. Graphene—the most studied material of the 2D family—displays unique electronic and spintronic properties. Exceptionally high electron mobilities, that surpass those in conventional materials such as silicon, make graphene a very interesting material for high-speed electronics. Simultaneously, long spin-diffusion lengths and spin-life times makes graphene an eligible spin-transport channel. In this thesis, we explore fundamental features of nanostructured graphene systems using large-scale modeling techniques.

Graphene perforations, or antidots, have received substantial interest in the prospect of opening large band gaps in the otherwise gapless graphene. Motivated by recent improvements of fabrication processes, such as forming graphene antidots and layer-by-layer stacking, we consider a hybrid bilayer graphene system: Graphene on graphene antidot lattice (GOAL). These systems can be engineered to select attractive features from either bilayer and monolayer graphene. For a certain set of optimized geometries, we obtain linearly dispersing bands with a high corresponding mobility, resembling that of monolayer graphene. Nevertheless, these linearly dispersive GOALs can be made gapped by breaking layer symmetry, using e.g. perpendicular electric fields.

In the area of graphene spintronics, the formation of magnetic moments is predicted as the result of breaking the graphene sublattice symmetry. We take advantage of this, and explore the fundamental features of zigzag-edged triangular graphene antidots (zz-TGAs). Their specific edge configurations give rise to highly desirable spin-filtering and spin-splitting transport features. The mechanisms behind these functionalities are studied in detail in lattices, devices, and finally in disordered systems of experimentally feasible scale.

We demonstrate that superlattices of triangular antidots exhibit large bands gaps, induced by sublattice symmetry breaking. Spin-polarized TGAs are shown to become half-metallic near the Fermi level, giving rise to perfectly spin-polarized densities of states. By studying the transport properties of devices with embedded zz-TGAs, we highlight an interesting spatial spin-splitting feature analogous to the spin Hall effect. Unlike the conventional spin Hall effect, this feature is obtained without spin-orbit interactions or topologically protected transport channels. Motivated by spin Hall effect measurements, we calculate transverse resistance signals in zz-TGA devices and show that these can provide a general diagnostic tool to detect the presence of zigzag edge magnetism. The extraordinary features of zz-TGAs at small scales motivate our study of their underlying mechanisms in larger, more realistically sized TGAs. Half-metallic, semiconducting and highly anisotropic transport behaviors can be induced in these systems. Furthermore, these properties are extremely robust in the face of substantial disorder, in stark contrast to what is seen for many other antidot-based devices. Ultimately, these properties may prove useful in spintronic devices, graphene-based transistors and integrated electronic circuits where a particular transport direction is preferred.

Resumé

Dette studie er motiveret af den seneste fremgang i forskningen inden for todimensionelle (2D) materialer. Nye teknologiske fremskridt indenfor nano-skala fabrikation opfordrer til intensiveret fokus på forandrede og kombinerede materialer. Grafen, som er et af de mest studerede 2D materialer, udviser unikke elektroniske og spintroniske egenskaber. Elektron-mobiliteten er langt højere end i konventionelle materialer så som silicium og gør grafen særdeles interessant indenfor højhastighedselektronik. Derudover er lange spin-diffusionslængder og spin-levetider er med til at gøre grafen et oplagt materiale til spin-transport. Denne afhandling har til formål at kortlægge fundamentale egenskaber for nanostrukturerede systemer i grafen ved brug af modelleringsteknikker specielt til store længdeskalaer.

Huller i grafen, også kaldet grafen antidots, er der stor interesse for på grund af påvirkningen på grafens egenskaber. Antidots har nemlig den effekt at inducere store båndgab i den elektroniske båndstruktur, der i perfekt grafen viser den lineære spredning. Den nyeste fremgang inden for fabrikationen af grafen antidots samt stabling af 2D materialer, motiverer et studie af et grafen bilagshybrid: Grafen på grafen antidot gitre (graphene on graphene antidots lattices, GOALs). Sådanne GOALs kan blive designet til at udvise egenskaber fra både bilags- og monolagsgrafen. Ved optimerede geometrier findes den lineære spredning, der kendetegner monolagsgrafen og den medfølgende høje elektron-mobilitet. Ikke desto mindre kan et båndgab åbnes ved at bryde symmetrien mellem lagene, for eksempel ved at benytte vinkelrette elektriske felter.

Dannelsen af magnetiske momenter er specielt interessant indenfor grafen spintronik. Her viser studier at sådanne momenter opstår ved at bryde symmetrien af undergitrene for grafen, for eksempel ved grafen zigzag (zz) kanter. Vi udnytter dette og udforsker de fundamentale egenskaber af zz-kantede, trekantede grafen antidots (zz-TGAs). Deres specielle kantstruktur giver anledning til eftertragtede spinfiltrering- og spin-delingsegenskaber. Detaljerne af disse mekanismer er studeret i antidot gitre, enheder og også i større og mere eksperimentalrealistisk skala.

Ved brug af gitre af spin-upolariseret zz-TGAs demonstrerer vi store båndgab til følge af brudet på undergittersymmetrien. Hvis vi i stedet også betragter spin-vekselvirkningen, finder vi at spin-polariserede zz-TGAs giver anledning til halv-metalliske bånd nær Fermi-niveauet, hvilket i sidste ende resulterer i perfekt spin-polariserede tilstandstætheder. Ved at kigge på transportegenskaberne finder vi, at enheder med zz-TGAs udviser en meget interessant rumlig spin-deling. Denne funktion er sammenlignelig med spin Hall effekten, men denne er opstået uden betragtninger om spin-orbit koblinger eller topologiske transportkanaler. Inspireret fra spin Hall effekteksperimenter beregner vi de transversale modstande i enheder med zz-TGAs, og her finder vi et antisymmetrisk signal, der er karakteristiske for de spin-polariserede TGAs. Hvis vi derimod betragter spin-upolariserede TGAs, finder vi symmetriske signaler. Dette kan fungere som et mål for de spin-polariserede TGAs, og endda også for muligheden af magnetiske grafenkanter. Selv hvis vi introducerer betydelige uregelmæssigheder og en uniform tilfældig fordeling, udviser TGAs halv-metalliske eller halvledende egenskaber. En interessant bemærkning er at på trods af den uniforme fordeling af TGAs, viser vores resultater signaturer af anisotropisk transport. I sidste ende kan dette bruges i integreret kredsløbsteknologi, hvor der er behov for specifikke transportretninger.

List of contributions

Paper I (attached):
Graphene of graphene antidot lattice: Electronic and transport properties,
Authors: Søren Schou Gregersen, Jesper Goor Pedersen, Stephen R. Power, and Antti-Pekka Jauho.
Physical Review B 91, 115424 (2015).

Paper II (attached):
Robust band gap and half-metallicity in graphene with triangular perforations,
Authors: Søren Schou Gregersen, Stephen R. Power, and Antti-Pekka Jauho.
Physical Review B 93, 245429 (2016).

Paper III (attached):
Nanostructured graphene for spintronics,
Authors: Søren Schou Gregersen, Stephen R. Power, and Antti-Pekka Jauho.
Physical Review B 95, 121406(R) (2017).

Paper IV (not attached):
Suppression of intrinsic roughness in encapsulated graphene,
Authors: Joachim Dahl Thomsen, Tue Gunst, Søren Schou Gregersen, Lene Gammelgaard, Bjarke Sørensen Jessen, David M. A. Mackenzie, Kenji Watanabe, Takashi Taniguchi, Peter Bøggild, Timothy J. Booth.
Recently submitted. (contribution in Supplemental Material).

Below is a list of conference contributions.

- *Graphene on graphene antidot lattices*, Graphene 2014, Toulouse, France,
  S. S. Gregersen, J. G. Pedersen, S. R. Power, and A.-P. Jauho

- *Graphene on graphene antidot lattices*, Graphene 2015, Bilbao, Spain,
  S. S. Gregersen, J. G. Pedersen, S. R. Power, and A.-P. Jauho

- *Graphene on graphene antidot lattices*, Carbonhagen 2015, Copenhagen, Denmark,
  S. S. Gregersen, J. G. Pedersen, S. R. Power, and A.-P. Jauho

- *Graphene with triangular perforations*, Graphene 2017, Genova, Italy,
  S. S. Gregersen, S. R. Power, and A.-P. Jauho

Nomenclature

Abbreviations

SHE	Spin Hall effect
zz(-edge)	Graphene zigzag(-edge)
ac(-edge)	Graphene armchair(-edge)
hBN	Hexagonal boron nitride
TMD	Transition-metal dichalcogenides
GAL	Graphene antidot lattice
GOAL	Graphene on graphene antidot lattice
TGA	Triangular graphene antidot
zz-TGA	Zz-edged triangular graphene antidot
ac-TGA	Ac-edged triangular graphene antidot
DOS	Density of states
LDOS	Local density of states
PDOS	Projected density of states

General notation and constants

e	Elementary charge of an electron (positive)	1.602×10^{-19} C
h	Planck's constant	6.63×10^{-34} Js
$\hbar = h/2\pi$	Reduced Planck's constant	1.05×10^{-34} Js
$\mathbf{M}$	Matrix or operator $\mathbf{M}$	
$[\mathbf{M}]_{ij}$	The ij'th element of $\mathbf{M}$	
$\mathbf{M}^{\dagger}$	Conjugate transpose $\mathbf{M}$	
$\mathrm{Tr}\,[\mathbf{M}]$	Trace of $\mathbf{M}$	
$\mathrm{Re}[z]$	Real part of complex number z	
$\mathrm{Im}[z]$	Imaginary part of complex number z	

Contents

Introduction

<div align="right">

1

</div>

The field of two-dimensional (2D) materials research [1–3] is thriving. The new and exciting 2D technologies, and the ever-increasing demands for smaller devices, are challenging otherwise well-established three dimensional (3D) conventions. New areas are emerging with intriguing possibilities, and which allow for previously un-accessible phenomena. Below we cover the basics of 2D electronics and spintronics, with particular focus on graphene based systems.

1.1 Two dimensional electronics

In the past decade, the number of studies in 2D materials has grown substantially [3]. The breakthrough came in 2004, with the first successful isolation of monolayer graphene [4] by mechanical exfoliation. Graphene is a single layer of carbon atoms arranged in a hexagonal lattice, which uniquely exhibits Dirac-fermion physics [5] and a linear bandstructure. This has since spawned entire research centers and huge conferences dedicated to the advancement of graphene and 2D material research.

As it turned out, graphene was to be only the first of a large series of 2D materials, each with their own unique properties as well as challenges. A whole host of different electronic properties are possible with 2D materials, ranging from insulating to superconducting. In particular, one material worth mentioning is hexagonal-boron nitride (hBN), another material with a hexagonal lattice with alternating boron and nitrogen atoms. With extremely flat surfaces and insulating behavior, hBN is quickly becoming the *de facto* standard substrate or encapsulating material for other 2D systems [6]. Following the rise of graphene, transition-metal dichalco-genides (TMDs) [7] are now competing with graphene as the primary focus of many researchers. Still other materials are continually gaining momentum, with huge efforts being made to understand the properties of silicene [8], germanene [9], and phosphorene [10], to name only a few.

The true potential however, may lie not in the individual materials but in the combination of these. Stacking materials layer-by-layer in a predefined sequence, allows for entirely new materials with unique properties to be envisioned. This is perfectly illustrated by the iconic figure in Fig. 1.1(a). Stacking has become particularly interesting with the latest progress in van der Waals (vdW) stacking of layered materials [11, 12]. The process illustrated in Fig. 1.1(b) uses *only* vdW forces, and in turn the resulting interfaces are kept clean from contaminants from processing agents.

Of the 2D materials, graphene is by far the most studied [3], with a wide range of unique properties. Graphene shows exceptional mechanical strength and im-permeability, which can be used to strengthen composites as well as in protective coatings [13, 14]. Graphene also displays remarkable optical properties, such as wavelength-independent absorption, which can be used for efficient photo detec-tion [14]. Finally, exceptionally high electron mobilities above $10^6 \, \mathrm{cm \, V^{-1} \, s^{-1}}$ have been demonstrated in graphene at room temperature [6], substantially higher than,
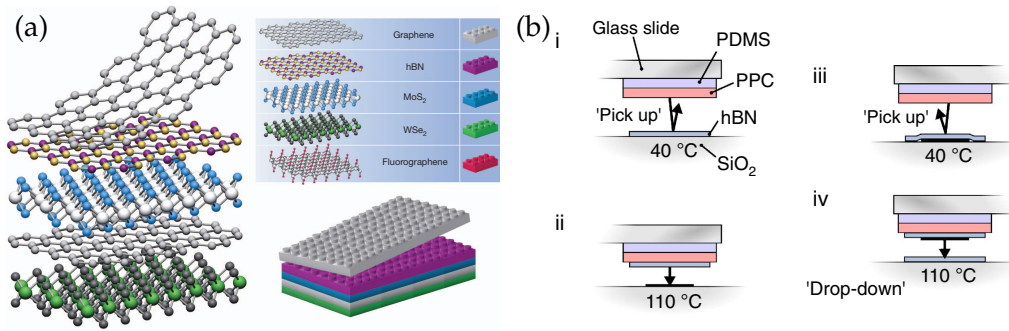
Figure 1.1: Illustration of stacked 2D materials. (a) The iconic LEGO-like stacking of 2D materials to create an entirely new material, reproduced from Geim and Grigorieva [11]. (b) The van der Waals (vdW) stacking technique, which keeps interfaces clean from processing agents, reproduced from Pizzocchero *et al.* [12].

for example, electron mobilities of silicon $\sim 10^3 \, \text{cm V}^{-1} \text{s}^{-1}$. This may prove very useful for high-speed electronics, where performance is limited by mobilities. In conventional electronics, the Dirac nature of electrons in graphene make these propagate straight through traditional potential barriers, known as *Klein tunneling* [5]. This makes a straightforward silicon replacement challenging. However, in particular for *spintronics*, graphene exhibits unusually long spin-diffusion lengths and spin-life times [15], which makes graphene a suitable choice for spintronic transport.

In terms of theoretical descriptions, graphene is an exceptionally "easy" material. Many first-principle calculations of graphene are reproducible by use of efficient tight-binding (TB) models [5]. In addition, while fabrication techniques are simultaneously improving, making smaller and smaller devices, simulation techniques and hardware are increasing the length-scales we are able to describe. Ultimately, the gap between theory and experiment is decreasing.

1.2 Spintronics

Spintronics aims to replace the carrier of information from the electronic charge to the spin-degree of freedom [16]. The advantages of spintronic logic devices are, for example, lower power dissipation, and improved computational scalability compared to traditional complementary metal–oxide–semiconductor (CMOS) technologies [17, 18]. One major challenge is, however, the choice of a suitable spin-channel. Graphene has many of the desired spin properties, and has recently seen substantial advances: For example, room-temperature spin transport over several µm [15], efficient spin injection [19, 20], induced magnetism [21–24], and an improved understanding of spin-orbit coupling and spin relaxation mechanisms [25, 26].

Of particular interest is the prospect of graphene magnetism via the formation of magnetic moments. This formation is predicted in graphene as the result of e.g. vacancy defects [21, 22, 28, 29], adatoms [22, 28, 30], and ferromagnetic substrates and molecular doping [23]. Finally, graphene zigzag (zz) edges are also predicted to form local ferromagnetic moments. In analogue with Lieb's theorem [31] for bipartite lattices, the magnetic moments are the result of local sublattice imbal-
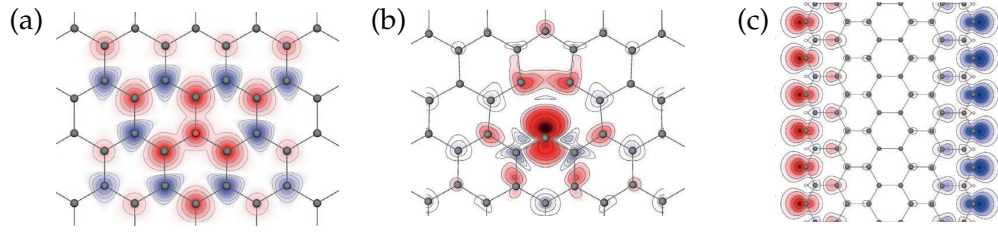
Figure 1.2: Illustration of magnetic moments in nanostructured graphene. Magnetic moment contour-maps surrounding (a) hydrogen adatoms, (b) vacancies, and (c) zigzag (zz)-edged nanoribbons (spin up: red, spin down: blue). Reproduced from Han *et al.* [27].
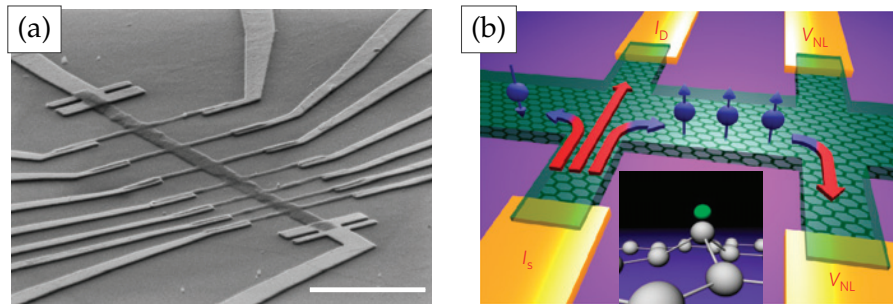
Figure 1.3: Nonlocal measurement of the graphene Spin Hall effect (SHE). A charge current is induced across source (I_S) and drain (I_D), which generates a left to right spin current. The spin current in turn generates a charge accumulation inducing a nonlocal voltage (V_{NL}) which can be measured. (a) Actual device. (a) Device schematic. Reproduced from Balakrishnan *et al.* [37].

ances. The magnetic moments of an hydrogen adatom and a vacancy are shown in Figs. 1.2(a) and 1.2(b), respectively. Because of the sublattice dependence, the magnetic moments orient oppositely on the two sublattices of graphene. This results in zz-edged nanoribbons with antiferromagnetic order between opposite edges; An example is shown in Fig. 1.2(c). This has given rise to innovative proposal for spintronic devices. For example, zz-nanoribbons in external in-plane electric fields has been proposed to generate half-metallic behavior [32], where the material is simultaneously a metal for one spin and an insulator for the other.

While first principle calculations predict the existence of magnetic moments, experimental signatures of magnetic graphene are few. Measurements via SQUID (superconducting quantum interference device) have been performed on graphene with fluorine adatoms, which indicate the existence of magnetic moments [21]. Furthermore, spin transport measurements in hydrogenated graphene have shown characteristic magneto-resistance dips, which can be explained through spin-scattering off of local magnetic moments [22]. More recently, measurements of graphene nanoribbons [33, 34], perforated graphene (graphene antidots) [35], and graphene-hBN zz-interfaces [36] also suggest the formation of magnetic moment at graphene zz-edges. In light of the above, we are motivated to explore such zz-edged nanostructured graphene systems and inspire further experiments.

Another extensively studied phenomena is the graphene spin Hall effect (SHE). In the SHE, an electrical current is used to generate a transverse spin current [38]. The

low spin-orbit coupling in graphene makes the inherent SHE small [27]. However, enhanced spin-orbit coupling has been claimed, for example through hydrogen absorption [37, 39], which has demonstrated significant SHE signals. Often the SHE effect is measured non-locally, where a combined SHE and *inverse* SHE is used to generate a measurable voltage. An example of a typical setup is shown in Fig. 1.3. On the left side, a charge current is induced transversely across two terminals, which in turn generates a longitudinal spin current (from left to right). On the right side, the reverse process generates charge accumulation and in turn a transverse (nonlocal) voltage drop, which can be measured. The graphene SHE and inverse SHE might solve two of the major challenges in graphene spintronics: spin generation and detection.

1.3 Graphene antidot lattices (GALs)

Nanostructuring, or nano-patterning graphene, gives rise to new electronic behavior, which might prove useful in combination with the unique properties of pristine graphene. In particular, graphene with small perforations, or antidots has spurred substantial interest. Pedersen *et al.* [40] were some of the first to propose the use of graphene antidots, in this case as a means towards spin qubits. However, it quickly became apparent that graphene antidot lattices (GALs) could open large band gaps in the otherwise gapless graphene. Large band gaps may be an alternative to enable the high on/off ratios needed for traditional transistor technology. Many studies have since found that the band gaps are difficult to experimentally demonstrate as they are inherently fragile against the commonly faced types of disorder [41–44]. Even so, experiments [45, 46] and theory [47] suggest that where band gaps are suppressed by disorder, transport gaps might form instead.

One of the key issues with GALs is the intricate influence of the superlattice vectors, an issue we face regularly in this thesis. A GAL may be critically dependent on the orientation and size of the periodically repeated pattern with respect to the graphene lattice. By critically I mean that, for example, a band gap may appear in some GALs, but completely vanish upon small changes in the pattern, even down to the scale of inter-atomic separation [41–43]. The dependency follows from a relation between the antidot superlattice and the underlying pristine graphene lattice, and we will refer to this concept as the antidot lattice *commensurability*. Another intricacy is the influence of antidot edges. The use of particular edges can make GALs transition from semi-conducting to metallic [48]. In addition, edge chirality may introduce yet another complication. Pristine features such as antidot lattice commensurability and antidot edges are inherently fragile against disorder. This has lead to a number of works studying the severity of various types of disorder [44, 47, 49].

In the prospect of obtaining gapped graphene, relevant fabrication processes have improved significantly. Circular antidots in regular lattices have been produced down to sizes of 25 nm diameters and 50 nm lattice periods [52]. In particular, a lot of effort has been put into producing particular edge types [50, 53, 54]. For example large control of zz-edged GALs was demonstrated by Shi *et al.* [50], illustrated in Fig. 1.4(a). Furthermore, high-resolution lithography by using hBN as a protective layer has produced high quality ballistic transport through GALs [52, 55]. Finally, even small triangular antidots have recently been fabricated [51], illustrated in Fig. 1.4(b). This is particularly interesting as we explore the electronic and transport
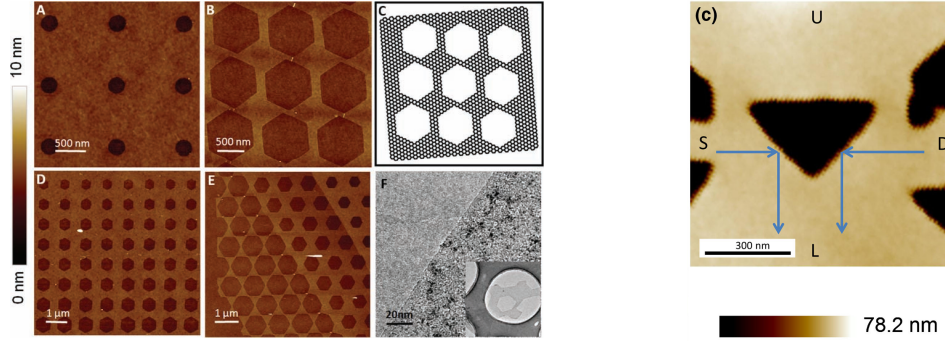
Figure 1.4: Controllable formation of graphene antidots with particular edges. (left) Zz-edged antidot production, reproduced from Shi *et al.* [50]. (right) Triangular hole (for ballistic rectifying), reproduced from Auton *et al.* [51].

properties of triangular antidots in this thesis.

1.4 Thesis outline

The remaining chapters in this thesis are structured as follows.

In **Chapters 2 and 3** we briefly go through, respectively, the electronic description and formalism, and the large-scale methods used to describe the electronic properties in samples of several millions of atomic sites. We will cover the Green's function formalism, Landauer-Büttiker transport, Chebyshev polynomial expansions, and the Kubo real-space method.

In **Chapter 4** the most important electronic properties of graphene and GALs are presented. This includes bandstructures, band gap scaling in GAL, and, in particular, antidot lattice commensurability.

The main parts of this thesis can be separated in two subjects: an example of a patterned graphene bilayer and zz-edged triangular graphene antidots (zz-TGAs). The first is an example of stacking two different graphene layers to generate new electronic behavior. The second is an extensive exploration into electronic and magnetic properties of TGAs, both in bulk and embedded devices.

In **Chapter 5** we discuss the work published in Paper I, in which we consider a patterned graphene bilayer: **G**raphene **O**n graphene **A**ntidot **L**attices (GOAL). We examine a graphene bilayer heterostructure, where a pristine layer of graphene is placed on top of another layer of graphene with a regular lattice of antidots. We demonstrate the electronic and transport properties considering a number of combinations of GAL layers. The bandstructure can be engineered to display *either* parabolic or linear dispersion, which nevertheless can be made gapped by breaking layer symmetry. As demonstrated in graphene bilayer, the band gaps can be tuned via a transverse electric field, e.g., by dual gating [56].

In the remaining chapters, we discuss the work published in Papers II and III, where we consider zz-TGAs both in bulk and devices.

We first explore the fundamental properties in TGA *lattices* in **Chapter 6**. Spin-unpolarized superlattices display large band gaps, in which we observe unusual

robustness against lattice disorder. On the other hand, spin-polarized TGAs have half-metallic regions near the Fermi level, accessible by gating. The large band gaps and half-metallic features are independent on conventional geometric rules (commensurability), in sharp contrast to, for example, the band gaps of conventional antidots. This in turn makes TGA lattice robust against lattice disorder in particular.

In **Chapter 7**, we move on to explore *device* transport properties. The spin-polarized TGA devices demonstrate an interesting spatial spin-splitting feature; Spin-unpolarized currents are injected and spin-dependently scattered to opposite sides of the device. This is somewhat analogous to the SHE, but without the need for spin-orbit interactions or topologically protected transport channels. The spin-splitting is enhanced by repeated scattering in arrays of TGAs, and the performance is demonstrated to be robust against typical disorders faced in experiments. We also consider the transverse resistance, which displays an antisymmetric signal, characteristic of the spin-polarized TGAs. Using the same device, but assuming spin-unpolarized TGAs, the transverse resistance is instead completely symmetric.

Finally, in **Chapter 8**, we consider (unpublished results of) TGAs in larger scales ($360\,\text{nm} \times 360\,\text{nm}$ samples and $5\,\text{nm}$ TGAs), where we examine the influence of disorder via the density of states and Kubo conductivities. Similar to the smaller cases, large-scale TGAs features such as band gaps and half-metallic properties are robust against disorder. Furthermore, the TGAs display an unusually large anisotropic behavior, with simultaneously quasi-ballistic behavior in one direction, and localized behavior in the other.

In the final **Chapter 9**, I present a summary of the results and discussions, and an outlook of further possibilities.

In **Appendices A, B and C** I present, respectively, a derivation of the recursive Green's function techniques, derivations and implementation of Chebyshev polynomial expansions and the real-space Kubo method, and attached publications.

Electronic theory

<div style="text-align: right; font-size: 3em;">2</div>

This chapter briefly presents the electronic theory used in this thesis, including the main formulas and common usage. In particular, Green's function techniques are mentioned, but further derived in detail in Appendix A.

2.1 Electronic and transport properties

Throughout the thesis, we use tight-binding (TB) models to describe the electronic and magnetic properties of different patterned graphene systems [5, 57–59]. Take for example the TB Hamiltonian

$$\mathbf{H} = \sum_i \epsilon_i \mathbf{n}_i + \sum_{\langle i,j \rangle} \gamma_{ij} \mathbf{c}_i^\dagger \mathbf{c}_j \qquad (2.1)$$

where $\mathbf{n}_i = \mathbf{c}_i^\dagger \mathbf{c}_i$ are the number operators and $\mathbf{c}_i^\dagger$ ($\mathbf{c}_i$) are the creation (annihilation) operators. The parameters ϵ_i are the on-site energies and γ_{ij} are the hoppings between neighboring pairs ($\langle i, j \rangle$). The actual values depend on context and are described later in the relevant chapters.

The electronic properties, for example the local or total density of states (LDOS or DOS) are for the most part determined in Green's function representation. See, for example, Datta [60, 61] and Bruus and Flensberg [62] for an in-depth introduction to Green's functions in condensed matter physics. The non-interacting Green's function between states α and β is defined in energy space $(E + i0^\pm - \mathbf{H}) [\mathbf{G}]_{\alpha\beta} = \delta_{\alpha\beta}$, which leads to the matrix form

$$\mathbf{G} = \left(E + i0^\pm - \mathbf{H} \right)^{-1} . \qquad (2.2)$$

The parameter $\eta = 0^\pm$ is nonzero for numerical stability (between $\pm 10^{-4}$ and $\pm 10^{-12}$ depending on needed precision), and will usually be omitted for brevity. Using $\eta = 0^+$ corresponds to the *retarded* Green's functions ($\mathbf{G}^r$) and $\eta = 0^-$ the *advanced* Green's functions ($\mathbf{G}^a$). We will not be breaking time-reversal symmetry (e.g. no magnetic fields), so $\mathbf{G}^r = [\mathbf{G}^a]^\dagger$. The LDOS at site i and DOS are determined from the Green's functions

$$\text{LDOS}(i, E) = -\frac{1}{\pi} \text{Im}[\mathbf{G}]_{ii} \text{ and} \qquad (2.3)$$

$$\text{DOS}(E) = \sum_i \text{LDOS}(i, E) = -\frac{1}{\pi} \text{Tr}\left[\text{Im}[\mathbf{G}]\right], \qquad (2.4)$$

where $\mathbf{G} = \mathbf{G}^r$ are the retarded Green's functions.

Green's function formalism provides a method to include perturbations. The response to an external perturbation $\mathbf{V}$ may be found from a Dyson equation [62, 63]

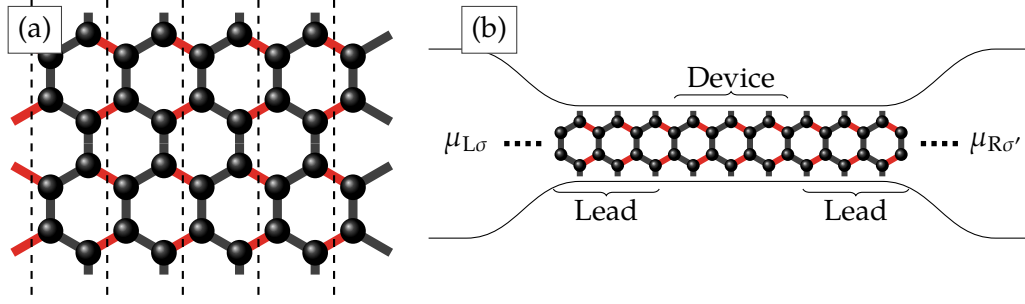$$\mathbf{G} = \mathbf{g} + \mathbf{g}\mathbf{V}\mathbf{G}, \qquad (2.5)$$

Figure 2.1: Illustrations of Landauer-Büttiker devices. (a) Two-lead device, for example a graphene nanoribbon, with leads left (L) and right (R). The leads have the chemical potentials μ_p, where p also denotes the spin index. (b) An example of a four-lead graphene device. The shaded areas enclose individual cells used in recursive Green's function techniques [63] (gray: periodic lead cells, red: device boundary cells, blue: internal device cells).

which relates the Green's functions of the perturbed system **G** to those of the unperturbed system **g**. From the Dyson equation, the local Green's functions of a device (D) coupled to an external perturbation (ex) read (derived in Appendix A)

$$\mathbf{G}_{\mathrm{DD}} = [E - \mathbf{H}_{\mathrm{D}} - \mathbf{\Sigma}_{\mathrm{ex}}]^{-1} \ . \tag{2.6}$$

The $\mathbf{\Sigma}_{\mathrm{ex}} = \mathbf{V}_{\mathrm{Dex}}\mathbf{g}_{\mathrm{ex}}\mathbf{V}_{\mathrm{exD}}$ is the self-energy: the energetic response in the device from the external perturbation. In particular, this allows to introduce couplings between two initially uncoupled (unperturbed) sub-systems, by considering the couplings as the perturbation. For example, joining initially uncoupled carbon chains to form graphene sheets as illustrated in Fig. 2.1(a). Here the chains (black) are perturbed by the longitudinal couplings (red).

As an extension to Eq. (2.6), recursive Green's function techniques [63] can be employed to lower the calculation cost of Eqs. (2.3) and (2.4). These techniques, presented in Appendix A, avoid the inversion of the full matrices in Eqs. (2.2) and (2.6). The implementations of the LDOS and DOS are presented in Appendix A.2.

Electronic transport properties are determined within the Landauer-Büttiker formalism. Landauer-Büttiker is a powerful tool that relates the chemical potentials and electronic currents through a mesoscopic system via transmission functions T. A number of good books give a detailed introduction to the subject, for example Datta [61] and Torres *et al.* [64]. The multi-channel Landauer-Büttiker formula defines the current through channel p as

$$I_p = \frac{e}{h} \sum_q \int_{-\infty}^{\infty} \mathrm{d}E \ \left[T_{qp} f \left(E - \mu_p \right) - T_{pq} f \left(E - \mu_q \right) \right] \ , \tag{2.7}$$

where T_{qp} are the transmissions between channels p and q, and $\mu_p = eV_p$ are the chemical potentials. Here, the channel indices p and q denote both the physical terminals, or leads, and the electronic spin-channels. For example, the transmission from, say, the left spin-up channel (L↑) to right spin-down channel (R↓) is $T_{\mathrm{R\downarrow L\uparrow}}$. The functions $f(E)$ are the usual Fermi-Dirac distribution functions. The zero temperature and low bias limit reads

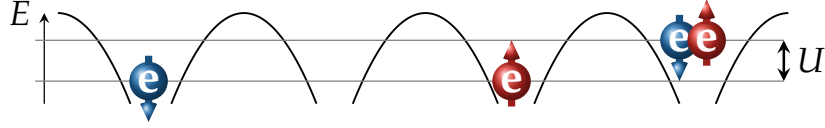$$I_p = G_0 \sum_q T_{qp} \left(V_p - V_q \right) \ , \tag{2.8}$$

Figure 2.2: Illustration of the on-site spin interaction of the Hubbard model. The electrons move in a background potential from the atomic lattice. If two electrons of different spin occupy the same space (right side) the they experience the Coulomb interaction with energy U. The type of the electronic spin is colored red for spin up and blue for spin down.

where the (single-spin) quantum of conductance is $G_0 = \frac{e^2}{h}$.

The transmissions are determined through the Fisher-Lee relations [65]

$$T_{pq}(E) = \text{Tr}\left[\mathbf{\Gamma}_p \mathbf{G}^\dagger \mathbf{\Gamma}_q \mathbf{G}\right] \, , \tag{2.9}$$

where $\mathbf{G} = [E - \mathbf{H}_\text{D} - \sum_p \mathbf{\Sigma}_p]$ is the retarded Green's function matrix of the device. The $\sum_p \mathbf{\Sigma}_p = \sum_p \mathbf{V}_p \mathbf{g}_p \mathbf{V}_p^\dagger$ is the *sum* of the self-energies from coupling to the leads, where $\mathbf{V}_p$ are the lead-to-device couplings and $\mathbf{g}_p$ is the uncoupled lead Green's function [60, 61]. The $\mathbf{\Gamma}_p = i\left[\mathbf{\Sigma}_p - \mathbf{\Sigma}_p^\dagger\right]$ are the level-broadenings from coupling to the leads. An example of a two-lead device is illustrated in Fig. 2.1(b): A graphene nanoribbon device. This example shows two graphene leads, left (L) and right (R), coupled to a central strip of graphene (the device). Notice that the leads can in principle be semi-infinite. Recursive techniques exist to optimize the calculations of transmission functions (Appendix A.4), as well as semi-infinite leads (Appendix A.3).

For a more detailed view into the electronic transport, we may also consider the local transmission currents from channel p between sites i and j [63]

$$\left[\mathbf{J}_p(E)\right]_{ij} = [\mathbf{H}]_{ij} \, \text{Im}[\mathbf{G}^r \mathbf{\Gamma}_p \mathbf{G}^a]_{ij} \, . \tag{2.10}$$

Although, it is often more convenient to use the alternative (atomic) form

$$\mathbf{J}_p(i, E) = \frac{1}{2} \sum_{j \in \langle i,j \rangle} \left[\mathbf{J}_p(E)\right]_{ij} \, . \tag{2.11}$$

which is the sum of all currents passing across the site i. The factor of two enters from summing over both incoming and outgoing currents.

2.2 Mean-field Hubbard model

In this thesis, we also explore the fundamentals of spin-interaction in graphene by way of a mean-field Hubbard model [66, 67]. Our model extends the above TB model by adding an on-site spin-interaction energy U (also referred to as the Hubbard U). It describes the energy gain with two electrons occupying the same space with opposite spin, see also Fig. 2.2. The opposite spin are referred to as spin *up* and *down*.

The Hamiltonian in the spin-interacting case is

$$\mathbf{H} = \underbrace{\sum_{\langle ij\sigma \rangle} t\mathbf{c}_{i\sigma}^{\dagger}\mathbf{c}_{j\sigma} + h.c.}_{\text{TB model}} + \underbrace{\sum_{i} U\mathbf{n}_{i\uparrow}\mathbf{n}_{i\downarrow}}_{\mathbf{H}_U: \text{ Hubbard model}} \tag{2.12}$$

This *two-particle* feature makes this a *many-particle* problem that we cannot solve in practice. The often used mean-field approach simplifies the problem to a single particle Hamiltonian interacting with a mean-field background, i.e., $\mathbf{n}_{i\sigma} = \langle \mathbf{n}_{i\sigma} \rangle + \delta n_{i\sigma}$. Using the common notation for the magnetic moments $m_i = \langle \mathbf{n}_{i\uparrow} \rangle - \langle \mathbf{n}_{i\downarrow} \rangle$ and local electron densities $n_i = \langle \mathbf{n}_{i\uparrow} \rangle + \langle \mathbf{n}_{i\downarrow} \rangle$ the Hubbard model becomes

$$\mathbf{H}_U \approx \sum_{i\sigma} U/2(n_i \pm m_i)\mathbf{n}_{i\sigma} \tag{2.13}$$

which can be solved self-consistently for the magnetic moments m_i and on-site densities n_i using

$$\langle \mathbf{n}_{i\sigma} \rangle = \int_{-\infty}^{E_F} dE\, \text{LDOS}(i\sigma, E)\,, \tag{2.14}$$

where $\text{LDOS}(i\sigma, E)$ is the LDOS at site i for electronic spin σ. An equivalent integral more suited for numerical implementation is derived in Appendix A.5.

Often it is advantageous to employ *mixing* between iterations, for example

$$m_i \leftarrow \alpha\,[m_i]_{\text{old}} + (1-\alpha)\,[m_i]_{\text{new}}\,, \tag{2.15}$$

$$n_i \leftarrow \alpha\,[n_i]_{\text{old}} + (1-\alpha)\,[n_i]_{\text{new}}\,, \tag{2.16}$$

In the case of graphene, however, $\alpha = 0$ yields reasonably fast convergence.

The self-consistent equation does not define a unique solution, and the final outcome depends on the initial guess (in a deterministic fashion). Fortunately, the ground state solution in graphene is readily obtained by starting with an initial *antiferromagnetic* guess, where the orientation of the magnetic moments are *opposite* on each of the graphene sublattices.

Large-scale electronic methods 3

This chapter presents the methods used in this thesis to calculate electronic properties of large-scale samples. The formulas are somewhat lengthly so their final forms are presented here and the derivations are written explicitly in Appendix B.

3.1 Polynomial expansion of the density of states

The inversion operation in determining the Green's functions $\mathbf{G}$ [Eq. (2.2)], for example to find the DOS, becomes numerically impractical or even impossible for very large systems e.g. several million sites. However, we wish to explore such large systems. Instead we can approximate the physically interesting quantities using Chebyshev polynomial expansions [68]. For a relatively small set of expansion coefficients (e.g. $N_{\text{Cby}} \in [10^2; 10^4]$) we are able to compute the DOS of several million atomic sites (even billions if we have the patience and computation memory).

The (orthogonal) Chebyshev polynomials are defined in the region $-1 < x < 1$

$$T_n(x) = \cos\left[n \arccos(x)\right], \tag{3.1}$$

for which the recursive relations follow

$$T_{n+1}(x) = 2x T_n(x) - T_{n-1}(x). \tag{3.2}$$

With the DOS defined as $\text{Tr}\left[\delta\left(E - \mathbf{H}\right)\right]$ we use the expansion [68, 69]

$$\delta(E - \mathbf{H}) = \frac{1}{\pi \Delta E \sqrt{1 - \tilde{E}^2}} \sum_{n=0}^{\infty} (\delta_{0n} + 1) T_n(\tilde{E}) T_n(\tilde{\mathbf{H}}) \tag{3.3}$$

where the *rescaled* energy $\tilde{E} = 2(E - \langle E \rangle)/\Delta E$ and Hamiltonian $\tilde{\mathbf{H}} = 2(\mathbf{H} - \langle E \rangle)/\Delta E$, such that energy spectrum is bounded $(E - \langle E \rangle) \in]-\Delta E/2; \Delta E/2[$. The last term $T_n(\tilde{\mathbf{H}})$ will require the eigenenergies of Schrödingers equation $\mathbf{H}\left|\psi\right\rangle = E\left|\psi\right\rangle$ to lie within the energy spectrum. (See also full derivation of Eq. (3.3) in Appendix B.2.)

The trace in the DOS [Eq. (2.4)] is replaced by a stochastic approximation

$$\text{Tr}\left[\cdots\right] \approx \frac{1}{N_R} \sum_{R}^{N_R} \langle R | \cdots | R \rangle, \tag{3.4}$$

where $|R\rangle = \sum_j \exp(i\phi_{Rj})\left|j\right\rangle$ are random-phase states, and ϕ_{Rj} are the random phases given to sites j [68]. This approximation is particularly well suited for large problem sizes D (the size of the Hamiltonian matrix)—the error scales as $1/\sqrt{N_R D}$ [68]. The final form of the approximation becomes [68] (derivation in Appendix B.5)

$$\text{DOS} \approx \frac{1}{\pi \Delta E N_R \sqrt{1 - \tilde{E}^2}} \sum_{n=0}^{N_\delta} g_n (\delta_{0n} + 1) T_n(\tilde{E}) \sum_{R}^{N_R} \langle R \left| T_n(\tilde{\mathbf{H}}) \right| R \rangle. \tag{3.5}$$
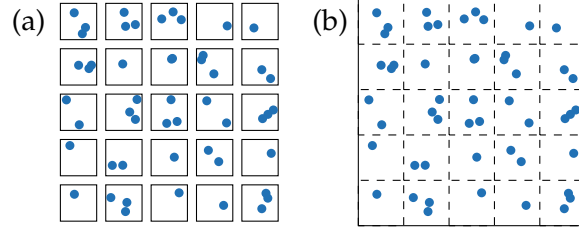
Figure 3.1: Illustration of the ensemble of separate disordered systems (a) and the combined disordered system (b). The disorder is here illustrated by blue dots. In case of the Chebyshev expansion of the DOS, the combined system (b) is *self-averaging*.

The truncation to only N_δ in the first sum of Chebyshev polynomials introduces errors, also known as Gibbs oscillations. The Gibbs oscillations can be severely reduced by the use of kernel coefficients g_n. In case of the DOS we will use the Jackson kernel [68].

Applying the Jackson kernel to an expansion of the δ-function yields a Gaussian-like approximation [68]

$$\delta(x - x_0) \sim \frac{1}{\sqrt{2\pi\sigma_J^2}} \exp\left[-\frac{(x - x_0)^2}{2\sigma_J^2}\right] . \tag{3.6}$$

In the worst case (near $x_0 = 0$), the broadening (or Gaussian width) is $\sigma_J \approx \pi\Delta x/N_\delta$, where Δx is the spectrum of x. Using graphene as an example (with $\Delta E \sim 10\,\text{eV}$) then the energy resolution of the expansion is $\sigma_{\text{graphene}} \sim 30\,\text{eV}/N_\delta$.

Using Eq. (3.2) to iteratively evaluate the last sum in Eq. (3.5), the problem boils down to a sum of sparse-matrix-vector products, which are particularly fast and memory efficient.

This form of the DOS is well suited for examining the average influence of disorder in bulk, or periodic samples. To properly consider all correlated effects, multiple realizations of the disorder are introduced *simultaneously*. This can be done in super cells, where the unit cell is repeated and the disorder is randomly distributed. Using exact Green's function techniques, these super cells cannot be very large, and we instead average over *ensembles* of smaller super cells. This kind of situation is illustrated in Fig. 3.1(a).

However, larger samples include more correlation effects, and, in turn, smaller ensembles can be used. This kind of situation is illustrated in Fig. 3.1(b). By considering Chebyshev expansions, the ensemble can be reduced considerably, even to the point where only a single sample is needed. An additional advantage is that the corresponding Brillouin zones are very small, and a single point in reciprocal space (e.g. the origin) is enough to capture the physical behavior. The error of the stochastic trace is even reduced by larger system sizes. In other words, the influence of disorder is readily studied through Chebyshev expansions using very large, disordered systems. It is worth noting that the system need not be a regular square array as illustrated in Fig. 3.1.

3.2 Kubo-Greenwood transport formalism

The Kubo-Greenwood formalism is based on the *fluctuation-dissipation theorem* which relates the conductivity with the velocity correlation function [70, 71]. An efficient order-N real-space method (*Kubo method* [64, 72–74]) allows to study the conductivity of large systems (millions of sites). With this method we can explore features which are out of reach for standard Landauer-Büttiker models. Nonetheless, some limitations exists for the Kubo method, which we will discuss at the end of this section.

The Kubo-Greenwood formula [70, 71] for the conductivity-tensor elements $[\sigma]_{\alpha\beta} \equiv \sigma_{\alpha\beta}$ reads

$$\sigma_{\alpha\beta}(\omega) = \frac{\pi\hbar e^2}{\Omega} \int dE \, \frac{f(E) - f(E + \hbar\omega)}{\hbar\omega} \, \text{Tr}\left[\mathbf{V}_\alpha^\dagger \delta\left(E - \mathbf{H}\right) \mathbf{V}_\beta \delta\left(E + \hbar\omega - \mathbf{H}\right)\right] , \quad (3.7)$$

where Ω is the sample volume and $\mathbf{V}_\alpha$ is the velocity operator in the α direction. Limiting to the diagonal, zero temperature, and the DC limit $\omega \to 0$ the conductivity can be expressed in the shorter form [64, 72, 75]

$$\sigma_{\alpha\alpha}(E) = \frac{\pi\hbar e^2}{\Omega} \, \text{Tr}\left[\mathbf{V}_\alpha^\dagger \delta\left(E - \mathbf{H}\right) \mathbf{V}_\alpha \delta\left(E - \mathbf{H}\right)\right] . \quad (3.8)$$

By replacing the last $\delta\left(E - \mathbf{H}\right)$ with $(1/2\pi\hbar) \int dt \, \exp\left[i(E - H)t/\hbar\right]$ and performing the integral we are left with

$$\sigma_{\alpha\alpha}(E) = \frac{e^2}{\Omega} \lim_{t \to \infty} \frac{d}{dt} \underbrace{\text{Tr}\left[\delta\left(E - \mathbf{H}\right)\left(\mathbf{X}_\alpha(t) - \mathbf{X}_\alpha(0)\right)^2\right]}_{\Omega\rho(E)\Delta X_\alpha^2(E,t)} , \quad (3.9)$$

where $\mathbf{X}_\alpha(t)$ is the position operator at time t (Heisenberg picture) in the α direction, $\rho(E) = \text{Tr}\left[\delta\left(E - \mathbf{H}\right)\right]/\Omega$ is the DOS per unit volume, and $\Delta X_\alpha^2(E, t)$ is the mean squared displacement (or spread). We can further generalize the formula to the *running conductivity* by lifting the $t \to \infty$ limit

$$\sigma_{\alpha\alpha}(E, t) = e^2 \rho(E) \frac{1}{t} \Delta X_\alpha^2(E, t) . \quad (3.10)$$

We have used a common approximation by replacing the $\frac{d}{dt} \to 1/t$, which is usually motivated by producing more smooth curves [64, 75]. Although this technically is an incorrect definition and should be used with caution, it simplifies the analysis and remains instructive of the qualitative physical behavior. Notice that it is a valid approximation in the (diffusive) case of $\Delta X_\alpha^2(E, t) \propto t$.

The Eq. (3.10) is used to find the running conductivities of large, disordered samples. We use periodic samples to avoid edge effects. We define the corresponding *diffusion coefficient*

$$D_\alpha(E, t) = \frac{1}{t} \Delta X_\alpha^2(E, t) , \quad (3.11)$$

and the *simulation lengths*

$$L_\alpha(E, t) = 2\sqrt{\Delta X_\alpha^2(E, t)} . \quad (3.12)$$

Notice that the simulation length is *not* the same length as the size of the simulation sample.

The particular form of the expression $\rho(E)\Delta X_\alpha^2(E,t) = \text{Tr}\left[\delta\left(E - \mathbf{H}\right)\left(\mathbf{X}_\alpha(t) - \mathbf{X}_\alpha(0)\right)^2\right]$ motivates the use of Chebyshev-polynomial expansions [Eq. (3.1)] and the stochastic trace approximation. We use the additional Chebyshev expansion of the exp-function [68] (Appendix B.2)

$$\exp(i\mathbf{H}t/\hbar) = \sum_n^\infty \left(\delta_{0n} + 1\right)\left(-i\right)^n J_n(\Delta E t/\hbar)T_n(\tilde{\mathbf{H}})\,, \qquad (3.13)$$

where $J_n(x)$ is the Bessel function of the first kind, and the rescaled Hamiltonian $\tilde{\mathbf{H}} = 2(\mathbf{H} - \langle E\rangle)/\Delta E$. The final form of the mean squared displacement is

$$\rho(E)\Delta X_\alpha^2(E,t) \approx \frac{1}{\pi\Delta E\sqrt{1 - \tilde{E}^2}} \sum_{n=0}^{N_\delta} g_n(\delta_{0n} + 1)T_n(\tilde{E}) \sum_R^{N_R} \left\langle\psi_R(t)\left|T_n(\tilde{\mathbf{H}})\right|\psi_R(t)\right\rangle\,,$$

$$(3.14)$$

where the δ-function from Eq. (3.9) is expanded in N_δ Chebyshev polynomials. The time-dependence has been bundled into the new states

$$\left|\psi_R(t)\right\rangle = [\mathbf{X}, \mathbf{U}(t)]\left|R\right\rangle = \sum_m^{N_{\exp}} \left(\delta_{0m} + 1\right)\left(-i\right)^m J_m(\Delta E t/\hbar)\left[\mathbf{X}, T_n(\tilde{\mathbf{H}})\right]\left|R\right\rangle\,, \quad (3.15)$$

where the expansion is truncated to $N_{\exp}$ polynomials, and $|R\rangle = \sum_j \exp(i\phi_{Rj})|j\rangle$ are random-phase states. However, instead of Eq. (3.15) for every time t, we *evolve* the time iteratively using $\left|\psi_R(t)\right\rangle \rightarrow \left|\psi_R(t + \delta t)\right\rangle$. In the end, this requires fewer expansions coefficients $N_{\exp}$.

The Kubo method relates the conductivity to the mean displacement of *wave-packets* initiated by the random-phase states as a function of time, illustrated in Fig. 3.2(a). By iteration, the wave-packets are continually evolved until the simulation saturates into a transport regime.

The quantum transport is divided into three important regimes: In the *ballistic* regime, the wave-packets experience no scattering and the conductivity diverges in the long time limit. In the *diffusive* regime, the strong scattering makes the conductivity saturate to a maximum value. In the *localized* regime, scattering dominates and wave-packets and the corresponding mean-squared displacement saturate.

The Kubo simulation of a sufficiently disordered system will undergo transitions between ballistic and diffusive, and often also between diffusive and localized. At the beginning of the simulation, the wave-packets will propagate only short distances, and very few scattering events will occur. This would manifest itself in a ballistic regime, where the $\Delta X_\alpha(E,t) \propto t$ and $\sigma_{\alpha\alpha}(E,t) \propto t$, illustrated in Fig. 3.2(b). If a sample is pristine (i.e. no structural imperfections), the simulation will remain in the ballistic regime. If, however, the sample is weakly disordered, the simulation may experience a quasi-ballistic behavior. Here the conductivity still diverges, however, slower than for the ballistic case (sub-linearly). Given enough disorder, the simulation transitions into the diffusive regime.

The onset of the diffusive regime is identified by a quadric-to-linear transition of the mean-squared displacement, and, in turn, the $\Delta X_\alpha(E,t) \propto \sqrt{t}$ and $\sigma_{\alpha\alpha}(E,t)$
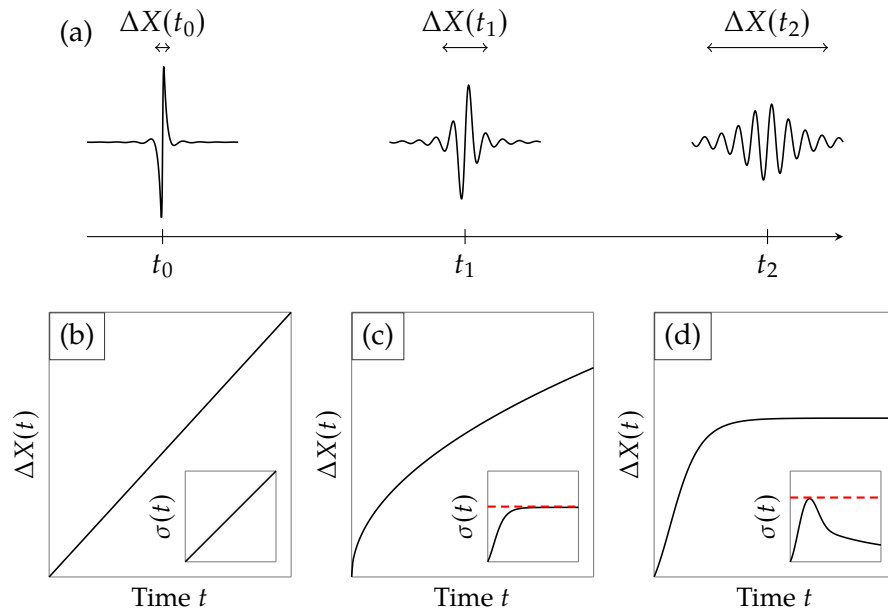
Figure 3.2: Schematic illustrations of the Kubo method simulation. (a) Schematic illustration of the time evolution of a wave packet. At start $t = 0$ the wave packet is extremely local to a particular site and the mean spread is $\Delta X(t = 0) = 0$. As the packet evolves the spreading increases, shown here at times t_0, $t_1 > t_0$, and $t_2 > t_1$. (b-d) Schematic illustrations of the three important transport regimes: the ballistic (b), the diffusive (c), and the localized (d). In all cases the main frames display the mean displacements $\Delta X(t)$ and the insets the corresponding conductivities $\sigma(t)$. The red dashed lines in the insets of (c) and (d) denote the semi-classical conductivities.

is constant (nonzero), illustrated in Fig. 3.2(c). If disorder is not too strong, the simulation may remain the diffusive regime and the semi-classical conductivity can readily be obtained through

$$\sigma_{\alpha\alpha,\text{SC}}(E) = \sigma_{\alpha\alpha}(E, t_{\max}),\tag{3.16}$$

illustrated by the red dashed line in the inset of Fig. 3.2(c). In many cases, however, the diffusive regime is short lived, and strong scattering causes the simulation to move into the localized regime.

At localization, the wave-packets and the mean-squared displacement saturates to a constant value, and $\sigma_{\alpha\alpha}(E, t) \propto 1/t$, illustrated in Fig. 3.2(d). Here, the common approach is to define the semi-classical conductivities as the maximum running conductivity

$$\sigma_{\alpha\alpha,\text{SC}}(E) = \max[\sigma_{\alpha\alpha}(E, t > 0)].\tag{3.17}$$

This is illustrated by the red dashed line in the inset of Fig. 3.2(d).

Using the above, we can analyze the different transport regimes of larger, more realistically sized samples. Furthermore, this allows us to explore the influence of experimentally sized features including the influence structural imperfections at the atomic scale.

Graphene and antidot latttices 4

The electronic properties of graphene are unique and remarkable (as discussed in Section 1.1) but also quite dependent on the precise atomic structure. Through nanostructuring, graphene can take on whole new features. As discussed in the introduction Section 1.3, graphene with small perforations, or antidots has received substantial interest due to the possibility of introducing large band gaps into the otherwise linear-dispersive material. This chapter presents the general electronic properties of graphene, and how these change when introducing a graphene antidot lattice (GAL).

4.1 Pristine graphene

Graphene is a 2D layer of carbon atoms arranged in a hexagonal lattice, illustrated in Fig. 4.1(a). The atomic structure is formed from the strong σ bonds: the sp^2 hybridization between the s and two p orbitals, deep in the valence energy region. This leaves the final p orbital, which forms a half-filled π band that dominates the electronic properties. The resulting atomic lattice is hexagonal—a bipartite with two sites in the unit cell, illustrated by the orange shaded area in Fig. 4.1(a). The two equivalent but independent sublattices are usually referred to as A and B.

The lattice vectors can be written as [see Fig. 4.1(a)]

$$\begin{aligned}
\mathbf{a}_1 &= (-a_{\text{zz}}, a_{\text{ac}})/2 \\
\mathbf{a}_2 &= (+a_{\text{zz}}, a_{\text{ac}})/2\,.
\end{aligned} \tag{4.1}$$

where the lattice constants are $a_{\text{zz}} = 2.46\,\text{Å}$ and $a_{\text{ac}} = \sqrt{3}a_{\text{zz}} = 4.26\,\text{Å}$, respectively. The hexagonal lattice further gives rise to a hexagonal Brillouin zone, illustrated in the inset of Fig. 4.1(a). In turn, the reciprocal vectors read

$$\begin{aligned}
\mathbf{b}_1 &= 2\pi(a_{\text{zz}}^{-1}, -a_{\text{ac}}^{-1}) \\
\mathbf{b}_2 &= 2\pi(a_{\text{zz}}^{-1}, +a_{\text{ac}}^{-1})\,.
\end{aligned} \tag{4.2}$$

where the high-symmetry points can be expressed

$$\begin{aligned}
\mathbf{K} &= (\mathbf{b}_1 + \mathbf{b}_2)/3 \\
\mathbf{K}' &= (2\mathbf{b}_1 - \mathbf{b}_2)/3 \\
\mathbf{M} &= (\mathbf{K} + \mathbf{K}')/2 \\
\mathbf{\Gamma} &= (0, 0)
\end{aligned} \tag{4.3}$$

Graphene is well described using the nearest-neighbor (NN) TB model [5]

$$\mathbf{H} = \sum_{\langle ij \rangle} t\mathbf{c}_i^\dagger \mathbf{c}_j + \text{H.c.,} \tag{4.4}$$
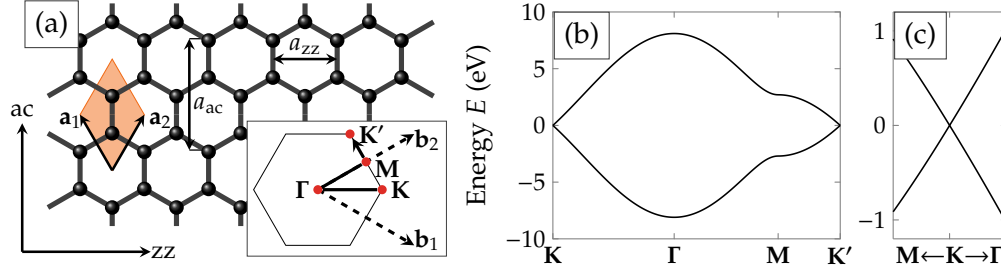
Figure 4.1: Atomic structure (a) and bandstructures (b) and (c) of pristine graphene. (a) The unit cell of graphene is displayed by the shaded orange box. Lattice vectors are $\mathbf{a}_1$ and $\mathbf{a}_2$, and lattice constants are $a_{zz} = 2.46\,\text{Å}$ and $a_{ac} = 4.26\,\text{Å}$. The inset displays the Brillouin zone of pristine graphene. The high-symmetry points $\mathbf{K}$, $\mathbf{\Gamma}$, $\mathbf{M}$, $\mathbf{K'}$ are illustrated by red points. Reciprocal lattice vectors are $\mathbf{b}_1$ and $\mathbf{b}_2$. The bandstructure high-symmetry path used in (b) is illustrated by the black path in the Brillouin zone in (a). (b) The bandstructure is calculated using the NN-TB model of graphene, using the NN hopping $t = -2.7\,\text{eV}$. (c) The bands near the Dirac points $\mathbf{K}$, and by symmetry the bands are similar at $\mathbf{K'}$.

where $\langle ij \rangle$ represents the set of NNs. The parameter t is the NN hopping, and its value depends on the context. It is usually fitted to experimental quantities or the results of first principle calculations. In the case of pristine graphene we use $t = 2.7\,\text{eV}$ [5].

The pristine Hamiltonian of graphene reads [5]

$$\mathbf{H}(\mathbf{k}) = \begin{bmatrix} 0 & t f(\mathbf{k}) \\ t f^*(\mathbf{k}) & 0 \end{bmatrix} \tag{4.5}$$

where

$$f(\mathbf{k}) = 2\cos\left(k_x a_{zz}\right) + 4\cos\left(k_x a_{zz}/2\right)\cos\left(k_y a_{ac}/2\right) \ . \tag{4.6}$$

The bandstructure along the of high-symmetry path of pristine graphene is displayed in Fig. 4.1(b), where the path is demonstrated in the Brillouin zone in Fig. 4.1(a). Notice in particular the linear bands near the (Dirac) points $\mathbf{K}$ and $\mathbf{K'}$. These particular bands give rise to many of the unique electronic properties of graphene [5].

4.2 The graphene antidot lattice

By introducing antidots into graphene, whole new features may emerge. In particular, large band gaps can form in GALs. The bandstructure of such an example is displayed in Fig. 4.2(a). A relation between the band gap and the antidot lattice was demonstrated by Pedersen *et al.* [40], $E_g \propto \sqrt{N_{rem}}/N_{tot}$, where N_{tot} and N_{rem} are, respectively, the *total* number of sites without the antidot and the number of *removed* sites with the antidot. This is reproduced in Fig. 4.2(b). The GALs from this study were arranged in a triangular superlattice, illustrated schematically in the inset of Fig. 4.2(b). The antidot lattice of Fig. 4.2(a) uses the same triangular superlattice, and the unit cell is illustrated in the inset.

This particular triangular superlattice results in GALs which always display band gaps, scaled as described above. However, one of the key issues with GALs is the
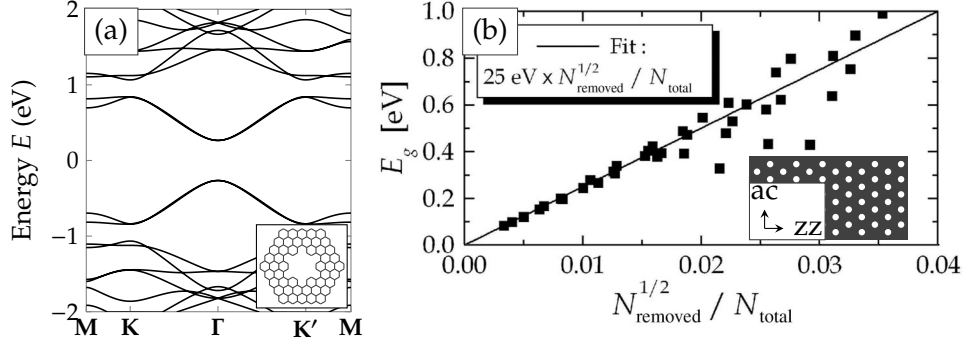
Figure 4.2: Bandstructure (a) and band gaps (b) of GALs. (a) The bandstructure of a gapped GAL, with the unit cell depicted in the inset. Notice that the Dirac points of pristine graphene have been folding on to the Γ point of the GAL Brillouin zone. (b) The band gap scaling of gapped GALs, $E_g \propto \sqrt{N_{rem}}/N_{tot}$. The inset illustrates the triangular superlattice, where all antidots are arranged on a triangular grid (the graphene lattice orientation is denoted by the zz and ac directions). The main panel in (b) has been reproduced from Pedersen *et al.* [40].

intricate influence of the superlattice vectors. A band gap may appear in some GALs, but completely vanish upon small changes in the superlattice vectors [41–43]. In this thesis, we denote this concept antidot lattice *commensurability*.

The geometrical rules that govern the opening of band gaps can be demonstrated by extending the pristine graphene TB model with the periodic perturbation $U(\mathbf{r})$. The superlattice vectors of the perturbation are defined

$$\begin{aligned} \mathbf{R}_1 &= n_1\mathbf{a}_1 + m_1\mathbf{a}_2 \\ \mathbf{R}_2 &= n_2\mathbf{a}_1 + m_2\mathbf{a}_2 \end{aligned} \tag{4.7}$$

where $\mathbf{a}_1$ and $\mathbf{a}_2$ are the pristine graphene lattice vectors [Eq. (4.1)], and n_1, n_2, m_1, and m_2 are integers. At the Dirac points, the perturbed Hamiltonian has the form

$$\mathbf{H}(\mathbf{K}) = \begin{bmatrix} U_{AA}(\mathbf{K}) & U_{AB}(\mathbf{K}) \\ U_{BA}(\mathbf{K}) & U_{BB}(\mathbf{K}) \end{bmatrix}, \tag{4.8}$$

where $f(\mathbf{K}) = 0$ [Eq. (4.6)]. We assume sublattice symmetry such that $U_{AA}(\mathbf{K}) = U_{BB}(\mathbf{K})$. Then, only when $U_{AB}(\mathbf{K}) = U_{BA}^*(\mathbf{K}) \neq 0$ can we open a band gap at the Dirac point in graphene. This is indeed the case when the reciprocal lattice of the periodic perturbation coincides with the Dirac points: when $\mathbf{R}_i\mathbf{K} = 2n\pi$ for either of $i \in \{1, 2\}$, where n is an integer. This can be written explicitly using $\mathbf{K} = (\mathbf{b}_1 + \mathbf{b}_2)/3$ [from Eq. (4.3)]

$$\mathbf{R}_i\mathbf{K} = \frac{n_i}{3}\mathbf{a}_1\mathbf{b}_1 + \frac{n_i}{3}\mathbf{a}_2\mathbf{b}_1 + \frac{m_i}{3}\mathbf{a}_1\mathbf{b}_2 + \frac{m_i}{3}\mathbf{a}_2\mathbf{b}_2 \tag{4.9}$$

$$= \frac{2\pi}{3}(n_i + m_i) \tag{4.10}$$

where $\mathbf{b}_1$ and $\mathbf{b}_2$ are the reciprocal lattice vectors of the graphene lattices [Eq. (4.2)]. This is satisfied when $(n_i + m_i)/3$ is an integer, or modulus$(n_i + m_i, 3) = 0$.

Some examples of GALs and their respective atomic structures and reciprocal lattices are shown in Fig. 4.3. These three similar GALs are either semimetallic (monolayer
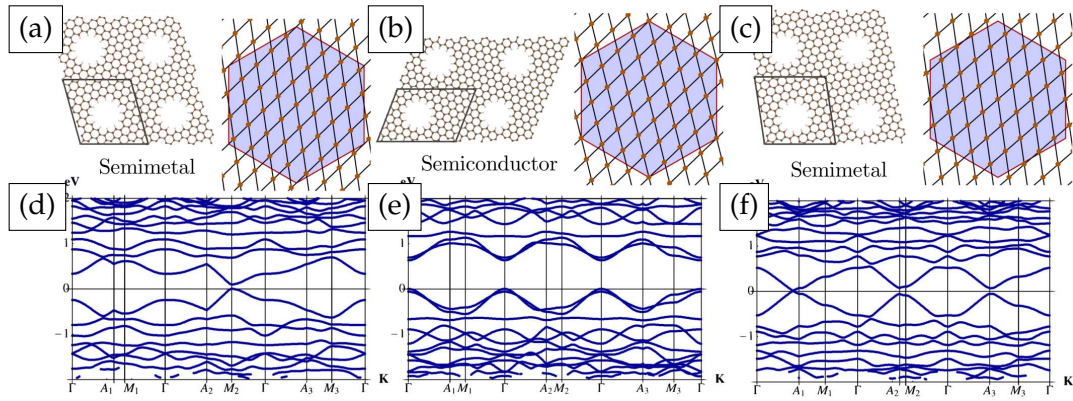
Figure 4.3: Lattice commensurability of graphene antidot lattices (GALs). Three different GALs (a),(b), and (c) with different electronic behaviors illustrated in the bandstructures, respectively, (d), (e), and (f). Next to the atomic structures in (a), (b), and (c) are the reciprocal lattices display on top of the pristine graphene Brillouin zone. Notice in (b) the reciprocal lattice points coincide with the Dirac point of graphene. Reproduced from Dvorak *et al.* [43].

graphene-like) or semiconducting, depending entirely on the superlattice orientation and size. On closer inspection, the semi-conducting GAL is the only geometry in which the reciprocal lattice points coincide with the Brillouin zone of graphene.

On top of the antidot lattice commensurability, the atomic structure of the antidot also plays a large role in the electronics. For example, in Chapter 6 we explore the fundamental differences between zz-edged triangular antidots compared the ac-edged triangular antidot. In particular, the zz-edged triangular antidots displays large band gaps, *irrespective* of commensurability arguments.

Patterned bilayer graphene

<div style="text-align: right">5</div>

Bilayer graphene [Illustrated in Fig. 5.1(a)] has interesting properties quite different from those of monolayer graphene [59]. The bandstructure [Fig. 5.1(b) with TB model of McCann and Koshino [59]] resembles that of monolayer graphene with an additional band splitting induced by the inter-layer coupling [blue arrows in Fig. 5.1(a)]. Close to the Dirac points (**K**) the bands show parabolic dispersion [black bands in Fig. 5.1(c)]. Furthermore, by breaking the layer-symmetry then sizable band gaps appear [red bands in Fig. 5.1(c)]. This could be achieved, for example, by applying a perpendicular electric field (transverse bias), thereby inducing opposite on-site potentials in the top and bottom layers. In Fig. 5.1(c) an inter-layer potential difference $U = 0.1\gamma_0$ is applied, where γ_0 is the NN TB hopping energy. However, the parabolic bands yield lower mobilities, and, in turn, degraded performance compared to the linearly-dispersive graphene monolayer.

The recent procedural optimization [12] of clean van der Waals (vdW) stacking of 2D materials [11] has paved a way to pursue stacked systems of *different* layers. Here we examine a bilayer graphene heterostructure, where a pristine layer of graphene is placed on top of different layer of graphene with a regular lattice of holes, or antidots, illustrated in Fig. 5.2. This class of graphene systems has been dubbed GOAL: graphene on graphene antidot lattice. Through geometric design we can engineer a band structure very different from the parabolic dispersion of regular bilayer graphene. We demonstrate below that GOALs can display linearly dispersing bands (with a high corresponding mobility), resembling that of monolayer graphene. Nevertheless, these can be made gapped by breaking layer symmetry.

The GOALs depend to a great extent on the orientation of the antidot lattice with respect to the graphene lattice. That is, GOALs depend on the antidot lattice commensurability, in much the same way as monolayer GALs (Section 4.2). We will examine two different orientations of the antidot lattices: one which always forms
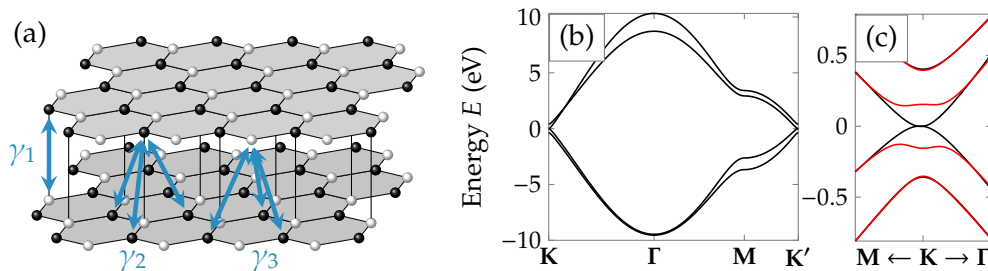

Figure 5.1: Structure (a) and electronic properties of pristine (b) and biased (c) bilayer graphene. (a) Atomic structure of bilayer graphene, with the inter-layer couplings γ_1, γ_2, and γ_3 illustrated by blue arrows. (b) Bandstructure of unbiased bilayer graphene. (c) Local bandstructure near **K** of unbiased (black) and biased ($U = 0.1\gamma_0$, red) bilayer graphene. The (full) TB model is reproduced from McCann and Koshino [59].
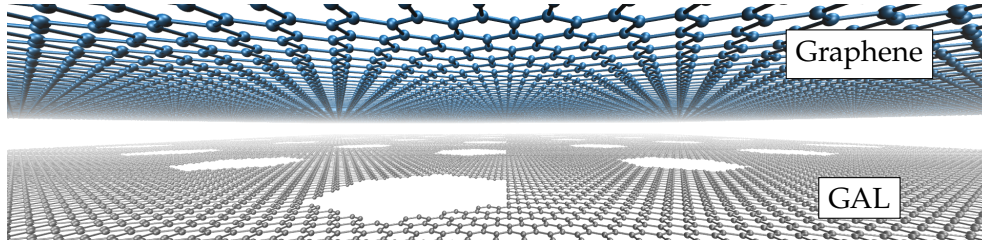
Figure 5.2: Illustration of GOAL: graphene (blue) on graphene antidot lattice (gray). The inter-layer distance has been exaggerated for illustrative purposes. We consider a distance similar to bilayer graphene.
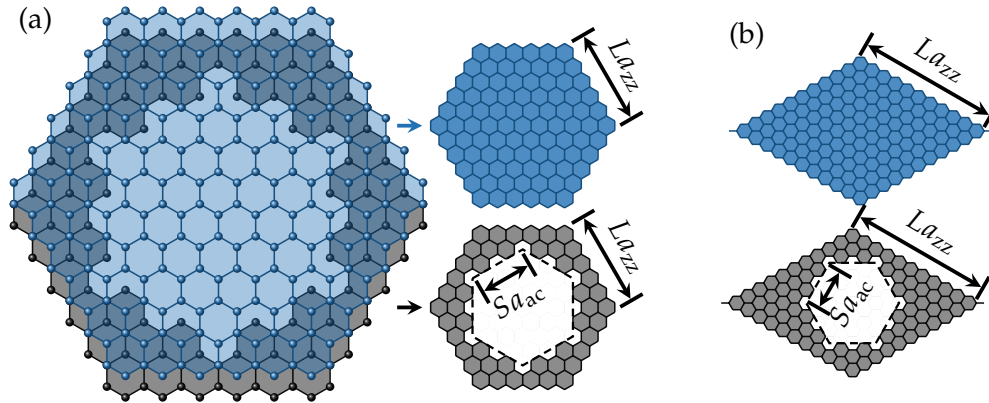

Figure 5.3: Illustrations and atomic structures of GOALs. (a) The Wigner-Seitz cell (left) and the individual layers (right) of the $\{L, S\} = \{6, 2\}$ GOAL. (b) The individual layers of the $\{11, 2\}_{\text{rot}}$ GOAL.

commensurate lattices, and another in which commensurability depends on the dimensions.

5.1 Graphene on antidot lattice (GOAL)

In regular bilayer graphene, the relative twist angle between the two layers has large impact on the electronic properties [76, 77]. We focus on the fundamental possibilities and consider perfect Bernal (AB) stacking without twisting of the layers. Indeed experiments with bilayer graphene have demonstrated manually twisting the top layer until it "locks" into place at the Bernal stacking angle [78].

We use two similar triangular superlattices, here referred to as the *regular* and the *rotated* antidot lattice. The regular lattice is defined by lattice vectors aligned parallel to the ac-directions. This leads to a hexagonal Wigner-Seitz cell, shown in Fig. 5.3(a). The *rotated* vectors align parallel to the zz-directions and the Wigner-Seitz cell takes the form of a rhombus, shown in Fig. 5.3(b).

The regular lattices are *always commensurate*, and the corresponding monolayer GALs are always gapped, as originally demonstrated by Pedersen *et al.* [40] (see also discussion in Section 4.2). On the other hand, the rotated lattices exhibit varying commensurability: one third of the possible superlattice vectors yield commensurate lattices, while the remaining yield incommensurate lattices. In addition to antidot

lattice commensurability, the exact shape of the antidot also has large influence on the electronic properties of antidot lattices [48, 79]. Extended zz-edges, which are generally present for large circular holes, will induce quasilocalized states that in monolayer GALs significantly quench any present band gap. We limit our analysis to hexagonal antidots to avoid this somewhat irregular property.

We adapt the nomenclature of Pedersen *et al.* [40] and denote GOALs by $\{L, S\}$ and $\{L, S\}_{\text{rot}}$, for the regular and rotated lattices, respectively. The geometry $\{L, S\}$ refers to a regular antidot lattice with a hexagonal unit cell of side length La_{zz} and a hexagonal antidot of side length Sa_{ac}. The geometry $\{L, S\}_{\text{rot}}$ refers to a rotated antidot lattice with a rhombus unit cell of side length La_{zz} and a hexagonal antidot of side length Sa_{ac}. (See also Fig. 5.3.) The lattice constants along the zz- and ac-directions are $a_{\text{zz}} = 2.46\,\text{Å}$ and $a_{\text{ac}} = 4.26\,\text{Å}$, respectively.

In regular bilayer graphene there are four distinct sublattices, two in each layer. The low-energy properties of bilayer graphene are dominated by the nondimers (sites above or below a hexagon ring). The dimers (below or above carbon sites) only play a minor role. The carbon sites of GOALs are not all true dimers or nondimers, since sites have been removed from the antidot layer. However, their low-energy behavior remains largely determined by the four original sublattices of bilayer graphene, irrespective of the removed sites. Under these circumstances we continue to refer to them collectively as dimers and nondimers, respectively.

The electronic properties are described using a NN bilayer TB model

$$\mathbf{H} = \sum_i \pm \frac{U}{2} \mathbf{c}_i^\dagger \mathbf{c}_i + \sum_{\langle ij \rangle} \gamma_0 \mathbf{c}_i^\dagger \mathbf{c}_j + \sum_{\langle\langle ij \rangle\rangle} \gamma_1 \mathbf{c}_i^\dagger \mathbf{c}_j + \text{H.c.}, \qquad (5.1)$$

where $\langle ij \rangle$ represents the intra-layer NNs and $\langle\langle ij \rangle\rangle$ represents the inter-layer NNs (dimers). The intra-layer coupling $\gamma_0 = -3.16\,\text{eV}$, the inter-layer coupling $\gamma_1 = 0.381\,\text{eV}$, and the onsite energies $\epsilon = \pm U/2$ with $+$ for top layer and $-$ for bottom layer. The inter-layer asymmetry U, also referred to as the transverse bias, is varied, but predicted to realistically lie between $\pm 0.3\,\text{eV}$ [80]. Demonstrated in Paper I, extending the model to include the skew hopping terms γ_3 and γ_4 has little impact on the properties within the energies of interest, so these terms are excluded.

The transport properties are determined using Landauer-Büttiker [Eq. (2.8)] along with the Fisher-Lee relations for the transmission functions and currents [Eqs. (2.9) and (2.11)].

5.2 The linear (parabolic) dispersion of GOAL

We first examine the electronic properties of GOALs in the absence of a transverse bias ($U = 0$). The most noticeable feature of commensurate GOALs is a transformation, near the Dirac-points, from the parabolic bandstructure of bilayer graphene to a linear bandstructure, illustrated in Fig. 5.4. The commensurate geometries $\{L, S\} = \{16, 6\}$ and $\{26, 6\}_{\text{rot}}$, respectively Figs. 5.4(a) and 5.4(b), both display linear bandstructures, regardless of antidot lattice orientation. On the other hand, incommensurate GOALs remain parabolic, as for example the $\{27, 6\}_{\text{rot}}$ GOAL in Fig. 5.4(c).
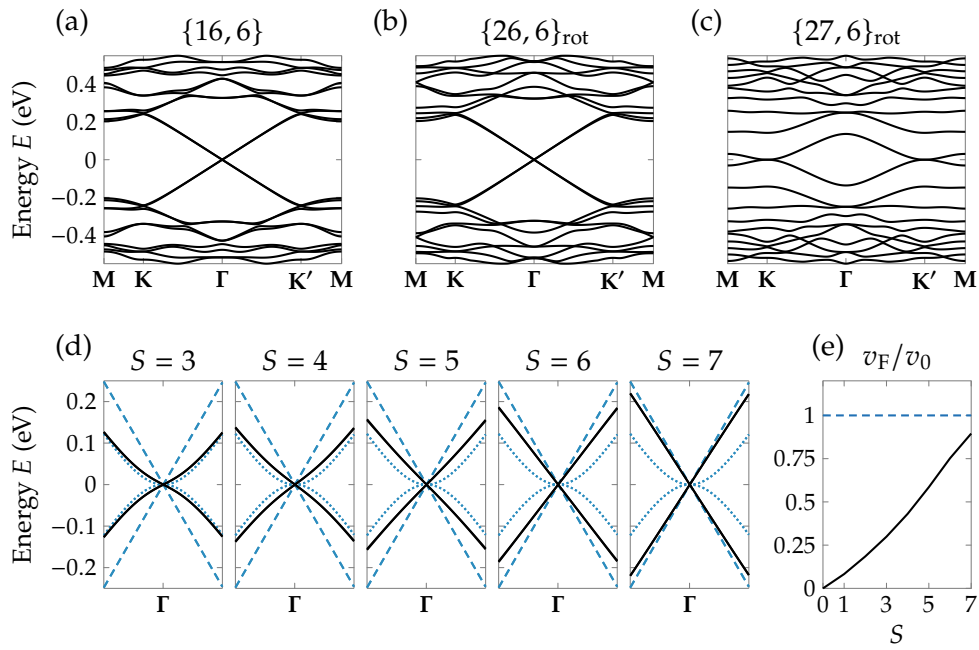
Figure 5.4: Bandstructures of commensurate and incommensurate GOALs. (a-c) Bandstructures of GOALs with $\{L, S\} = \{16, 6\}$ (a), $\{26, 6\}$ (b), and $\{27, 6\}_{\text{rot}}$ (c). (d) Bandstructures of $\{16, S\}$ GOALs near the Dirac point. The size of the antidot varies from $S = 3$ to $S = 7$ (left to right). We compare the GOALs (black solid) with monolayer (blue dashed) and bilayer (blue dotted) graphene. (e) The $E_{\text{F}} = 0$ Fermi velocity of $\{16, S\}$ GOALs.
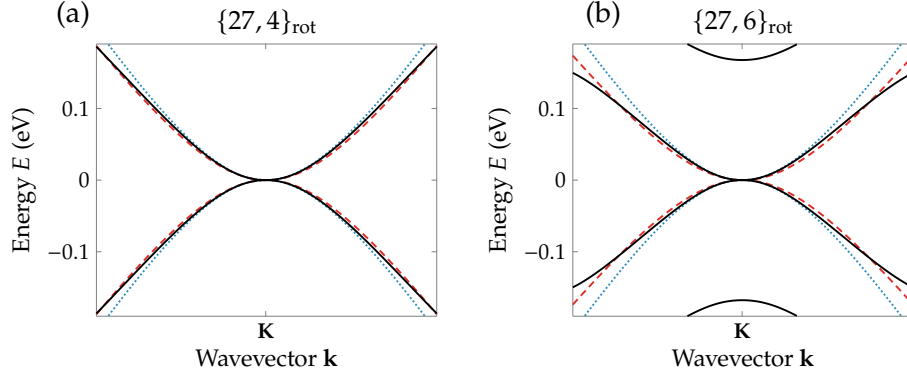
Figure 5.5: Bandstructures of rotated GOALs $\{27,4\}_{\text{rot}}$ (b) and $\{27,6\}_{\text{rot}}$. The bandstructures of GOAL (black solid) are compared to those of regular bilayer graphene (blue dotted) and the GOAL continuum model (red dashed).

The transition towards linear bands (when present) is gradual. As the antidot size increases (or the density of antidots decreases), the bandstructures of commensurate GOALs transform from bilayer-like to monolayer-like. In the panels of Fig. 5.4(d), we see the transition of the low energy bands of the $\{16, S\}$ GOALs as the antidot size is varied. We compare the GOALs (black solid) with monolayer (blue dashed) and bilayer (blue dotted) graphene. It is apparent that the bands of GOAL resemble bilayer graphene at small S (left-most panels). At large S (right-most panels) the bands begin to resemble those of monolayer graphene. This transition *does not* occur with an ever increasing curvature at the Dirac-point. Instead the bands always remain linear for $S > 0$, but with a regularly increasing Fermi velocity v_F ($E_\text{F} = 0$). Albeit, at small S this linear part is confined to a narrow window of energies. The Fermi velocities v_F are shown in Fig. 5.4(e), quantifying the transition from bilayer $v_\text{F} = 0$ towards monolayer $v_\text{F} = v_0$, where v_0 is the Fermi velocity of monolayer graphene.

One of the consequences of incommensurate GAL is a dispersion which resembles monolayer graphene with a (smaller) renormalized velocity v_GAL. This can be used to approximate the bandstructures of incommensurate GOALs. Within the low-energy continuum model of bilayer graphene [59],

$$E_\pm(k) = \pm \frac{\gamma_1}{2} \left[\sqrt{1 + 4\hbar^2 v_0^2 k^2 / \gamma_1^2} - 1 \right], \tag{5.2}$$

we replace the monolayer velocity v_0 with an average layer velocity $\bar{v}_\text{F} = (v_0 + v_\text{GAL})/2$. The TB bandstructures and the continuum models (solid and dashed, respectively) are shown in Figs. 5.5(a) and 5.5(b) for the $\{27,4\}_{\text{rot}}$ and $\{27,6\}_{\text{rot}}$ GOALs, respectively.

The electronic behavior of a GOAL can be understood from the isolated behavior of the associated antidot layer. In Fig. 5.6(a) the normalized projected density of states (PDOS/DOS) of the four sublattices of bilayer graphene are shown as a function of the antidot size, demonstrated with the $\{16, S\}$ geometries. The PDOS reveals a gradual shift from evenly distributed between the two layers towards mostly top layer (graphene layer) distribution—effectively it transforms from bilayer-like PDOS towards monolayer-like PDOS. We might expect a simple redistribution of the PDOS across remaining sites due to missing sites in the bottom (antidot) layer.
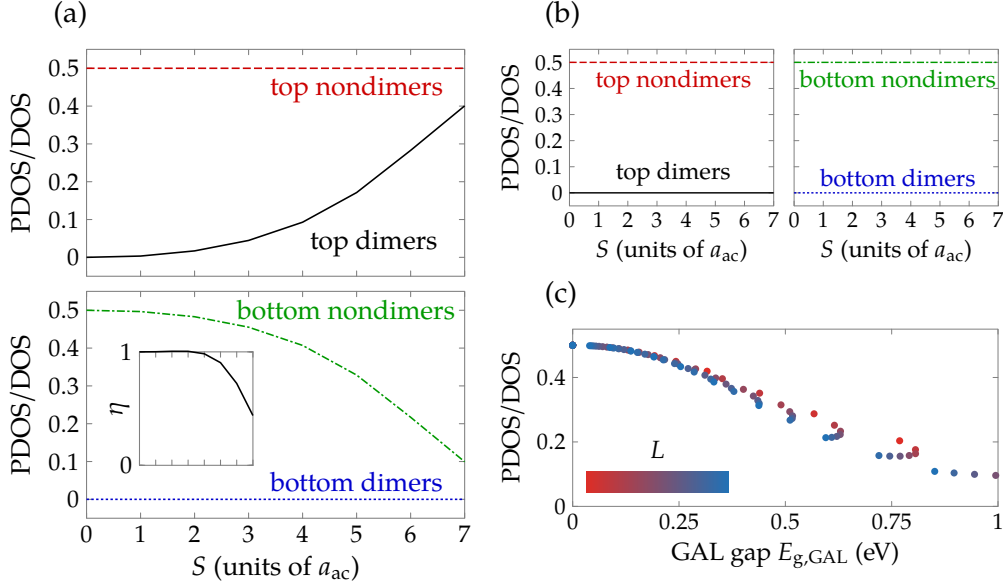
Figure 5.6: The projected density of states (PDOS) of regular (a) and rotated (b) GOALs as a function of antidot size. The PDOS is projected on top dimers (black solid), top nondimers (red dashed), bottom dimers (green, dotted), and bottom nondimers (blue dot-dashed). The inset in (a) shows the relative PDOS of the bottom antidot layer $\eta = \text{PDOS}_{\text{GAL}}/\text{DOS} \times N_{\text{total}}/N_{\text{GAL}}$. (c) The PDOS of the bottom antidot layer as a function of the isolated GAL layer.

To examine this possibility, we define η as the relative PDOS of the antidot layer, $\eta = \text{PDOS}_{\text{GAL}}/\text{DOS} \times N_{\text{total}}/N_{\text{GAL}}$. The inset of Fig. 5.6(a) (bottom) shows a gradually decreasing $\eta < 1$. That is, the states are *pushed* more into the top layer (graphene layer) than a simple redistribution can account for. This is further supported by considering the incommensurate $\{27, S\}_{\text{rot}}$ GOAL in Fig. 5.6(b), for which the PDOS remains evenly distributed in the two layers, regardless of antidot size. We note that at large antidots with very small spacing between them this simple picture breaks down. The small constrictions introduce other confining effects and the bottom (antidot) layer becomes slightly gapped in spite of incommensurability.

The single layer confinement is a strong indication that the governing mechanism behind the electronic behavior is the band gap of the isolated antidot layer. This is firmly supported by Fig. 5.6(c), which displays the normalized PDOS of the antidot layer as a function of the isolated antidot layer band gap $E_{\text{g,GAL}}$. As the local band gap of the antidot layer increases, the electronic states of GOAL are pushed into the top (graphene) layer towards monolayer confinement. Ultimately, this results in the monolayer-like dispersion we observe in GOALs.

5.3 Transverse bias and induced band gaps

Now we consider the case of a nonzero transverse bias U. In regular bilayer graphene a potential difference between the layers induces a band gap, the size of which scales approximately linearly with the potential. Through the same mechanism, GOALs also open band gaps tuned via the interlayer asymmetry. In Figs. 5.7(a) and 5.7(b),
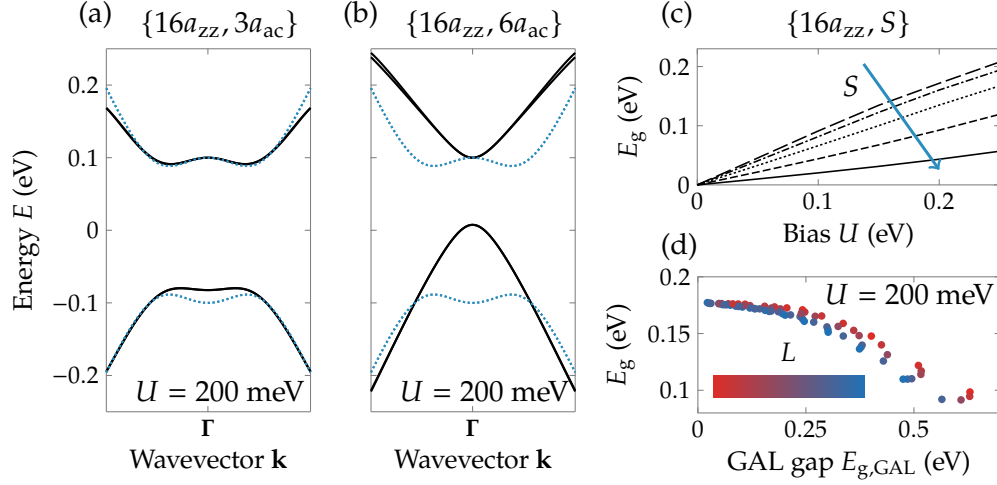
Figure 5.7: Bandstructures and band gaps of transverse biased GOALs. (a) Bandstructure of the $\{16, 3\}$ GOAL (solid) and regular bilayer graphene (dotted) at $U = 200$ meV. (b) Same as (a) for the $\{16, 6\}$ GOAL. (c) Band gaps of $\{16, S\}$ GOALs as a function of antidot size. (d) Band gaps of various GOALs versus the corresponding isolated GAL band gaps.

the near-Dirac bandstructures of the commensurate $\{16, 3\}$ and $\{16, 6\}$ GOALs (solid) display sizable band gaps. Compared to regular bilayer graphene (dotted) the band gaps are smaller, and, in addition, show electron-hole asymmetry.

The induced band gaps increases near-linearly with the size of the inter-layer potential difference U. Furthermore, as the size of the antidot increases the induced band gap *decreases*. Both features are illustrated in Fig. 5.7(c), which displays the size of band gap E_g versus the size of the antidot and the transverse bias.

The electron-hole asymmetry appears in GOALs as a result of the atomic imbalance between the two layers. Combined with the equal but opposite shift in the on-site energies of the two layers, the GOALs inevitably exhibit a shifted energy spectrum compared to regular bilayer graphene. The effect is minor for small antidots [Fig. 5.7(a)] but has a significant impact on larger antidots [Fig. 5.7(b)].

As in case of $\{16, 6\}$ in Fig. 5.7(b), it is particularly worth noting that biased GOALs need not display the "Mexican hat" shape of regular bilayer graphene, identified by the double dip (or peak) in the bilayer bandstructure. Instead, the bands resemble gapped graphene with parabolic bands. This has interesting implications, for example larger group velocities which is very attractive for faster electronics.

Similar to the zero-bias case, the transition cannot be attributed solely to the reduction of atomic sites in the bottom layer, but is instead governed by the electronic behavior of the isolated GAL layer. The mechanism is illustrated in Fig. 5.7(d) which compares the GOAL band gap with the isolated GAL band gap at $U = 200$ meV. There is a clear trend that the correlates the band gap of the GAL with the band gap of the GOAL. The slight deviation as a function of antidot lattice L is caused by atomic asymmetry between the layers, which is not directly related to the antidot layer band gap.

While we find the largest band gaps in systems whose unbiased electronic structure
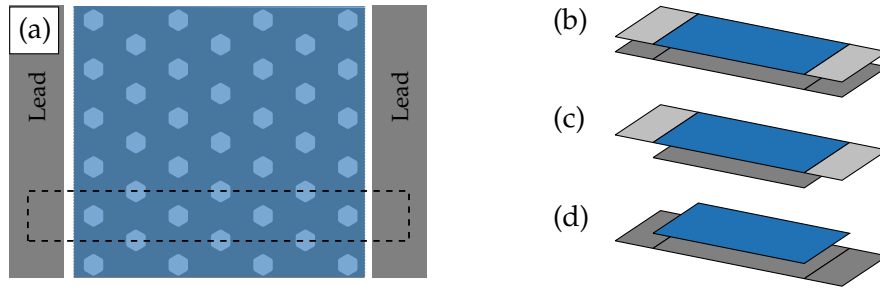
Figure 5.8: Illustrations of the GOAL devices (a) with three different contact models (b-d). A strip of GOAL—infinite in the transverse direction—is coupled to either bilayer (b), top layer (c), or bottom layer (d) leads.

resembles that of bilayer graphene, there are a range of $\{L, S\}$ which yield both linear dispersion wit large Fermi velocities, and can open sizable band gaps. The $\{16, 6\}$ shown here is one such example, but the $\{12, 4\}$ displays similar features also.

5.4 Transport through GOAL device

In regular bilayer ribbons and flakes the choice of contact has important implications on transport [81, 82]. We will explore three different ways to contact a finite-width strip of GOAL [see Fig. 5.8(a)]: bilayer leads, monolayer top leads, or monolayer bottom leads. These are illustrated in Figs. 5.8(b), 5.8(c) and 5.8(d) respectively.

The devices are periodic along the transverse direction with the unit cell outlined (dashed) in Fig. 5.8(a). The transport is chosen along the zz-direction, where the space between antidots is smaller. This effectively allows for a more narrow unit cell, with fewer columns of antidots. Our unit cell contains seven consecutive columns of antidots in the bottom layer. This number is enough to form a transport gap in the corresponding monolayer antidot lattice [48]. Wider devices yield qualitatively the same results as those described below.

We demonstrated in the previous section that the dispersion is governed by the localization in the respective layers. Similarly, the transmissions through GOALs are largely understood by the localization within the layers. The transmissions of the $\{16, 6\}$ (black solid) and $\{16, 3\}$ (black dashed) GOALs are displayed in Fig. 5.9(a). In the case of $\{16, 3\}$, the GOAL electronically resembles bilayer graphene [see left-most panel in Fig. 5.4(d)]. In turn, this yields transmission near those of bilayer graphene (blue dashdotted). On the other hand, the $\{16, 6\}$ GOAL resembles mostly monolayer graphene, and yields near-monolayer transmission. As displayed in Fig. 5.9(a), this behavior occurs over a sizable range of energies. A current map at $E = 100\,\text{meV}$ is illustrated in Fig. 5.9(b). Here, it is quite apparent that the monolayer-like transmission is the result of mostly top-layer confined transport. The additional Fabry-Perot-like oscillations—particularly clear in the case of $\{16, 6\}$—are the result of scattering at the device interfaces. The period of the oscillations varies with the width of the device (not shown).

If we consider a monolayer top lead instead, the transmissions are additionally affected by the bilayer/monolayer wave matching between the lead and device. The
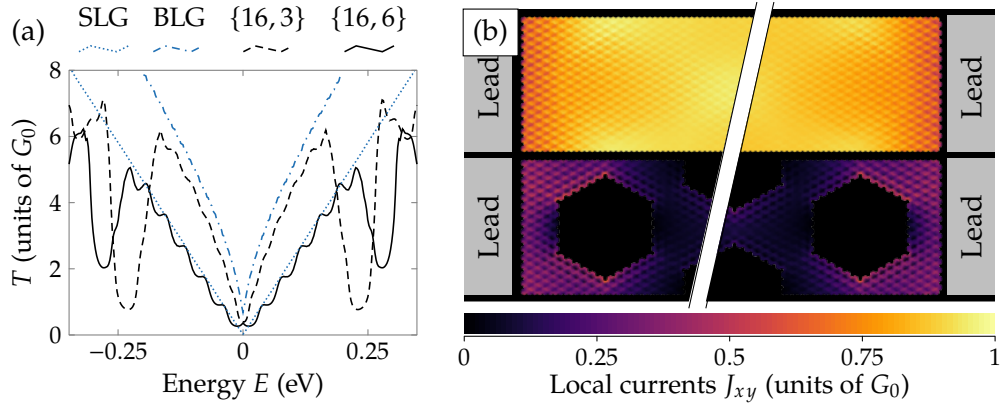
Figure 5.9: Transmission coefficients and currents of bilayer coupled GOAL devices [see Fig. 5.8(b)]. (a) The transmission coefficients of a {16, 6} (solid) and a {16, 3} (dashed) GOAL compared to monolayer (dotted) and bilayer graphene (dashdotted). (b) The in-plane currents through a {16, 6} GOAL at $E = 100\,\text{meV}$. The quantum of conductance is $G_0 = 2e^2/\hbar$.
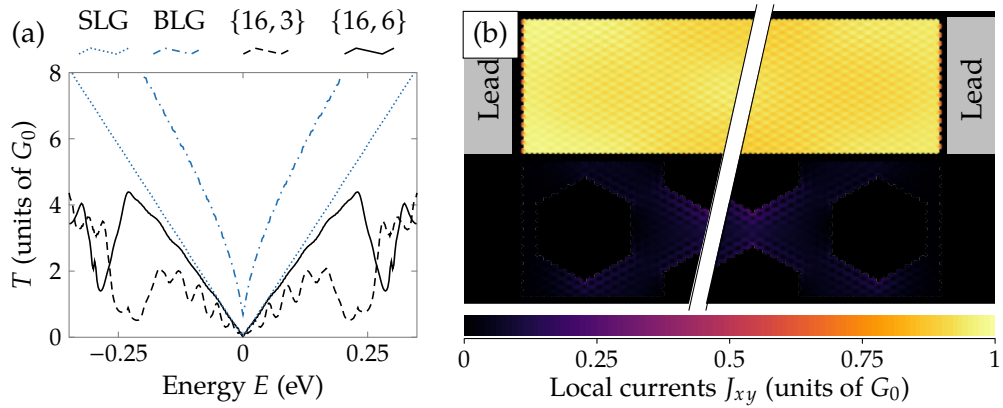

Figure 5.10: Transmission coefficients and currents of top layer coupled GOAL devices [see Fig. 5.8(c)]. (a) The transmission coefficients of a {16, 6} (solid) and a {16, 3} (dashed) GOAL compared to monolayer (dotted) and bilayer graphene (dashdotted). (b) The in-plane currents through a {16, 6} GOAL at $E = 100\,\text{meV}$.
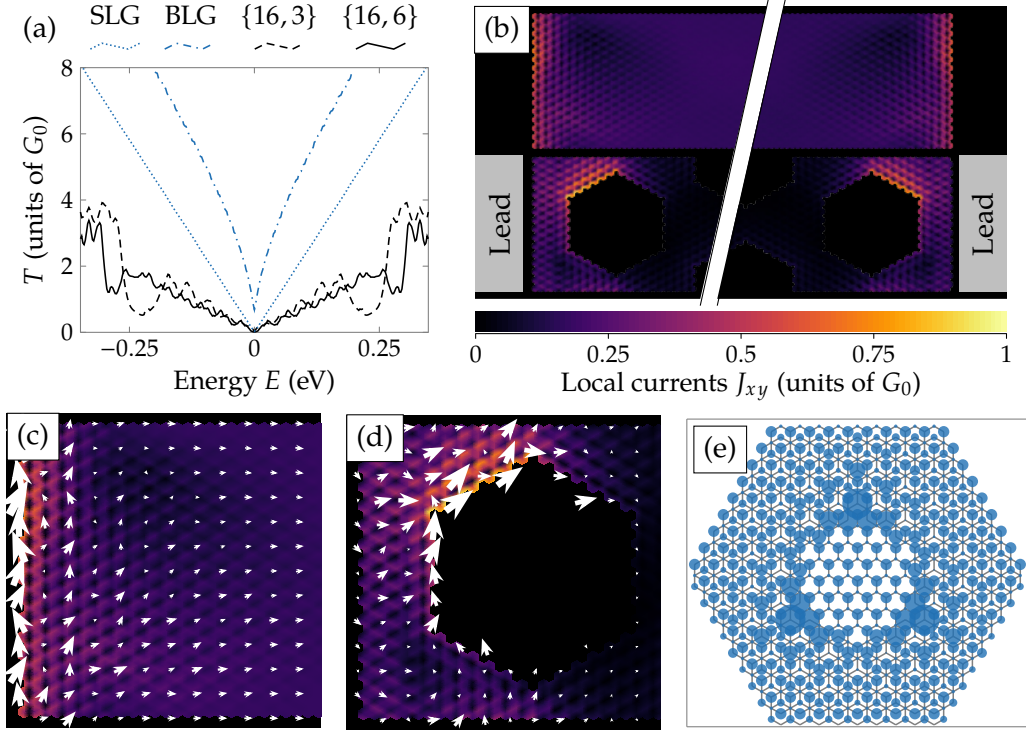
Figure 5.11: Transmission coefficients and currents of bottom layer coupled GOAL devices (see Fig. 5.8(d)). (a) The transmission coefficients of a $\{16, 6\}$ (solid) and a $\{16, 3\}$ (dashed) GOAL compared to monolayer (dotted) and bilayer graphene (dashdotted). (b) The in-plane currents through a $\{16, 6\}$ GOAL at $E = 100\,\text{meV}$. (c) Closer view of the near-entry currents including the directions in the top layer of a $\{16, 6\}$ GOAL at $E = 100\,\text{meV}$. (d) Same as (c) but for the bottom layer. (e) The $E = 0\,\text{meV}$ local density of states (LDOS) of a $\{9, 2\}$ GOAL; qualitatively similar to a $\{16, 6\}$ GOAL.

transmissions are displayed in Fig. 5.10(a). The $\{16, 3\}$ GOAL displays additional scattering and larger oscillations due to the the lead/device wave mismatch. On the other hand, the $\{16, 6\}$ GOAL sufficiently decouples the bottom layer from the top, and the oscillations almost vanished The transmission is even closer to that of monolayer graphene. The current maps of the $\{16, 6\}$ GOAL, Fig. 5.10(b), reveal almost zero current in the bottom layer, clearly indicating electronic decoupling. It is worth noting that, wave matching also has an impact in some cases of bilayer leads. If the band gap of the monolayer GAL is sufficiently large, the bottom layer *completely* decouples electronically from the top, and the wave mismatch between lead and device causes additional scattering.

The bottom monolayer leads yield by far the lowest transmissions. Fig. 5.11(a) displays the transmission of the $\{16, 3\}$ and $\{16, 6\}$ GOALs, and Fig. 5.11(b) displays the current map at $E = 100\,\text{meV}$. In either GOAL, and the transmissions become limited by the smaller inter-layer coupling $\gamma_1 \sim \gamma_0/10$. Both cases also demonstrate significant oscillations from interface scattering.

However, another interesting feature emerges from bottom layer coupling. In Fig. 5.11(b) the currents injected from left introduce a particularly large *transverse*

current at the beginning of the top layer. These are illustrated more clearly in Figs. 5.11(c) and 5.11(d), respectively top and bottom layer, displaying the direction of the current with arrows. The transverse direction is understood by examining the profile of the LDOS, shown for a single unit cell in Fig. 5.11(e). GOALs display reduced C_3 symmetry compared to the C_6 symmetry of regular bilayer graphene. This is particularly clear at the antidot corners shown in Fig. 5.3(a). In turn, this makes a three-fold distribution of the LDOS, centered at every second corner of the bottom layer antidot. In the zz-direction, this vertical asymmetry will in turn induce large transverse currents. Transport in the ac-direction does not experience this vertical asymmetry, and the transverse currents are zero. This interesting side effect could provide alternative inter-layer transport features.

5.5 Discussion and summary

GOALs demonstrate the possibility of obtaining a high mobility device with the addition of tunable band gaps. By careful design, we can structure the GOAL geometries to display either parabolic or linear dispersion. For a certain set of optimized geometries, for example the $\{16a_{zz}, 6a_{ac}\}$ GOAL presented in this chapter, near-monolayer dispersion is achieved. Nevertheless, these linearly dispersive GOALs can be made gapped by breaking layer symmetry. We demonstrate this using a fixed, layer-dependent on-site potential. However, inspired by the experiments in bilayer graphene [83], we could imagine this induced via perpendicular electric fields. For example, we may use electronic gates both below and above the device (dual-gating).

The mechanism behind the electronic behavior is attributed to the confinement of electronic states in the pristine top layer. The confinement depends, in turn, entirely on the electronic behavior of the bottom GAL layer, regardless of the exact geometry of the antidot lattice. If the isolated GAL layer is gapped, the electronics states are redistributed such that they reside mostly in the top layer.

It is worth pointing out the we presented only results using the NN TB model of pristine bilayer graphene. However, demonstrated in Paper I, upon extending the number of bilayer couplings the linear dispersing bands split into two, with slightly different Fermi velocities [84]. Ultimately, we expect the systems to reflect the same principle features as outline above.

From this fundamental study of GOALs, there are a number of paths to extend our analysis. For example, twisting the layers is expected to have a significant effect on the electronic behavior. In bilayer graphene twisting can change the behavior from parabolic dispersion even to a linear dispersion. Additionally, we assumed uniform on-site potential shifts throughout the respective layers. In reality, such patterning of the bottom layer would likely change the overall electron distribution and the potential profile. Given the large influence of the bilayer graphene sublattices, changes in the electron distributions could induce entirely different behavior. Such effects motivate a more extensive studies to examine the influence of twisting or non-uniform potential distributions.

The indifference to the exact geometry of the antidot lattice suggests a generality beyond the particular bilayer structure considered here. We could similarly imagine coupling two other layered materials, where one is gapped and the other is metallic.

While the combined behavior will likely be metallic, an external influence may induce additional features only enabled by the coupling of the two layers. Such a composite system could bring interesting possibilities yet unseen into pristine graphene systems.

Robust band gaps and half-metallic antidot lattices

6

Nanostructured graphene has been predicted to support magnetic moments at vacancy sites and zz-edges [27]. Many proposed spintronic devices rely on magnetic moments, for example spin-filters [85–88] and half-metals [32, 86, 88, 89]. Half-metals in particular, with metallic or semiconducting behavior for different spin channels, make perfect platforms for embedded spin manipulation. A number of experimental works suggest that zz-edged magnetism is possible [22, 33, 35], even though clear experimental signatures are still missing. In this chapter we consider superlattices of triangular graphene antidots (TGAs) with perimeters shaped entirely with either zz-edges (zz-TGAs) or ac-edges (ac-TGAs).

The zz-edge is sublattice antisymmetric, where either side of the zz-chain is comprised only of one particular sublattice type. For clarity the chain is illustrated in Fig. 6.1(a) with sublattices A and B colored black and white, respectively. Depending on which side of the chain is exposed, a local sublattice imbalance may arise, which in turn will induce magnetic moments. The magnetic moments signify spin-polarization, and the two orientations are denoted *up* and *down*. The mechanism can be understood from Lieb's theorem [31] in bipartite lattices, which states that the size of the total magnetic moment is equal to the difference in total number of sites in the two graphene sublattices. In, for example, zz-edged graphene nanoribbons [Fig. 6.1(b)] the system displays antiferromagnetic ordering, where one edge is counterbalanced by the other with the opposite spin polarization. This is readily transferred to the antidot case with zz-edges as shown in Fig. 6.1(c). Many antidots, e.g. circular, hexagonal, or diamond shaped, have balanced zz-edges and a total magnetic moment of zero. In contrast, zz-TGAs only expose a *single sublattice*, and the total magnetic moment is therefore nonzero.

Below we demonstrate that zz-TGAs have properties very different from the other
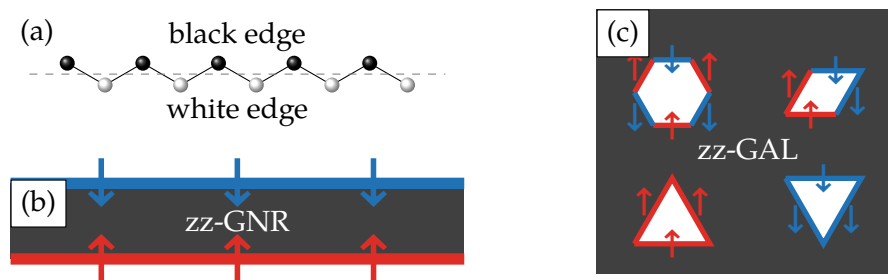
Figure 6.1: Illustrations of spin-polarized graphene zz-edges. (a) Bare zz-edge illustrating the sublattice imbalance on either side. The two sublattices of graphene have been colored black and white, respectively. (b) Antiferromagnetic moments in zz-edged graphene nanoribbons (zz-GNR). (c) Anti- and ferromagnetic moments in examples of zz-edged GALs (zz-GAL). Orientation of the magnetic moments are illustrated red (spin up) and blue (spin down).
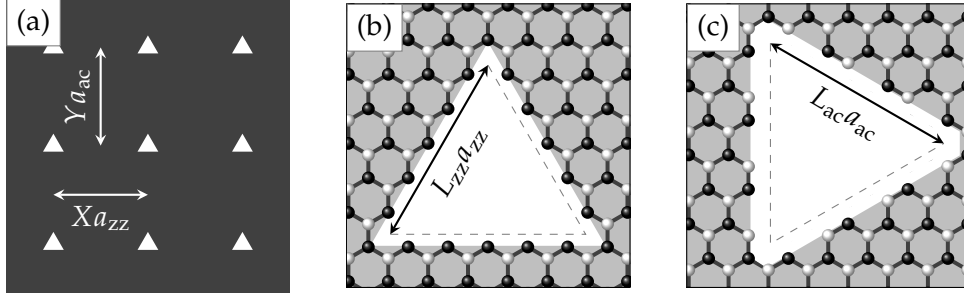
Figure 6.2: Schematic (a) and atomic structure of the L_{zz} = 5 zz-edged (b) and L_{ac} = 3 ac-edged (c) triangular graphene antidots (zz-TGA and ac-TGA). The antidot spacing in (a) are X = 25 and Y = 15. The sublattices A and B of graphene are colored black and white, respectively. Notice in if the zz-TGA in (b) was rotated 180°, the edge sublattice would change from black sites to white sites.

antidots [90]. The zz-TGA lattices are shown to display large band gaps in the spin-unpolarized form (before considering spin-dependency), half-metallicity when spin-polarized, and are unusually robust against disorder.

6.1 Triangular antidots in graphene

We consider a periodic array of TGAs as illustrated schematically in Fig. 6.2(a). The antidots are laid out in an approximately square lattice, with all TGAs oriented in the same direction. We will later consider the case where every second antidot is "flipped" (or rotated 180°) such that global sublattice symmetry is maintained. The rectangular lattice is known to allow for both commensurate and incommensurate antidot lattices, i.e., those expected (or not) to have an electronic band gap only due to superlattice [42]. (See also Section 4.2.) The rectangular lattice makes an excellent testbed to explore the properties in both the commensurate and incommensurate lattices.

We compare the zz-TGA and the ac-TGA with similar sizes, shown in Figs. 6.2(b) and 6.2(c), respectively. The sublattices have been colored to clarify the edge structures. In Fig. 6.2(b) the zz-edges are all *black* (sublattice A), while the ac-edges in Fig. 6.2(c) are sublattice *balanced*. Regular antidots, e.g. circular, rectangular, and hexagonal, all depend critically on commensurability. The ac-TGAs also depend on commensurability, and function to illustrate the fundamental differences between the zz-TGAs and the regular antidots.

We adapt the notation from Pedersen *et al.* [40]. The geometries are denoted $\{X, Y, L_{geo}\}$, with horizontal spacing Xa_{zz}, vertical spacing Ya_{ac}, and antidot side length $L_{geo}a_{geo}$. The subscript geo $\in$ [zz, ac] denotes the antidot edge type. (See also Fig. 6.2.) The lattice constants along the zz- and ac-directions are a_{zz} = 2.46 Å and a_{ac} = 4.26 Å, respectively. With this notation, the rectangular lattices are commensurate when $X = 3n$ where n is a positive integer, and incommensurate otherwise [see also Eq. (4.10)]. The zz- and ac-TGAs can be compared using $L_{zz} = \sqrt{3}L_{ac} \equiv L$.
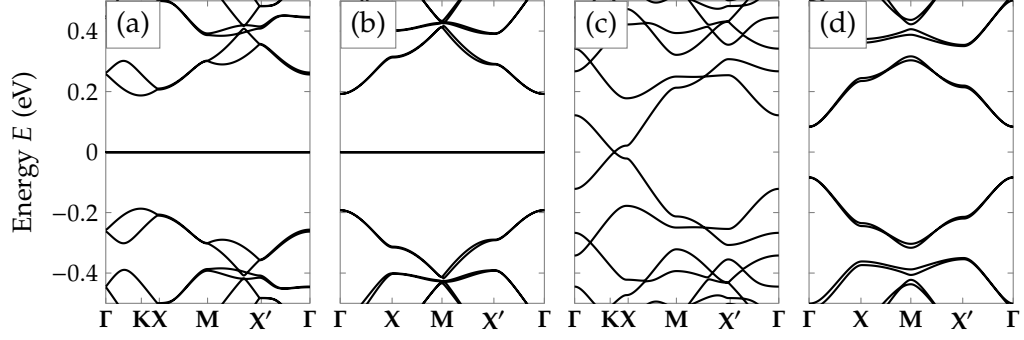
Figure 6.3: Bandstructures of zz- and ac-TGA lattices: (a) $\{25, 15, 5zz\}$, (b) $\{24, 15, 5zz\}$, (c) $\{25, 15, 3ac\}$, and (d) $\{24, 15, 3ac\}$. Notice in particular the $E = 0$ midgap states in (a) and (b) (the zz-TGAs). Also note the folding of the Dirac **K**-point onto the **Γ**-point in (a) and (c).
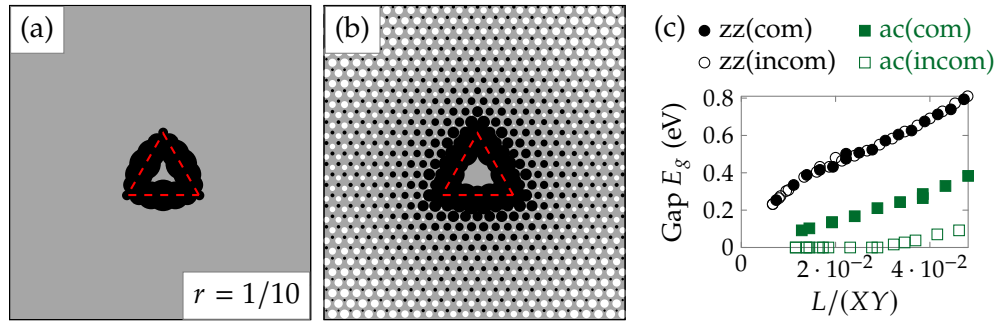

Figure 6.4: The LDOS of a zz-TGA lattice at $E = 0$ (a) and $E = 0.27$ eV (b), and band gaps as a function of $L/(XY)$ (c) in both zz- and ac-TGA lattice. The LDOS is displayed via circles, where the radii $\propto r \times \text{LDOS}(i)$, and $r \neq 1$ is given in the bottom corner. The LDOS is colored black and white for, respectively, the A and B sublattices. The symbols at the top of (c) denote the edge type and commensurability.

The calculations are performed using the NN-TB model Hamiltonian

$$\mathbf{H} = \sum_i \epsilon_i \mathbf{n}_i + \sum_{\langle ij \rangle} t\mathbf{c}_i^\dagger \mathbf{c}_j + \text{H.c.}, \tag{6.1}$$

where the NN coupling takes the value $t = -2.7$ eV for first-NN and zero otherwise. The spin-polarization is introduced using a mean-field Hubbard model (Section 2.2). The spin-dependence enters via on-site energies $\epsilon_i = \pm U m_i / 2$, with $-$ for spin up and $+$ for spin down and magnetic moments $m_i = n_{i\uparrow} - n_{i\downarrow}$. While extending to a third-NN TB model does change the spin-unpolarized behavior significantly, the spin polarized properties are qualitatively the same [demonstrated in Paper II]. Here we focus on the first-NN model which demonstrates the fundamental mechanisms.

6.2 Sublattice induced band gaps

We first consider the spin-unpolarized cases ($U = 0$). The bandstructures for the $\{25, 15, 5zz\}$ and $\{24, 15, 5zz\}$ geometries are shown in Figs. 6.3(a) and 6.3(b), respectively. The zz-TGA lattices display large band gaps and *completely flat* degenerate

bands exactly in the middle of the gap at $E = 0$. The midgap bands are identified as zz-edge states illustrated via the LDOS at $E = 0$ in Fig. 6.4(a). The LDOS has been colored black or white according to sublattice, and in Fig. 6.4(a) only the edge sublattice (black) is observed. Low-dispersive edge states are expected for extended zz-edged structures, for example in zz-nanoribbons [66, 91] or other zz-edged antidots [92–94].

However, the $\{25, 15, 5zz\}$ lattice is not commensurate, and band gaps are not expected from the geometric rules which govern regular antidots. Instead, we might have anticipated the behavior illustrated in Figs. 6.3(c) and 6.3(d) using the ac-TGA lattices $\{25, 15, 3ac\}$ and $\{24, 15, 3ac\}$. Only the (former) commensurate ac-antidot lattice is gapped, in full compliance with usual antidot behavior exhibited by for example circular or hexagonal antidots [40, 41]. The (latter) incommensurate ac-antidot lattice is metallic instead.

The difference between zz- and ac-TGAs is further quantified via the size of the band gaps E_{g}. Pedersen *et al.* [40] have demonstrated the scaling behavior $E_{\mathrm{g}} \propto N_{rem}^{1/2}/N_{tot}$ of regular antidots in commensurate lattices. The numbers N_{rem} and N_{tot} are, respectively, the number of atoms removed by the antidot and the total number of atoms without the antidot in the unit cell. Fig. 6.4(c) illustrates the band gaps versus $L/(XY) \propto N_{rem}^{1/2}/N_{tot}$ of both zz- (circles) and ac-TGA (squares) lattices. The commensurate and incommensurate lattices are marked by hollow and filled symbols, respectively. The ac-TGAs follow conventional geometric considerations, where incommensurate lattices are gapless. At larger $L/(XY)$, the ideal picture breaks down and even the incommensurate lattices have nonzero gaps. At these dimensions the ac-TGAs become separated by only a few atoms, and there is competition between periodicity and confinement band gap mechanisms. In contrast to ac-TGAs, the zz-TGAs exhibit band gaps throughout. Furthermore, the band gaps of zz-TGAs are about twice as large when compared to ac-TGAs.

Band gaps irrespective of commensurability suggest that more is in play than confinement effects. Instead, these recurring band gaps are the result of the strong sublattice imbalance of a zz-TGA. For example, in narrow zz-nanoribbons or zz-hexagonal antidots the local sublattice imbalance is "canceled" with nearby edges of the other sublattice type. In zz-TGAs "cancellation" is not possible. Instead a *sublattice dependent confinement* occurs. The confinement is illustrated via the LDOS at the conduction bands $E = 0.1|t| = 0.27\,\mathrm{eV}$ in Fig. 6.4(b). The LDOS near the antidot shows only edge-sublattice occupation (black circles). Nonzero dispersion relies on nonzero LDOS at *both* sublattices, particularly so in the NN-TB model which couples only neighboring sites. The regions between antidots displays nonzero LDOS at both sublattices, which is where we then expect the dispersion to take place. This confinement is analogous to a local *mass* term—a staggered on-site energy shift with positive values on one sublattice and negative on the other—which in otherwise pristine graphene opens a large band gap. Sublattice induced band gaps have also been demonstrated in other sublattice-patterned graphene systems [95, 96].

Lattice commensurability is a feature of the pristine lattice that is greatly influenced by lattice disorder. In GALs with regular antidots (circular, hexagonal, etc.) geometric disorders in the form of varying position and size quench any present band gaps [44, 49]. However, such disorder does not affect sublattice symmetries, and we can expect the band gaps of zz-TGAs to be robust against geometrical disorder. The disorder is explored further below, but first we consider the pristine spin-polarized
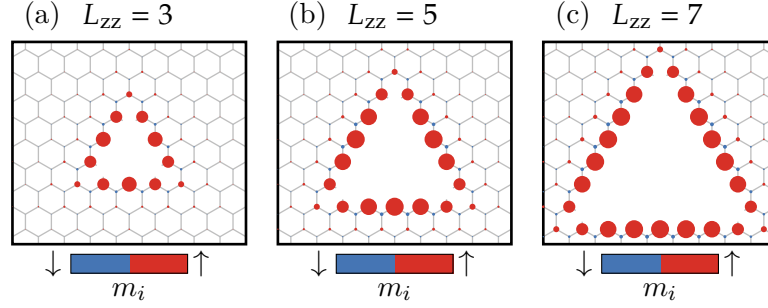
Figure 6.5: Magnetic moment profiles of the zz-TGA lattice with $L_{zz} = 3$ (a), $L_{zz} = 5$ (b), and $L_{zz} = 7$ (c). All three cases have $X = 25$ and $Y = 15$. The magnetic moments are displayed with circles, where the radii $\propto m_i$. The orientation is noted by color; red and blue for spin up or down, respectively. Note that the atomic sites immediately next the edge sites, in fact, have small blue circles (difficult to see in the printed version).

case.

6.3 Half-metallic graphene antidot lattice

We now consider zz-TGA systems where spin polarization effects are included using the spin-dependent on-site potentials calculated using the mean-field Hubbard approach. The ac-TGAs are sublattice balanced and display zero magnetic moments, so their behavior is unchanged from the previous section. The magnetic moment distributions of three zz-TGAs are displayed in Fig. 6.5. The distributions follow a general pattern: The magnetic moments reach a maximum $m_i \sim 0.31$ at the zz-edges, and are reduced near the TGA corners. Long uninterrupted zz-edges have mostly constant magnetic moments, similar to that calculated for infinite zz-edged graphene nanoribbons. At short zz-edges $L_{zz} < 5$, however, the corners are so close to each other that even the maximum of the magnetic-moment is reduced, as for example with $L_{zz} = 3$ in Fig. 6.5(a). The corners can be compared to kinks at chiral zz-edges, which locally display similar reductions in the magnetic moments [97]. All TGAs conform to Lieb's theorem [31] such that the total magnetic moment $M = \sum_i m_i \mu_B = \Delta N \mu_B$, where the total sublattice imbalance $\Delta N = |N_A - N_B|$. This also happens to be number of zz edge atoms i.e. $\Delta N = L_{zz}$. Additionally, the magnetic profiles are mostly independent of the superlattice geometry, except for very narrow spacings between antidots. This independence suggests that neighboring antidots do not significantly influence each other's magnetic moment distribution. This becomes useful for simulating super structures with several zz-TGAs. For example, in studying disorder (Section 6.4), we can assume the magnetic profiles of individual zz-TGA are independent on the others. Such super structures are otherwise impractical to calculate within the full Hubbard model.

The spin-polarized bandstructure of the $\{25, 15, 5zz\}$ is displayed in Fig. 6.6(a). The spin-splitting introduces two spin-polarized bands, one for each spin, on either side of the Fermi level $E = 0$ (red and blue bands, respectively). These give rise to half-metallic regions, where the corresponding DOS would becomes perfectly spin-polarized [90]. The half-metallic regions are separated by a small band gap of a couple of tens of meV. The transition towards spin-polarized bands is illustrated in
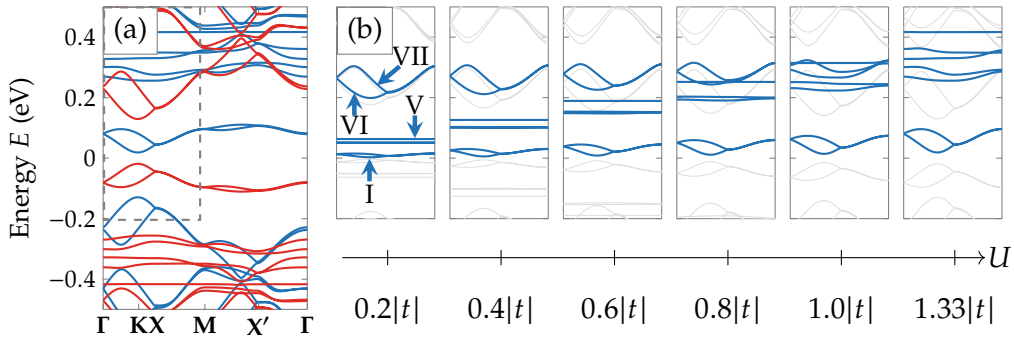
Figure 6.6: Spin-polarized band structure of the zz-edged TGA. (a) The band-structure of the $\{25, 15, 5zz\}$ geometry. (b) The bandstructure within the dashed box in (a), as we vary the parameter $U \in [0.2|t|; 1.33|t|]$. Spin-up bands are blue and spin-down bands are red. In (b) only a subset of spin-down bands are shown clearly (see main text). These are denoted I-VII in the order illustrated in left-most panel of (b).
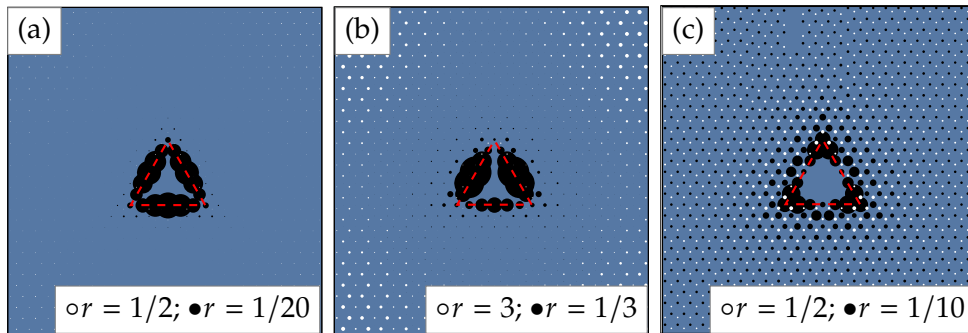

Figure 6.7: The spin-down LDOS at $E = 0.155|t|$ [(a) near the bands V], $E = 0.135|t|$ [(b) bands VI-VII], and $E = 0.02|t|$ [(c) I-II] of the spin-polarized zz-TGA. The LDOS is displayed via circles, where the radii $\propto r \times \mathrm{LDOS}(i)$, and r is given in the bottom corner. The LDOS is colored black and white for, respectively, the A and B sublattices.

Fig. 6.6(b) by artificially varying the exchange parameter $U \in [0; 3.6\,\mathrm{eV}]$, where only the relevant $E > 0$ spin down bands are colored (blue). In case of $\{25, 15, 5zz\}$ there are seven relevant bands, denoted I through VII in the order shown at $U = 0.2|t|$ (left-most panel).

Bands I-V are the spin-split versions of the lowest spin-unpolarized edge-states, and bands VI and VII are the spin-unpolarized conduction bands. The transition in Fig. 6.6(b) shows how the nearly dispersionless band V spin-splits to the largest degree, i.e., the spin-down band has moved the furthest (upwards) in energy. In fact, band V travels *past* the spin-unpolarized conduction bands VI and VII, and settles above band VII at full $U = 1.33|t|$ (right-most panel). The degree of spin-splitting scales with the size of corresponding magnetic moments, and the spin-down LDOS in Fig. 6.7(a) reveals that band V is predominantly localized near the middle of the zz-edges, where the largest magnetic moments are located. As band V spin-splits past bands VI and VII [at $U = 1.0|t|$], the latter two bands flatten as well. In Fig. 6.7(b) the LDOS of the spin-down bands VI and VII displays hybridized edges-states. The LDOS also reveals some occupation on both sublattices, albeit very little on the non-edge sublattice. This small occupation of both sublattices explains why only slight dispersion is observed in the bandstructure. The two lowest bands I and II remain near the Fermi level. The spin down LDOS in Fig. 6.7(c) of the half-metallic region (bands I and II) shows localization near the corners of the antidot, where the magnetic moments are lower compared to the remainder of the zz-edges. Furthermore, Fig. 6.7(c) shows significant LDOS at *both* sublattices in the region between antidots, which gives rise to nonzero dispersion.

The final bandstructure at $U = 1.33|t|$ has half-metallic regions near the Fermi level, whose states show significant LDOS at the *corners* of the zz-TGAs.

6.3.1 Restoring sublattice symmetry

Before we consider disordered TGA lattices in the next section, we first consider the effect of pairing two zz-TGAs with opposite sublattices. A $180°$ in-plane rotation of a zz-TGA will expose the other sublattice at the edges [see also Fig. 6.1(c)], and, in turn, flip the orientations of the magnetic moments. The *flipped* case is displayed in Fig. 6.8(a). We note that in this case sublattices and magnetic moments are *balanced* i.e. the total quantities $\Delta N = |N_A - N_B| = 0$ and $M = \sum_i m_i = 0$.

In the spin-unpolarized case with $U = 0$, the bandstructure [Fig. 6.8(b)] reveals that the sublattice balanced zz-TGAs are metallic (zero band gap). By restoring the sublattice symmetry the band gap closes. However, local sublattice imbalance still exists, and the spin polarized case gives rise to magnetic moments. The spin-polarized bandstructure [Fig. 6.8(b)] becomes gapped from band spin-splitting. Furthermore, the bands are completely spin symmetric. By examining Fig. 6.8(a), it is clear that an axis-mirror transformation of the unit cell is equivalent to flipping the signs of all the magnetic moments.

By introducing *flipped* TGAs the half-metallic behavior is replaced by metallic behavior, and both spins are equivalent. This important feature is used in later chapters considering device transport and conductivities.
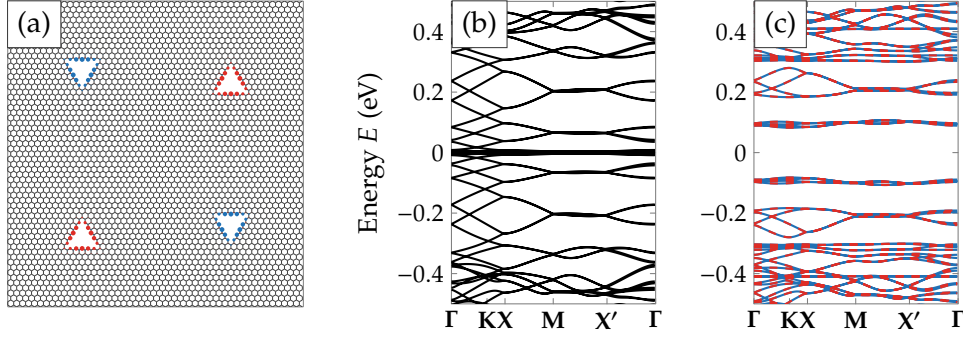
Figure 6.8: Geometry (a) and corresponding bandstructures in the spin-unpolarized (b) and polarized (c) cases of the *flipped* zz-TGA lattice. The magnetic moments in (a) are displayed via circles, where radii $\propto m_i$ (spin up: red, spin up: blue). Both spin types in (c) display the same bandstructure (blue and red dashed).

6.4 Disorder robustness

Previous studies of regular antidots (circular, hexagonal, etc.) find that band gaps are severely degraded by disorder [44, 49]. Pristine commensurability depends on atomically precise superlattice vectors, and any disorder in the superlattice will break the periodic symmetry. The influence of disorder was studied in Paper II by considering the bandstructures of disordered superlattices. This work strongly suggested that the zz-TGA lattices are unusually robust against disorder. However, by employing the large-scale Chebyshev expansion for the DOS [Eq. (3.5)], becomes even clearer.

We first consider large sheets of randomly distributed zz- and ac-TGAs. The samples are approximately 460 nm × 460 nm graphene sheets with 2900 antidots embedded. The average space between TGAs is $\Delta X \approx 8nm$. The density of antidots is about half of what we have considered so far in this chapter. The magnetic moment distributions surrounding each antidot are assumed independent, and determined individually. These distributions are calculated in periodic systems using $\{25, 15, L\}$ unit cells, and then embedded in graphene to form a final "patchwork". To further ensure valid magnetic moments, we prevent unit cells from overlapping in the disordered samples. This gives a minimum distance of $X_{min} = 25a_{zz} \sim 6nm$. We compare these disordered samples with a similarly spaced pristine (commensurate) lattice $\{36, 21, L\}$. For comparability, both the disordered and the pristine cases are calculated using Chebyshev expansions.

The DOS ($E > 0$) is shown in Fig. 6.9(a) for spin-unpolarized zz- (black) and ac-TGAs (gray) in both the pristine (dotted) and disordered cases (solid). The inset in Fig. 6.9(a) shows a schematic that illustrates the disordered systems, where the TGAs are distributed completely randomly. The differences between ac and zz are striking; while the ac band gaps are completely quenched (grey arrow), zz gaps are only slightly reduced from energy-level broadening (black arrow). Even in the spin polarized zz-TGAs [Fig. 6.9(b)] the half-metallic regions remain, and the small band gap separating the two half-metallic regions is near identical, even slightly increased. The spin-up and spin-down band edges both move slightly further away from the Fermi level $E = 0$ (see red and blue arrows). At higher energies $E > 100\,meV$, outside
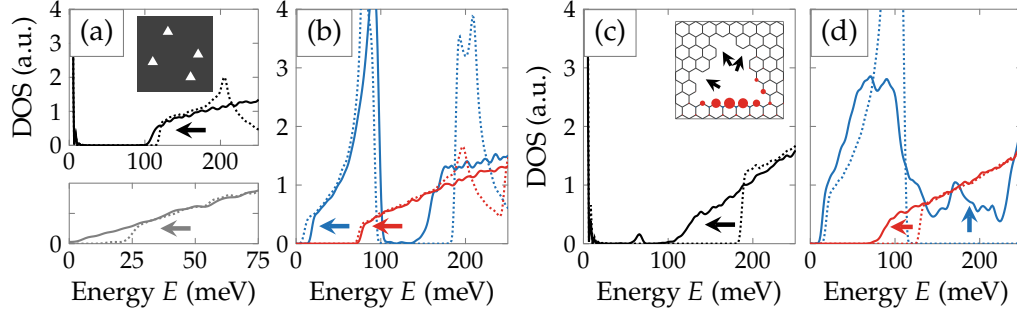
Figure 6.9: Pristine (dashed) and disordered (solid) DOS of the zz- and ac-TGA lattices: Lattice disorder for the spin-unpolarized (a) and polarized (b) cases, and edge disorder for the spin-unpolarized (c) and polarized (d) cases. In (a) and (c) the zz- (top) and ac-TGA (bottom) DOS are shown in black and gray, respectively. In (b) and (d) the zz-TGA DOS are shown in red and blue for spin up and down, respectively. The arrows denote interesting differences from the pristine case to the disordered case. The insert in (a) and (c) illustrate the disordered samples in (a-d). In (c), the inset has black arrows that indicate the removed atoms in the illustrated case.

the half-metallic regions, the influence is more pronounced. Peaks are smeared out and bands gaps reduced in size. Overall though, the zz-TGAs are unusually robust against lattice disorder when compared to ac-TGAs, and by extension the regular antidot geometries.

However, the zz-TGAs *are* susceptible to disorder of the edges themselves. The spin unpolarized and polarized DOS of an edge-disordered lattice are shown in Figs. 6.9(c) and 6.9(d), respectively. Now we consider a proper superlattice with atomically precise positions of the zz-TGAs, while randomly removing edge atoms with a certain probability $p_{etch} = 0.05$. The "etching" occurs $N_{etch} = 3$ times. An example of a single antidot and associated magnetic moment distribution is shown in the inset of Fig. 6.9(c). Edge disorder has a much greater influence than in the case of lattice-only disorder. In the spin-unpolarized case, the edge disorder generates hybridized states which appear in the otherwise gapped region (e.g. at $E = 70\,\text{meV}$), and severely reduces the band gap. In the spin polarized zz-TGA case, the spin polarized band edges have moved closer to the Fermi level (e.g. red arrow). This reduces the half-metallic region, which is nonetheless still significant. Furthermore, the pristine half-metallic DOS has been redistributed, and the previously spin down gapped region between $110\,\text{meV} < E < 250\,\text{meV}$ has been "filled out" by nonzero DOS (blue arrow). Compared to lattice-only disorder, the edge disorder has reduced the half-metallic region, but not completely closed it.

The band gaps and half-metallic features of zz-TGAs are induced by sublattice imbalance, *independently* of the superlattice, and are therefore robust against lattice disorder. We exploit this in later chapters when considering larger and more experimentally feasible sized zz-TGAs (Chapter 8).

6.5 Discussion and summary

As the result of breaking the graphene sublattice symmetry, superlattices of spin-unpolarized zz-TGAs exhibit large bands gaps that exceed those of complementary ac-TGAs. By also considering spin-interaction, spin-polarized zz-TGAs become half-metallic near the Fermi level, giving rise to perfectly spin-polarized DOS. We demonstrate that in the case of zz-TGAs, these features are present irrespective of conventional geometric rules (antidot commensurability), in sharp contrast to, for example, the band gaps of conventional antidots. In fact, the behavior is a reaction to the strong sublattice imbalance induced by a zz-TGA. Consequently, these features, such as the half-metallicity, are particularly robust in the face of disorder.

As an interesting possibility, we also considered restoring sublattice symmetry by introducing zz-TGAs oriented oppositely, where every second antidot is flipped in plane. In such a system, the spin-unpolarized TGAs are completely metallic, and the spin-polarized TGAs are semi-conducting. Since the magnetic moments of the flipped zz-TGAs are exactly opposite to the regular zz-TGAs, electronic spin types are equivalent.

The magnetic moments predicted by the Hubbard are in good agreement with *ab initio* calculations [98]. While the Hubbard model does not take non-local exchange into account and ignores spin dynamics, the resulting magnetic moments are supported by the extended Ruderman-Kittel-Kasuya-Yosida (RKKY) theory predictions [99, 100]. A possible future work could involve extending our model and examine the exchange between TGAs. At the moment, our model assumes *exact* periodicity i.e. all magnetic moments throughout the superlattice are ferromagnetically ordered. Nonetheless, the non-local exchange between triangles is expected to grow with the number of locally ordered magnetic moments. As such, the inter-triangle exchanges should be stronger than those between, e.g., vacancy defects with similar separations. It would be worthwhile, however, to explore the larger length scales, and identify where the exchange coupling is too small to preserve ferromagnetic ordering between zz-TGAs.

The possibility of half-metallicity induced by the formation of antidots is particularly interesting in the field of graphene spintronics, and we are motivated to study the spin-dependent transport properties of zz-TGAs. By embedding half-metallic TGAs into devices, we could filter electrons according to spin. These devices would act as a conductor for one spin and an insulator for the other. However, the triangular-shapes of our antidots also introduce geometrical asymmetries. For this reason, it is interesting to study also the skew transport properties. In the next chapter, we explore various transport properties of devices with a small number of embedded zz-TGAs.

Triangular antidot spin filter

<div style="text-align: right">7</div>

As discussed in the previous chapter (Chapter 6), nanostructured graphene with extended zz-edges are predicted to locally form ferromagnetic moments. To induce global ferromagnetism, however, the nanostructured pattern must break the overall sublattice symmetry [32, 87, 101]. Indeed, zz-edged triangular graphene antidots (zz-TGAs) break the sublattice symmetry and induce large global ferromagnetic moments [86, 88, 90, 102–104]. The magnetic moment profile of such a zz-TGA is displayed in Fig. 7.1(a). In Chapter 6 (Paper II), we demonstrated that *lattices* of zz-TGAs induce half-metallic bands near the Fermi level. Here, we focus on the spin-dependent transport properties of nanostructured graphene devices with a small number of embedded zz-TGAs.

The fundamental mechanisms are first examined in the case of a device with a single TGA, illustrated in Fig. 7.1(b). We will later extend our analysis to multiple antidots arranged in a rectangular array—this setup is illustrated in Fig. 7.1(c). In the latter case, the horizontal and vertical spacings between antidots are $X = 25a_{zz}$ and $Y = 15a_{ac}$, respectively. In all cases, the TGA side lengths are $L_\triangle = 5a_{zz}$ throughout. The remaining dimensions are illustrated in Fig. 7.1(b), and given explicitly in the figure caption. The lattice constants along the zz- and ac-directions are $a_{zz} = 2.46\,\text{Å}$ and $a_{ac} = 4.26\,\text{Å}$, respectively.

The devices are built with four arms which terminate in metallic contacts: left (L), right (R), top (T), and bottom (B). The four graphene segments in the four arms are assumed nonmagnetic in order to isolate the magnetic influence of the antidots. Furthermore, the contacts are considered either nonmagnetic or ferromagnetic. In other words, the metallic contacts inject either spin-unpolarized electrons or electrons of a single spin orientation.

The cross-shape geometries illustrated in Figs. 7.1(b) and 7.1(c) are useful in order to quantify the longitudinal, transverse, and skew transport mechanisms. Ultimately,
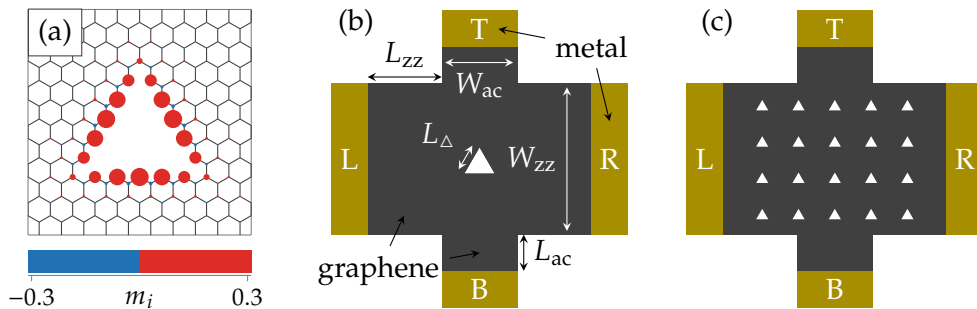
Figure 7.1: Magnetic moments of the $L_\triangle = 5a_{zz}$ zz-TGAs (a), and device schematics (b) and (c). (a) Magnetic moments represented by circles with radii $\propto m_i$. (b) Schematic of the single-TGA device with dimensions $W_{zz} \approx 6\,\text{nm}$, $W_{ac} \approx 4\,\text{nm}$, and $L_{zz} \approx L_{ac} \approx 2\,\text{nm}$. (c) Schematic of the 5×4 TGA-array device with dimensions $W_{zz} \approx 26\,\text{nm}$ and $W_{ac} \approx 16\,\text{nm}$.

Figure 7.2: Illustrations of the spatial spin-splitting feature of a regular TGA device (a) and a flipped TGA (180° rotation) device (b). The underlying images display the spin current maps $J^s = J^\uparrow - J^\downarrow$ injecting from left (L), w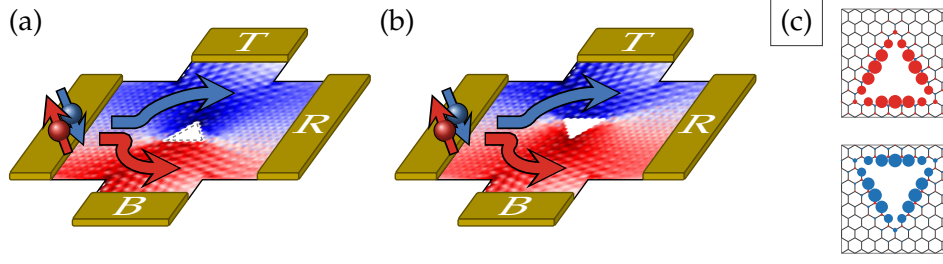ith colors $J^s > 0$ red and $J^s < 0$ blue. (c) Illustrates the magnetic moments surrounding the regular TGA (top) and the flipped TGA (bottom), the TGAs of (a) and (b), respectively. The colors are red for spin up and blue for down.

we will demonstrate that these devices display a spatial-spin splitting property analogous to the spin Hall effect (SHE) [38]. The spatial spin-splitting is illustrated in Fig. 7.2(a) by arrows, where the underlying color map illustrates the distribution of spin currents $J^s = J^\uparrow - J^\downarrow$. Spin-unpolarized currents enter from left and near the antidot they scatter spin-dependently. Spin-up (red) currents are scattered *below* the antidot and spin-down (blue) currents *above*. The large spin-polarized currents then collected at opposite T and B contacts.

The sixfold symmetry of the graphene lattice allows only for two orientations of zz-TGAs, demonstrated in Fig. 7.2(c). With a 180° in-plane rotation, the zz-edges expose the other sublattice, yielding magnetic moments of the *opposite* orientation. In our devices, a 180° in-plane rotation inverts *both* the scattering directions and the spin-polarization simultaneously. An independent inversion of either quantity flips the direction of the spin-dependent currents, but inverting both restores the same qualitative behavior. The rotated device is demonstrated in Fig. 7.2(b), and we note that the individual spin channels are diverted to the same sides of the device as before. This makes TGA devices further robust against (random) 180° in-plane rotations, demonstrated below in Section 7.2.

The TB model is identical to that presented in the previous chapter, see Eq. (6.1), where the magnetic moments are calculated from a self-consistent solution of the Hubbard model within the mean field approximation. The magnetic moments are calculated for each TGA individually in *periodic lattices* using a $X = 25a_{zz}$ by $Y = 15a_{ac}$ square unit cell ($\approx$ 6 nm × 6 nm). The same lattices are explored in the previous chapter Chapter 6. Notice that the spacings between TGAs in the array devices [Fig. 7.1(c)] correspond to the dimensions of the unit cells of the periodic lattices.

The transport properties are calculated using Landauer-Büttiker [Eq. (2.8)] along with the Fisher-Lee relations for the transmission functions and currents [Eqs. (2.9) and (2.11)]. We further define the spin and charge transmissions $T^s_{pq}(E) = T^\uparrow_{pq}(E) - T^\downarrow_{pq}(E)$, and $T^c_{pq}(E) = T^\uparrow_{pq}(E) + T^\downarrow_{pq}(E)$, and local currents $\mathbf{J}^s_p(E) = \mathbf{J}^\uparrow_p(E) - \mathbf{J}^\downarrow_p(E)$, and $\mathbf{J}^c_p(E) = \mathbf{J}^\uparrow_p(E) + \mathbf{J}^\downarrow_p(E)$, respectively. The metallic contacts are included using an effective self-energy $\Sigma_{\text{metal}} = -i|t|$ added to the edge sites of the metal/graphene interfaces [105]. For spin-polarized (ferromagnetic) contacts, the self-energy for
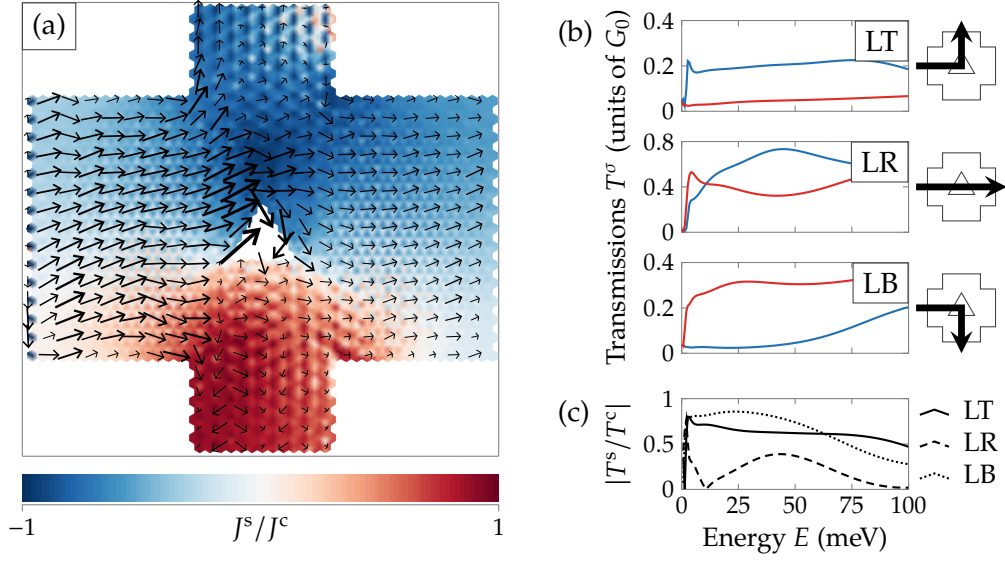
Figure 7.3: Current maps (a), transmissions (b), and spin-polarizations (c) through a single TGA device. (a) The current map with arrows scaled and oriented by the charge current $\mathbf{J}_L^c$. The underlying color map displays the current spin polarization J_L^s/J_L^c. (b) Transmission coefficients from the L lead to either T, R, or B, (LT, LR, and LB panels, respectively). The colors are red: spin up and blue: spin down. (c) The spin-polarizations T^s/T^c for LT (solid), LR (dashed), and LB (dotted).

one spin channel is set to zero. The devices are built such that T and B graphene segments (ac-nanoribbons) are metallic.

7.1 Four-lead device transmissions

The most striking electronic transport feature of a TGA is the spatial spin-splitting. For a qualitative picture, we consider current maps of left-injected local charge currents $\mathbf{J}_L^c$ and corresponding spin polarization $|\mathbf{J}_L^s|/|\mathbf{J}_L^c| = J_L^s/J_L^c$. A current map at the energy $E = 40$ meV of the single-TGA device is displayed in Fig. 7.3(a). The arrows illustrate the direction and magnitude of the charge currents, and the underlying color map displays the local spin-polarizations. The current distribution indicates an overall left-to-right (LR) transport, with a slight concentration at the top corner of the TGA. Nevertheless, small currents can be spotted running from left-to-top (LT) and left-to-bottom (LB). However, the spin-polarization of the currents reveals strongly spin-dependent transport directions. Namely, the spin-up electrons travel below the antidot and spin-down electrons travel above.

We can quantify the spatial spin-splitting using the spin-resolved LT, LR, and LB transmissions, as well as their respective spin-polarizations T^s/T^c. The former are illustrated in Fig. 7.3(b) and the latter in Fig. 7.3(c). Over a wide range of energies, the transmissions display significant LR charge transmission and largely spin-polarized LT and LB transmissions [solid and dotted in Fig. 7.3(c)]. In particular, the LT and LB spin-polarizations are between 70 % and 90 % for energies $E < 60$ meV. Meanwhile, the LR transmissions are only moderately spin polarized [dashed in Fig. 7.3(c)].
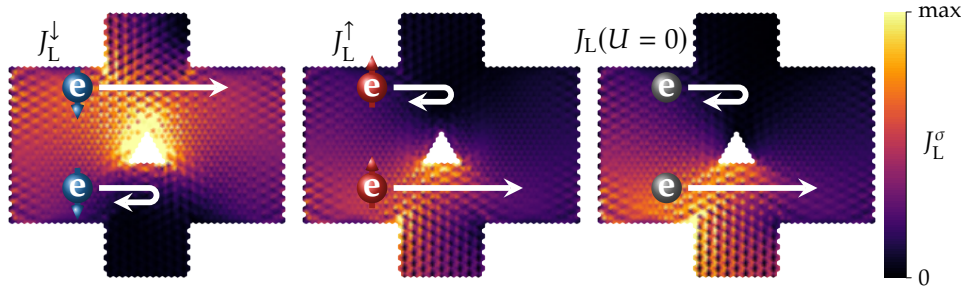
Figure 7.4: Spin-resolved current maps J_L^σ at $E = 40$ meV for the spin-polarized and spin-unpolarized zz-TGA. The spin-up (left) and spin-down (middle), and in the (single-spin) spin-unpolarized TGA (right) share the color scale on the right. Schematic illustrations of the scattering are displayed on top of the current maps with white arrows, and electrons colored according to spin type: red for spin up, and blue for spin down.

It is interesting to note, that while TGA *lattices* are half-metallic, a single-TGA does not generate a pure spin-filter, in which one spin is entirely blocked (backscattered). Even so, a spin-dependent bending of the currents does give rise to transverse, largely spin-polarized currents.

To explain the mechanism behind the spin-splitting, we compare the spin-polarized TGA to the *spin-unpolarized* TGA. In Fig. 7.4 the spin-resolved currents $J_L^\uparrow$ and $J_L^\downarrow$ of a spin-polarized TGA device are displayed next to the (single-spin) currents of a spin-unpolarized TGA ($U = 0$), where $J_L^\uparrow = J_L^\downarrow$. While the spin-down currents (left panel) appear unique, the spin-up currents are remarkably similar to the spin-unpolarized TGA currents (middle and right panels, respectively). The spin-up currents—or indeed the currents of both spins in the unpolarized antidot case—are explained by geometrical considerations. Representative paths for currents of each spin type are illustrated schematically in Fig. 7.4 using white arrows. Above the antidot, the top corner of the TGA interrupts the longitudinal paths, and electrons are backscattered. Below the antidot, however, the path is straight and nanoribbonlike. From wave-function matching arguments, spin-up electrons incident from left would backscatter at the top of the antidot, effectively bending down towards the nanoribbonlike section at the bottom. We note that there are no on-site energies near $E = 40$ meV for the spin-up electrons, $\epsilon_i = -m_i U/2$ (negative), so their behavior is similar to spin-unpolarized electrons.

On the other hand, spin-down currents are greatly influenced by the on-site energies near this energy since $\epsilon_i = +m_i U/2$ (positive). Notice especially that the spin-down currents in Fig. 7.4 (left panel) appear the most dense at the *top corner* of the antidot. It was demonstrated in Section 6.3 that the LDOS of TGA *lattices* suggests significant dispersion at the corners in particular. Furthermore, the LDOS also indicates sublattice asymmetries at the bottom of the antidots, which for the spin-down electrons will act as scattering centers. Ultimately, the spin-down currents are backscattered at the bottom of the antidot, and effectively bend upwards towards the top corner.

The spatial spin-splitting is thus a combined result of the geometrical skew scattering of the spin-up currents, and an opposite skew scattering of spin-down currents due
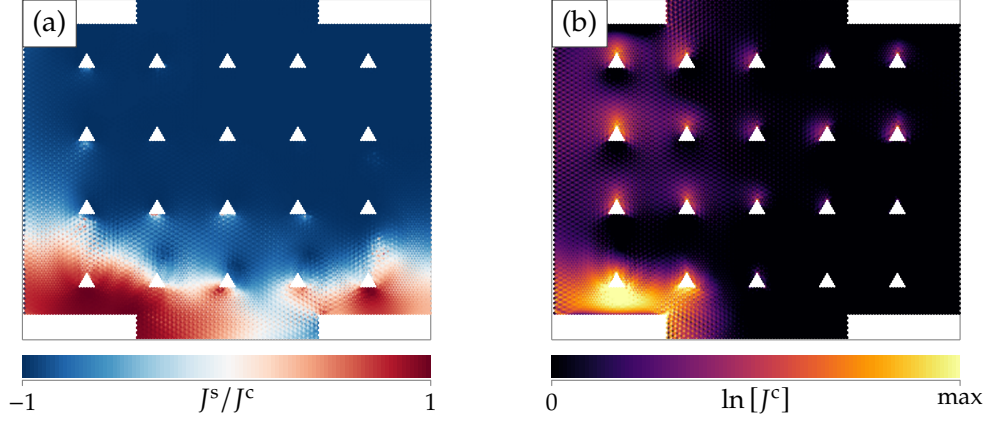
Figure 7.5: Current spin-polarization J^s/J^c (a) and charge current J^c maps (b) at $E = 40\,\text{meV}$ through the 5×4 TGA array. Note that the charge current in (b) is displayed logarithmically, $\ln[J^c]$.
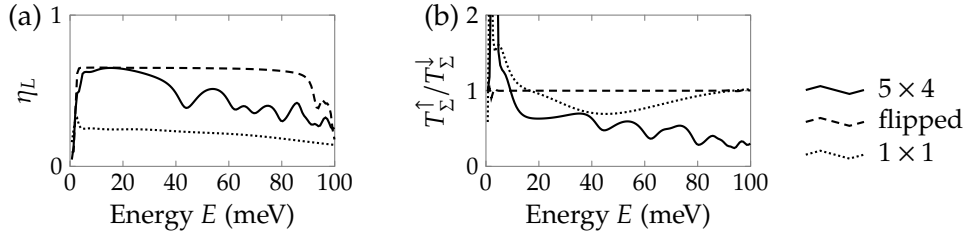

Figure 7.6: Splitting efficiencies η_L (a) and spin selectivities $T_\Sigma^\uparrow/T_\Sigma^\downarrow$ (b) of TGA devices (see main text). The legend is displayed on the right.

to spin-polarized the localized states.

The spatial spin-splitting feature is enhanced with arrays of multiple TGAs. Initially, we consider a device with a 5×4 array of TGAs which all have the same alignment [see schematic in Fig. 7.1(c)], and the magnetic profiles of each antidot are identical. We will later consider rotating the antidots in-plane, which results in magnetic moments with both signs. The spin-polarization and charge current maps at $E = 40\,\text{meV}$ are displayed in, respectively, Figs. 7.5(a) and 7.5(b) for the 5×4 TGA-array device. In contrast to the single-TGA device, the currents in the array device decay visibly from L to R [Fig. 7.5(b)], and further demonstrate near-perfect LT spin-polarization [Fig. 7.5(a)].

For convenience, we introduce here a figure of merit: the spin-splitting efficiency from left-injected currents

$$\eta_L = \frac{T_{LB}^s - T_{LT}^s}{T_{LB}^c + T_{LT}^c + T_{LR}^c}. \tag{7.1}$$

A value of $\eta_L = 1$ means perfect spatial spin splitting of all left-inject into top and bottom leads. The efficiencies of the single-TGA (1×1) and the 5×4 TGA-array devices are shown in Fig. 7.6(a). The 5×4 array (solid curve) is more than twice as efficient as the single TGA (dotted curve), for all considered energies $0 \leq E \leq 100\,\text{meV}$. By simultaneously reducing LR currents and increasing LT and LB spin-polarizations, the efficiency in turn significantly improves.
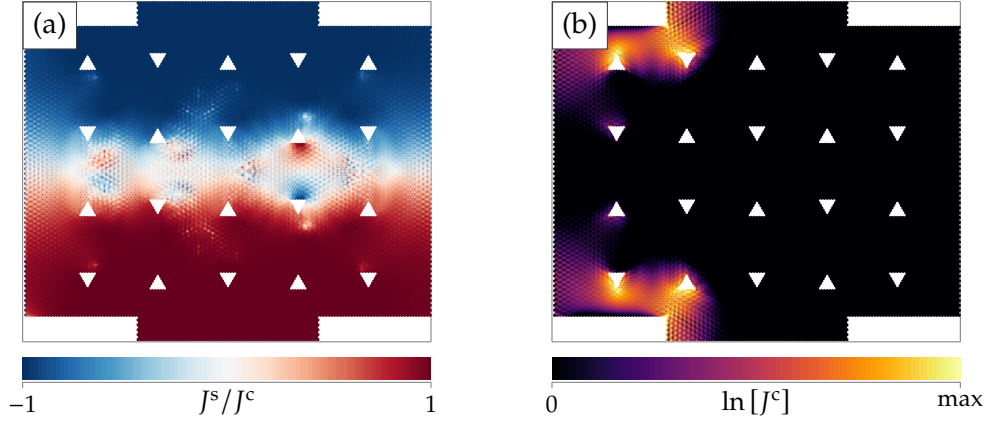
Figure 7.7: Current spin-polarization J^s/J^c (a) and charge current J^c maps (b) at $E = 40\,\text{meV}$ through the flipped 5×4 TGA array. Note that the charge current in (b) is displayed logarithmically, $\ln[J^c]$.

A closer examination of the spin-down currents [the top part of the device in right panel of Fig. 7.5] reveal a magnitude continuously decreasing *longitudinally* along the device. At each antidot, the spin-down currents bend slightly upwards towards the T lead. The net effect can be describes as *repeated scattering* from single TGAs. This effect is somewhat similar to a previously described ratchet effect for triangular perturbations in graphene [106], where skew scattering is reported.

While the TGA-array device is far more efficient compared to the single-TGA device, the former is still *limited* by the half-metallic region induced by the TGA array. This is made clear by comparing the total spin-up transmission and the total spin-down transmission. We introduce the additional figure of merit: the spin selectivity $T_\Sigma^\uparrow/T_\Sigma^\downarrow$, where $T_\Sigma^\sigma = T_{LT}^\sigma + T_{LR}^\sigma + T_{LB}^\sigma$. In Fig. 7.6(b) we display the spin-selectivities for both the single TGA (1×1) and the 5×4 TGA array. Because of the half-metallic properties of multiple TGAs, spin-up electrons are blocked from entering the array. Both for the single and, in particular, the array case, the spin-selectivities are $T_\Sigma^\uparrow/T_\Sigma^\downarrow < 1$. The spin-current blocking is also noticeable in Fig. 7.5, where the area of spin-up currents is very small compared to spin down (red versus blue areas).

Alternatively, as demonstrated in the previous chapter (Section 6.3.1), TGA lattices where every second antidot has been rotated 180° are semi-conducting, and spins are interchangeable. With this in mind, we consider the *flipped* 5×4 antidot array, where every second antidot has been rotated 180°. Current maps at $E = 40\,\text{meV}$ are shown in Fig. 7.7, and the efficiency as well as spin-selectivity are also displayed in Figs. 7.6(a) and 7.6(b), respectively.

The current maps reveal a transverse spin polarization, which is completely *anti-symmetric*. Electrons of both spin types can now penetrate the array region, and each antidot (regardless of orientation) will bend the spin-up currents below and spin-down currents above [see also Fig. 7.2(b)]. The spin-selectivity in the flipped case [Fig. 7.6(b) (dashed curve)] is almost exclusively $T_\Sigma^\uparrow/T_\Sigma^\downarrow = 1$. With near-perfect LT and LB spin polarizations, the flipped case yields the largest spin-splitting efficiency (dashed curve) of those considered in Fig. 7.6(a). In effect, the flipped case is a better illustration of the ideal repeated scattering of single TGAs, as now neither
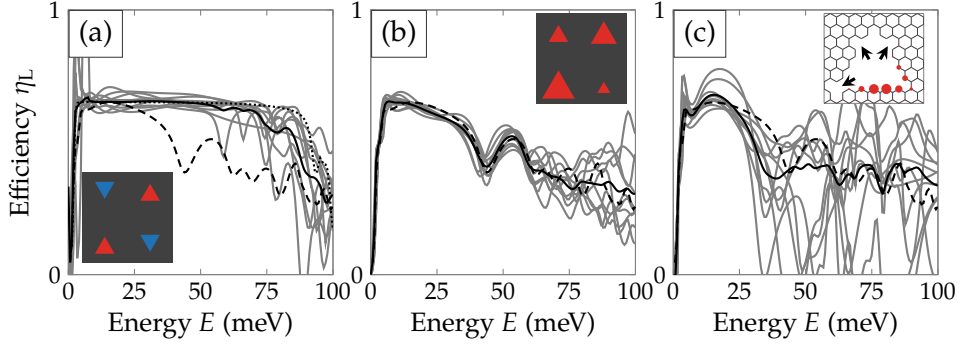
Figure 7.8: Spin-splitting efficiencies of disordered TGA arrays devices. Disorder types: (a) randomly flipped TGAs, (b) randomly varied side lengths, and (a) randomly removed edge atoms. The individual realizations are illustrated in gray, and the configurational average in solid black. The pristine 5×4 array device is illustrated in dashed black. In (a) we also illustrate the pristine flipped 5×4 array device in dotted black. The insets illustrate the type of disorder.

spin is blocked from entering the array.

7.2 Disordered devices

We now consider the influence of disorder. We previously demonstrated [Paper II, and previous chapter (Section 6.4)] that TGA lattices are unusually robust against disorder, with persistent band gaps and half-metallicity. We demonstrate below that our TGA devices are similarly robust with respect to spatial spin-splitting. We consider several 5×4 array devices with three types of disorder: random $180°$ in-plane rotation, side length variation, and edge disorder. Despite any of these types of disorder, our TGA devices still show significant spatial spin-splitting for the levels of disorder considered here. Each type of disorder is considered using 10 different realizations.

For the first type of disorder, the TGAs are randomly rotated in-plane, which simultaneously flips the signs of the magnetic moments [illustrated via blue and red triangles in the inset of Fig. 7.8(a)]. The efficiencies η_L of 10 disorder realizations along with the configurational average (gray and solid black curves, respectively) are displayed in Fig. 7.8(a). These are compared to the pristine case of a 5×4 TGA-array (black, dashed), with all TGAs oriented the *same* [reproduced from Fig. 7.6]. Overall, both the individual and the average efficiencies are for the most part larger than in the pristine case. Furthermore, the efficiencies of the individual realizations are very similar within the range $0 \leq E \leq 50$ meV. This is understood from regular and flipped single-TGA devices yielding qualitatively the same spatial spin-splitting [Figs. 7.2(a) and 7.2(b)]. For comparison, we also display the flipped case, where every second antidot has been rotated (black, dotted), and the efficiency is very close to the disordered average. This further supports that rotating TGAs, ordered or at random, can significantly increase the efficiencies. Notice the optimal energy range $0 \leq E \leq 50$ meV, where all realizations have high efficiencies very close the configurational average.

In the second type of disorder [in Fig. 7.8(b)], we consider the effect of varying the
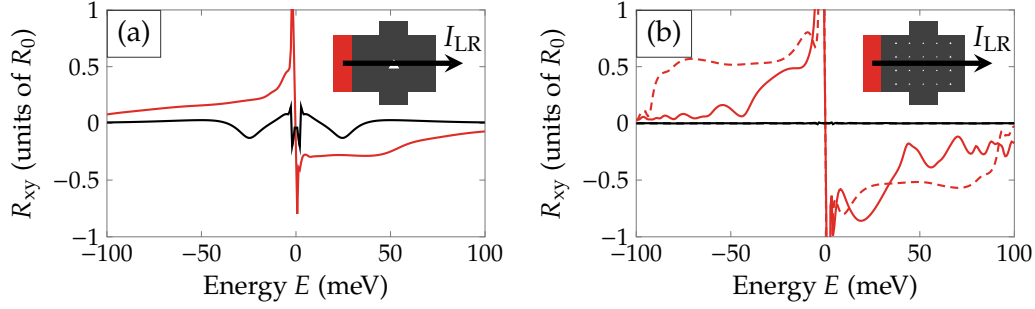
Figure 7.9: Transverse/Hall resistance $R_{xy} = V_{\text{TB}}/I_{\text{L}}^{\text{c}}$ of the single-TGA device (a) and the 5×4 TGA-array devices (b). L and R are source and drain, T and B are voltage probes. Both the spin polarized TGAs (red) and the spin unpolarized TGAs (black) are considered. In (b) we also consider the *flipped* 5×4 TGA array (dashed).

side lengths $L_\triangle \to L_\triangle \pm \delta L$ [inset in Fig. 7.8(b)]. The lengths are varied by $\delta L \in \{0, 1a_{\text{zz}}, 2a_{\text{zz}}\}$. Varying the side lengths has the least effect of those types of disorder that we consider. There is very little variation of efficiency between realizations, and in the range $0 \le E \le 50\,\text{meV}$ all configurations have very similar efficiencies. By increasing (decreasing) the side length $L_\triangle$, the total magnetic moments of the individual TGAs increase (decrease) as well. The *average* magnetic moment is then (nearly) unchanged. These results emphasize that it is the presence of multiple spin-dependent scatterers with similar qualitative behavior and not their exact positioning or size, which enhances the spin-splitting effect.

Finally, we also consider edge disorder in Fig. 7.8(c). The edge disorder is implemented by randomly removing edge atoms (atoms with only two neighbors) with a certain probability $p = 0.05$. This "etch" is performed $N_{\text{etch}} = 3$ times. Edge disorder has been demonstrated (Section 6.4) to severely reduce the magnetic moments surrounding the antidots, and can be described as kind of a worst case scenario. An example of a disordered TGA and its distribution of magnetic moments is shown in the inset of Fig. 7.8(c). For this particular TGA three edge atoms have been removed, illustrated with black arrows in the inset of Fig. 7.8(c). The efficiencies in Fig. 7.8(c) show the largest influence of disorder—only in the range $0 \le E \le 25\,\text{meV}$ do we observe significantly sized efficiencies. However, for experimental purposes an energy window of approximately $25\,\text{meV}$ is sufficient. The level of edge disorder considered here is particularly severe for small antidots with short edges. In some cases, this can completely suppress the magnetic moments along an edge. For larger, more experimentally feasible antidots, such disorder should have a smaller effect, and the energy window for large efficiencies should be less influenced.

7.3 Transverse resistances

Inspired by the SHE-like transport signatures of TGA devices, we consider the transverse resistances of our four-terminal devices. This is a measure of skew transport, in which the induced transverse potential difference V_{TB} is measured as a

function of a longitudinal current I_{LR}. The transverse resistance is given

$$R_{xy} = V_{TB}/I^c_{LR} , \tag{7.2}$$

where the transverse potential difference $V_{TB} = V_T - V_B$. The L and R leads are source and drain and T and B are voltage probes i.e. they carry zero (charge) current $I^c_T = I^c_B = 0$. By current conservation the L and R currents are then equal and opposite $I^c_L = -I^c_R = I_{LR}$. We further assume *spin mixing* in the T and B leads, which then get the spin-unpolarized potentials $V^\uparrow_T = V^\downarrow_T = V_T$ and $V^\uparrow_B = V^\downarrow_B = V_B$. The source and drain potentials are set to $V_L = V_{LR}$ and $V_R = 0$ (reference value). The resistance is determined by solving the Landauer-Büttiker current equation for the unknown V_T, V_B, and the longitudinal current I^c_L.

The transverse potential difference is $V_{TB} \propto T^c_{LT} T^c_{RB} - T^c_{RT} T^c_{LB}$, which is zero in case of left-right symmetry. Instead, in Fig. 7.9 we consider spin-up polarized L leads, illustrated via red L contacts in the respective insets. The transverse resistance of a single-TGA device is shown in Fig. 7.9(a). The device displays a characteristic antisymmetric resistance with respect to energy (red curve). Considering the same device but with *spin-unpolarized* ($U = 0$) TGAs (black curve), the observed resistance is symmetric instead.

In the spin-polarized case, the current through the T contact is dominantly by the top-to-right (TR) transmission of spin-down electrons, such that $I^c_T \rightarrow T^\downarrow_{TR} V_T$. In order for the voltage probe to rest at $I^c_T = 0$, the electronic potential of the T contact settles towards that of the R lead, i.e., $V_T \rightarrow 0$. At the same time, at the B contact, both the left and right spin-up transmissions dominate, such that $I^c_B \rightarrow T^\uparrow_{BL}(2V_B - V_{LR})$ and $T^\uparrow_{BL} = T^\uparrow_{BR}$. The B electronic potential at rest ($I^c_T = 0$) then remains approximately midway between the L and R potential i.e. $V_B \rightarrow V_{LR}/2$. Ultimately, this results in a negative transverse potential difference $V_T - V_B < 0$ and in turn a negative resistance $R_{xy} < 0$. Inverting the sign of the energy flips the spin-dependent scattering directions, and, in turn, inverts both the transverse potential and the resistance. In contrast, a spin-unpolarized TGA is electron-hole symmetric, and the transverse resistance (black curves) becomes symmetric as well. Notice that the resistance of the spin-unpolarized TGA device is nonzero. This originates from the spin-polarized L lead, or, in other words, the left-right *asymmetry*.

The influence of spin-polarized TGAs is even more pronounced in case of the 5×4 array device (solid curves) and the *flipped* array device (dashed curves) [Fig. 7.9(b)]. Both the resistances are larger than for a single-TGA device, and furthermore the spin-unpolarized TGAs display near-zero resistances. The improved signal is related to the larger spin-splitting efficiencies of TGA-array devices. In particular, the flipped array device shows the most clear signal of spin-polarized TGAs.

The antisymmetric resistance gives a clear distinction between magnetic and non-magnetic TGAs. It further provides an indirect measure of the spin-splitting induced by TGAs, and an excellent measure of proof-of-concept and TGA-based spatial spin-splitting. It may even be be used to detect spin-polarized signals in more general graphene nanostructures.
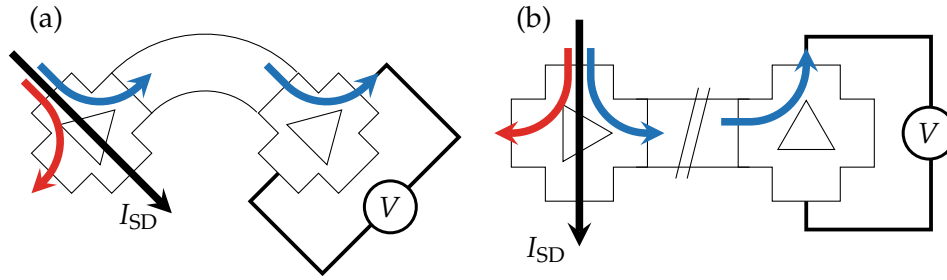
Figure 7.10: Illustrations of a dual TGA setup, to both generate and measure spin currents generated from the spatial spin-splitting of the devices. (a) The spin-preserving bend, where two devices are coupled through a 90° turn. (b) The spin-preserving grain boundary, where two devices are coupled through a straight channel that undergoes a 90° rotation of the underlying graphene lattice. The black arrows illustrate the source-drain *spin-unpolarized* currents. The generated spin-polarized currents are colored red and blue, for spin-up and down, respectively. The final device illustrates the transverse potential measurement.

7.4   Discussion and summary

The zz-TGA devices demonstrate an intriguing spatial spin-splitting feature. Spin-polarized currents injected from either left or right are spin-dependently scattered into top and bottom leads, and the scattering directions can be flipped by gating. The effect is somewhat analogous to the spin Hall effect. However, this effect is obtained without the need for spin-orbit interactions or topologically protected transport channels. By avoiding spin-orbit coupling, a major source of spin relaxation, we may be able to maintain the excellent spin-transport properties of graphene over long distances.

The performance of TGA devices are shown to be very robust against typical disorders faced in experiments. Similar to the TGA lattices (Section 6.4), the influence of positional and size disorder is minor. Even when edges are disordered to such an extent, that the magnetic moments may nearly vanish at certain TGAs, still we observe significant performance.

Inspired by the spin Hall effect measurements, we consider the transverse resistance of our devices. A nonzero resistance is demonstrated, antisymmetric with respect to energy, characteristic of the spin-polarized TGAs. With a similar device, but assuming spin-unpolarized ($m_i \rightarrow 0$) TGAs, the transverse resistance is instead symmetric. This may prove to be an excellent measure of, not only the quality of the spatial spin splitting, but a proof of spin-polarized TGAs, and by extension magnetic graphene edges.

When considering the transverse resistance, we used single-spin injected currents. This usually requires an external ferromagnetic contact, which are often used in spin-precession and spin-transport lifetime experiments [27]. As an interesting extension to our simulations we could employ a dual setup, where one TGA device is used to split the currents, and another to convert the spin-polarized currents into a (measurable) charge voltage difference. Unfortunately, such a setup would require the top (or bottom) lead of one TGA device to couple to the left (or right) of another.

In a single sheet of graphene, there is no way to make such a setup with *zz-edged* TGAs, as a 90° rotation will not yield another zz-TGA. It would require a 90° turn to couple two TGA devices of different orientation, illustrated in Fig. 7.11(a). Another option is to introduce a grain boundary and subsequent rotation of second device, illustrated in Fig. 7.11(b). Most importantly, the electrons cannot lose information of spin between devices, i.e., the coupling must be spin-preserving. Both methods would make an all-TGA experiment possible, which would further promote the use of spatial spin-splitting in TGA devices.

The prospect of being able to filter or even split spin currents, without the use of spin-orbit couplings or topological transport channels, has large implications on the field of spintronics. In particular, TGAs could be a path towards realizing efficient graphene-based spin generators and detectors.

Large scale triangular antidots 8

The two previous chapters have demonstrated principle features that motivate future experiments using embedded zz-TGAs (zz-edged triangular graphene antidots). In particular, we have demonstrated that zz-TGA lattices display near-Fermi level half-metallicity when all antidots are oriented the same (aligned) [90]. If, however, every second antidot is flipped (rotated 180° in-plane), lattices instead display semiconducting behavior (Section 6.3.1). One of the most remarkable features was presented in cross-shaped devices with embedded TGAs, where spin-dependent scattering was demonstrated to direct electrons of different spins to opposite leads (spatial spin-splitting) [107]. In all cases, these features were explored using zz-TGAs with side lengths $L \sim 1\,\text{nm}$, which would be very challenging to produce in experiment. Here, we look at how the mechanisms we have discovered may have signatures in systems much closer to what is currently experimentally feasible.

Triangular holes with side lengths $L \sim 0.3\,\mu\text{m}$ have been fabricated in graphene flakes using electron beam lithography [51]. Even though edge-alignment was not considered in this case, we can imagine rough alignment to crystalline edges of the graphene flakes. Additionally, the lithography mask could be replaced with hBN—a recent study demonstrates fabrication of atomically precise zz-edged holes in hBN with controllable side lengths L between $\sim 2\,\text{nm}$ and $10\,\text{nm}$ [108]. Controlled edge formation in graphene nanostructures is also progressing, with recent advances in growth of zz-edged triangular nanoislands [109, 110]. To study length scales significantly larger than the atomic details, we consider $L \sim 5\,\text{nm}$, which is still small enough to consider a large number of TGAs. Furthermore, some fabrication techniques are based on seeded growth, where the distribution might be difficult to control. Such methods result in large samples with extreme positional disorder. In this chapter, we study such samples that no longer resemble lattices. Additionally, we compare the effects of pristine and disordered zz-TGAs. We consider both side length variation and edge disorder.

To explore these samples, we employ large-scale methods which allow for studying systems of millions of atomic sites. In particular, we study the electronic behavior using the Chebyshev expansion of the DOS, and the quantum transport properties via the Kubo method [64, 68, 72–74]. The Kubo-method allows to study the diagonal conductivities σ_{xx} and σ_{yy}. However, through collaboration [1] we have also studied the off-diagonal conductivities σ_{xy} and σ_{yx} using an alternative Kubo method [69], and these preliminary results are also presented below (Section 8.3). The off-diagonal conductivities allow for studying the large-scale equivalent of the previously observed spatial spin splitting: the spin Hall conductivity $\sigma_{xy}^{\text{s}} = \sigma_{xy}^{\uparrow} - \sigma_{xy}^{\downarrow}$.

With access to both the transverse and longitudinal quantum transport, we also examine the transport anisotropy σ_{yy}/σ_{xx}. As demonstrated below, the zz-TGAs indeed display significant transport anisotropy, where samples are more conductive in one direction, while being more resistive in the other. This opens the possibility of engineering anisotropic features, which can be used to build electronic

---

[1]Stephan Roche's group at ICN2, Barcelona; Stephan Roche and Jose H. García, in particular.
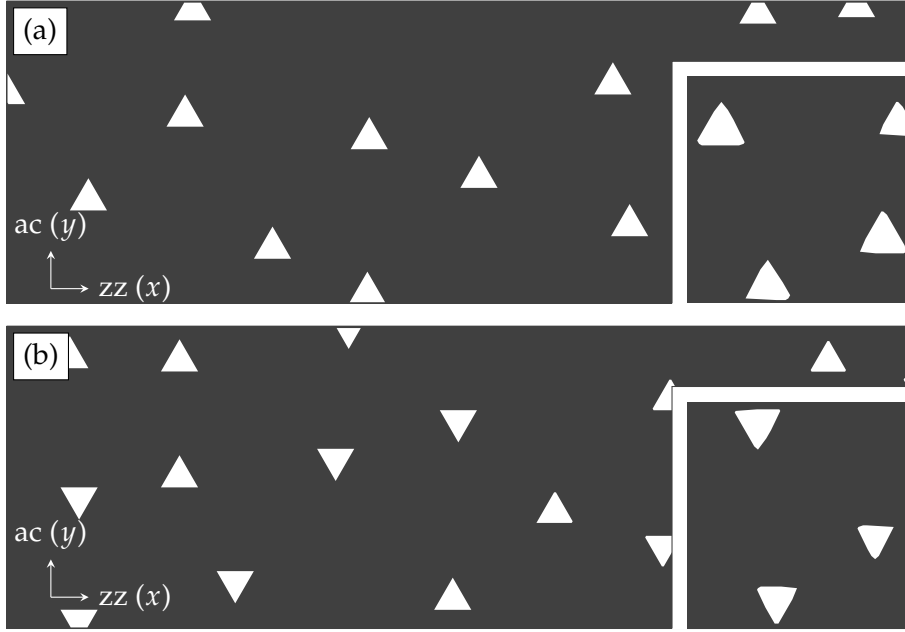
Figure 8.1: Illustrations of the *aligned* (a) and the *flipped* (b) TGA samples. The insets illustrate the corresponding disordered TGAs. The illustrations in (a) and (b) are approximately 120 nm × 80 nm. The samples considered in the simulations are in full 360 nm × 360 nm.

circuits or waveguides [111], optical circuits [112], or communications devices [113]. Anisotropic transport has been demonstrated in graphene through stretching [114, 115], periodic nanofacets [116], and even suggested in an-isotropically arranged GALs [117], where antidots are spaced closer in one direction and further in the other. In contrast to these other methods, the zz-TGAs considered here are distributed uniformly, and anisotropic features originate solely from the orientation of the individual zz-TGAs.

We study the electronic and transport properties for two uniform distributions of TGAs: The *aligned* case, where every TGA is oriented in the same direction, and the *flipped* case, where antidots are randomly oriented in opposite directions. The aligned sample is illustrated in Fig. 8.1(a), and the flipped in Fig. 8.1(b). The zz- and ac-directions are noted in the bottom left corner: respectively, the x- and y-directions. Furthermore, we consider pristine and disordered TGAs; The disorder is illustrated in the insets of Figs. 8.1(a) and 8.1(b). All samples are approximately 360 nm×360 nm, periodic in both directions, and contain 400 embedded TGAs (~ 5 million atoms). The side lengths of the pristine TGAs are $L = 20a_{zz}$, and the disordered TGAs are $L = 22a_{zz}$. The lattice constant along the zz-direction is $a_{zz} = 2.46$ Å. The difference in side lengths is relatively small and is not expected to have a major influence on the results demonstrated below.

The TB model is identical to that presented in the previous two chapters, see Eq. (6.1), where the magnetic moments are calculated from a self-consistent solution of the Hubbard model within the mean field approximation. The magnetic-moment distributions surrounding each antidot are assumed independent, and determined individually. These distributions are calculated in periodic systems using $50a_{zz} \times 30a_{ac}$ unit cells (~ 12 nm × 12 nm), and then embedded randomly in the graphene
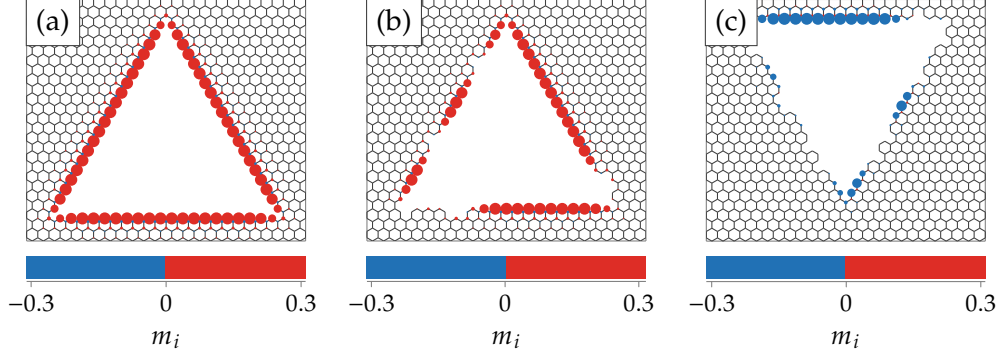
Figure 8.2: Illustration of an $L = 20a_{zz}$ pristine (a) and an $L = 22a_{zz}$ disordered (b) TGA, including a 180° rotated TGA (c). The disorder in (b) and (c) includes side length variation $L \rightarrow L \pm \delta L$, where $\delta L = 8a_{zz}$, and edge disorder by "etch" percentage $p = 0.05$ for $N_{etch} = 4$ times. The magnetic moments are illustrated by circles with radii $\propto m_i$.

samples. To ensure valid magnetic profiles, we prevent unit cells from overlapping in the samples. This gives a minimum distance of $X_{min} \sim 12\,nm$.

The DOS are calculated using the Chebyshev expansion [Eq. (3.5)], and the diagonal conductivities σ_{xx} and σ_{yy} using the real-space Kubo method [Eq. (3.14)]. When considering only the DOS, we use $N_\delta = 20000$ expansion coefficients [see Eq. (3.5)]; This is the upper limit of our system size. Upon further increase of N_δ, additional oscillations occur from the periodicity of our samples. For the conductivities, how-ever, we instead use a lower $N_\delta = 4000$ for optimal performance, and $N_{exp} \leq 5000$ expansion coefficients for the time evolutions [see Eq. (3.14)]. Preliminary tests indi-cate that the qualitative behavior demonstrated below does not change significantly with increased sample sizes or N_δ.

The off-diagonal conductivities are calculated using the method from García *et al.* [69], and have been calculated by José H. García based on Hamiltonians supplied from the above models.

8.1 Influence of disorder

In the face of disorder, small-scale zz-TGAs have been demonstrated to display robust half-metallicity in aligned lattices (Section 6.4). Here, we consider the influence of disorder on large-scale TGAs via the DOS using two types of disorder: Side length variation $L = 22a_{zz} \pm \delta L$, where $\delta L \leq 8a_{zz}$, and edge disorder, where edge atoms are removed with a certain probability $p = 0.05$. The latter "etch" is performed $N_{etch} = 4$ times. Variation of the side length was previously shown to have minor impact on the qualitative transport-scattering mechanisms of small-scale TGAs. Edge disorder, on the other hand, was shown to severely reduce the corresponding magnetic moment distributions.

A pristine TGA with $L = 20a_{zz}$ is displayed along with its associated magnetic moments in Fig. 8.2(a). By comparison to small-scale TGAs [e.g. Fig. 6.5], the pristine magnetic moments distributions are remarkably similar. The magnetic moments along the zz-edges are for the most part constant, decay perpendicularly
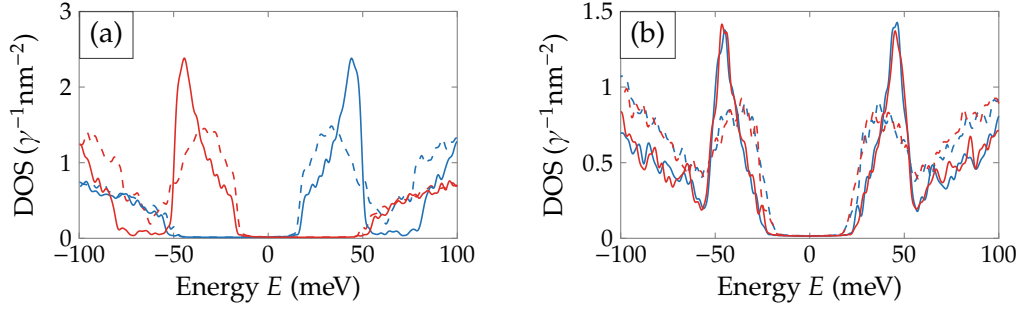
Figure 8.3: The DOS of an $L = 20a_{zz}$ pristine (solid) and an $L = 22a_{zz}$ disordered (dashed) TGA sample, in the *aligned* (a) and *flipped* cases (b). The spin-up DOS is colored red and spin-down blue.

to the edges, and are nearly zero after only a couple of a_{zz}. The distributions indicate that the magnetic profiles of each TGA do not influence each other.

The magnetic moments of two disordered TGAs are illustrated in Figs. 8.2(b) and 8.2(c). These display a regular and flipped TGA, respectively, and in both cases, the magnetic moments are reduced in size. In the second case [Fig. 8.2(c)] the flipped TGA is oppositely spin-polarized. Notice in the second case, at certain edges (e.g. bottom-left edge) the magnetic moments have almost vanished. However, compared to previous demonstrations of edge disorder (Section 6.3), both of these large-scale TGAs still display significantly sized magnetic moments.

The Chebyshev-expanded DOS of the samples, shown in Fig. 8.3, reveal that the effects of disorder are quite similar in the aligned and the flipped case. The half-metallic peaks (and the metallic peaks in the flipped case) at $E = \pm 40$ meV form as the result of spin-polarized edge states (Chapter 6). The most obvious difference between the pristine (solid) and disordered cases (dashed) is the smearing out of these peaks. However, regardless of disorder these peaks preserve their respective half-metallic (aligned) or metallic (flipped) behavior. It is worth pointing out that in the flipped cases, the spin types are nearly equivalent, but with very small differences. In fact, also in the aligned case, the DOS of the two spins are nearly antisymmetric with respect to energy. In a perfectly infinite sample, we expect spin types in the aligned case to be exactly antisymmetric with respect to energy. Similarly, in the flipped case, we expect spin types to be exactly equivalent. The finite size of our samples introduces these small spin-type differences, and increasing the sample sizes will average these artifacts out (not shown).

The disorder in both the aligned and flipped cases has only a minor impact on the DOS. Namely, the band gaps and the half-metallicity are both observed even in the presence of disorder. Notice, in particular, that these features of zz-TGAs emerge *without* the need of periodic superlattices.

8.2 Spin-dependent conductivities

Using the efficient real-space Kubo method, we study the quantum transport in our four samples. The running conductivity, which is the conductivity of the simulation wave-packets as a function of time, gives access to study of the ballistic, diffusive, and localization regimes of a given sample. We first consider the aligned case,
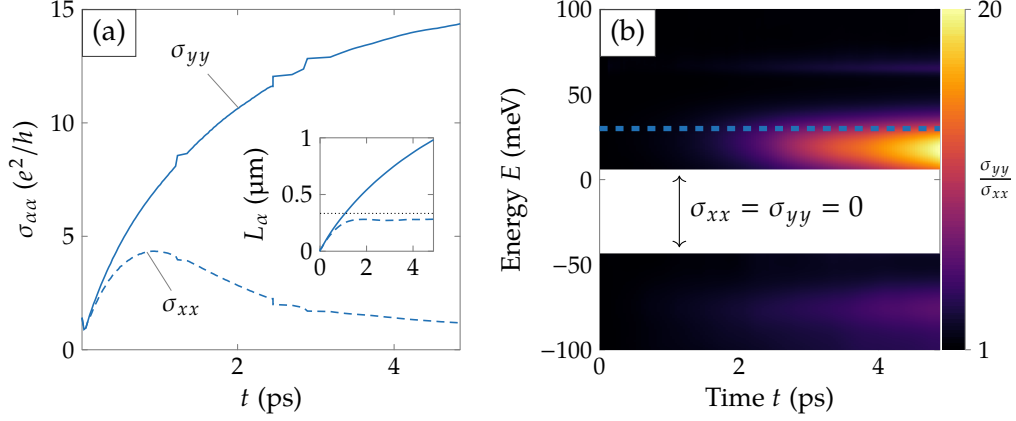
Figure 8.4: Spin-down running conductivities σ_{yy} (solid) and σ_{xx} (dashed) at $E = 30$ meV (a) and transport anisotropy σ_{yy}/σ_{xx} (b) of the aligned sample in the pristine case. The inset in (a) displays the lengths $L_{\alpha\in\{x,y\}} = 2\sqrt{\Delta X_\alpha^2(E,t)}$, and the dotted line denotes the actual length of the sample $L_{\text{sample}} \sim 360$ nm. The transport anisotropy σ_{yy}/σ_{xx} in (b) is illustrated as a color map, as a function of energy E and time t. In the energy interval -45 meV $\lesssim E \lesssim 5$ meV (white area), the spin-down conductivities are zero from the spectral gap in the DOS, and the anisotropy is ill-defined. The dashed line in (b) corresponds to the $E = 30$ meV displayed in (a).

which is half-metallic, and for 15 meV $< E <$ 50 meV only the spin-down displays a nonzero DOS and, in turn, nonzero conductivities [apparent from Fig. 8.3(a)].

The first considered sample contains pristine, aligned TGAs. The conductivities of this sample reveal a huge anisotropy, as for example illustrated via the spin-down conductivities at $E = 30$ meV displayed in Fig. 8.4(a). The σ_{yy} conductivity (solid) shows quasi-ballistic behavior, i.e., σ_{yy} increases sub-linearly yet does not saturate within the accessible time range of 5 ps. Meanwhile, the σ_{xx} conductivity (dashed) saturates to a maximal value at $t \sim 1$ ps, signifying the onset of the diffusive regime. At larger times, $t > 1$ ps, localizing effects dominate and the conductivity decays inversely proportional to time, $\sigma_{xx} \sim 1/t$. The quasi-ballistic simulation length $L_x = 2\sqrt{\Delta X_x^2(E,t)}$ [inset in Fig. 8.4(a)] is revealed to far exceed the samples size $L_x > L_{\text{sample}} \sim 360$ nm. Meanwhile, along the localization direction the simulation length saturates just within the sample size, $L_y \sim L_{\text{sample}}$. At the point of $L_\alpha \gtrsim L_{\text{sample}}$, the wave-packets become larger than the simulation samples. The corresponding conductivities may develop artifacts which originate solely from the periodicity, making any quantitative analysis challenging. Nevertheless, the huge anisotropy in the conductivities strongly suggest significantly higher scattering along the zz-direction compared to the ac-direction.

Indeed, if we examine the anisotropy σ_{yy}/σ_{xx} of the spin-down conductivities, displayed in Fig. 8.4(b) as a function of both energy and time, it reveals that $\sigma_{yy}/\sigma_{xx} >$ 1 throughout. Notice that the spin-down spectral gap -45 meV $\lesssim E \lesssim 5$ meV (white area) displays conductivities $\sigma_{xx} = \sigma_{yy} = 0$, and the corresponding anisotropy is ill-defined. The anisotropy displays particularly high values in the half-metallic interval 15 meV $\lesssim E \lesssim$ 50 meV—up to $\sigma_{yy}/\sigma_{xx} \sim 20$ at times $t = t_{\text{max}} \sim 5$ ps. Throughout this particular energy interval, the simulations display quasi-ballistic
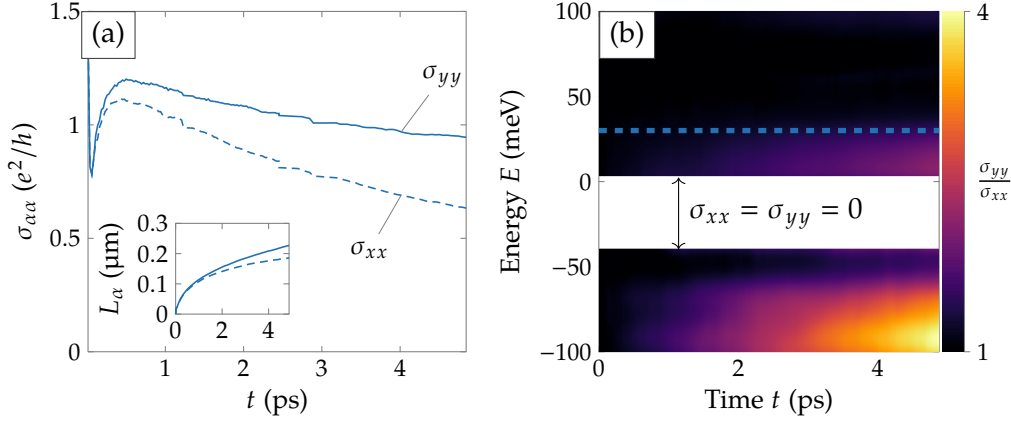
Figure 8.5: Spin-down running conductivities σ_{yy} (solid) and σ_{xx} (dashed) at $E = 30\,\text{meV}$ (a) and transport anisotropy σ_{yy}/σ_{xx} (b) of the aligned sample in the disordered case. The corresponding lengths L_α are displayed in the inset. The transport anisotropy σ_{yy}/σ_{xx} is illustrated as a color map. In the energy interval $-45\,\text{meV} \lesssim E \lesssim 5\,\text{meV}$ (white area), the spin-down conductivities are zero from the spectral gap in the DOS. The dashed line in (b) corresponds to the $E = 30\,\text{meV}$ displayed in (a).

behavior and over-simulated lengths L_y (not shown). This suggests that the large anisotropies observed in this pristine case are induced by quasi-ballistic transport channels in the ac-direction.

The second sample contains aligned TGAs with individual disorder, and while it displays lowered conductivities in general, it also displays anisotropic transport features. The spin-down conductivities at $E = 30\,\text{meV}$ are displayed in Fig. 8.5(a). In the disordered case, both the σ_{yy} (solid) and the σ_{xx} (dashed) conductivities saturate near $t \sim 0.5\,\text{ps}$ and afterwards begin to localize. For completeness, the corresponding simulations lengths are displayed in the inset of Fig. 8.5(a), and both remain within the sample size. The anisotropic map is displayed in Fig. 8.5(b). While the sample remains anisotropic $\sigma_{yy}/\sigma_{xx} > 1$ throughout, in the half-metallic interval $15\,\text{meV} \lesssim E \lesssim 50\,\text{meV}$ the huge anisotropy has reduced considerably. At the remaining energies, the anisotropy is qualitatively the sames as for the pristine case. The large peak in the anisotropy near $E \sim -100\,\text{meV}$ corresponds to a metallic region in the DOS [see Fig. 8.3(a)]. The bands structures of small-scale TGAs suggest that these are highly dispersive spin-polarized bands [see for example Chapter 6 and Fig. 6.6], which are not present for the opposite side of the Fermi level $E \sim 100\,\text{meV}$.

In aligned TGAs, disorder has the effect of suppressing the quasi-ballistic transport channels in the ac-direction. However, significant anisotropic features are observed in both the pristine and disordered cases. This highlights the possibility of observing similar anisotropic features in experiment.

The corresponding semi-classical limits (the maximum conductivities) are found to occur at times $t_{\text{SC}} \lesssim 1\,\text{ps}$, where the t_{SC} differs for each energy. For example, in Fig. 8.5(a) the semi-classical limit reads $t_{\text{SC}} \sim 0.5\,\text{ps}$. The spin-up (red) and spin-down (blue) 2D semi-classical conductivities $\sigma_{\text{SC}} = \sigma_{xx,\text{SC}} + \sigma_{yy,\text{SC}}$ are displayed in Fig. 8.6(a). The conductivities σ_{SC} are largely proportional to the DOS, in which case
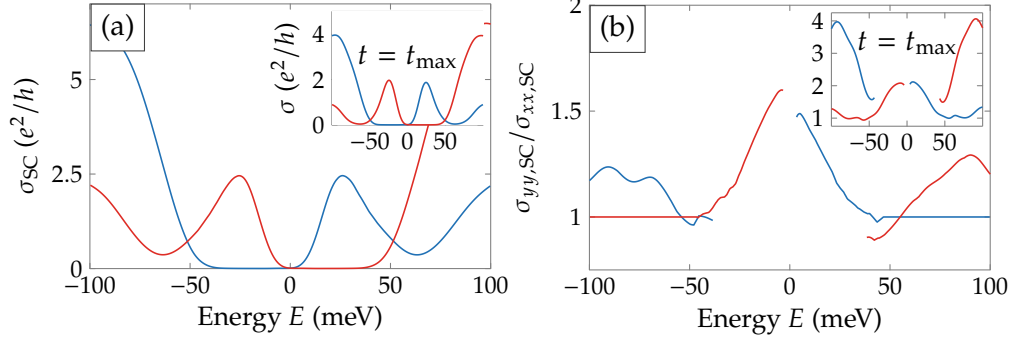
Figure 8.6: The semi-classical conductivities $\sigma_{SC} = \sigma_{xx,SC} + \sigma_{yy,SC}$ (a) and anisotropies $\sigma_{yy,SC}/\sigma_{xx,SC}$ of spin-up (red) and spin-down (blue) electrons in the aligned sample in the disordered case. The insets display the corresponding $t = t_{max} \sim 5\,\text{ps}$ conductivities and anisotropies. The anisotropies in (b) are discontinuous in the corresponding spectral gaps where the conductivities of the respective spin types are zero.
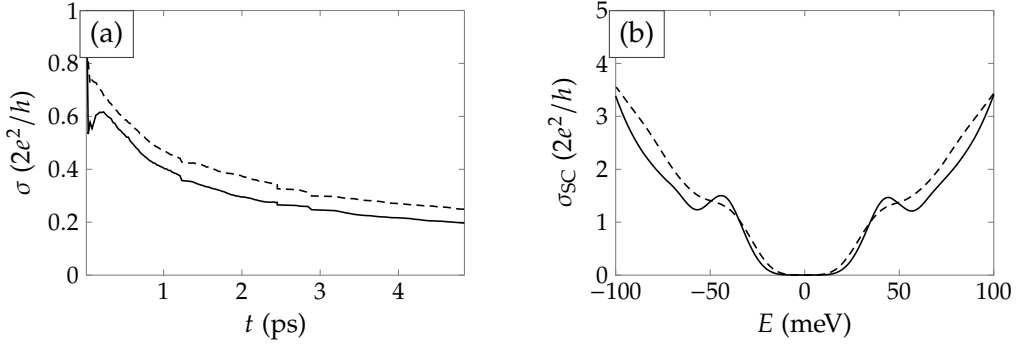

Figure 8.7: Running conductivities (a) and the semi-classical conductivity (b) of the pristine (solid) and disordered (dashed) TGAs samples in the flipped case.

no additional transport gaps are formed. This even hold true for conductivities at longer times, illustrated by the conductivities σ at $t_{max} \sim 4.8$ in the inset of Fig. 8.6(a). This means that in the face of disorder, the conductivities are not suppressed to the point of preventing transport. In comparison, similar studies of disordered GALs with *circular* antidots was demonstrated to close spectral gaps and subsequently open transport gaps [118].

The semi-classical ratios $\sigma_{yy,SC}/\sigma_{xx,SC}$ for both spin-up (red) and spin-down conductivities (blue) are displayed in Fig. 8.6(b). Notice that the curves are dis-continuous where $\sigma_{xx} = \sigma_{yy} = 0$. At the semi-classical limit, the anisotropy is the highest in the half-metallic intervals $15\,\text{meV} \lesssim |E| \lesssim 50\,\text{meV}$. Whereas, from the anisotropy map in Fig. 8.5(b) it is apparent that this changes in the localizing regime. To emphasize, the anisotropy is also displayed at $t = t_{max}$ in the inset of Fig. 8.6(b). In the localizing regime, the anisotropy is largest near $E \sim \pm 100\,\text{meV}$. The anisotropy mechanism shows clear signs of different impact in the different transport regimes.

We now consider the flipped samples. Because spins are nearly equivalent, we examine the total (charge) conductivities $\sigma \rightarrow \sigma^{\uparrow} + \sigma^{\downarrow}$. The conductivities of both the pristine and disordered, flipped TGAs are the lowest compared to the previous
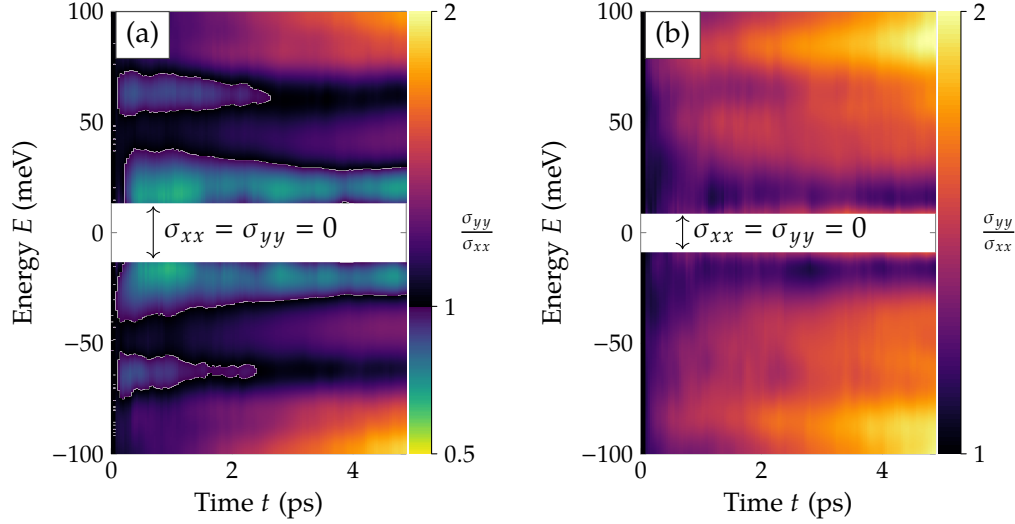
Figure 8.8: Transport anisotropy of pristine and disordered TGAs in the flipped case. The transport anisotropy σ_{yy}/σ_{xx} is displayed as a function of energy E and time t. In the white area, the conductivities are zero from the corresponding spectral gaps in the DOS. Notice in particular, the color function in (a) is divided in two: from 0.5 to 1, and 1 to 2. The cross-over can be identified by a discontinuous color shift from full black to slight purple.

cases. The 2D conductivities $\sigma = \sigma_{xx} + \sigma_{yy}$ at $E = 30$ meV are displayed in Fig. 8.7(a). Both the pristine (solid) and disordered (dashed) are displayed. By introducing zz-TGAs of opposite orientation, we effectively introduce transport channels for both spins. However, we simultaneously introduce increased scattering, as now every antidot acts as a scattering center for every second electron: either spin up or spin down. The conductivities in both cases show localizing behavior, and the semi-classical conductivities σ_{SC} are displayed in Fig. 8.7(b). The σ_{SC} reveals no additional transport gaps, albeit less pronounced peaks at $E = \pm 40$ meV.

The transport anisotropies σ_{yy}/σ_{xx} of the flipped samples with pristine and disordered TGAs are displayed in Figs. 8.8(a) and 8.8(b), respectively. In the case of pristine TGAs, it is interesting to note that along the energy axis the anisotropy oscillates between > 1 and < 1. In particular, a reduced $\sigma_{yy}/\sigma_{xx} < 1$ is revealed near ± 30 meV. On the other hand, the disordered case displays $\sigma_{yy}/\sigma_{xx} > 1$ throughout, similar to the previous cases.

The mechanisms behind the anisotropic transport of zz-TGA are not completely understood. However, these findings are highly suggestive of both anisotropic transport, and, above all, robust band gaps and half-metallic conductivities These features strongly motivate further studies.

8.3   Off-diagonal conductivities

We now move on to consider the off-diagonal conductivities of uniformly distributed TGAs. The off-diagonal conductivities express the average conductivity of skew scattering processes, i.e., how much deflection an electron experiences on average. Unlike the diagonal conductivities, these off-diagonal conductivities are signed, and
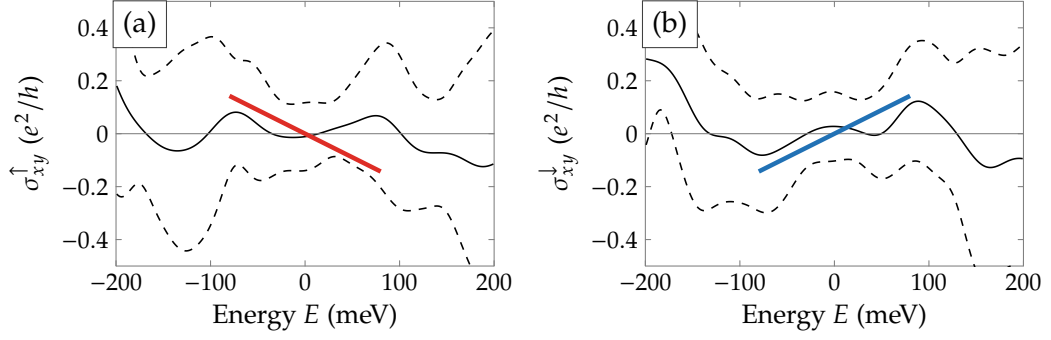
Figure 8.9: Off-diagonal conductivities of spin-up (a) and spin-down (b) electrons in a pristine TGA sample in the flipped case. The values are displayed in solid and the standard deviation in dashed. Illustrative lines of the expected trends are displayed, added to emphasize the possible trend in (b). Notice that the sample used here is larger than in previous sections, approximately $\sim 500\,\text{nm} \times 500\,\text{nm}$.

the sign corresponds to the scattering direction: positive is upwards, and negative is downwards. The TGA devices have demonstrated exactly such skew scattering mechanisms (spatial spin-splitting), where transversely generated spin-polarized currents flow in opposite directions according to spin. Of particular interest here are the spin-resolved conductivities $\sigma_{xy}^{\uparrow}$ and $\sigma_{xy}^{\downarrow}$, as we might expect such quantities to be nonzero at the magnetic resonance peaks of the DOS.

We use the alternative Kubo-method [69], which because of its framework requires far more random phase states compared to that above. We calculate a statistical average of 30 random phase vectors, and also decrease $N_\delta = 1000$ for efficiency. This results in an energy resolution of $\delta E \approx 30\,\text{meV}$. Instead of the samples we have considered so far, we make this particular sample larger $\sim 510\,\text{nm} \times 510\,\text{nm}$ (~10 million atoms). To further increase any present signals, we embed 1400 pristine TGAs (twice as dense), and reduce the minimum distance $X_{\text{min}} \sim 10\,\text{nm}$. We consider only the flipped case. The single-spin off-diagonal conductivities for spin-up and spin-down are displayed in Figs. 8.9(a) and 8.9(b), respectively. Both the values (solid) and the standard-deviation errors (dashed) are displayed.

Because of a highly oscillating values for each random phase state, the errors are, in fact, larger than the actual conductivities. This means that we cannot say whether the off-diagonal conductivities are zero or not. Even so, trends may be identified in the spin-down conductivity [Fig. 8.9(b)]. In accordance with the previously observed spatial spin-splitting, at positive energies we expect $\sigma_{xy}^{\uparrow} < 1$ and $\sigma_{xy}^{\downarrow} > 1$. We also expect antisymmetry with respect to energy. The expected antisymmetric behavior is illustrated by a red (spin-up) and a blue (spin-down) line in Fig. 8.9, where the slopes have been manipulated to emphasize the trends. Both the values and the errors of the spin-down conductivities in Fig. 8.9(b) appear to follow the expected trend. In the spin-up conductivity, the picture is not as clear, and the values do not follow the trend. In fact, the spin-up conductivity appears closer to symmetric than antisymmetric. Even so, it is important to notice that the conductivities are not *trivially* zero. This fact motivates further investigation and future studies of such effects as the spin Hall conductivity in TGA samples.

8.4 Discussion and summary

Samples of uniformly distributed, large-scale zz-TGAs perform extraordinarily well, even in the face of disorder. In samples with all TGAs oriented in the same direction (aligned TGAs), both the DOS and conductivities display half-metallic behavior near the Fermi level. More importantly, this is observed regardless of the disorders we consider. The same disorder was demonstrated to have severe impact on the individual magnetic profiles of TGAs. In other samples with oppositely oriented TGAs (flipped TGAs), the DOS and conductivities display semi-conducting behavior, with a similarly robust band gap. These finding suggest excellent scaling behavior with respect to disorder, and strongly motivate experiments using zz-TGAs.

In addition, the conductivities also display significant anisotropic transport signatures. In particular, the pristine, aligned case suggested simultaneous quasi-ballistic transport in one direction and localized transport in the other. Even with disorder, the anisotropy presented itself in both the aligned and flipped cases, with particular favor to the ac-direction. This may prove interesting for the design of integrated electronic circuits. The possibility of inducing anisotropic features by a random distribution of antidots is an intriguing feature in itself.

Finally, to explore macroscopic signatures of the spatial spin-splitting demonstrated in small-scale TGAs, we presented results of an off-diagonal conductivity simulation. Although the results were inconclusive due to errors larger than the signal, the results were *not* trivially zero. This motivates a further study into the effects surrounding large-scale TGAs with respect to the spin-dependent scattering processes. As it stands at present, the currently employed method appears impractical because of the highly oscillating values, which in turn make the simulations converge very slowly. A method to circumvent these difficulties would yield a perfect demonstration of effects that could be indistinguishable from the spin Hall effect on a macro-scale.

Summary and outlook

<div style="text-align: right; font-size: 3em;">9</div>

The increasing possibilities in nanostructure-fabrication paves the way for developing new technologies by altering or combining old ones. Be it graphene or other two-dimensional materials, advanced material control and manipulation encourages the exploration of new features in both theory and experiment.

By employing the Landauer-Büttiker formalism, combined with Green's function methods, we explore the fundamental features of two systems with interesting electronic properties. Firstly, the hybrid bilayer system: graphene on graphene antidot lattice (GOAL), which demonstrates both the tunable band gaps of bilayer graphene as well as the linear dispersion of monolayer graphene. Secondly, the zigzag-edged triangular graphene antidots (zz-TGAs), which because of their specific edge configuration, give rise to highly desirable spin-filtering and spin-splitting transport features. Here, the spin-polarization of zz-TGAs is considered using a mean-field approximation of the Hubbard model. Finally, we employ efficient large-scale methods to study the mechanisms of zz-TGAs in disordered systems of experimentally feasible scale. Below we summarize the principle findings that are presented in this thesis.

In **Chapter 5** we demonstrate that by careful design of the underlying graphene antidot lattice (GAL), the dispersive properties of GOALs can be engineered. The bandstructure can display either parabolic or linear dispersion. For a certain set of optimized geometries, we obtain linearly dispersing bands with a high corresponding mobility, resembling that of monolayer graphene. Nevertheless, these linearly dispersing GOALs can be made gapped by breaking layer symmetry, for example, using perpendicular electric fields. The linear dispersion forms as a result of electronic states confined to the pristine top layer, which, in turn, depends entirely on the electronic behavior of the bottom GAL layer. If the *isolated* GAL layer is spectrally gapped, the corresponding GOALs display top-layer confinement and subsequent linear dispersion.

The possibility of a high mobility device with tunable band gaps is particular interesting for high-speed electronic—conventional technologies are bound by their mobilities, which in graphene is uniquely high. It is interesting to note that GOALs depend on the electronic behavior, and not the exact orientation of the bottom GAL layer. This suggests a generality beyond this particular bilayer considered here, and similar features could be envisioned in comparable bilayer hybrids.

In **Chapter 6** we explore the fundamental electronic properties of rectangular lattices of zz-TGAs. The zz-TGAs consist of three zz-edges, all of which expose atomic sites of the same sublattice. In turn, this gives rise to a net sublattice imbalance, which manifests itself as large band gaps in spin-unpolarized superlattices of zz-TGAs. If we also consider spin interactions, spin-polarized bands form on either side of the Fermi level with *opposite* electronic spin. In effect, these superlattices show half-metallic regions, where the densities of states are perfectly spin-polarized. We may also consider restoring sublattice symmetry by introducing TGAs of the opposite orientation, where every second antidot is flipped in plane. In such a system, the

spin-unpolarized TGAs are completely metallic, and the spin-polarized TGAs are semi-conducting, where spins are exactly equivalent. Finally, we also consider the influence of positional and edge disorder. Both the band gaps and the half-metallic regions are preserved despite severe levels of disorder.

The durability of TGAs is surprising in the light of regular antidot lattices, which display strongly sensitive band gaps. Because of sublattice imbalance, the TGAs do not follow conventional geometric rules, which govern the regular antidot lattices. Instead, TGAs are entirely dependent on the quality of the zz-edges, and not the individual positions or sizes of the antidots. In lattices of spin-unpolarized TGAs, the formation of large band gaps could prove beneficial for graphene electronics or optics. Meanwhile, the spin-polarized TGAs with inherent half-metallicity might prove valuable for graphene spintronics. In particular, the half-metallicity allows for straightforward spin-filtering by complete electronic backscattering of one spin type, while transmitting the other.

In **Chapter 7** we turn to embedded zz-TGAs in devices and employ a cross-shape geometry to examine the longitudinal, transverse, and skew transport. The zz-TGA devices demonstrate a remarkable spatial spin-splitting feature, analogous to the spin Hall effect. Spin-unpolarized currents enter the device from left or right and spin-polarized currents are generated surrounding the antidot. The currents then exit at top and bottom leads with near-perfect, *oppositely* polarized currents. However, rather than spin-orbit interactions or topologically protected transport channels, this feature comes naturally from the mean-field solution to the Hubbard model. The spin-splitting feature is enhanced by repeated scattering in arrays of TGAs, and is demonstrated to perform well under the influence of disorders typically faced in experiments. Ultimately, using the transverse resistance we demonstrate an antisymmetric signal, characteristic of spin-polarized TGAs. Using the same device, but assuming spin-unpolarized TGAs, the transverse resistance is instead completely symmetric. This gives an unambiguous signal for detecting spin-polarized or spin-unpolarized zz-TGAs.

The spatial spin-splitting could perform as an alternative to the spin Hall effect, and potentially be used to generate or detect spin currents—a major challenge in graphene spintronics. Furthermore, the transverse resistance might also be an excellent proof of spin-polarized TGAs, and by extension, the spin-polarization of graphene zz-edges.

In **Chapter 8** we consider disordered TGAs in length scales closer to those of experiments (side lengths $L \sim 5\,\mathrm{nm}$). The large-scale TGAs display robust half-metallic and semi-conducting properties, suggesting excellent scaling behavior with respect to disorder. In addition, the large-scale TGAs show signatures of anisotropic transport. This even gave rise to simultaneously quasi-ballistic behavior in one direction, and localized behavior in the other. Finally, we considered the spin Hall conductivity; The large scale equivalent of the spatial spin-splitting observed in devices. While the results were inconclusive, we underline the nonexistence of a trivial zero in the spin Hall conductivity. Indeed, if we can find a method to circumvent the difficulties of the current method, this result would be a perfect demonstration of inducing effects indistinguishable from the spin Hall effect on a macro-scale.

9.0.1 Outlook

The GOAL system we have explored here is an excellent example of how coupling two layers electronically may induce new behavior. Exploring such combined systems further is motivated by the ever improving stacking techniques. While we consider perfectly stacked patterned bilayers, instead, we could explore more loosely coupled systems, which are less challenging to fabricate experimentally. For example, through Moiré patterns, or even indirectly via Coulomb drag effects.

However, it would be particularly interesting to improve on the work presented for zz-TGAs. The preliminary results demonstrated here of the spin Hall conductivities proved quite challenging. If possible, improvement on the method could be a huge step towards determining the true potential of zz-TGAs. This could be possible by designing the perfect system of TGAs such as to induce faster convergence. However, it is more likely that an alternative route to the same or similar macroscopic quantities is more beneficial. This, in turn, might require a more in depth understanding on the scaling properties of the TGAs. An efficient method for exploring such a large parameter space might also be needed.

Finally, we could also consider completely different paths for using spin-polarized TGAs. For example, proximity induced magnetic moments have been proposed in graphene on a EuO substrate [119]. Interestingly, a recent *ab initio* study on triangular holes in hexagonal boron nitride (hBN) has demonstrated magnetic profiles largely resembling that of TGAs [120]. Coupled with the fact that holes in hBN naturally form in triangular patterns, a dual-layered hBN-graphene system could act as an interesting alternative to TGAs.

Appendices

Chapter 9   Summary and outlook

Green's function techniques

A

In this chapter, we consider the problem of determining the Green's function matrix of a large-sized Hamiltonian. The Green's function of a particular Hamiltonian $\mathbf{H}$ is defined using

$$\mathbf{G}(E) = [E - \mathbf{H}]^{-1} . \tag{A.1}$$

where the energy is slightly offset from the real axis $E = \mathrm{Re}[E] + i0^{\pm}$, and $\mathbf{G}$ and $\mathbf{H}$ are matrices. The sign of the imaginary part of energy defines whether this is a retarded or an advanced Green's function. Note, however, that either version is allowed during the following derivations. From a numerical point of view the imaginary part must be small but *nonzero* to stabilize the matrix inversion.

Inverting matrices is a notoriously difficult operation—it is approximately an $O(D^{2.3})$ operation, with D being the problem size (the Hamiltonian matrix size is $D \times D$). Fortunately, there are a number of recursive techniques which allow efficient evaluation of a certain class of problems.

For many of the operations below, the Hamiltonians may be rearranged into a layered, or chained form. While the layers often are physically separable layers of a device, they do not strictly need to be. The form must satisfy two important conditions: Firstly, the individual layers in the device may only couple to their neighbors. Secondly, the layers express *separate* parts of the Hamiltonian (no overlap). The Hamiltonian then has an equivalent tri-block diagonal matrix form

$$\mathbf{H} = \begin{bmatrix} \mathbf{H}_1 & \mathbf{V}_{12} & 0 & \cdots \\ \mathbf{V}_{21} & \mathbf{H}_2 & & \\ 0 & & \ddots & \\ \vdots & & & \mathbf{H}_N \end{bmatrix} , \tag{A.2}$$

i.e. individual layers, or cells, in the diagonal and hoppings in the off-diagonals.

A.1 Self-energy

The self-energy is demonstrated using a device (D) coupled to an external perturbation (ex), illustrated on the left side of Fig. A.1(a). The explicit Green's function matrix [Eq. (A.1)] then reads

$$\begin{bmatrix} \mathbf{g}_{\mathrm{D}}^{-1} & -\mathbf{V}_{\mathrm{Dex}} \\ -\mathbf{V}_{\mathrm{exD}} & \mathbf{g}_{\mathrm{ex}}^{-1} \end{bmatrix} \begin{bmatrix} \mathbf{G}_{\mathrm{DD}} & \mathbf{G}_{\mathrm{Dex}} \\ \mathbf{G}_{\mathrm{exD}} & \mathbf{G}_{\mathrm{exex}} \end{bmatrix} = \begin{bmatrix} 1 & 0 \\ 0 & 1 \end{bmatrix} \tag{A.3}$$

which can also be expressed

$$\mathbf{G}_{\mathrm{DD}} = \mathbf{g}_{\mathrm{D}} + \mathbf{g}_{\mathrm{D}}\mathbf{V}_{\mathrm{Dex}}\mathbf{G}_{\mathrm{exD}} , \tag{A.4}$$

$$\mathbf{G}_{\mathrm{exex}} = \mathbf{g}_{\mathrm{ex}} + \mathbf{g}_{\mathrm{ex}}\mathbf{V}_{\mathrm{exD}}\mathbf{G}_{\mathrm{Dex}} , \tag{A.5}$$

$$\mathbf{G}_{\mathrm{Dex}} = \mathbf{g}_{\mathrm{D}}\mathbf{V}_{\mathrm{Dex}}\mathbf{G}_{\mathrm{exex}} , \tag{A.6}$$

$$\mathbf{G}_{\mathrm{exD}} = \mathbf{g}_{\mathrm{ex}}\mathbf{V}_{\mathrm{exD}}\mathbf{G}_{\mathrm{DD}} . \tag{A.7}$$
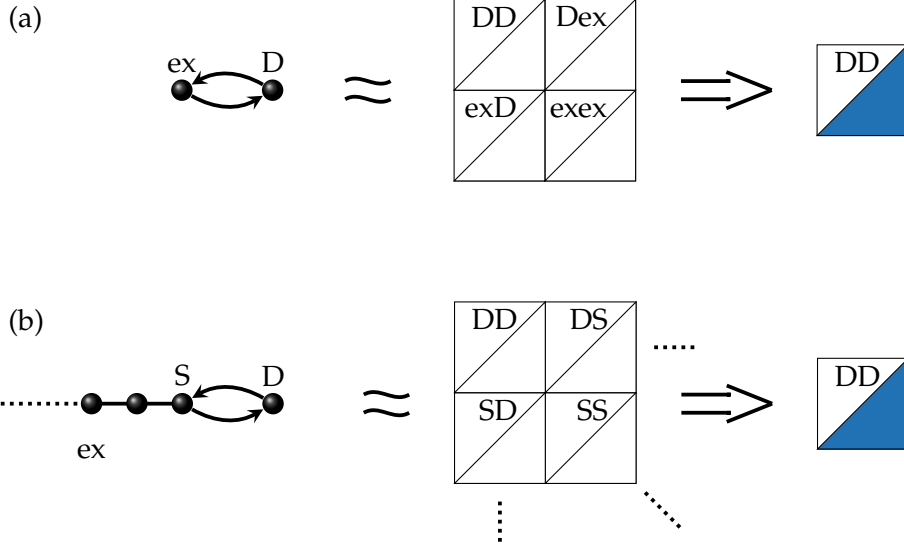
Figure A.1: Illustration of the self-energy formulas in case of (a) coupling to a single external perturbation, and (b) coupling to a external perturbation chain. The panels illustrate the physical samples (left), the full Green's function matrix $\mathbf{G}$ (middle), and the local Green's function $\mathbf{G}_{DD}$ *after* perturbation. Straight lines indicate initially coupled systems, and curved arrows the perturbation. Lower blue triangles illustrate applied self-energies.

The first equation in particular [Eq. (A.4)] can be rearranged

$$\mathbf{G}_{DD} = [E - \mathbf{H}_D - \mathbf{\Sigma}_{ex}]^{-1}, \text{ where } \mathbf{\Sigma}_{ex} = \mathbf{V}_{Dex}\mathbf{g}_{ex}\mathbf{V}_{exD}. \tag{A.8}$$

which defines the self-energy of the device in response to the external perturbation. The full explicit Green's function matrix is illustrated in the middle of Fig. A.1(a). By using the self-energy, we can express the local device region *without* further considering the external perturbation. This situation is illustrated in the right of Fig. A.1(a), where the lower blue triangle denotes the added self-energy.

The self-energy in Eq. (A.8) can also describe indirection couplings. Consider the device (D) divided into a left (L) and a right (R) side, *which are not coupled*. However, these *do* couple indirectly via an external perturbation (ex). The definition in Eq. (A.8) is rewritten such that the local self-energies of the separate left and right sides are explicit

$$\mathbf{\Sigma}_{ex} = \begin{bmatrix} \mathbf{\Sigma}_L & \gamma_{LR} \\ \gamma_{RL} & \mathbf{\Sigma}_R \end{bmatrix}, \tag{A.9}$$

where $\mathbf{\Sigma}_L = \mathbf{V}_{Lex}\mathbf{g}_{ex}\mathbf{V}_{Lex}$ and $\mathbf{\Sigma}_R = \mathbf{V}_{Rex}\mathbf{g}_{ex}\mathbf{V}_{Rex}$ are the left and right self-energies, and $\gamma_{LR} = \mathbf{V}_{Lex}\mathbf{g}_{ex}\mathbf{V}_{Rex}$ and $\gamma_{RL} = \mathbf{V}_{Rex}\mathbf{g}_{ex}\mathbf{V}_{Lex}$ are the self-energy hoppings. The self-energy hoppings now describe the indirect coupling through the external perturbation.

The remaining Eqs. (A.5) to (A.7) can used to determine the Green's functions of the entire system. In the following, consider the iterative *building* of a chain, from cell 1 to N, [e.g. similar to the Hamiltonian in Eq. (A.2)]. The surface of the chain is illustrated in the left side of Fig. A.1(b). In this case, Eqs. (A.4) to (A.7) are written

explicitly for each of the local Green's functions at the build step n

$$\mathbf{G}_{(n+1)(n+1)} = \left[E - \mathbf{H}_{(n+1)} - \Sigma_n \right]^{-1}, \text{where } \Sigma_n = \mathbf{V}_{(n+1)n}\mathbf{g}_n\mathbf{V}_{n(n+1)}, \quad (A.10)$$

$$\mathbf{G}_{ij} = \mathbf{g}_{ij} + \mathbf{g}_{in}\mathbf{V}_{n(n+1)}\mathbf{G}_{(n+1)(n+1)}\mathbf{V}_{(n+1)n}\mathbf{g}_{nj}, \quad (A.11)$$

$$\mathbf{G}_{(n+1)i} = \mathbf{g}_{(n+1)}\mathbf{V}_{(n+1)i}\mathbf{G}_{ii}, \quad (A.12)$$

$$\mathbf{G}_{i(n+1)} = \mathbf{g}_i\mathbf{V}_{i(n+1)}\mathbf{G}_{(n+1)(n+1)}. \quad (A.13)$$

There are particularly useful for determining the diagonal and first column and row. It is also worth noting the Eq. (A.10) now describes the self-energy of the entire chain, by use only of the *surface* Green's function $\mathbf{g}_n$. The full explicit Green's function matrix is illustrated in the middle of Fig. A.1(b), and the surface on the right of Fig. A.1(a).

A.2 Density of states

The LDOS is defined via the Green's function matrix

$$\text{LDOS}(i, E) = -\frac{1}{\pi}\text{Im}[\mathbf{G}]_{ii}. \quad (A.14)$$

To solve this efficiently, we can employ a recursive scheme.

Consider a linear chain of N coupled cells. First, we build the chain from left to right using Eq. (A.10)

$$\mathbf{g}_n = [E - \mathbf{H}_n - \Sigma_n]^{-1}, \text{where } \Sigma_n = \mathbf{V}_{n(n-1)}\mathbf{g}_{(n-1)}\mathbf{V}_{(n-1)n}, \quad (A.15)$$

To determine the full diagonal, we realize that at the end of the above sweep all cells have been coupled, and we obtain $\mathbf{g}_N = \mathbf{G}_{NN}$. Then Eq. (A.11) allows for a backwards iteration

$$\mathbf{G}_n = \mathbf{g}_n + \mathbf{g}_n\mathbf{V}_{n(n+1)}\mathbf{G}_{(n+1)}\mathbf{V}_{(n+1)n}\mathbf{g}_n, \quad (A.16)$$

The DOS is a straightforward simplification of the above. It is defined

$$\text{DOS}(E) = -\frac{1}{\pi}\text{Tr}\left[\text{Im}[\mathbf{G}]\right]. \quad (A.17)$$

Using the relation in Eq. (A.16), we find the partial trace

$$\text{Tr}[\mathbf{G}] = \sum_{i \leq n}\text{Tr}[\mathbf{G}_{ii}] = \text{Tr}[\mathbf{G}_{nn}] + \text{Tr}[\mathbf{g}] + \sum_{i < n}\text{Tr}\left[\mathbf{g}_{i(n-1)}\mathbf{V}_{(n-1)n}\mathbf{G}_{nn}\mathbf{V}_{n(n-1)}\mathbf{g}_{(n-1)i}\right] \quad (A.18)$$

Using the rotation property of the trace we get the following form

$$\text{Tr}[\mathbf{G}] = \text{Tr}[\mathbf{G}_{nn}] + \text{Tr}[\mathbf{g}] + \text{Tr}\left[\mathbf{G}_{nn}\mathbf{V}_{n(n-1)}\sum_{i < n}\mathbf{g}_{(n-1)i}\mathbf{g}_{i(n-1)}\mathbf{V}_{(n-1)n}\right] \quad (A.19)$$

$$= \text{Tr}[\mathbf{G}_{nn}] + \text{Tr}[\mathbf{g}] + \text{Tr}\left[\mathbf{G}_{nn}\mathbf{V}_{n(n-1)}\mathbf{A}_{(n-1)}\mathbf{V}_{(n-1)n}\right] \quad (A.20)$$

where we have introduced an intermediate matrix $\mathbf{A}_{(n-1)} = \sum_{i<n} \mathbf{g}_{(n-1)i}\mathbf{g}_{i(n-1)}$. However, an alternative, but identical form reads $\mathbf{A}_n = \sum_{i\leq n} \mathbf{G}_{ni}\mathbf{G}_{in}$, but which defines the intermediate matrix of *this* step—for the equation above we will need the previous $\mathbf{A}_{(n-1)}$. Using the relations from Eqs. (A.6) and (A.7), we create the recursive relation

$$\mathbf{A}_n = \sum_{i\leq n} \mathbf{G}_{ni}\mathbf{G}_{in} = \mathbf{G}_{nn}\mathbf{G}_{nn} + \sum_{i\leq n-1} \mathbf{G}_{ni}\mathbf{G}_{in} \tag{A.21}$$

$$= \mathbf{G}_{nn}\mathbf{G}_{nn} + \mathbf{G}_{nn}\mathbf{V}_{n(n-1)} \left(\sum_{i\leq n-1} \mathbf{g}_{(n-1)i}\mathbf{g}_{i(n-1)} \right) \mathbf{V}_{(n-1)n}\mathbf{G}_{nn} \tag{A.22}$$

$$= \mathbf{G}_{nn} \left[\mathbf{V}_{n(n-1)}\mathbf{A}_{(n-1)}\mathbf{V}_{(n-1)n} + 1 \right] \mathbf{G}_{nn} \tag{A.23}$$

By using the above equations, the trace can be calculated recursively by a single forward sweep

$$T_n = \mathrm{Tr}\,[\mathbf{G}] = T_{(n-1)} + \mathrm{Tr}\left[\mathbf{G}_{nn} \left(\mathbf{V}_{n(n-1)}\mathbf{A}_{(n-1)}\mathbf{V}_{(n-1)n} + 1 \right) \right] , \text{ where} \tag{A.24}$$

$$\mathbf{A}_n = \mathbf{G}_{nn} \left[\mathbf{V}_{n(n-1)}\mathbf{A}_{(n-1)}\mathbf{V}_{(n-1)n} + 1 \right] \mathbf{G}_{nn} \tag{A.25}$$

where T_n is the trace at step n.

A.3 Semi-infinite leads

The semi-infinite lead is a chain of *identical* cells. We distinguish the bulk (B) unit cells, which have neighboring cells on both sides, and the surface (S) cell which has only one neighbor on its side.

We consider the case of a bulk unit cell as the perturbation, thereby inducing indirect couplings between the remaining cells. By straightforward use of Eq. (A.9), we find the self-energies

$$\mathbf{\Sigma}_B = \mathbf{V}_L\mathbf{g}_B\mathbf{V}_R + \mathbf{V}_L\mathbf{g}_B\mathbf{V}_R \tag{A.26}$$

$$\mathbf{\Sigma}_S = \mathbf{V}_R\mathbf{g}_B\mathbf{V}_L \tag{A.27}$$

$$\mathbf{\gamma}_L = \mathbf{V}_L\mathbf{g}_B\mathbf{V}_L \tag{A.28}$$

$$\mathbf{\gamma}_R = \mathbf{V}_R\mathbf{g}_B\mathbf{V}_R \tag{A.29}$$

where $\mathbf{g}_B = [E - \mathbf{H}_B]^{-1}$, and $\mathbf{\gamma}_L$ ($\mathbf{\gamma}_R$) is the self-energy hopping from one bulk cell to the cell of its left (right). Notice above that the surface cell has only one neighbor, hence one self-energy term.

If we were to consider every second bulk cell as a perturbation *simultaneously*, we may realized that the bulk self-energies above may be applied to every remaining cell in the semi-infinite lead. However, the resulting system is now exactly equivalent to a new semi-infinite lead, with Hamiltonians corrected by self-energies. In other words, the new system displays $\mathbf{H}'_B = \mathbf{H}_B + \mathbf{\Sigma}_B$ and $\mathbf{H}'_S = \mathbf{H}_S + \mathbf{\Sigma}_S$, and the hoppings $\mathbf{V}'_L = \mathbf{\gamma}_L$ and $\mathbf{V}'_R = \mathbf{\gamma}_R$. The above equations can be repeated until to the effective hoppings $\mathbf{V}'_L$ are below a certain tolerance.

The above algorithm works well for small unit cells in the leads. However, if the unit cell are large the inversion in $\mathbf{g}_B$ make the calculations cumbersome. Instead,
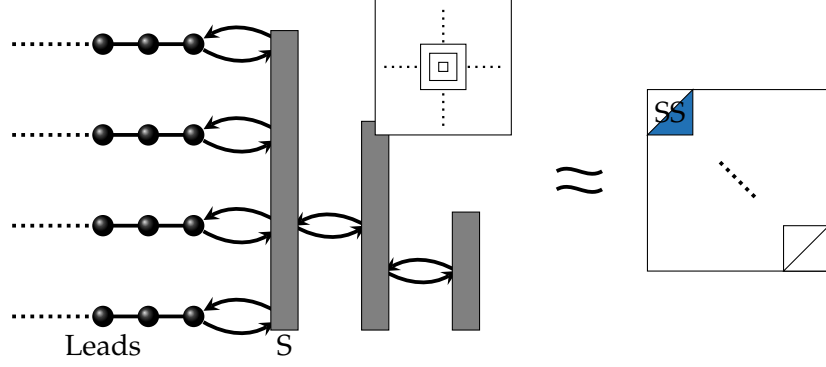
Figure A.2: Illustration of the self-energy formulas in case of coupling to a set of semi-infinite leads. The figure illustrates the sample setup (left) and the device Green's function matrix $\mathbf{G}_{DD}$ (right) *after* coupling the semi-infinite leads. The set illustrates a physical sample, which can be arranged into the setup in main panel. Lower blue triangles illustrate applied self-energies.

we may further use recursion to first simplify the unit cells of the leads, and then use the above algorithm to find the surface Green's function.

For each sub-cell in the lead unit cells, apart from the last, we consider it a perturbation and subsequently remove it. Similar to above, when considering the cell $i = 1, 2, ..., N - 1$ as the perturbation, the self-energies are given

$$\boldsymbol{\Sigma}_{i+1} = \mathbf{V}_{(i+1)i}\mathbf{g}_i\mathbf{V}_{i(i+1)} \tag{A.30}$$

$$\mathbf{V}'_{N(i+1)} = \mathbf{V}'_{Ni}\mathbf{g}_i\mathbf{V}'_{i(i+1)} \tag{A.31}$$

$$\mathbf{V}'_{(i+1)N} = \mathbf{V}'_{(i+1)i}\mathbf{g}_i\mathbf{V}'_{iN} \tag{A.32}$$

And for each of the removed sub-cells, we add the self-energy to the unit-cell surface

$$\boldsymbol{\Sigma}_B = \sum_i \mathbf{V}'_{Ni}\mathbf{g}_i\mathbf{V}'_{iN} \tag{A.33}$$

$$\tag{A.34}$$

At $i = N$, the simplified surface cell can be used $\boldsymbol{\Sigma}_S = \boldsymbol{\Sigma}_N$.

A.4 Multi-terminal transmissions

In a multiterminal setup, we need to differentiate between what couples to the device, and what does not. Illustrated on the left of Fig. A.2, we rearrange the system such that all leads are external perturbations on one site. The boundary which they all couple to is denoted the surface of the device, and the leads are included using the self-energies, illustrated on the right of Fig. A.2.

$$\mathbf{g}_S = [E - \mathbf{H}_S - \boldsymbol{\Sigma}_S]^{-1}, \text{ where } \boldsymbol{\Sigma}_S = \sum_p \boldsymbol{\Sigma}_p, \tag{A.35}$$

where $\boldsymbol{\Sigma}_p$ are the self-energies from the leads.

When considering the transmissions, we consider all parts of the device *which do not couple to the leads* as external perturbations, Using Eq. (A.10), we recursively add the
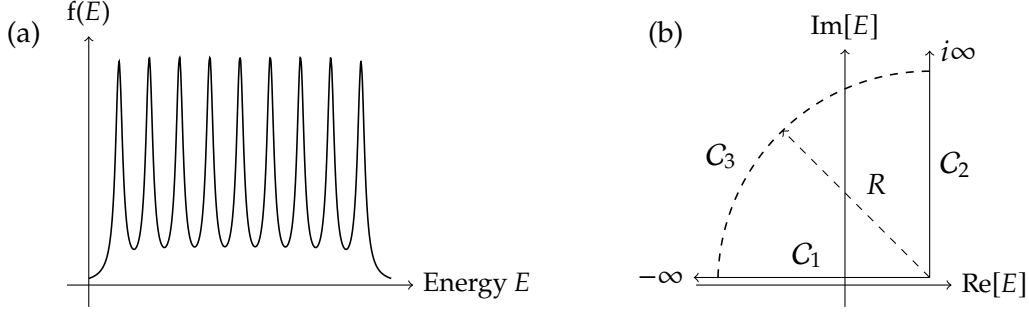
Figure A.3: Schematics of a function resembling the Green's function (a), and an optimal contour path in the complex energy plane (b).

cells furthest from the leads as a self energy

$$\mathbf{g}_n = [E - \mathbf{H}_n - \mathbf{\Sigma}_n]^{-1} \text{, where } \mathbf{\Sigma}_n = \mathbf{V}_{n(n-1)}\mathbf{g}_{(n-1)}\mathbf{V}_{(n-1)n} \,. \quad (A.36)$$

At the end of the recursion, we have only the final cells which couple to the leads, and we use that the Green's function of the device coupled to the leads p is

$$\mathbf{G}_D = \left[E - \mathbf{H}_n - \mathbf{\Sigma}_D - \sum_p \mathbf{\Sigma}_p \right]^{-1} \quad (A.37)$$

and the final transmissions are

$$T_{pq}(E) = \text{Tr}\left[\mathbf{\Gamma}_p \mathbf{G}^\dagger \mathbf{\Gamma}_q \mathbf{G} \right] \,, \quad (A.38)$$

where $\mathbf{\Gamma}_p = i \left[\mathbf{\Sigma}_p - \mathbf{\Sigma}_p^\dagger \right]$ are the level-broadenings from coupling to the leads.

When considering the currents, we need the nonlocal Green's functions $\mathbf{G}_{Si}$ and $\mathbf{G}_{iS}$. Following the same iterations as in the LDOS, at the end Eqs. (A.12) and (A.12) allows for a backwards iteration

$$\mathbf{G}_{Ni} = \mathbf{G}_{N(i+1)}\mathbf{V}_{(i+1)i}\mathbf{g}_i \,, \quad (A.39)$$
$$\mathbf{G}_{iN} = \mathbf{g}_i\mathbf{V}_{i(i+1)}\mathbf{G}_{(i+1)N} \,. \quad (A.40)$$

and the final currents straightforward

$$\left[\mathbf{J}_p(E) \right]_{ij} = [\mathbf{H}]_{ij}\,\text{Im}[\mathbf{G}_{Ni}\mathbf{\Gamma}_p\mathbf{G}_{Ni}^\dagger]_{ij} \,. \quad (A.41)$$

A.5 Integrating the Greens function

Some physical quantities require integrating the Green's function, for example the electron densities $n(E) = -1/\pi\text{Im}[\int_{-\infty}^\infty dE' \, f(E' - E)\mathbf{G}(E')]$. However, the Green's functions are particularly difficult to numerically integrate due to their close resemblance to δ-functions. For illustrative purpose, the Green's function can be thought of as the function displayed in Fig. A.3(a). Here, I introduce a well behaved integral along an alternative contour.

At zero temperature, the integral reads

$$\int_{-\infty}^{E} dE' \, \mathbf{G}(E' + i0^{\pm}) \tag{A.42}$$

which we can relate to the quarter-circle contour integral ($\oint$) demonstrated in Fig. A.3(b). The contour is divided into three paths C_1, C_2, and C_3. The path C_1 is the desired path near the real axis, $Z = -\infty \to E$. The path C_2 is the alternative path along the imaginary axis, $Z = E \to \pm i\infty + E$. The path C_3 is the final path that connects the two, along a quater-circle in from the positive imaginary axis to the negative real axis, $Z = \pm i\infty + E \curvearrowright -\infty$.

$$\oint dE' \, \mathbf{G}(E' + i0^{\pm}) = \int_{C_1} dZ \, \mathbf{G}(Z + i0^{\pm}) + \int_{C_2} dZ \, \mathbf{G}(Z + i0^{\pm}) + \int_{C_3} dZ \, \mathbf{G}(Z + i0^{\pm}) \tag{A.43}$$

where $\int_{C_1} dZ \leftrightarrow \int_{-\infty}^{E} dE'$. At zero temperature there are no poles in this contour ($\oint \to 0$), and the original integral is given

$$\int_{-\infty}^{E} dE' \, \mathbf{G}(E' + i0^{\pm}) = -\int_{C_2} dZ \, \mathbf{G}(Z + i0^{\pm}) - \int_{C_3} dZ \, \mathbf{G}(Z + i0^{\pm}) \tag{A.44}$$

In the curved integral we make the transformation $Z = R\exp(i\phi) + E$ such that $dZ = iR\exp(i\phi)d\phi$. The curved integral now reads

$$\int_{C_3} dZ \, \mathbf{G}(Z + i0^{\pm}) = i \lim_{R \to \infty} \int_{\pm \pi/2}^{\pm \pi} d\phi \, R\exp(i\phi) \left[R\exp(i\phi) + E + i0^{\pm} - \mathbf{H} \right]^{-1} \tag{A.45}$$

$$= i \int_{\pm \pi/2}^{\pm \pi} d\phi \, \lim_{R \to \infty} \left[1 + i0^{\pm}/R + E/R - \mathbf{H}\exp(-i\phi)/R \right]^{-1} \tag{A.46}$$

$$= \pm i\pi/2 \tag{A.47}$$

Finally, the original integral can be replaced by

$$\int_{-\infty}^{E} dE' \, \mathbf{G}(E' + i0^{\pm}) = \mp i\pi/2 - i \int_{0}^{\infty} dE' \, \mathbf{G}(iE' + E + i0^{\pm}) \tag{A.48}$$

Chebyshev polynomial methods $\qquad$ B

The Chebyshev polynomials of the first kind $T_n(x)$ are confined to the open region $x \in]-1, 1[$, where n is an integer. In this thesis we deal only with positive n. The polynomials can be expressed in trigonometric form

$$T_n(x) = \cos(n \arccos(x)) \ , \ -1 < x < 1 \tag{B.1}$$

which yields the useful recursive relations

$$\begin{aligned} T_0(x) &= 1 \\ T_1(x) &= x \\ T_{n+1}(x) &= 2xT_n(x) - T_{n-1}(x) \end{aligned} \tag{B.2}$$

The polynomials are orthogonal with respect to the weight function $w(x) = \frac{1}{\pi}\sqrt{1 - x^2}$, such that

$$(\delta_{0n} + 1) \int_{-1}^{1} \mathrm{d}x \ w(x)T_n(x)T_m(x) = \delta_{nm} \ . \tag{B.3}$$

A function $f(x)$ for which $x \in]-1, 1[$ can straight forwardly be expanded in a set of Chebyshev polynomials. However, in general the function $f(x)$ is bounded by a larger spectrum $x \in]\overline{x} + \Delta x, \overline{x} - \Delta x[$ and we introduce a variable transformation into the expansion

$$f(x) = f(\Delta x \ \tilde{x} + \overline{x}) = \sum_{n=0}^{\infty} c_n T_n(\tilde{x}) \ , \ -1 < \tilde{x} < 1 \ , \tag{B.4}$$

where the *rescaled* variable $\tilde{x} = (x - \overline{x})/\Delta x$. The expansion coefficients c_n are defined

$$c_n = (\delta_{0n} + 1) \int_{-1}^{1} \mathrm{d}\tilde{x} \ w(\tilde{x})f(\Delta x \ \tilde{x} + \overline{x})T_n(\tilde{x}) \ . \tag{B.5}$$

Finally, two other useful relation read

$$T_n\left(T_m(x)\right) = T_{nm}(x) \text{ and} \tag{B.6}$$

$$2T_n(x)T_m(x) = T_{n+m}(x) + T_{|n-m|}(x) \ , \tag{B.7}$$

and using the latter relation we find

$$\begin{aligned} T_{2n}(x) &= 2T_n(x)T_n(x) - T_0(x) \\ T_{2n+1}(x) &= 2T_{n+1}(x)T_n(x) - T_1(x) \ . \end{aligned} \tag{B.8}$$

A useful point of note is that the evaluation of $T_n(x)$ has a particularly well suited choice of variable $x = \cos\theta$, which yields a simple fast-Fourier transform

$$T_n(\cos\theta) = \cos n\theta \ . \tag{B.9}$$

B.1 δ-function expansion

With $\delta(x - x_0)$, where $x \in]\overline{x} + \Delta x, \overline{x} - \Delta x[$ and $\overline{x} + \Delta x < x_0 < \overline{x} - \Delta x$, we consider the function $f(\tilde{x}) = \delta(\tilde{x} - \tilde{x}_0)/w(\tilde{x})$, where the rescaled $\tilde{x} = (x - \overline{x})/\Delta x$ and $\tilde{x}_0 = (x_0 - \overline{x})/\Delta x$. The expansion coefficients from Eq. (B.5) then become simple evaluations

$$c_n = (\delta_{0n} + 1) \int_{-1}^{1} d\tilde{x}\, w(\tilde{x}) \frac{\delta(\tilde{x} - \tilde{x}_0)}{w(\tilde{x})} T_n(\tilde{x})$$

$$= (\delta_{0n} + 1) T_n(\tilde{x}_0). \tag{B.10}$$

The final form of the expansion is

$$\delta(x - x_0) = \frac{1}{\Delta x} f(\tilde{x}) w(\tilde{x}) = \frac{w(\tilde{x})}{\Delta x} \sum_{n=0}^{\infty} (\delta_{0n} + 1) T_n(\tilde{x}) T_n(\tilde{x}_0). \tag{B.11}$$

Notice that we can exchange x and x_0 above, such that an equivalent expansion reads

$$\delta(x - x_0) = \frac{w(\tilde{x})}{\Delta x} \sum_{n=0}^{\infty} (\delta_{0n} + 1) T_n(\tilde{x}) T_n(\tilde{x}_0). \tag{B.12}$$

B.2 exp-function expansion

With $\exp(-ix)$, where $x \in]\overline{x} + \Delta x, \overline{x} - \Delta x[$, the expansion coefficients from Eq. (B.5) read

$$c_n = (\delta_{0n} + 1) \int_{-1}^{1} d\tilde{x}\, w(\tilde{x}) e^{-i(\Delta x\, \tilde{x} + \overline{x})} T_n(\tilde{x})$$

$$= (\delta_{0n} + 1) e^{-i\overline{x}} (-i)^n J_n(\Delta x), \tag{B.13}$$

where the usual $\tilde{x} = (x - \overline{x})/\Delta x$. The $J_n(x)$ is the Bessel function of the first kind, and final expression is

$$e^{-ix} = e^{-i\overline{x}} \sum_{n=0}^{\infty} (\delta_{0n} + 1)(-i)^n J_n(\Delta x) T_n(\tilde{x}) \tag{B.14}$$

B.3 Kernels

Now we have expressed our difficult function in terms of infinite sums. In practice though, we need to truncate our sum to a finite number of polynomials N, such that

$$f(\Delta x\, \tilde{x} + \overline{x}) \approx \sum_{n=0}^{N} c_n T_n(\tilde{x}) \tag{B.15}$$

The error we introduce by truncating the sum will oscillate, also known as Gibbs oscillations. These can be alleviated through the use of kernels. A Kernel is a

Appendix B   Chebyshev polynomial methods

convolution of the expansion function $\tilde{c}_n = g_n c_n$, where g_n are the kernel scaling coefficients.

In general we use the Jackson Kernel,

$$g_n = \frac{(N_{\text{Cby}} - n + 1)\cos\left(\frac{\pi n}{N_{\text{Cby}}+1}\right) + \cot\left(\frac{\pi}{N_{\text{Cby}}+1}\right)\sin\left(\frac{\pi n}{N_{\text{Cby}}+1}\right)}{N_{\text{Cby}} + 1} \qquad (B.16)$$

Of particular interest, applying the Jackson kernel to an expansion of the δ-function yields a Gaussian-like approximation [68]

$$\delta(x - x_0) \sim \frac{1}{\sqrt{2\pi\sigma_J^2}} \exp\left[-\frac{(x-x_0)^2}{2\sigma_J^2}\right] . \qquad (B.17)$$

In the worst case (near $x_0 = 0$), the broadening (or Gaussian width) is $\sigma_J \approx \pi \Delta x / N_\delta$, where Δx is the spectrum of x.

Other kernels also exist and an overview is presented in Weiße *et al.* [68].

B.4 Stochastic evaluation of traces

Before we move to applications of the Chebyshev expansions, we include an approximation of traces for large problem sizes. The trace can be replaced by a stochastic trace using random phase states $|R\rangle$

$$\text{Tr}\,[A] \approx \frac{1}{N_R}\sum_R^{N_R} \langle R|\,A\,|R\rangle \qquad (B.18)$$

where the random phase states are

$$|R\rangle = \frac{1}{D}\sum_j e^{i\phi_{Rj}}\mathbf{c}_j^\dagger\,|0\rangle \qquad (B.19)$$

where $\phi_{Rj} \in [-\pi; \pi]$ is the random phase of the state R on orbital j, N_R is the number of random states, and D is the number of orbitals, or indeed the problem size.

The error of the approximation is $\propto 1/\sqrt{DN_R}$. Ensuring $1/\sqrt{DN_R} = 10^{-4}$ yields the condition $N_R = 10^8/D$, in which case a system with 10^8 orbitals or more needs only one random state to evaluate the trace.

B.5 Density of states

The density of states can be expressed

$$\text{DOS} = \text{Tr}\,[\delta\,(E - \mathbf{H})] . \qquad (B.20)$$

Using the Chebyshev expansion of the δ-function Eq. (B.11)

$$\text{DOS} \approx \frac{1}{\Delta E} \sum_{n=0}^{N} (\delta_{0n} + 1) \, T_n(\tilde{E}) \, \text{Tr} \left[T_n(\tilde{\mathbf{H}}) \right] \tag{B.21}$$

$$\approx \frac{1}{\Delta E N_R} \sum_{n=0}^{N} (\delta_{0n} + 1) \, T_n(\tilde{E}) \sum_{R}^{N_R} \langle R | \, T_n(\tilde{\mathbf{H}}) \, | R \rangle \,, \tag{B.22}$$

where the rescaled energy $\tilde{E} = 2(E - \langle E \rangle)/\Delta E$ and Hamiltonian $\tilde{\mathbf{H}} = 2(\mathbf{H} - \langle E \rangle)/\Delta E$, such that energy spectrum is bounded $(E - \langle E \rangle) \in\,] - \Delta E/2; \Delta E/2[$. The final form in Eq. (B.22) uses the stochastic trace from Eq. (B.18).

The form $\langle R | \, T_n(\tilde{\mathbf{H}}) \, | R \rangle$ is readily solved using the recursive relations from Eq. (B.2)

$$T_{n+1}(\tilde{\mathbf{H}}) \, | R \rangle = 2\tilde{\mathbf{H}} T_n(\tilde{\mathbf{H}}) \, | R \rangle - T_{n-1}(\tilde{\mathbf{H}}) \, | R \rangle \,. \tag{B.23}$$

However, we can employ a slight simplification by using the additional relations from Eq. (B.8)

$$\langle R | \, T_{2n}(\tilde{\mathbf{H}}) \, | R \rangle = 2 \underbrace{\langle R | \, T_n(\tilde{\mathbf{H}})}_{\langle \alpha_n |} \underbrace{T_n(\tilde{\mathbf{H}}) \, | R \rangle}_{| \alpha_n \rangle} - \underbrace{\langle R | \, T_0(\tilde{\mathbf{H}}) \, | R \rangle}_{1} \,, \text{ and} \tag{B.24}$$

$$\langle R | \, T_{2n+1}(\tilde{\mathbf{H}}) \, | R \rangle = 2 \underbrace{\langle R | \, T_{n+1}(\tilde{\mathbf{H}})}_{\langle \alpha_{n+1} |} \underbrace{T_n(\tilde{\mathbf{H}}) \, | R \rangle}_{| \alpha_n \rangle} - \underbrace{\langle R |}_{\langle \alpha_0 |} \underbrace{T_1(\tilde{\mathbf{H}}) \, | R \rangle}_{| \alpha_1 \rangle} \,. \tag{B.25}$$

For each state $| \alpha_n \rangle$ we gain the values of both of the above, and effectively the first sum in Eq. (B.22) can be evaluated twice as fast.

The power of the Chebyshev expansion really emerges at large sparse matrices $\mathbf{H}$. By using Eqs. (B.24) and (B.25) to iteratively evaluate the sums in Eq. (B.22), the problem boils down to a sum of sparse-matrix-vector products, which are particularly fast and memory efficient.

B.6 Electronic mean squared displacement

The electronic mean squared displacement is defined in the Kubo method [72] [see also Section 3.2]

$$\Delta X_\alpha^2(E, t) = \frac{\text{Tr} \left[\delta \left(E - \mathbf{H} \right) \left(\mathbf{X}_\alpha(t) - \mathbf{X}_\alpha(0) \right)^2 \right]}{\text{Tr} \left[\delta \left(E - \mathbf{H} \right) \right]} \,, \tag{B.26}$$

where $\mathbf{X}_\alpha(t) = \mathbf{U}(-t) \mathbf{X}_\alpha \mathbf{U}(t)$ is the position operator in the α-direction (Heisenberg picture), and $\mathbf{U}(t) = e^{-i\mathbf{H}t/\hbar}$ is the evolution operator

To evaluate ΔX_α^2, we first recognize the DOS in the denominator, which can be calculated using Eq. (B.22). The numerator is rearranged to a symmetric form

$$C = \text{Tr} \left[\delta \left(E - \mathbf{H} \right) \left(\mathbf{X}_\alpha(t) - \mathbf{X}_\alpha(0) \right)^2 \right] = \text{Tr} \left[\left[\mathbf{X}, \mathbf{U}(t) \right]^\dagger \delta \left(E - \mathbf{H} \right) \left[\mathbf{X}, \mathbf{U}(t) \right] \right] \tag{B.27}$$

where $[\mathbf{A}, \mathbf{B}]$ is the commutator between the $\mathbf{A}$ and $\mathbf{B}$. Then we replace the exact trace with the stochastic approximation from Eq. (B.18)

$$C \approx \frac{1}{N_R} \sum_R^{N_R} \underbrace{\langle R| [\mathbf{X}, \mathbf{U}(t)]^\dagger}_{\langle \psi_R(t)|} \delta (E - \mathbf{H}) \underbrace{[\mathbf{X}, \mathbf{U}(t)] |R\rangle}_{|\psi_R(t)\rangle} \tag{B.28}$$

$$\approx \frac{1}{aN_R} \sum_{n=0}^{N_\delta} (\delta_{0n} + 1) \, T_n(\tilde{E}) \sum_R^{N_R} \left\langle \psi_R(t) \middle| T_n(\tilde{\mathbf{H}}) \middle| \psi_R(t) \right\rangle , \tag{B.29}$$

where in the last step we replaced the δ-function with the Chebyshev expansion from Eq. (B.18). Notice that this form is exactly that of the DOS, where $|R\rangle \rightarrow \left| \psi_R(t) \right\rangle$, and we can follow the exact same steps as in Eqs. (B.23) to (B.25).

The entire time evolution is now bundled in to the states $\left| \psi_R(t) \right\rangle = [\mathbf{X}, \mathbf{U}(t)] |R\rangle$. The time evolution operator is replaced by its Chebyshev approximation in Eq. (B.14). However, it is worth noting that the number of expansion coefficients drops considerable for small time evolutions δt rather than large.

From the state $\left| \psi_R(t) \right\rangle$ at time t we find the evolved state at time $t + \delta t$,

$$\left| \psi_R(t + \delta t) \right\rangle = [\mathbf{X}, \mathbf{U}(t + \delta t)] |R\rangle \tag{B.30}$$

$$= [\mathbf{U}(\delta t) [\mathbf{X}, \mathbf{U}(t)] + [\mathbf{X}, \mathbf{U}(\delta t)] \mathbf{U}(t)] |R\rangle \tag{B.31}$$

$$= \mathbf{U}(\delta t) \left| \psi_R(t) \right\rangle + [\mathbf{X}, \mathbf{U}(\delta t)] \underbrace{\mathbf{U}(t) |R\rangle}_{|R(t)\rangle} . \tag{B.32}$$

We divide this evolution into three steps

$$|\mathcal{S}_1(t + \delta t)\rangle = \mathbf{U}(\delta t) \left| \psi_R(t) \right\rangle \tag{B.33}$$

$$|\mathcal{S}_2(t + \delta t)\rangle = [\mathbf{X}, \mathbf{U}(\delta t)] |R(t)\rangle \tag{B.34}$$

$$|\mathcal{S}_3(t + \delta t)\rangle = \mathbf{U}(\delta t) |R(t)\rangle , \tag{B.35}$$

such that we find

$$\left| \psi_R(t + \delta t) \right\rangle = |\mathcal{S}_1(t + \delta t)\rangle + |\mathcal{S}_2(t + \delta t)\rangle \tag{B.36}$$

$$|R(t + \delta t)\rangle = |\mathcal{S}_3(t + \delta t)\rangle . \tag{B.37}$$

The time evolution operators are approximated by Chebyshev approximations from Eq. (B.14), and we get

$$|\mathcal{S}_1(t + \delta t)\rangle \approx e^{-ib\delta t/\hbar} \sum_{n=0}^{N_{\exp}} (\delta_{0n} + 1) \, (-i)^n J_n(a\delta t/\hbar) T_n(\tilde{\mathbf{H}}) \left| \psi_R(t) \right\rangle \tag{B.38}$$

$$|\mathcal{S}_2(t + \delta t)\rangle \approx e^{-ib\delta t/\hbar} \sum_{n=0}^{N_{\exp}} (\delta_{0n} + 1) \, (-i)^n J_n(a\delta t/\hbar) \left[\mathbf{X}, T_n(\tilde{\mathbf{H}}) \right] |R(t)\rangle \tag{B.39}$$

$$|\mathcal{S}_3(t + \delta t)\rangle \approx e^{-ib\delta t/\hbar} \sum_{n=0}^{N_{\exp}} (\delta_{0n} + 1) \, (-i)^n J_n(a\delta t/\hbar) T_n(\tilde{\mathbf{H}}) |R(t)\rangle , \tag{B.40}$$

Steps one and three are readily solved using the recursive relations from Eq. (B.2) [same as in Eq. (B.23)]

$$\underbrace{T_{n+1}(\tilde{\mathbf{H}})\big|\psi_R(t)\big\rangle}_{|\beta_{n+1}\rangle} = 2\tilde{\mathbf{H}}\,\underbrace{T_n(\tilde{\mathbf{H}})\big|\psi_R(t)\big\rangle}_{|\beta_n\rangle} - \underbrace{T_{n-1}(\tilde{\mathbf{H}})\big|\psi_R(t)\big\rangle}_{|\beta_{n-1}\rangle} \tag{B.41}$$

$$\underbrace{T_{n+1}(\tilde{\mathbf{H}})\,|R(t)\rangle}_{|\gamma_{n+1}\rangle} = 2\tilde{\mathbf{H}}\,\underbrace{T_n(\tilde{\mathbf{H}})\,|R(t)\rangle}_{|\gamma_n\rangle} - \underbrace{T_{n-1}(\tilde{\mathbf{H}})\,|R(t)\rangle}_{|\gamma_{n-1}\rangle} \ . \tag{B.42}$$

The final step ($\mathcal{S}_2$) is solve using the recursive relations from Eq. (B.2) with in the commutator $\big[\mathbf{X}, T_n(\tilde{\mathbf{H}})\big]$. We find

$$\underbrace{\big[\mathbf{X}, T_{n+1}(\tilde{\mathbf{H}})\big]\,|R(t)\rangle}_{|\eta_{n+1}\rangle} = 2\,\big[\mathbf{X}, \tilde{\mathbf{H}}T_n(\tilde{\mathbf{H}})\big]\,|R(t)\rangle - \big[\mathbf{X}, T_{n-1}(\tilde{\mathbf{H}})\big]\,|R(t)\rangle \tag{B.43}$$

$$= 2\tilde{\mathbf{H}}\,\underbrace{\big[\mathbf{X}, T_n(\tilde{\mathbf{H}})\big]\,|R(t)\rangle}_{|\eta_n\rangle} + 2\,\big[\mathbf{X}, \tilde{\mathbf{H}}\big]\,\underbrace{T_n(\tilde{\mathbf{H}})\,|R(t)\rangle}_{|\gamma_n\rangle} - \underbrace{\big[\mathbf{X}, T_{n-1}(\tilde{\mathbf{H}})\big]\,|R(t)\rangle}_{|\eta_{n-1}\rangle} \tag{B.44}$$

where we have used the commutator relation $[A, BC] = B[A, C] + [A, B]C$.

The final set of master equations become

$$\big|\psi_R(t + \delta t)\big\rangle = \sum_{n=0}^{N} (\delta_{0n} + 1)\,(-i)^n\,J_n(a\delta t/\hbar)\left(\big|\beta_n\big\rangle + \big|\eta_n\big\rangle\right) \tag{B.45}$$

$$|R(t + \delta t)\rangle = \sum_{n=0}^{N} (\delta_{0n} + 1)\,(-i)^n\,J_n(a\delta t/\hbar)\big|\gamma_n\big\rangle \tag{B.46}$$

For each evolution $t \to t + \delta t$ we need the β, η, and γ states. To then determine the full ΔX_α^2 [Eq. (B.29)], the α states are determined from the newly evolved states $\big|\psi_R(t + \delta t)\big\rangle$.

Publications

Paper I

Graphene on graphene antidot lattices: Electronic and transport properties

Authors:
Søren Schou Gregersen, Jesper Goor Pedersen,
Stephen R. Power, and Antti-Pekka Jauho

Graphene on graphene antidot lattices: Electronic and transport properties

Søren Schou Gregersen, Jesper Goor Pedersen, Stephen R. Power, and Antti-Pekka Jauho

Center for Nanostructured Graphene (CNG), Department of Micro- and Nanotechnology Engineering,

Technical University of Denmark, DK-2800 Kongens Lyngby, Denmark

Graphene bilayer systems are known to exhibit a band gap when the layer symmetry is broken by applying a perpendicular electric field. The resulting band structure resembles that of a conventional semiconductor with a parabolic dispersion. Here, we introduce a bilayer graphene heterostructure, where single-layer graphene is placed on top of another layer of graphene with a regular lattice of antidots. We dub this class of graphene systems GOAL: graphene on graphene antidot lattice. By varying the structure geometry, band-structure engineering can be performed to obtain linearly dispersing bands (with a high concomitant mobility), which nevertheless can be made gapped with a perpendicular field. We analyze the electronic structure and transport properties of various types of GOALs, and draw general conclusions about their properties to aid their design in experiments.

I. INTRODUCTION

The intrinsic properties of graphene, including ballistic transport, physical strength, and optical near-transparency, are very attractive for consumer electronics as well as for fundamental research platforms [1,2]. One of the main attractions of graphene is the prospect of manipulating its electronic properties and introducing a band gap, making the semimetal into a semiconductor as required for many electronic applications [3–5]. As conventional potential barriers in graphene can exhibit Klein tunneling [1,2], much research has focused on finding methods to introduce a band gap in graphene. Most proposals use structural modifications of graphene systems, such as nanoribbons, or superlattice structures imposed by periodic gating or strain [6–14]. More recent attempts use chemical modification through absorption or substitution [15,16]. Periodic perforation of graphene sheets, to form so-called graphene antidot lattices (GAL), is of particular interest since theoretical predictions suggest the possibility of obtaining sizable band gaps [17–22]. The band gaps of nanostructured graphene are, however, very sensitive to disorder and defects [23,24]. Current nanostructure fabrication methods, e.g., block copolymer [25,26] or e-beam [27–32] lithography, will inevitably yield systems with a significant degree of disorder, especially near perforation edges. Yet another emerging strategy towards altering the intrinsic behavior of graphene is to use structures composed of several 2D materials. Bilayer graphene opens a band gap when an asymmetry is introduced between the two graphene layers [3,33–37]. This is usually obtained by applying an electric field to create a potential difference between the top and bottom layers. A transistor based on bilayer graphene has already been reported with a high on-off ratio ∼100 [3]. Large areas of bilayer graphene can be fabricated, without etching, by mechanical exfoliation [38] or by growth on a substrate [36], which reduces the risk of generating imperfections. Unfortunately, most of these gapped or modified graphene systems lack the linear band structure of pristine graphene, e.g., bilayer graphene has a parabolic dispersion [35,36]. The implication of the parabolic bands is a lower mobility and thus degraded device performance [5]. To overcome this, we propose the use of heterogeneous multilayered structures. Bilayer superlattices have been studied in detail, with, e.g., periodic potential barriers [39], and dual-layer antidot lattices [40]. A 1- or 2D potential modulation of the potential in bilayer graphene has even been predicted to yield linear dispersion [41]. However, heterostructure bilayers composed of two different single-layer systems are not widely studied. Stacked heterostructures from multiple 2D materials created and held together only by van der Waals (vdW) forces [47] are particularly interesting as the interfaces may be kept clean from processing chemicals.

Previous studies have theoretically looked into single-layer doping in bilayer graphene, [42–45] and experimentally single-sided oxygenation of bilayer graphene [46], the latter of which reports electronic decoupling of one of the layers. In this work, we propose an all-carbon heterostructure that serves as a hybrid between single- and bilayer graphene. It exhibits essentially linear bands at zero transverse bias while retaining the possibility of a bias-tunable band gap when dual-gating the top and bottom layers. The material is a bilayer heterostructure composed of a pristine graphene layer and a GAL layer, which we call **G**raphene **O**n (graphene) **A**ntidot **L**attice (GOAL). We can hypothesize at least two methods in which a GOAL-based device could be realized experimentally, by either employing standard lithography [27–32] to etch the antidot pattern in only a single layer of bilayer graphene, or alternatively, by creating a sheet of GAL and then transferring pristine graphene on top using vdW stacking techniques. [47]

The remainder of this paper is organized as follows. The atomic structure and the tight-binding model used for describing GOAL systems is introduced in Sec. II. Section III examines the properties of a representative sample of GOALs both with and without an applied bias. In Sec. IV, the effects of different schemes for injecting current into and out of a GOAL device are addressed using two-lead transport simulations. Finally, in Sec. V, we discuss the implications of the investigated GOAL properties, the limitations of such systems and considerations relating to feasibility and application.

II. GEOMETRIES AND METHODS

We consider a heterostructure consisting of a single layer of pristine graphene on top of a layer of GAL, as illustrated
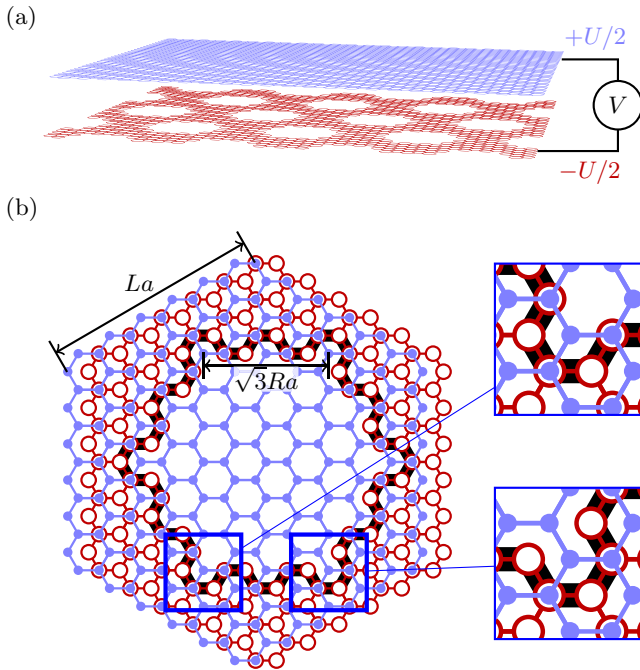
FIG. 1. (Color online) (a) Schematic illustration of the considered structures, consisting of a single graphene layer (blue) on top of a GAL layer (red), arranged in an AB stacking. (b) A closer view of the atomic structure of the Wigner-Seitz cell of a $\{L,R\} = \{6,2\}$ GOAL, with carbon atoms in the graphene (GAL) layer illustrated with blue filled circles (red open circles). The integers L and R used for denoting a given geometry are illustrated and the antidot hole edge is highlighted by a black line. The GAL superlattice of the illustrated geometry is of the type that always has a band gap, as explained in the main text. Zooms of two different corners of the antidot, corresponding to the thick blue outlines are shown on the right. The corner site in the bottom-left corner is a dimer, identified by the filled blue circle on top of an open red circle. Conversely, the corner site in the bottom-right corner is a nondimer, identified by only either a filled blue or open red circle. This gives rise to a C_3 symmetry, as discussed in the main text.

schematically in Fig. 1(a). The twist angle between the layers greatly influences the electronic properties of bilayer graphene [34,48], and we expect the properties of the proposed GOAL structures to also depend on the angle between the two layers. However, for simplicity, we focus in this paper on perfect Bernal (AB) stacking of the two layers. We discuss the possible influence of the angle in more detail in the final section of the paper. Furthermore, experiments suggest the possibility of manually twisting the top layer until it "locks" into place at the Bernal stacking angle [49].

Similar to the intricate edge dependence observed for graphene nanoribbons [7], the exact shape of the antidot greatly influences the electronic properties of isolated GALs. In particular, extended regions of zigzag edges, which will generally be present for larger, circular holes, tend to induce quasilocalized states that significantly quench any present band gap [20,21]. To simplify the analysis of the proposed structures, we focus on hexagonal holes with armchair edges. Experimental techniques exist that tend to favor the creation

of specific edge geometries [27,32,50,51]. In addition to the hole shape, the orientation of the GAL superlattice with respect to the pristine graphene lattice has a profound impact on the electronic properties [18,21]. The orientation of a superlattice may be defined by the vectors between two neighboring antidots $\mathbf{R} = n_1\mathbf{a}_1 + n_2\mathbf{a}_2$, where $\mathbf{a}_1$ and $\mathbf{a}_2$ are the lattice vectors of pristine graphene. It has been shown that if $\mathrm{mod}(n_1 - n_2, 3) = 0$ for any $\mathbf{R}$, the degeneracy at the Dirac point will break and a band gap is induced [18,52,53]. In this paper, we consider GALs with two types of triangular superlattices: those with vectors parallel to carbon-carbon bonds, which always induce a band gap, and those with vectors parallel to the pristine graphene lattice vectors, which only induce gaps for a subset of superlattices. We only briefly discuss GOALs where the superlattice of the GAL layer is of the latter type, which we refer to as *rotated* GOALs and *rotated* GALs, respectively, and focus mostly on the GAL superlattices for which band gaps are always present. We demonstrate below that GOALs containing gapped GAL layers display similar properties regardless of the superlattice type, whereas GOALs with nongapped GAL layers essentially behave as bilayer graphene with a renormalized Fermi velocity.

The Wigner-Seitz cell of a specific GOAL is illustrated in Fig. 1(b), where the red open circles represent the GAL layer atoms and the blue filled circles are the graphene layer atoms. To denote a given GOAL, we use the notation $\{L,R\}$, where La is the side length of the hexagonal unit cell, while $\sqrt{3}Ra$ is the side length of the hexagonal hole in the GAL layer, with $a = 2.46$Å the graphene lattice constant. We use $\{L,R\}_{\mathrm{rot}}$ to refer to GOALs in which the isolated GAL layer is of the rotated type, as discussed above. Note that in this case, the Wigner-Seitz cell is not as shown in Fig. 1 but is rather in the shape of a rhombus with side length La [18]. The condition for band gaps reads $L = 3n + 2$, where $n = 0, 1, \cdot$ for isolated rotated GALs and within our model the other two thirds of the rotated GALs are gapless. The superlattice constant of a GOAL is $\Lambda = \sqrt{3}La$, while for a rotated GOAL it becomes $\Lambda_{\mathrm{rot}} = (L + 1)a$.

In Bernal-stacked bilayer graphene there are four distinct sublattices, two in each layer. Within each layer, we refer to these as dimer and nondimer sites, and these sit directly above or below carbon sites (dimers) or the centers of hexagons (nondimers) in the other layer. These sites are illustrated in the right of Fig. 1(b), where two of the antidot corners have been magnified. It has been shown that the low-energy properties of bilayer graphene are dominated by nondimer sites, and can be described using an effective two-band model with parabolic bands touching at the Fermi energy [35]. The introduction of the hole, forming the GAL layer of the GOAL system results in a higher number of sites from each sublattice in the graphene layer than in the GAL layer, but within our model maintains the sublattice symmetry within each individual layer. The interlayer asymmetry has important consequences when applying a bias across the layers, which we will discuss below in Sec. III B. Furthermore, the structures of GOALs no longer display a 60° rotational symmetry. Neighboring corners of a hexagonal hole are now associated with sites from opposite sublattices, as can be seen on the right of Fig. 1(b), reducing the C_6 symmetry of bilayer graphene to C_3. Not all carbon sites in the graphene layer of a GOAL system are *true* dimers

or nondimers, as the respective sites or hexagons below may have been removed by the holes. However, they still exhibit similar behavior to other sites in the same sublattice and we will thus collectively refer to them as dimers and nondimers, respectively.

To calculate the electronic properties of the proposed structures, we use a nearest-neighbor tight-binding model. The low-energy properties of single-layer graphene are quite accurately described by a model taking into account just the nearest-neighbor hopping term, γ_0. For bilayer graphene, additional interlayer hopping terms need to be included. We consider the Slonczewski-Weiss-McClure model [35] with the direct intralayer hopping term γ_1 between AB dimers and the skew hopping terms γ_3 and γ_4 between dimers and nondimers. As we show below in Sec. III, omitting the skew hopping terms has no qualitative impact on the results obtained. Therefore in most our calculations we disregard the skew hopping terms which are responsible for trigonal warping and electron-hole asymmetry in bilayer graphene [35]. Furthermore, we do not include any on-site energy difference between dimer and nondimer sites [35]. The Hamiltonian then reads

$$\mathbf{H} = \sum_{i,j \in \{\mathrm{nn}\}} \gamma_0 \mathbf{c}_i \mathbf{c}_j^\dagger + \sum_{i,j \in \{\mathrm{dimers}\}} \gamma_1 \mathbf{c}_i \mathbf{c}_j^\dagger + \mathrm{H.c.}, \quad (1)$$

where {nn} is the collection of nearest-neighbor pairs within each layer and {dimers} is the collection of dimer pairs. We take $\gamma_0 = -3.16\,\mathrm{eV}$ and $\gamma_1 = 0.381\,\mathrm{eV}$ [35,54]. An interlayer bias U (initially $U = 0$) can be included via a shift $\pm U/2$ of the on-site energies on the GAL and the graphene layer, respectively. We define a positive bias to be one where the on-site energies of the graphene (GAL) layer are increased (decreased), as illustrated in Fig. 1(a).

III. ELECTRONIC PROPERTIES

We begin by examining the electronic band structures of some GOAL systems in the absence of a transverse bias. The left-most panel of Fig. 2 shows the band structure of a {16,6} GOAL. The {16,R} GOALs all contain GAL layers with a triangular superlattice, which in their isolated form

are gapped for all R. The solid lines show the band structure calculated with intralayer and direct interlayer hoppings only, whereas the dashed lines show the results obtained when including also the skew hopping terms, $\gamma_3 = -0.38\,\mathrm{eV}$ and $\gamma_4 = 0.14\,\mathrm{eV}$ [35,54]. The most striking features of the {16,6} band structure are the linear bands near the Fermi energy, resembling the linear bands of single-layer graphene. The reduced Brillouin zone of the GOAL means that the K and K$'$ points of pristine graphene are folded onto the Γ point. The most significant consequence of the skew hopping terms is to split the linear band into two linear bands with slightly different Fermi velocities. The band splitting and the difference in Fermi velocities becomes more pronounced in cases near pristine bilayer graphene, where the antidot size is relatively small. As we are mainly interested in a qualitative study of the proposed structures we disregard the skew hopping terms from hereon.

To illustrate the transition from the parabolic bands of bilayer graphene to the linear bands of single-layer graphene as the antidot size is increased, we show in the right panels of Fig. 2 the dispersion relation near the Γ point for the {16,R} GOALs with increasing values of R. For comparison, the dashed (dotted) lines illustrate the pristine single-layer (bilayer) graphene dispersion, folded into the Γ point. As the antidot size is increased, a transition from bilayer to single-layer-graphene-like (SLG-like) electronic properties is quite apparent, but with Fermi velocities that are slightly smaller than that of single-layer graphene. This transition is also clear from Fig. 3, which plots the Fermi velocity of the {16,R} GOALs at $E = 0$ as a function of R. The transition towards SLG-like bands does not occur via an ever increasing curvature of two parabolic bands touching at the Fermi energy. Instead, we always observe a region of linear bands for $R > 0$, albeit the energy range in which the bands are linear is very narrow for small antidot sizes, and is accompanied by a strongly reduced Fermi velocity. Thus the low-energy band structure of GOAL can be considered as the crossing of two bands, similar to the case of single-layer graphene.

As the antidot size is increased, more atoms are removed from the GAL layer and this leads to an effective reduction
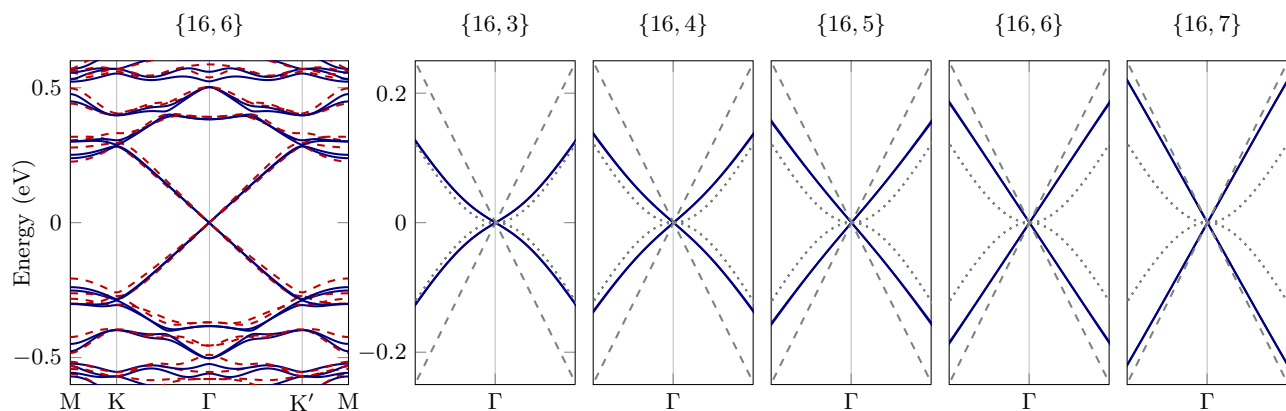

FIG. 2. (Color online) Band structures of {16,R} GOALs. The left-most panel shows the full band structure within our model (solid blue lines), and for comparison the results obtained if skew scattering terms are included (red dashed lines). The right panels show a section of the band structure of GOALs near the Γ point, for increasing antidot sizes, in solid lines. Dashed gray lines show the corresponding single-layer graphene dispersion, while dotted gray lines illustrate the bilayer graphene dispersion.
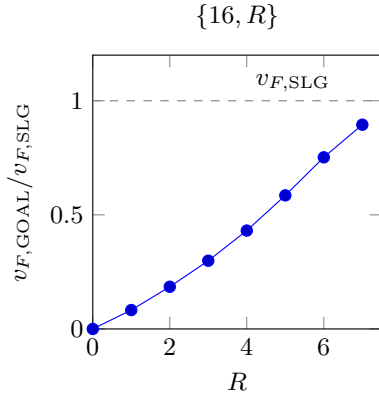
FIG. 3. (Color online) The Fermi velocity $v_{F,\text{GOAL}}$ of $\{16,R\}$ GOALs as a function of R. The $v_{F,\text{GOAL}}$ is shown relative to the Fermi velocity of pristine graphene $v_{F,\text{SLG}}$.

in the amount of bilayer graphene in the GOAL. We can quantify this via the relative area of bilayer graphene in the system, i.e., the ratio of the GAL and SLG layer areas, $f_{\text{BLG}} = A_{\text{GAL}}/A_{\text{SLG}} = 1 - \frac{2\pi}{3\sqrt{3}}\frac{R^2}{L^2}$. It is reasonable to ask whether the cause of the transition from parabolic to linear bands is simply caused by a reduction in $f_{\text{BLG}} \to 0$ as R is increased. To determine whether this is indeed the case, we show in Fig. 4 the band structures near the Dirac point for two $\{27,R\}_{\text{rot}}$ GOALs, which consist of gapless rotated GAL layers. The superlattice constants of the $\{27,R\}_{\text{rot}}$ and the corresponding $\{16,R\}$ GOALs are roughly similar ($\Lambda/\Lambda_{\text{rot}} \approx 1.01$) yielding very similar relative areas f_{BLG}. The band structures for the two $\{27,R\}_{\text{rot}}$ GOALs are shown in solid lines together with those of bilayer graphene in dashed gray lines. These rotated GOALs show a completely different dispersion, with no transition towards linear bands as the antidot size increases, even beyond the sizes shown in the figure. Despite having similar bilayer relative areas f_{BLG} to the GOALs considered in Fig. 2, the
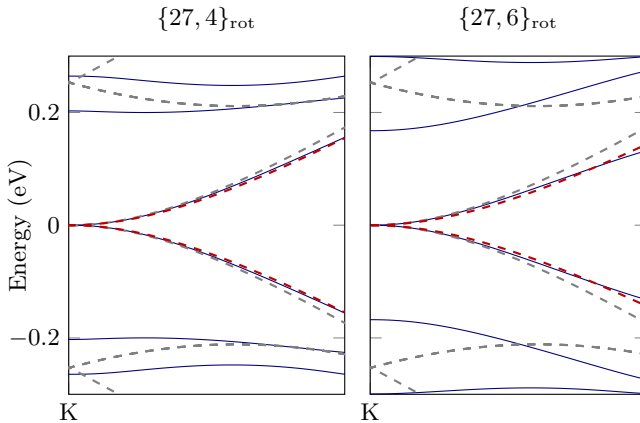
band structures of the rotated GOALs remain parabolic and closely resemble that of pristine bilayer graphene.

We note that the isolated rotated GALs are gapless and that their band structures retain linear bands similar to pristine single-layer graphene, renormalized to a lower Fermi velocity [18]. This suggests that GOALs with gapless rotated GAL layers can be described by a model similar to that of bilayer graphene, but with a renormalized Fermi velocity. The low-energy dispersion of bilayer graphene is well described in a continuum model [35],

$$E = \pm 1/2\gamma_1 \left[\sqrt{(1 + 4\hbar^2 v_F^2 k^2/\gamma_1^2} - 1 \right], \qquad (2)$$

where v_F is the Fermi velocity of single-layer graphene. To model the rotated GOAL, we replace the Fermi velocity with the average Fermi velocity of the pristine graphene and renormalized GAL velocities, $\bar{v}_F$. The results of this simple model are illustrated by red dashed lines in Fig. 4, and indeed show quite good agreement with the full tight-binding results. Interestingly, rotated GOALs with *gapped* rotated GAL layers (e.g., $\{26,R\}_{\text{rot}}$, not shown) display no qualitative difference from the regular GOALs with gapped nonrotated GAL layers.

A. Distribution of states

The transition from parabolic to linear bands can thus not be explained entirely by the relative area of bilayer graphene, f_{BLG}, in the GOAL system, but instead depends critically on the existence of a band gap in the isolated GAL layer. To illustrate how the band gap of the GAL layer induces the SLG-like behavior in the combined system, we show the projected density of states (PDOS) at the Fermi energy $E = 0$ for each layer of the $\{9,2\}$ and $\{9,3\}$ GOALs in Figs. 5(a) and 5(b). We will later discuss the differences in $\{15,R\}_{\text{rot}}$ GOALs which consist of gapless GAL layers. The properties illustrated by the $\{9,R\}$ GOALs are qualitatively similar to those of $\{16,R\}$. The PDOS of the two layers are displayed separately, with the graphene layer above and the GAL layer below. Furthermore, the PDOS of dimers and nondimers are illustrated by filled red and blue circles, respectively. The size of the filled circles represents the value of the PDOS, which is normalized relative to that of pristine single-layer graphene shown by the open circles. The PDOS of the $\{9,2\}$ and $\{9,3\}$ GOALs are illustrated in Figs. 5(a) and 5(b), respectively. We recall that in the case of pristine single-layer (bilayer) graphene the Fermi energy density of states is equally distributed across all sites (all nondimer sites). Examining first the graphene layers of the GOAL systems, we note that, unlike in bilayer graphene, there is a nonzero PDOS on dimer sites. Furthermore, this is equally distributed within the graphene layer, regardless of whether or not the sites are above another carbon site or above an antidot. Comparing the $\{9,2\}$ and $\{9,3\}$ cases, we see that the PDOS on dimer sites in the graphene layer increases with the antidot size. Meanwhile, the PDOS of the graphene layer nondimers remains unchanged from that of single-layer graphene as the antidot size varies. Interestingly, in the GAL layer dimer PDOS remains zero for all antidot sizes. The PDOS of the nondimer sites in the GAL layer displays a C_3 symmetry, yielding a three-fold symmetric confinement around antidot corners associated with nondimer

FIG. 4. (Color online) Band structures near the Dirac point of two $\{27,R\}_{\text{rot}}$ GOALs with gapless GAL layers. The solid lines indicate the GOAL band structures, while the dashed gray lines are the band structure of pristine bilayer graphene. The dashed red lines show the bilayer graphene band structure with a renormalized Fermi velocity, as discussed in the main text.
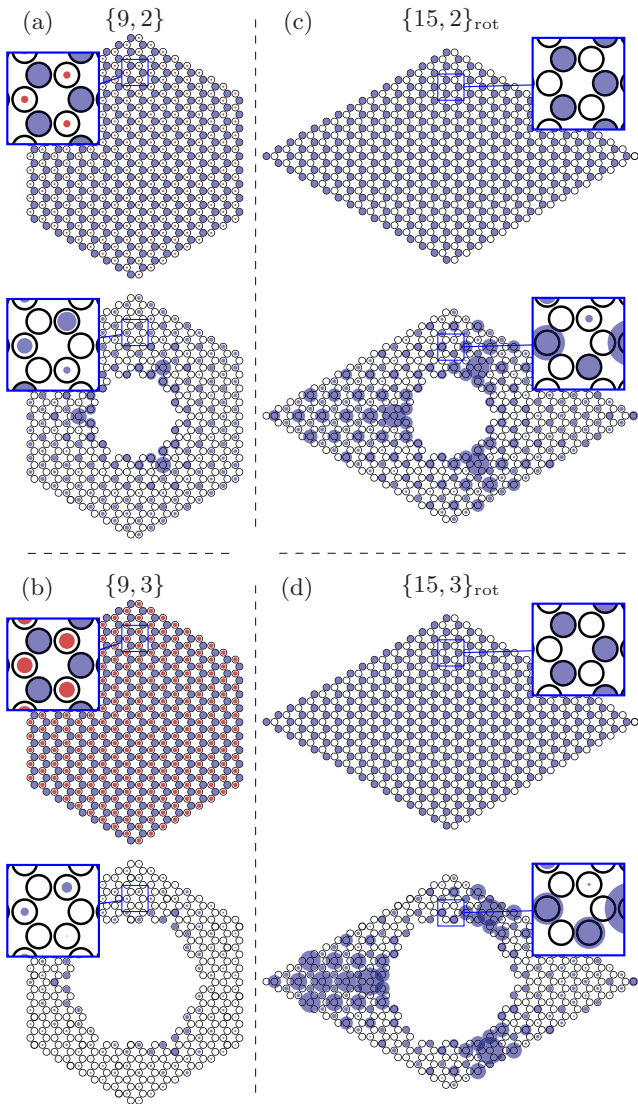
FIG. 5. (Color online) The projected density of states at the Fermi energy $E = 0$. For the four systems considered, the PDOS of the two layers are displayed separately; the graphene layer above the GAL layer. The panels illustrate the PDOS of the $\{9,2\}$ GOAL (a), the $\{9,3\}$ GOAL (b), the $\{15,2\}_{\text{rot}}$ GOAL (c), and the $\{15,3\}_{\text{rot}}$ GOAL (d). The PDOS of dimer sites are illustrated by red filled circles and PDOS of nondimer sites by blue filled circles. Their sizes represent the value of the PDOS relative to that of pristine single-layer graphene, shown by open circles. Thus, if the PDOS is lower than that of pristine graphene, the filled circles are smaller than the open circles and vice versa.

FIG. 6. (Color online) The integrated PDOS (overlap) of various GOALs. (a) The overlap of the graphene layer for $\{16,R\}$ (solid lines) and $\{27,R\}_{\text{rot}}$ (dashed lines) GOALs. The inset displays the dimer overlap in the graphene layer for the $\{16,R\}$ GOALs. The overlap of the nondimers in the graphene layer, $\mathcal{O}_{\text{SLG,nondimers}}$, does not change. (b) The relative overlap of the GAL layer for the $\{16,R\}$ (solid lines) and $\{27,R\}_{\text{rot}}$ (dashed lines) GOALs. (c) The overlap with the GAL layer at the Γ point vs the band gap of the isolated GAL layer for $\{L,R\}$ GOALs with $L \in [7;24]$ and valid R within $[0,L]$. The color of each dot indicates the value of L.

sites. Furthermore, the PDOS of the GAL layer nondimers clearly decreases as the antidot size is increased. The net result of these features is that, for large antidots, the PDOS eventually displays a distribution largely confined in the graphene layer. This emerges from a decrease in the GAL layer nondimer PDOS and an increase in that of the graphene layer dimer sites.

We can illustrate these findings more clearly by considering the PDOS integrated over all sites within each of the layers,

which we quantify via the overlap

$$\mathcal{O}_i(E) \equiv \sum_n \sum_{m \in i} |c_m(E_n)|^2 \delta(E - E_n), \tag{3}$$

where $c_m(E_n)$ is the expansion coefficient of the nth eigenstate on to the π orbital centered at the mth atomic site, and where i denotes the layer, $i \in \{\text{GAL}, \text{SLG}\}$. A value of $\mathcal{O}_{\text{SLG}}(E) = \mathcal{O}_{\text{GAL}}(E) = \frac{1}{2}$ thus corresponds to an equal distribution of the eigenstates across both layers. The graphene layer localization at the Fermi energy is illustrated for $\{16,R\}$ GOALs in Fig. 6(a). The solid line in the figure shows the graphene layer overlap as a function of antidot size. As R is increased, the graphene layer overlap increases, i.e., the density of states become more confined in the graphene layer. The increased confinement is purely due to increased dimer PDOS, as apparent from the inset in Fig. 6(a), which displays the dimer overlap in the graphene layer, obtained by limiting the sum in Eq. (3) to dimer sites, as a function of antidot size. The increased graphene layer localization could be due to a simple redistribution of the density of states on to the remaining sites, where the overlap is proportional to the number of sites in the particular layer. We therefore consider the relative overlap $\mathcal{O}_i N_{\text{Tot}} / N_i$, with N_{Tot} denoting the total number of carbon

atoms with $R = 0$, while N_i the number of carbon atoms within the layer i. The value $\mathcal{O}_{\text{GAL}} N_{\text{Tot}}/N_{\text{GAL}} = 1$ thus denotes a GOAL with layer overlaps proportional to the number of sites in that particular layer. We show the relative overlap $\mathcal{O}_{\text{GAL}} N_{\text{Tot}}/N_{\text{GAL}}$ of the $\{16, R\}$ GOALs in Fig. 6(b). The solid line shows the relative overlap of the GAL layer as a function of the antidot size. The relative overlap is below unity for any nonzero R and decreases with increasing antidot size. Thus the GAL layer confinement decreases more quickly than a simple redistribution can account for, pushing the density of states even further into the graphene layer. This transition from bilayer to single-layer confinement is critically dependent on the GAL band gap, and we therefore illustrate the GAL layer overlap for various $\{L, R\}$ GOALs as a function of the isolated GAL gap in Fig. 6(c). Each GOAL is represented by a point colored by the value of L. We find that the overlap in the GAL layer decreases with the GAL band gap in a largely one-to-one correlation, except at high GAL band gaps obtained through rather impractical antidot lattices, e.g., where the distance between antidots is only slightly larger than the antidot size. As the GAL band gap increases states are pushed out of the GAL layer and into the graphene layer, effectively localizing the states in a single-layer yielding the SLG-like behavior. This occurs, as we saw in Fig. 5, via a transfer of states between the GAL layer nondimer and graphene layer dimer sites as the antidot size, and thus the band gap, is increased.

To further illustrate the importance of the GAL band gap, we now consider the rotated GOALs which consist of gapless GAL layers and display a renormalized bilayerlike dispersion. The PDOS at $E = 0$ for the $\{15, 2\}_{\text{rot}}$ and $\{15, 3\}_{\text{rot}}$ GOALs are illustrated in Figs. 5(c) and 5(d), respectively. The most notable feature in the rotated GOAL systems, as opposed to the nonrotated $\{9, R\}$ GOALs, is the zero PDOS of dimer sites in both layers of the rotated GOALs. The PDOS of the nondimer sites in the graphene layer remains unaffected by the introduction of an antidot and the increasing of R. Therefore the PDOS of the GAL layer nondimer sites must increase. This is more clearly seen in Fig. 6(a) where the graphene layer overlap of the $\{27, R\}_{\text{rot}}$ GOALs is illustrated by the dotted red line. As the antidot size increases, no changes occur in the overlap of the graphene layer and hence also not in the overlap of the GAL layer. In Fig. 6(b), we display the relative overlap of the GAL layer of the $\{27, R\}_{\text{rot}}$ by the dotted red line. In these rotated GOALs, the relative overlap increases above unity, corresponding to the redistribution of the PDOS onto the remaining nondimer sites within the GAL layer. This is also seen in the GAL layers of the $\{15, R\}_{\text{rot}}$ GOALs shown in right panels of Fig. 5, where the PDOS of the individual nondimer sites has been significantly increased compared to the $\{9, R\}$ GOALs. GOALs with gapless GAL layers do not push states into the graphene layer, but instead simply redistribute the density of states in the nondimer sites of the GAL layer. A low-energy distribution of states amongst nondimer sites only is a noted property of bilayer graphene, and confirms again the relation between the properties of rotated GOALs and those of the pristine bilayer. We limit the remainder of this paper to an investigation of the nonrotated GOALs, where the migration of states from the GAL to the graphene layer leads to an even distribution of states amongst the sublattices of the graphene layer, and thus to SLG-like behavior.

B. Bias-tunable band gaps

We now turn to biased structures. A potential difference between the layers induces a band gap in the case of pristine bilayer graphene, the size of which can be tuned by the bias voltage [33,35,36,55]. The potential U can be created by a uniform electric field perpendicular to the two layers. In experimental systems, the voltage difference V is an induced quantity from the larger applied potential V_{ext} that due to screening and interlayer coupling is significantly reduced. For bilayer graphene, the potential is uniform within the two layers and the induced voltage difference can be assumed linearly proportional to the applied voltage $V \propto V_{\text{ext}}$, in which case currently U has been predicted to realistically lie between ± 0.3 eV [55]. We note that in GOAL the edges will likely induce an inhomogeneous potential distribution. To find this, distribution requires a self-consistent solution to the Poisson equation and band structure, a level of complication beyond the current scope. We limit our model to include the bias via a uniformly distributed on-site energy shift $\pm U/2$ for the graphene and GAL layers respectively.

In a biased GOAL system, the interlayer asymmetry of the on-site energies opens a band gap around the Dirac point. We illustrate this in Fig. 7(a) through the band structures of two biased $\{16, R\}$ GOALs at $U = 0.2$ eV. In this figure, the bands of biased $\{16, 3\}$ and $\{16, 6\}$ GOALs are shown in dashed red and solid blue lines respectively, together with the bands of pristine biased bilayer graphene in dotted gray lines. The band gap of biased $\{16, 6\}$ GOAL is smaller than that of biased bilayer graphene or of the smaller antidot GOAL. The change of the gap size is quantified in Fig. 7(b) where we illustrate the band gaps of several biased $\{16, R\}$ GOALs as a function of U. Each $\{16, R\}$ GOAL is shown as a solid line colored according to the value of R. Additionally, the band gap of biased bilayer graphene is shown as a dashed line. The band structures of the two biased $\{16, R\}$ GOALs in Fig. 7(a) further display electron-hole asymmetry. This arises due to the atomic imbalance between the two layers combined with the equal but opposite on-site energy shifts used to model the bias. While the effect is minor in case of small antidots, for larger antidots the net energy shift caused by the imbalanced bias distribution yields a valence band shifted towards $E = 0$. We note also that the band structure of the biased $\{16, 6\}$ GOAL resembles that of gapped graphene, identified by the absence of the "Mexican hat" profile of biased bilayer graphene [35]. The absence of the flat profiles of biased bilayer graphene yields larger group velocities, which in turn is very attractive in fast electronic applications. The transition between the bilayer graphene and gapped SLG-like dispersion is smooth, and similar to the zero-bias case can not be contributed solely to the reduced area f_{BLG}. To illustrate this, we plot the biased GOAL band gap dependence on the isolated GAL gap for various $\{L, R\}$ GOALs in Fig. 7(c) at $U = 0.2$ eV, where each GOAL is represented by a point colored by the value of L. The figure demonstrates clearly that an increase in the isolated GAL gap will cause a decrease of the biased GOAL band gap. Although perhaps counterintuitive, this behavior is the direct result of GOALs with large band gap GAL layers exhibiting graphene layer confinement. This effectively reduces the interlayer asymmetry felt by the electronic states
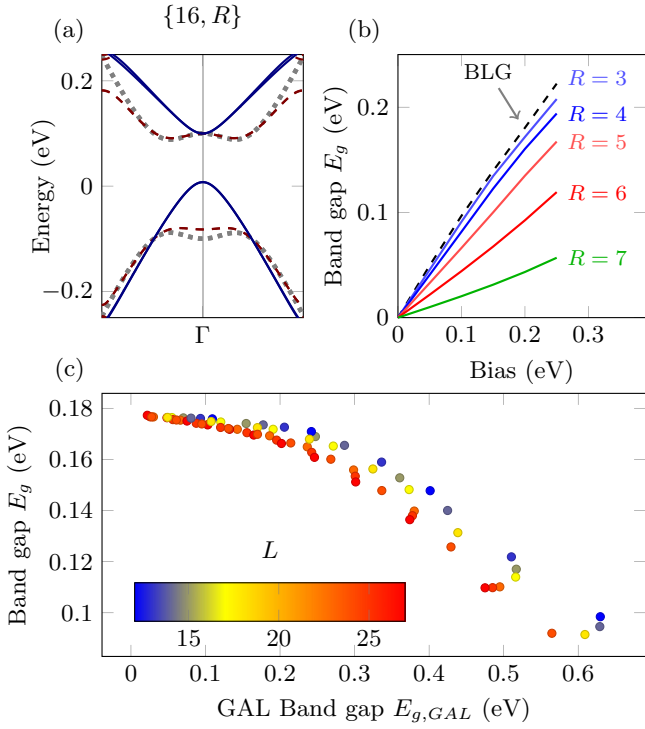
FIG. 7. (Color online) Band structures and gaps of biased various GOALs. (a) Band structures for the {16,3} (red, dashed) and {16,6} GOALs (blue, solid) and pristine bilayer graphene (gray, dotted), with a bias $U = 0.2$ eV applied across the layers. The bands resemble biased bilayer graphene, i.e., the "Mexican hat" profile, for the small antidot {16,3} and gapped single-layer graphene for the large antidot {16,6} GOAL. (b) Band gaps for {16,R} GOALs with $R = 3,4,5,6,7$ and an increasing bias. Note the near-linear dependence on the bias for all antidot sizes. (c) The band gap of {L,R} GOALs with a bias $U = 0.2$ eV applied across the layers versus the isolated GAL layer gap, with $L \in [7; 26]$ and valid R within $[0,L]$. The color of each dot indicates the value of L.

and reduces the band gap of the combined structure. Figure 7(c) displays a clear correlation between the GAL band gap and the biased GOAL band gap, though it does display increased spreading as the GAL band gap is increased. This spreading signifies an additional complication due to the uniform on-site energy shift $\pm U/2$ in the two asymmetric layers. While the largest band gaps are found for GOAL systems whose unbiased electronic structure most closely resembles that of bilayer graphene, there is a range of {L,R} values that yield both sizable band gaps and largely linear dispersion relations, e.g., the {16,6} shown here and also the {12,4} case. This presents the interesting possibility of combining high Fermi velocity electronic transport similar to single-layer graphene with a gate-controllable band gap.

IV. TRANSPORT PROPERTIES

We mentioned two ways of experimentally fabricating GOAL devices; either by single-layer etching bilayer graphene or stacking a graphene sheet onto a GAL sheet. Most experimental transport measurements in bilayer graphene have been performed with top-contacts to inject current, and using
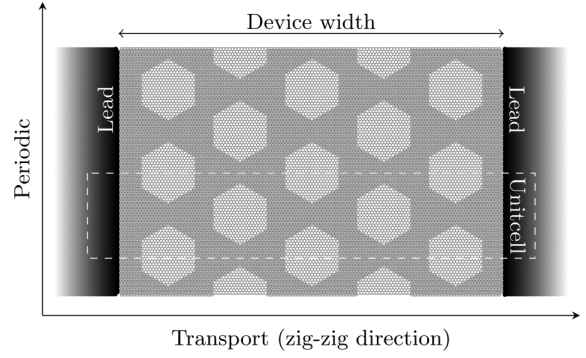
FIG. 8. A schematic illustration of the GOAL device transport model. The incoming and outgoing leads (black), both of which are semi-infinite sheets of either single- or bilayer graphene, are coupled to a central GOAL device (gray). Bilayer leads are coupled to both layers of the GOAL device, while single-layer leads are coupled to either layer of the GOAL device. The considered model is periodic in the transverse direction.

dual-gates to control the interlayer bias [56–58]. With recent advances in side-contacts, first in single-layer graphene [59] and then in bilayer graphene [60], there are now several ways of injecting current into a bilayer material such as GOAL. The consequence of the choice of contacts has been studied for pristine bilayer graphene ribbons and flakes [61,62]. To illustrate the consequences of the choice of contacts, we consider the electronic transport through a finite-width strip of GOAL. To calculate the transport properties, we employ the Landauer-Büttiker formalism. The transport is calculated between two leads composed of either single or bilayer graphene. A schematic illustration of the transport model is shown in Fig. 8. In case of bilayer leads, these are connected to both the graphene and GAL layers, while single-layer leads are coupled to either the graphene or the GAL layer. Both the leads and the device are periodic in the transverse direction, and the unit cell used in calculations is outlined by the dashed rectangle. We consider transport in the zigzag direction. This yields a dense cross-section of antidots, effectively reducing the width of the GOAL device needed to represent large-width GOAL transport [20]. Our calculations are performed on strips of GOAL with seven antidots rows present along the transport direction. This width yields a well defined transport gap in the isolated GAL layer [20].

With respect to the Landauer-Büttiker formula $G(E) = \frac{2e^2}{h}\mathcal{T}(E)$, the transmission $\mathcal{T}$ is determined using the Fisher-Lee relation which couples the transport to the Green's function of the full system [63,64]. The two leads are accounted for in the central device through the left (L) and right (R) self-energies $\boldsymbol{\Sigma}_{\mathrm{L}}$ and $\boldsymbol{\Sigma}_{\mathrm{R}}$. The retarded Green's function at energy E then reads

$$\mathbf{G}(E) = [E + i\eta - \mathbf{H}_{\mathrm{D}} - \boldsymbol{\Sigma}_{\mathrm{L}}(E) - \boldsymbol{\Sigma}_{\mathrm{R}}(E)]^{-1}, \quad (4)$$

where $\mathbf{H}_{\mathrm{D}}$ is the isolated Hamiltonian of the device region and $i\eta$ is a small imaginary parameter needed for numerical stability. Finally, the transmission is determined using the relation

$$\mathcal{T}(E) = \mathrm{Tr}[\boldsymbol{\Gamma}_{\mathrm{R}}(E)\mathbf{G}(E)\boldsymbol{\Gamma}_{\mathrm{L}}(E)\mathbf{G}^{\dagger}(E)], \quad (5)$$

where the $\mathbf{\Gamma}_{(\mathrm{L/R})}(E) = -2\mathrm{Im}[\mathbf{\Sigma}_{(\mathrm{L/R})}(E)]$ are the linewidths for the respective leads. Bond currents through the device at specific energies are useful quantities in establishing how current flows through different parts of the device [63]. The current between two neighboring sites i and j at the energy E is [65]

$$I_{ij}(E) = \frac{4e}{h}\mathrm{Im}\{H_{ij}[\mathbf{G}(E)\mathbf{\Gamma}_L(E)\mathbf{G}^*(E)]_{ij}\}, \quad (6)$$

where $H_{ij} = [\mathbf{H}]_{ij}$ is the hopping term between the sites i and j. The transport calculations use both approximative recursive Green's function techniques to determine the lead self-energies and exact techniques for the device region to significantly speed up calculations, following Ref. [63].

A. Transmission

We consider two illustrative examples, the {16,3} and {16,6} GOALs. From previous sections, we recall that the {16,3} and {16,6} GOALs exhibit bilayerlike and single-layer-like dispersions, respectively. The transmissions between bilayer graphene leads connected to the {16,3} and the {16,6} GOAL devices are shown by solid blue lines in Figs. 9(a) and 9(b), respectively. These transmissions are compared with pristine single- and bilayer graphene transmission, shown by dashed black and dotted gray lines, respectively. Close to the Fermi energy, the transmission of the {16,3} GOAL appears very similar to the pristine bilayer case, but with a slightly smaller magnitude. This is consistent with the bilayerlike dispersion of the {16,3} GOAL. In contrast, the {16,6} GOAL transmission appears very similar to that of single-layer graphene. The qualitative transition from bilayerlike to single-layer-like transport behavior as a function of isolated GAL band gap is similar to that previously noted for the band dispersion. Furthermore, an oscillatory behavior is observed which is particularly apparent for the {16,6} transmission. By increasing the number of antidot rows beyond seven (not shown) the transmissions yield an increased oscillation frequency, suggesting a Fabry-Perot like interference between scatterings at the lead-device interfaces. The low transmission valleys just above $|E| \approx 0.2$ eV, which are present for both GOALs, appear at the end of the linear dispersion region and the onset of higher order bands.

The transmission between single-layer graphene leads coupled to the graphene layer of the GOALs is shown in Figs. 9(c) and 9(d) (solid blue lines), compared again to pristine single- and bilayer graphene transmission (dashed black and dotted gray lines, respectively). The transmission through the graphene layer of the {16,3} GOAL is much lower than single-layer graphene transmission. This generally occurs for GOALs containing small-gap GAL layers due to wave mismatching, where the single-layer nature of the incoming wave is mismatched with the propagating bilayer waves in the GOAL device. We note that this also occurs in cases of bilayer graphene leads coupled to extremely large GAL gapped GOALs, e.g., like {12,5} where the incoming bilayer wave is mismatched with the single-layer nature of the GOAL device. However, in the {16,6} GOAL, the layers are sufficiently decoupled to have single-layer-like propagating states, thus yielding a single-layer-like transmission. Likewise,
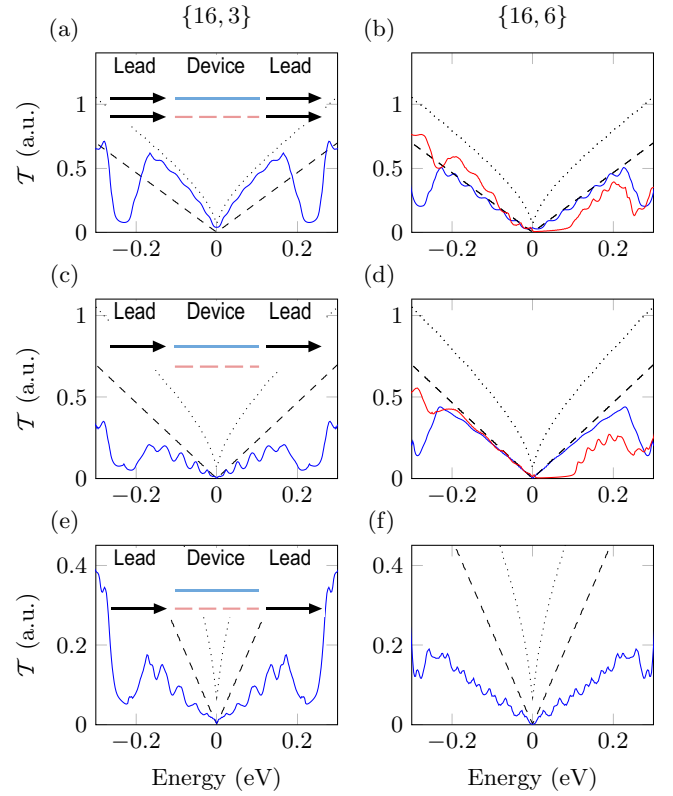

FIG. 9. (Color online) The transmission through {16,3} and {16,6} GOALs. The couplings are displayed in the insets of the left panels. (a,b) Transport between two bilayer graphene leads through a central {16,3} and {16,6} GOAL device, respectively. (c,d) transport between two single-layer graphene leads through a central {16,3} and {16,6} GOAL device coupling into the graphene layer, respectively. (e,f) transport between two single-layer graphene leads through a central {16,3} and {16,6} GOAL device coupling into the GAL layer, respectively. The central devices of [(a), (c), and (e)] and [(b), (d), and (f)] have the same widths, receptively. The transmissions are displayed in solid blue lines along with pristine single- and bilayer graphene transmission, dashed black and dotted gray lines, respectively. Additionally, (b) and (d) display transmission through a biased {16,6} GOAL device coupled to bilayer graphene leads or single-layer graphene leads coupled to the graphene layer, respectively, in solid red lines.

the Fabry-Perot oscillations have disappeared signifying lowered interface scattering, while they remain for the {16,3} GOAL. The transmission between single-layer leads coupled to the GAL layer of {16,3} and {16,6} GOALs is shown in Figs. 9(e) and 9(f), respectively. In this case, the transmissions for both GOAL devices are lower than that of single-layer graphene. The current must flow through either the GAL layer or couple in to and out of the graphene layer, which limits the transmission by the GAL band gap or the interlayer couplings.

Finally, we consider the {16,6} GOAL devices with an applied bias of $U = 0.2$ eV. The single layer and bilayer contact transmissions are illustrated in Figs. 9(b) and 9(d) by red solid lines. The band gap of the GOAL system forms a corresponding transport gap, effectively providing a SLG-like material with a tunable transport gap. The optimal

configuration for injecting current into a GOAL-based device should contact both layers, e.g., a side-contacted device.

B. Bond currents

In order to clarify the single-layer-like transport of GOALs, we now examine the bond currents in the systems studied above. We distinguish between in-plane and out-of-plane currents; currents flowing within either layer or currents flowing between the layers, respectively. The model is the same as for the transmission illustrated in Fig. 8, where semi-infinite leads are coupled to a central GOAL device.

We consider the two cases where GOAL devices displayed transmissions similar to single-layer graphene, i.e., the {16,6} GOAL device connected to either bilayer graphene leads or single-layer graphene leads which couple to the graphene layer only. We illustrate current maps of the {16,6} GOAL device at the energy $E = 0.1$ eV in Fig. 10. In Fig. 10(a) the currents of the {16,6} GOAL device coupled to the bilayer leads is shown. We plot the in-plane currents in each layer of the GOAL device separately, and show those of the graphene layer above those of the GAL layer. These currents are displayed as vector maps, which are scaled relative to the maximum current in both layers. The most notable feature of the in-plane currents of the {16,6} GOAL device with bilayer leads is the confinement of the current to the graphene layer throughout most of the device. The out-of-plane current components are shown below the in-plane components as normalized color maps. Blue shading represents for current flow from the GAL layer to the graphene layer, whilst red represents current from graphene layer to GAL layer. This map displays a large current entering the graphene layer at the left interface and leaving at the right, yielding largely single-layer current transport. The current within the GAL layer is not zero, and as the energy E is increased the current within the GAL layer increases in magnitude. The current thus becomes more and more bilayerlike as the energy of transport in increased, consistent with moving away from the band gap of the GAL layer. In Fig. 10(b), the bond currents in the {16,6} GOAL device with a graphene layer connection to the single-layer leads are shown. The in plane currents in this case also display noticeable confinement in the graphene layer. However, in this case, we observe that the in-plane current within the GAL layer is significantly larger. The out-of-plane current map suggests the current flows to the GAL layer near the left electrode and oscillates between the two layers near antidot edges, before returning to the graphene layer at the right electrode. In both of these transport configurations, the current is largely confined to the graphene layer, yielding a transmission similar to, but slightly smaller than, single-layer transport.

Another interesting behavior occurs in the final case of single-layer leads connected to the GAL layer, illustrated in Fig. 10(c). In this case, the transport currents in a {16,6} GOAL exhibit large edge currents within the graphene layer along the transverse (periodic) direction. This behavior is a consequence of the high localization at every other corner in the hexagonal antidots, see Fig. 5, such that the zigzag transport direction will always scatter the current asymmetrically along the transverse direction. If the same calculation is done along
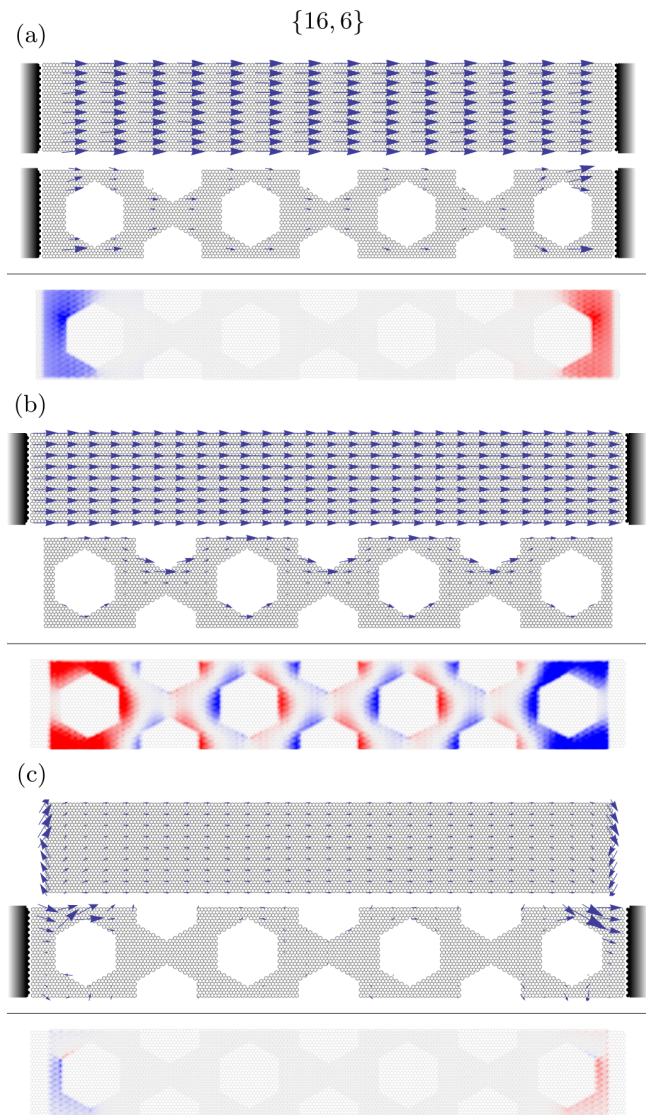

FIG. 10. (Color online) Current maps of GOAL transport devices. In all panels, the in-plane current maps are displayed separately, the graphene layer above the GAL layer, and the out of plane current maps are displayed below. The in plane currents are displayed as relative vectors scaled with the maximum in plane current within both layers. The out of plane currents are displayed as shaded areas colored according to the value, blue shading indicates current from the GAL layer into the graphene and red vice versa. (a) The current maps of the {16,6} GOAL device coupled to bilayer graphene leads. (b) The current maps of the {16,6} GOAL device coupled from the graphene layer to single-layer graphene leads. (c) The current maps of the {16,6} GOAL device coupled from the GAL layer to single-layer graphene leads.

the armchair transport-direction, the scattering at the corners is symmetric and one finds much smaller and symmetric transverse currents. Even though the transmission here is far smaller than single-layer graphene transport, the high transverse currents induced in the graphene layer suggest that interesting interlayer transport couplings may be possible.

V. DISCUSSION AND CONCLUSION

In this work, we have studied the electronic and transport properties of an all-carbon bilayer heterostructure consisting of a layer of pristine graphene atop a layer of nanostructured graphene. In order to determine the general properties of such a heterostructure, we considered antidots as the ideal testbed, where structurally similar configurations yield entirely different single-layer properties. These antidots were arranged into a triangular, or rotated triangular, superlattice orientation, yielding respectively gapped and gapless antidot layers. The electronic properties of the unbiased composite GOAL structures were seen to depend critically on the existence of this band gap in the isolated GAL layer. A gapped GAL layer, regardless of superlattice orientation, will push electronic states into the graphene layer. This is evident from the graphene layer confinement of the density of states, shown in Fig. 6(c), which increases with the GAL band gap. As a consequence, the sublattice distribution of states seen in bilayer graphene is broken. Instead, we find an approximately even distribution of states between sublattices in the graphene layer, i.e., dimers as well as nondimers. Upon increasing the graphene layer confinement, the GOAL dispersion becomes linear near the Dirac point, and furthermore, the Fermi velocity increases until (at high GAL band gaps) it resembles that of pristine single-layer graphene. Conversely, if the isolated GAL layer does not contain a gap, the GOAL composite retains a bilayerlike dispersion, except for a slight renormalization of the Fermi velocity. The electronic state distribution in such GOALs is unchanged in the graphene layer, i.e., entirely located on nondimers, while it is redistributed amongst the remaining sites in the GAL layer in a manner that conserves the pristine bilayer sublattice asymmetry. The dependence on the gap, and not directly the superlattice orientation or dimension, suggests a generality beyond this particular heterostructure.

Introducing an interlayer bias to the GOALs with single-layer-like dispersion induces band gaps smaller than those predicted for pristine bilayer graphene. The GOAL band gap size decreases as the band gap of its associated isolated GAL layer is increased. While GOALs with large-gap GAL layers have significantly reduced band gaps in the combined GOAL systems, specific GOAL structures were seen to exhibit both SLG-like dispersion and a sizable, tunable band gap. Certain structures, such as the {16,6} and {12,4} GOALs, were identified which retained a high Fermi velocity in the unbiased case and sizable band gap in the biased case. Additionally, these GOAL systems when biased display gapped graphenelike bands, as opposed to the "mexican hat" shape bands of bilayer graphene. The consequence is higher electron velocities than those in regular gapped bilayer graphene, which is of great interest in high-speed electronics. Introducing a band gap in bilayer systems has been successfully done in experiments [36,56,66], and our results suggest a possibility of manipulating and fine tuning similar electronic behavior by nanostructuring of one of the layers.

In this work, we have limited our study to Bernal-stacked GOAL systems and to the most important coupling parameters, the intralayer hopping γ_0 and interlayer hopping γ_1. Nonetheless, we expect more elaborate models to show the same qualitative results. The inclusion of additional interlayer couplings, responsible for electron-hole asymmetry and trigonal warping [35], causes only a minor splitting of the bands near the Dirac point into two separate linear bands with slightly different Fermi velocities. While this effect is more pronounced in GOALs with gapless or smaller gap GAL layers, our focus is mainly on the more interesting single-layer-like GOALs with larger gap GAL layers. It would however be very interesting to verify or modify these parameters through the use of *ab initio* calculations specifically for GOALs. Additionally, we employ a simple uniform potential distribution to describe the bias, which neglects edge effects that are likely to arise in these structures. Given the intricate edge distribution of the density of states, the correct potential distribution may induce changes in the band edges of biased GOALs. We also do not employ disorder or twisting of the GOAL systems. In the case of disorder, this tends to decrease the band gap on an isolated GAL system. The dispersion of the corresponding GOALs may exhibit transitions towards bilayerlike dispersion. However, antidots with a hexagonal armchair shapes display higher stability against disorder than circular or hexagons with extended zigzag edges [24]. By using experimental methods that prefer armchair edged shapes, this transition can be limited. In case of twisting, models have been developed to illustrate what effect a small-angle twist has on the electronic properties in pristine twisted bilayer graphene [34,67]. Depending on the angle, the dispersion relations of twisted bilayers range from the parabolic bands of Bernal-stacked bilayer graphene to linear bands with a low Fermi velocity [67]. In the case of GOAL-based systems, the effect might be similar, i.e., decreasing the Fermi velocity. Furthermore, when the twisted bilayer graphene dispersion becomes linear the application of a perpendicular electric field is no longer guaranteed to open a band gap [34]. As such, the inclusion of a twist angle would require a more extensive study.

We have also studied transport properties including different contact configurations. The transmission through GOALs exhibiting single-layer-like dispersion has approximatively the same magnitude as transmission through pristine graphene. Furthermore, the current flow was largely confined to the graphene layer of the GOAL. This follows from the electronic transport in pristine biased bilayer graphene, which depends greatly on the sublattice balances of the system. The current density is greatest in the layer where the charge density is distributed equally across nondimers and dimers [37]. The transport properties of GOALs also depend greatly on the type of contact to the device, similar to the case of pristine bilayer graphene [61,62]. As the GOALs are bilayer materials, their propagating waves are also usually bilayer, albeit largely confined in the graphene layer. This holds true except at very large GAL band gaps. As such, GOALs display the highest transmission when coupling to bilayer graphene leads. Unlike isolated GAL devices, the GAL layer of a GOAL device does not act as a barrier for transport. Instead, the graphenelike transmission should be viewed as a result of *mostly* single-layer confinement of the propagating states. Coupling from single-layer leads, the mismatch between the incoming single-layer states and bilayerlike device states gives rise to increased interface scattering. Except for very large GAL band gaps, this leads to transmissions below that

of single-layer graphene. The transmissions through GOAL devices with large-gapped GAL layers resemble that of SLG, suggesting single-layer-like propagation states. In contrast to this, where single-layer leads connect only to the GAL layer the transmission is always low. Both the lead/device wave mismatch and the current flow between the layers lead to the reduced transmission. Furthermore, in these cases, the transport can display significant transverse currents within the graphene layer due to asymmetric scattering at hole edges. For realistic devices, the best transmission is gained by injecting current into both layers, e.g., a side contact.

In this study, we have demonstrated that the bilayer heterostructure can exhibit single-layer-like behavior similar to that of pristine graphene, while still allowing a tunable band gap. The bilayers in this paper are seen to display a critical dependence on the band gap within the nanostructured layer. All results suggest that, as this band gap is increased, the electronic states localize in the pristine layer, which yields monolayer behavior. From this, we expect that such a bilayer, with a gapless and a gapped layer, will transition from monolayer to bilayer behavior as the band gap within the gapped layer decreases. Modifications, which decrease such a gap may include structural defects, disorder and other imperfections, which in turn would lead to more bilayerlike

behavior. Many of the features discussed in this work may also be of relevance to other instances of 2D heterostructures where a metallic or semimetallic layer is coupled to a semiconducting or insulating layer. We expect that in these cases a similar interplay between the electronic properties of the individual layers, and the redistribution of states when they are stacked, will determine the electronic and transport properties. Such similar bilayer systems could include other forms of patterning of the nanostructured, e.g., with dopants [42–44,68], absorbants [15,45,46], or a Moiré potentials arising from coupling to a substrate [69]. Given the intense research currently underway in the field of nanostructured graphene, and the recent experimental progress in 2D heterostructure stacking, we believe that this type of composite system could bring interesting possibilities yet unseen in pristine graphene systems.

[1] A. K. Geim and K. S. Novoselov, Nat. Mater. **6**, 183 (2007).

[2] A. H. Castro Neto, N. M. R. Peres, K. S. Novoselov, and A. K. Geim, Rev. Mod. Phys. **81**, 109 (2009).

[3] F. Xia, D. B. Farmer, Y.-M. Lin, and P. Avouris, Nano Lett. **10**, 715 (2010).

[4] F. Schwierz, Proc. IEEE **101**, 1567 (2013).

[5] F. Schwierz, Nat. Nanotechnol. **5**, 487 (2010).

[6] M. Y. Han, B. Özyilmaz, Y. Zhang, and P. Kim, Phys. Rev. Lett. **98**, 206805 (2007).

[7] K. Nakada, M. Fujita, G. Dresselhaus, and M. S. Dresselhaus, Phys. Rev. B **54**, 17954 (1996).

[8] L. Brey and H. A. Fertig, Phys. Rev. B **73**, 235411 (2006).

[9] M. Ezawa, Phys. Rev. B **73**, 045432 (2006).

[10] V. M. Pereira, A. H. Castro Neto, and N. M. R. Peres, Phys. Rev. B **80**, 045401 (2009).

[11] V. M. Pereira and A. H. Castro Neto, Phys. Rev. Lett. **103**, 046801 (2009).

[12] J. G. Pedersen and T. G. Pedersen, Phys. Rev. B **85**, 235432 (2012).

[13] T. Low, F. Guinea, and M. I. Katsnelson, Phys. Rev. B **83**, 195436 (2011).

[14] M. Neek-Amal, L. Covaci, and F. M. Peeters, Phys. Rev. B **86**, 041405 (2012).

[15] R. Balog, B. Jørgensen, L. Nilsson, M. Andersen, E. Rienks, M. Bianchi, M. Fanetti, E. Laegsgaard, A. Baraldi, S. Lizzit, Z. Sljivancanin, F. Besenbacher, B. Hammer, T. G. Pedersen, P. Hofmann, and L. Hornekaer, Nat. Mater. **9**, 315 (2010).

[16] P. A. Denis, Chem. Phys. Lett. **492**, 251 (2010).

[17] T. G. Pedersen, C. Flindt, J. G. Pedersen, N. A. Mortensen, A.-P. Jauho, and K. Pedersen, Phys. Rev. Lett. **100**, 136804 (2008).

[18] R. Petersen, T. G. Pedersen, and A.-P. Jauho, ACS nano **5**, 523 (2011).

[19] J. G. Pedersen, T. Gunst, T. Markussen, and T. G. Pedersen, Phys. Rev. B **86**, 245410 (2012).

[20] T. Gunst, T. Markussen, A.-P. Jauho, and M. Brandbyge, Phys. Rev. B **84**, 155449 (2011).

[21] S. J. Brun, M. R. Thomsen, and T. G. Pedersen, J. Phys.: Condens. Matter **26**, 265301 (2014).

[22] M. R. Thomsen, S. J. Brun, and T. G. Pedersen, J. Phys.: Condens. Matter **26**, 335301 (2014).

[23] S. Yuan, R. Roldán, A.-P. Jauho, and M. I. Katsnelson, Phys. Rev. B **87**, 085430 (2013).

[24] S. R. Power and A.-P. Jauho, Phys. Rev. B **90**, 115408 (2014).

[25] M. Kim, N. S. Safron, E. Han, M. S. Arnold, and P. Gopalan, Nano Lett. **10**, 1125 (2010).

[26] M. Kim, N. S. Safron, E. Han, M. S. Arnold, and P. Gopalan, ACS nano **6**, 9846 (2012).

[27] F. Oberhuber, S. Blien, S. Heydrich, F. Yaghobian, T. Korn, C. Schuller, C. Strunk, D. Weiss, and J. Eroms, Appl. Phys. Lett. **103**, 143111 (2013).

[28] A. J. M. Giesbers, E. C. Peters, M. Burghard, and K. Kern, Phys. Rev. B **86**, 045445 (2012).

[29] J. Eroms and D. Weiss, New J. Phys. **11**, 095021 (2009).

[30] T. Shen, Y. Q. Wu, M. A. Capano, L. P. Rokhinson, L. W. Engel, and P. D. Ye, Appl. Phys. Lett. **93**, 122102 (2008).

[31] J. Bai, X. Zhong, S. Jiang, Y. Huang, and X. Duan, Nat. Nanotechnol. **5**, 190 (2010).

[32] Q. Xu, M.-Y. Wu, G. F. Schneider, L. Houben, S. K. Malladi, C. Dekker, E. Yucelen, R. E. Dunin-Borkowski, and H. W. Zandbergen, ACS Nano **7**, 1566 (2013).

[33] E. V. Castro, K. S. Novoselov, S. V. Morozov, N. M. R. Peres, J. M. B. Lopes dos Santos, J. Nilsson, F. Guinea, A. K. Geim, and A. H. Castro Neto, J. Phys.: Condens. Matter **22**, 175503 (2010).

[34] J. M. B. Lopes dos Santos, N. M. R. Peres, and A. H. Castro Neto, Phys. Rev. Lett. **99**, 256802 (2007).

[35] E. McCann and M. Koshino, Rep. Prog. Phys. **76**, 56503 (2013).

[36] T. Ohta, A. Bostwick, T. Seyller, K. Horn, and E. Rotenberg, Science **313**, 951 (2006).

[37] C. J. Páez, D. A. Bahamon, and A. L. C. Pereira, Phys. Rev. B **90**, 125426 (2014).

[38] Y. Zhang, T.-T. Tang, C. Girit, Z. Hao, M. C. Martin, A. Zettl, M. F. Crommie, Y. R. Shen, and F. Wang, Nature (London) **459**, 820 (2009).

[39] M. Barbier, P. Vasilopoulos, and F. M. Peeters, Phil. Trans. A **368**, 5499 (2010).

[40] D. G. Kvashnin, P. Vancsó, L. Y. Antipina, G. I. Márk, L. P. Biró, P. B. Sorokin, and L. A. Chernozatonskii, Nano Res. **1**, 1 (2014).

[41] M. Killi, S. Wu, and A. Paramekanti, Phys. Rev. Lett. **107**, 086801 (2011).

[42] S. O. Guillaume, B. Zheng, J. C. Charlier, and L. Henrard, Phys. Rev. B **85**, 035444 (2012).

[43] A. J. Samuels and J. D. Carey, ACS Nano **7**, 2790 (2013).

[44] Y. Mao, G. Malcolm Stocks, and J. Zhong, New J. Phys. **12**, 033046 (2010).

[45] H. P. O. Collado, G. Usaj, and C. A. Balseiro, Phys. Rev. B **91**, 045435 (2015).

[46] A. Felten, B. S. Flavel, L. Britnell, A. Eckmann, P. Louette, J. J. Pireaux, M. Hirtz, R. Krupke, and C. Casiraghi, Small **9**, 631 (2013).

[47] A. K. Geim and I. V. Grigorieva, Nature (London) **499**, 419 (2013).

[48] D. S. Lee, C. Riedl, T. Beringer, A. H. Castro Neto, K. von Klitzing, U. Starke, and J. H. Smet, Phys. Rev. Lett. **107**, 216602 (2011).

[49] M. Dienwiebel, G. S. Verhoeven, N. Pradeep, J. W. M. Frenken, J. A. Heimberg, and H. W. Zandbergen, Phys. Rev. Lett. **92**, 126101 (2004).

[50] X. Jia, M. Hofmann, V. Meunier, B. G. Sumpter, J. Campos-Delgado, J. M. Romo-Herrera, H. Son, Y.-P. Hsieh, A. Reina, J. Kong, M. Terrones, and M. S. Dresselhaus, Science **323**, 1701 (2009).

[51] F. Pizzocchero, M. Vanin, J. Kling, T. W. Hansen, K. W. Jacobsen, P. Bøggild, and T. J. Booth, J. Phys. Chem. C **118**, 4296 (2014).

[52] T. W. Odom, J.-L. Huang, P. Kim, and C. M. Lieber, J. Phys. Chem. B **104**, 2794 (2000).

[53] F. Ouyang, S. Peng, Z. Liu, and Z. Liu, ACS Nano **5**, 4023 (2011).

[54] A. B. Kuzmenko, I. Crassee, D. van der Marel, P. Blake, and K. S. Novoselov, Phys. Rev. B **80**, 165406 (2009).

[55] J. Nilsson, A. H. Castro Neto, F. Guinea, and N. M. R. Peres, Phys. Rev. B **76**, 165416 (2007).

[56] J. B. Oostinga, H. B. Heersche, X. Liu, A. F. Morpurgo, and L. M. K. Vandersypen, Nat. Mater. **7**, 151 (2008).

[57] X. Du, I. Skachko, A. Barker, and E. Y. Andrei, Nat. Nanotechnol. **3**, 491 (2008).

[58] R. T. Weitz, M. T. Allen, B. E. Feldman, J. Martin, and A. Yacoby, Science **330**, 812 (2010).

[59] L. Wang, I. Meric, P. Y. Huang, Q. Gao, Y. Gao, H. Tran, T. Taniguchi, K. Watanabe, L. M. Campos, D. A. Muller, J. Guo, P. Kim, J. Hone, K. L. Shepard, and C. R. Dean, Science **342**, 614 (2013).

[60] P. Maher, L. Wang, Y. Gao, C. Forsythe, T. Taniguchi, K. Watanabe, D. Abanin, Z. Papić, P. Cadden-Zimansky, J. Hone, P. Kim, and C. R. Dean, Science **345**, 61 (2014).

[61] J. W. González, H. Santos, M. Pacheco, L. Chico, and L. Brey, Phys. Rev. B **81**, 195406 (2010).

[62] J. W. González, H. Santos, E. Prada, L. Brey, and L. Chico, Phys. Rev. B **83**, 205402 (2011).

[63] C. H. Lewenkopf and E. R. Mucciolo, J. Comp. Electron. **12**, 203 (2013).

[64] S. Datta, *Electronic Transport in Mesoscopic Systems*, 3rd ed. (Cambridge University Press, Cambridge, 1995).

[65] A. Cresti, R. Farchioni, G. Grosso, and G. P. Parravicini, Phys. Rev. B **68**, 075306 (2003).

[66] E. V. Castro, K. S. Novoselov, S. V. Morozov, N. M. R. Peres, J. M. B. Lopes dos Santos, J. Nilsson, F. Guinea, A. K. Geim, and A. H. Castro Neto, Phys. Rev. Lett. **99**, 216802 (2007).

[67] J. M. B. Lopes dos Santos, N. M. R. Peres, and A. H. Castro Neto, Phys. Rev. B **86**, 155449 (2012).

[68] Z. Jin, J. Yao, C. Kittrell, and J. M. Tour, ACS Nano **5**, 4112 (2011).

[69] G. Giovannetti, P. A. Khomyakov, G. Brocks, P. Kelly, and J. van den Brink, Phys. Rev. B **76**, 073103 (2007).

Paper II

Robust band gap and half-metallicity in graphene with triangular perforations

Authors:
Søren Schou Gregersen, Stephen R. Power,
and Antti-Pekka Jauho

Robust band gap and half-metallicity in graphene with triangular perforations

Søren Schou Gregersen,[1,*] Stephen R. Power,[1,2,†] and Antti-Pekka Jauho[1]

[1]*Center for Nanostructured Graphene (CNG), DTU Nanotech, Department of Micro- and Nanotechnology, Technical University of Denmark, DK-2800 Kongens Lyngby, Denmark*

[2]*Department of Physics and Nanotechnology, Aalborg University, Skjernvej 4A, DK-9220 Aalborg East, Denmark*

Ideal graphene antidot lattices are predicted to show promising band gap behavior (i.e., $E_G \simeq 500$ meV) under carefully specified conditions. However, for the structures studied so far this behavior is critically dependent on superlattice geometry and is not robust against experimentally realistic disorders. Here we study a rectangular array of triangular antidots with zigzag edge geometries and show that their band gap behavior qualitatively differs from the standard behavior which is exhibited, e.g., by rectangular arrays of armchair-edged triangles. In the spin unpolarized case, zigzag-edged antidots give rise to large band gaps compared to armchair-edged antidots, irrespective of the rules which govern the existence of gaps in armchair-edged antidot lattices. In addition the zigzag-edged antidots appear more robust than armchair-edged antidots in the presence of geometrical disorder. The inclusion of spin polarization within a mean-field Hubbard approach gives rise to a large overall magnetic moment at each antidot due to the sublattice imbalance imposed by the triangular geometry. Half-metallic behavior arises from the formation of spin-split dispersive states near the Fermi energy, reducing the band gaps compared to the unpolarized case. This behavior is also found to be robust in the presence of disorder. Our results highlight the possibilities of using triangular perforations in graphene to open electronic band gaps in systems with experimentally realistic levels of disorder, and furthermore, of exploiting the strong spin dependence of the system for spintronic applications.

I. INTRODUCTION

Two-dimensional materials continually gain interest and achieve huge advances towards industrial realization in a number of fields, particularly electronics and spintronics. Graphene is the most studied material within the two-dimensional family [1] due to unique properties such as high electron mobilities [2] above 10^5 cm V^{-1} s^{-1}, gate-tunable carrier concentration [3], and predicted long spin-relaxation lengths [4] of several μm. These studies have led to substantial efforts in fabricating and processing clean graphene systems [5] as well as pushing the limits of nanostructuring, e.g., by high-resolution lithography [6,7]. To realize graphene-based electronics and in particular transistors, opening a band gap has been one of the main drivers of both theoretical and experimental work. Many studies propose using structural modifications of graphene systems, such as nanoribbons [8], or superlattice structures imposed by periodic gating [9,10] or strain [11,12], to achieve a band gap. More recent attempts have considered chemical modification through absorption, substitution, or sublattice symmetry breaking, for example, by doping [13–16]. Periodic patterning of graphene sheets, for example, periodic perforation to form so-called graphene antidot lattices (GAL) or nanomeshes, is of particular interest since theoretical predictions suggest the possibility of obtaining sizable band gaps [17,18]. Several groups have realized these structures in the laboratory [19–22]. Band gaps induced in periodically patterned graphene are however very sensitive to disorder and defects [23]. Current fabrication methods will inevitably yield systems with a significant degree of disorder. A clear

experimental signature of minibands and -gaps has yet been elusive. In the magnetic and spintronic areas, the possibility of making graphene magnetic or realizing graphene-based spintronics has also attracted a lot of attention [4]. It has been predicted that pristine graphene exhibits uniquely long spin-relaxation times [4] ~ 1 μs, although to date experiments [24–26] still find relaxation times at least two orders of magnitudes lower; reasons for this are still under debate. Inducing magnetic ordering, or at least magnetic moments, is desirable in order to achieve tunable magnetism useful for magnetic information storage or spin-manipulation devices. There have been many works, theoretical and experimental, studying magnetic moments induced by vacancy defects [27–30], adatoms [27,30,31], substrate coupling, and molecular doping [32]. Nanostructured graphene is also predicted to display significant spin polarization at certain extended edges, namely those with a zigzag (zz) geometry [33,34]. Recent experimental findings also support the prospect of magnetic zz edges even with a reasonable amount of edge roughness observed [35–37].

In this paper, we propose using superlattices of triangular shaped GALs with entirely zz edges to gain large spin polarization, as confirmed by previous *ab initio* studies [38,39]. Graphene nanostructures which contain *noncomplementary* zz edges, e.g., triangles and Christmas trees (stacked triangles), display unique global ferromagnetic order [34,38,39], as we also will illustrate for the GAL case in Sec. III B below. In contrast, *complementary* zz-edged nanostructures, e.g., zz-edged hexagons, rhombi (two triangles back to back), or straight nanoribbons, display antiferromagnetic ordering [33,34,40]. Even before spin polarization is considered, we show through our tight-binding study how zz-edged triangular antidot lattices form exceptionally robust band gaps. When the effects of spin are included, a similarly robust half-metallicity is displayed

*sorgre@nanotech.dtu.dk
†spow@nanotech.dtu.dk

near the Fermi level, allowing for only either spin up or down states at a particular energy. In contrast to the half-metallic behavior predicted for nanoribbon devices [33], triangular antidots naturally exhibit half-metallicity without the need for difficult side gates and transverse electrical fields. We envisage that triangular antidots could be fabricated, for example, through lithography using patterned hexagonal boron nitride as a mask. Hexagonal boron nitride naturally etches into triangular holes due to the different etch rates of the two species, i.e., boron and nitrogen [41]. Kinks or chirality within triangle edges may form during fabrication, but it is likely that they will still display a magnetic signature, albeit reduced, in accordance with theory for chiral graphene nanoribbons [42]. Our findings suggest a realistic path towards fabricating realistic spin polarized graphene nanostructures which could act as components in graphene-based spintronic devices.

The remainder of this paper is organized as follows. The system geometries and electronic and spin polarization models are described in Sec. II. Then we present our results in Sec. III, first considering several representative geometries in Sec. III A of both zz-edged and armchair(ac)-edged triangles without spin polarization. Next we focus on a single zz-edged antidot lattice and include spin interaction in Sec. III B. Finally we consider the robustness of our results by extending the tight-binding description in Sec. III C and by considering the effect of positional disorder in Sec. III D. In Sec. IV, we discuss our findings and other important considerations.

II. GEOMETRY AND MODEL

Rectangular arrays of triangular antidots are considered as shown schematically in Fig. 1. Specific geometries are denoted using $\{X,Y,L_{geo}\}$ where X and Y represent the interantidot spacings in the two in-plane directions, L is the side length of the triangular antidot, and the index $geo = ac$ or zz denotes the edge geometry of the triangles. X and Y take integer values and the associated antidot separations are Xa and $Y\sqrt{3}a$, respectively, where the graphene lattice constant $a = 2.46$ Å. The rectangular superlattice makes for an ideal test bed for antidot lattices. The electronic properties change qualitatively with the superlattice dimensions, e.g.,
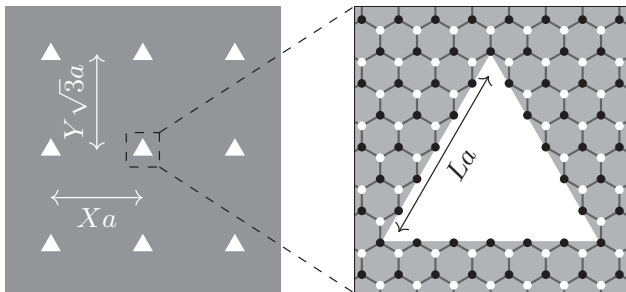
FIG. 1. Schematic of the $\{25,15,5zz\}$ triangular antidot super-lattice geometry (*left*) and the approximately square unit cell with $X = 25, Y = 15$, and $L = 5zz$-triangular antidot (*right*). The A and B sublattices of graphene are denoted by white and black circles, respectively. The antidot spacings are approximately 6 nm, and the triangular side lengths are approximately 1 nm.

a semiconducting superlattice can become metallic and vice versa by changing the unit cell dimensions by just one lattice constant [17,18,43,44]. For any periodic external potential imposed onto graphene, for example, an antidot lattice, if the Fourier transformed potential is zero at the Dirac points of pristine graphene a band gap *cannot* form. Antidot lattices for which the Fourier transformed potentials are *nonzero* at the Dirac points have sizable band gaps. This criterion is from hereon referred to as the *periodicity selection rules* [44]. For rectangular superlattices, due to the lattice orientation chosen, the periodicity selection rules depend critically on the X spacing. All antidot lattices for which $X = 3p$ where $p = 1,2,3,...$ are semiconducting, while for all other antidot lattices the existence of gaps or not depends on the particular antidot. Embedding the same triangular antidots into several rectangular superlattices which display different electronic behavior allows us to identify properties which arise due to the triangles themselves. The triangular antidots we consider are aligned to have either zz edges as shown in Fig. 1 or ac edges (not shown). The latter ac-edged triangles are rotated by 30° with respect to those in Fig. 1 and the side length is scaled differently for the two orientations. L corresponds to a side length of La for the zigzag case and $(L\sqrt{3}a)$ for the armchair case.

Spin polarization at single-point defects, as well as that at zz edges, is usually interpreted via Lieb's theorem [45]. The theorem states that the total ground state magnetic moment of a half-filled bipartite lattice is given by the sublattice imbalance, $M = \mu_B|N_A - N_B| \equiv \mu_B\Delta N$, where N_A and N_B are the number of sites belonging to each sublattice. Creating a zz triangle, such as that in Fig. 1, involves removing a different number of sites from the two sublattices and results in edge atoms belonging only to a single sublattice; with the orientation shown in Fig. 1 this is sublattice B. Accordingly, zz triangles form *nonzero* total magnetic moments, in full compliance with Lieb's theorem [38,39]. Rotating the antidot 180° flips the triangle orientation and also swaps the edge sublattice. Thus the relative edge sublattices of two adjacent triangular antidots can be determined by a quick visual inspection. The ac triangle has both sublattices present at the edge and is not expected to exhibit spin polarization [42]. We examine both the $\{X,Y,L\} = \{24,15,(5zz/3ac)\}$ and $\{25,15,(5zz/3ac)\}$ geometries; i.e., two geometries differing by a along the x direction and with either zz- or ac-edged triangular perforations; we later focus on the $\{25,15,5zz\}$ superlattice with the zz triangle displayed in Fig. 1. The side lengths of the zz- and ac-edged triangles are similar for these geometries. The two triangle orientations highlight the fundamental differences between zz-edged triangular antidots and the other antidot families represented by the ac-edged cases.

The calculations in Secs. III A and III B are performed using a nearest neighbor (NN) tight-binding Hamiltonian

$$H_\sigma = \sum_i \epsilon_{i\sigma} \boldsymbol{c}_{i\sigma}^\dagger \boldsymbol{c}_{i\sigma} + \sum_{ij} t_{ij} \boldsymbol{c}_{i\sigma}^\dagger \boldsymbol{c}_{j\sigma}. \quad (1)$$

The operator $\boldsymbol{c}_{i\sigma}^\dagger$ ($\boldsymbol{c}_{i\sigma}$) creates (annihilates) an electron with spin σ on site i, and the hopping parameter t_{ij} takes the value $t = -2.7$ eV when sites i and j are nearest neighbor sites and is zero otherwise. $|t|$ is taken as the unit of energy throughout

the paper. In Secs. III C and III D we will consider an extension to a third nearest neighbor model (3NN) by including terms $t_2 = -0.074|t|$ and $t_3 = -0.067|t|$ connecting second and third nearest neighbor sites, respectively [46]. The inclusion of t_2 results in a band-center shift, which we compensate for by adding a uniform on-site shift so that the Fermi energy lies at $E = 0$. Electron-electron interactions and the resulting spin polarization are included via spin-dependent on-site energy terms found from a self-consistent solution of the Hubbard model within the mean field approximation

$$\epsilon_{i\sigma} = \pm \frac{U}{2} m_i, \tag{2}$$

with $+$ for $\sigma = \uparrow$ and $-$ for $\sigma = \downarrow$, the on-site magnetic moments $m_i = \langle \boldsymbol{n}_{i\uparrow} \rangle - \langle \boldsymbol{n}_{i\downarrow} \rangle$, and $\boldsymbol{n}_{i\sigma}$ is the number operator. We use the on-site Hubbard parameter $U = 1.33|t|$ which has been shown to give results in good agreement with full *ab initio* calculations for nanoribbon systems [47,48]. The self-consistent Hubbard calculations are initiated with an antiferromagnetic guess, $m_i = \pm c$, with opposite signs used for the two sublattices A and B, and then iterated to convergence.

III. RESULTS

A. Unpolarized antidots with different lattice geometries

We first consider periodic structures of zz- or ac-triangular antidots in the $U = 0$ case. The band structures of zz and ac-triangular antidots, together with their total density of states and that projected onto the (edge) B sublattice, are shown in Fig. 2. The zz cases shown in Figs. 2(a) and 2(b) for the {24,15,5zz} and {25,15,5zz} geometries, respectively, display both sizable band gaps and dispersionless midgap states. The fivefold degenerate midgap states originate from the single-sublattice zz edges. The level of degeneracy is equal to the sublattice imbalance ΔN, which also equals the number of zz chains along the triangle edges $L = 5$. Similar midgap states are also observed in other noncomplementary zz-edged nanostructures, e.g., triangular quantum dots [49–51] and wide nanoribbons [46,52], where the degeneracy is proportional to the global sublattice imbalance in the quantum dots, and to the local imbalance in the wide nanoribbons. Such zz-edge states are localized on the edge sublattice. Within the NN approximation states localized in a single sublattice remain completely dispersionless. If higher order hopping parameters are included, such states can also become dispersive, as we will discuss in Sec. III C below.

The other characteristic of zz-edged triangular antidot lattices apparent from Figs. 2(a) and 2(b) is the formation of large electronic band gaps surrounding the dispersionless midgap states. In comparison, the ac cases shown in Figs. 2(c) and 2(d) reveal that the {24,15,3ac} is gapped and the {25,15,3ac} is metallic. These are in full compliance with periodicity selection rules, which in rectangular lattices predicts bands gaps only for cases with $X = 3p$. The zz-triangular antidots with large band gaps regardless of X indicate a different band gap mechanism. This hypothesis is supported by examining the band gaps of several triangular antidot lattices.
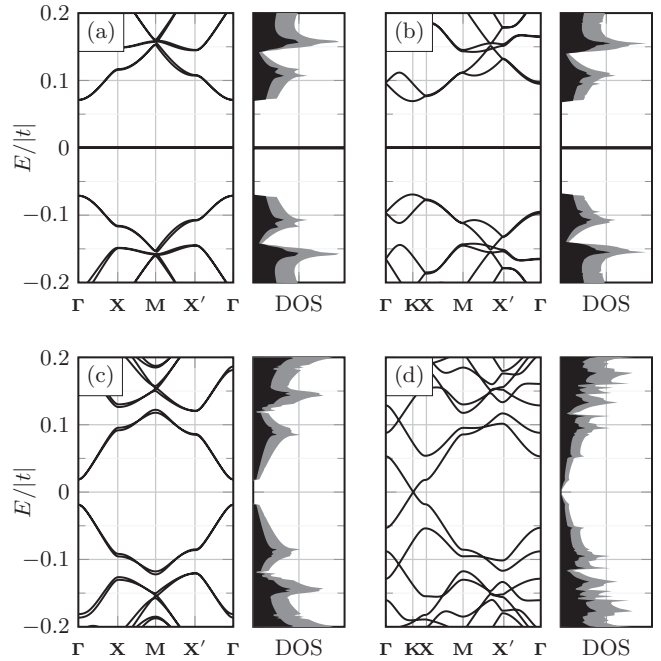
FIG. 2. Unpolarized band structures and densities of states (DOS) of different triangular antidot systems. (a) {24,15,5zz}, (b) {25,15,5zz}, (c) {24,15,3ac}, and (d) {25,15,3ac} geometries, respectively. The DOS projected onto the edge sublattice B (*black*) is shown together with the total DOS (*gray*). The structures in (a) and (b) notably show very large and narrow peaks in the DOS at the Fermi level $E = 0$.

Pedersen *et al.* demonstrated that a scaling behavior $E_{\mathrm{gap}} \propto \frac{N_{\mathrm{rem}}^{1/2}}{N_{\mathrm{tot}}} \propto \frac{L}{XY}$ was followed by many gapped graphene antidot lattices [17], where N_{rem} and N_{tot} are, respectively, the number of atoms removed to form an antidot and the total number of atoms in the superlattice unit cell before the antidot atoms are removed. In Fig. 3, a linear behavior is clearly noted for those ac-edged systems with periodicity selection rules predicting semiconducting behavior (filled green squares) whereas those for metallic superlattices (hollow green squares) have zero band gap in almost all cases. We associate the breakdown of
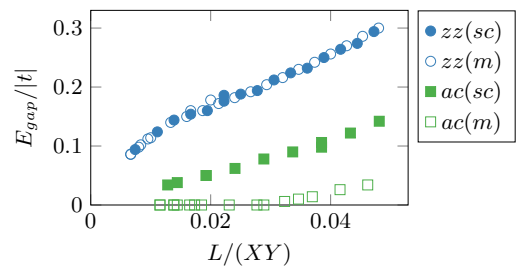

FIG. 3. Unpolarized band gaps for various geometries as the dimensionless parameters X, Y, and L are varied. The zigzag (blue) and armchair (green) triangle geometries are divided into groups where the superlattice is expected to display semiconducting (*sc*, filled) or metallic (*m*, hollow) behavior, according to the periodicity selection rules. For a rectangular superlattice this distinction depends solely on the value of X.

this trend for metallic systems with large $\frac{L}{XY}$ to large antidots in small unit cells, where additional band gap behavior is now induced by small constrictions between the antidots. The zz triangles are meanwhile consistently gapped (blue circles), irrespective of the behavior predicted by periodicity arguments. The band gap magnitude has an approximately linear dependence on $\frac{L}{XY}$, but the slope is much greater than the ac case. The reason zz-edged triangular antidot lattices are consistently gapped is the global sublattice imbalance which induces *sublattice symmetry breaking*. Independent of the periodicity selection rules, sublattice symmetry breaking imposes an effective nonzero potential between sublattices in a similar manner to a *mass* term, i.e., a staggered on-site potential, with a different on-site potential for each sublattice. In other systems where sublattice symmetry is broken, for example, by doping such a term also opens a band gap [15,16].

The sublattice-projected densities of states (DOS) for zz-triangle lattices in Figs. 2(a) and 2(b) show that each sublattice contributes equally to the DOS at all energies except at the $E = 0$ edge states which reside only on the B sublattice. However the local density of states (LDOS), shown in Fig. 4, reveals a more complex picture. The edge state localization is clear in Fig. 4(a) where the LDOS is mapped at $E = 0$ by circles whose radius is proportional to the LDOS at that site. White and black circles are used for sites on the A and B sublattices, respectively, and we note that only large black circles near the triangle edges are found at this energy. Despite the equal contributions from sublattice projected DOS at other energies, the LDOS distributes inhomogeneously around the triangles. This is shown in Fig. 4(b) for the conduction band energy $E = 0.1|t|$, where we note that the B sublattice contribution to the DOS is now spread throughout most of the unit cell, but is significantly larger near the triangle edges. The A sublattice has a vanishing LDOS in this region and its DOS contribution is mostly distributed at sites midway between neighboring antidots. The dispersion of the states at this energy is due to the large regions where both sublattices have a significant occupation. The different electron distributions for the A and B sublattices suggest different
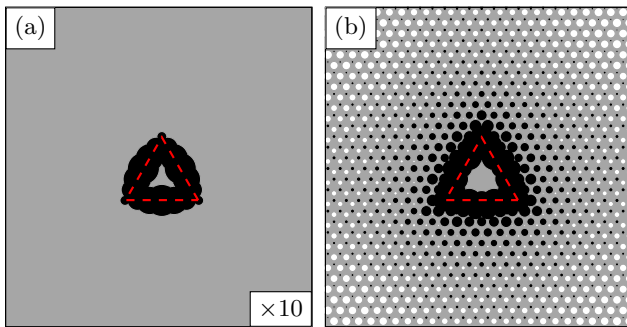
FIG. 4. Unpolarized local density of states (LDOS) of the $\{25,15,5zz\}$ system. (a) The LDOS at the energy $E = 0$ and (b) at the energy $E = 0.1|t|$. A white (black) circle is placed on every site on the A (B) sublattice, and its radius is scaled by the LDOS at that site. The zz-triangle edge is shown by a dashed red line. For clarity, the radii in (a) are reduced by a factor of 10 relative to those in (b).
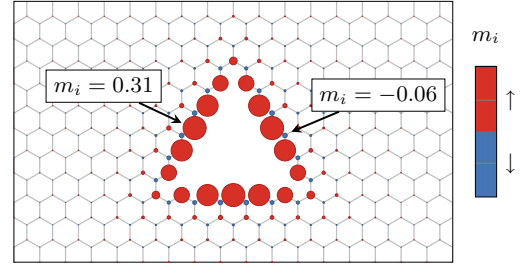
FIG. 5. The magnetic moments surrounding a triangular antidot in the $\{25,15,5zz\}$ geometry. Spin up ($m_i > 0$, red) and spin down ($m_i < 0$, blue) moments are represented by circles whose radii are scaled by $|m_i|$ at each site. The largest spin up ($m_i = 0.31$) and spin down ($m_i = -0.06$) moments are located, respectively, on an edge and on a site immediately next to the edge. The moments throughout the structure are antiferromagnetic, i.e., the sign of a moment is determined by the sublattice on which it resides.

effective scattering potentials for the different sublattices. The inhomogeneous LDOS distribution, together with the band gap formation regardless of periodicity selection rules, suggests that sublattice symmetry breaking is the driving mechanism behind band gap formation and not the periodic selection rules usually forming band gaps in graphene antidot lattices. Importantly, this suggests that band gap behavior in zz triangles should be stable against geometrical variations as long as the sublattice imbalance is maintained. Since the dimensions X and Y of the antidot lattice play a minor role, one may expect that lattices made of triangular zz-edged antidots are robust against disorder, as we discuss in Sec. III D below.

B. Effect of spin polarization

A nonzero Hubbard interaction ($U = 1.33|t|$) leads to spin dependence in zz-edged triangle systems through the formation of magnetic moments m_i.

The self-consistent solution to the Hubbard model using the $\{25,15,5zz\}$ geometry is shown in Fig. 5. Different superlattice and triangle dimensions always yield a similar pattern, namely a distribution with antiferromagnetic alignment between moments on the different sublattices. The magnitude of the moments is maximum at the zz edges, decreases slightly towards the corners of the triangles, and quickly decays perpendicular to the zz edges. Similar moment distributions have been reported in *ab initio* studies of triangular perforations [38]. Triangles with large side lengths have long segments with approximately constant magnetic moments with a maximum $m_i \sim 0.31 \ \mu_B$. Only below $L < 5$ do these constant-moment segments vanish and the maximum moment decreases. All the geometries considered are consistent with Lieb's theorem such that $M = \sum_i m_i \mu_B = \mu_B \Delta N \equiv \mu_B L$. The triangle corners are geometrically similar to the kinks arising in chiral graphene nanoribbons, which display a similar drop in moment values [42]. The magnetic moment profile is found to be almost completely independent of the superlattice geometry, suggesting that nearby triangles do not influence each other unless they are very near.

The spin-split band structure of the $\{25,15,5zz\}$ system is shown in Fig. 6(a), together with the spin up (red) and
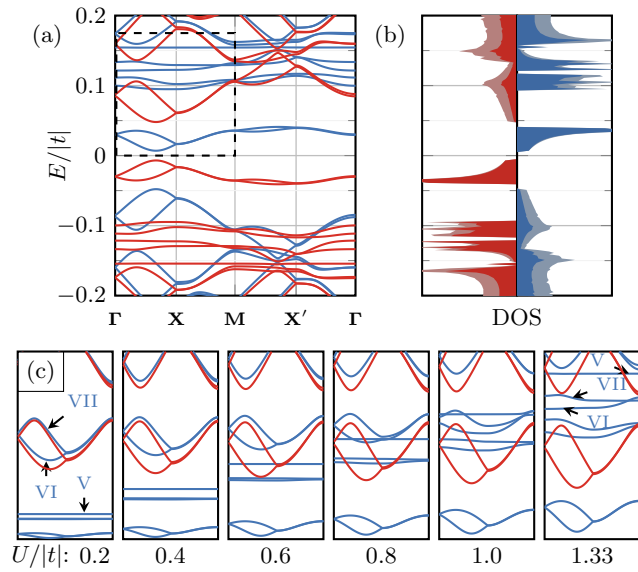
FIG. 6. The effect of Hubbard interaction U on the $\{25,15,5zz\}$ geometry. (a) The spin polarized band structures with spin up ($\uparrow$, *red*) and spin down ($\downarrow$, *blue*). (b) The densities of states. Projection on the edge sublattice B (*darker* shading, $\uparrow$: *red*, $\downarrow$: *blue*), and the total DOS (*lighter* shading, $\uparrow$: *red*, $\downarrow$: *blue*) (c) A zoom of the band structure [dashed box in (a)] for varying interaction strength $U/t = 0.2 \cdots 1.33$.

FIG. 7. Polarized LDOS of $\{25,15,5zz\}$. (a) At energy $E = 0.155|t|$, (b) $E = 0.02|t|$, (c) $E = 0.135|t|$, and (d) $E = 0.1|t|$. A white (black) circle is placed on every site on the A (B) sublattice, and its radius is scaled by the LDOS at that site. The zz-triangle edge is shown by a dashed line. For clarity, the radii in (a)–(c) are reduced by factors denoted in the *lower right corner* relative to those in (d).

spin down (blue) DOS in Fig. 6(b). As before, the lighter regions show the total DOS, and the darker regions show its projection onto the edge B sublattice. There are a number of key differences from the unpolarized band structure of the same geometry system in Fig. 2(b) compared to the spin polarized band structure in Fig. 6(a). The fivefold degenerate dispersionless bands are no longer present at zero energy, and the band gap is considerably reduced by the presence of dispersive bands at the energies $E = \pm 0.02|t|$. These bands have opposite spin orientations on either side of $E = 0$, as do the five low-dispersive nondegenerate bands in the energy range $(\pm)0.1|t| \to 0.15|t|$. To examine the formation of this band structure the Hubbard interaction U is varied from a low $U = 0.2|t|$ to $U = 1.33|t|$ in Fig. 6(c), left to right. The band structures in these panels correspond to the region shown by the dashed box in Fig. 6(a). We denote three low energy spin down bands V, VI, and VII at low Hubbard-interaction strength $U = 0.2|t|$, the fifth through seventh lowest energy spin down bands in this region. In the unpolarized band structure, band V corresponds to one of the fivefold degenerate dispersionless bands whereas VI and VII form the conduction bands. The V, VI, and VII bands are labeled both at the left- and rightmost panels for clarity. These panels reveal how the formerly degenerate and dispersionless bands undergo different degrees of spin splitting. The highest of these (V) initially at low U (left) appears below both bands VI and VII and finally at high U (right) appears above said bands. The degree of spin splitting is determined by the LDOS distribution and the magnitude of the magnetic moments. High degrees of spin splitting can be attributed to a LDOS localized around areas with large
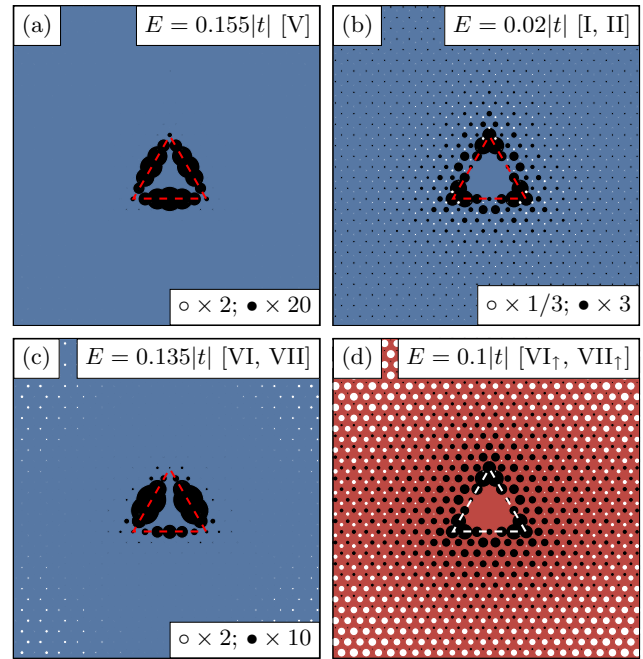
magnetic moments, which is confirmed by examining the spin polarized LDOS.

At $U = 1.33|t|$ and $E = 0.155|t|$, corresponding to the zz-edge states band V and shown in Fig. 7(a), the LDOS is localized almost entirely on magnetic edge sites, consistent with a large degree of spin splitting. Meanwhile, the LDOS of the spin polarized conduction bands at $E = 0.02|t|$ shown in Fig. 7(b) is mostly localized near the triangle corners which have smaller magnetic moments, consistent with a small degree of spin splitting. Further, the dispersion of the conduction bands is shown to emerge due to a nonzero occupation of the A sublattice as shown in Fig. 7(b). In the unpolarized case bands VI and VII define the conduction band edge, but as U increases [see Fig. 6(c)], the spin-down versions flatten and increase in energy, whereas the spin-up versions broaden and decrease slightly in energy. We noted earlier that the unpolarized cases displayed LDOS contributions from both sublattices, which overlapped to form dispersive conduction bands. When spin polarized, this distribution is quite different for each spin. The LDOS of the spin-down band shown in Fig. 7(c) is localized almost entirely on B sublattice sites near the center of the zz-edge sections, which leads to a flattening of the dispersion and an upwards energy shift. Conversely, the LDOS of the spin-up bands shown in Fig. 7(d) is localized both on the B sublattice near the antidot corners and on sites from both sublattices further away from the triangle. The more homogeneous distribution of the spin-up bands leads to further broadening and a weaker downwards shift from spin splitting.
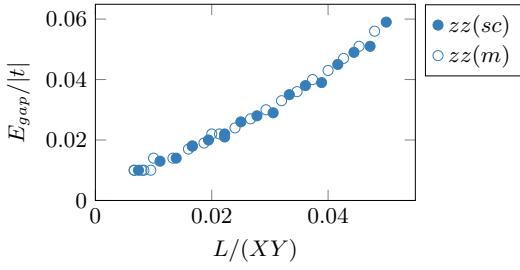
FIG. 8. Polarized band gaps for various geometries with zz-triangular antidots embedded varying X, Y, and L. The geometries are divided into groups where the superlattice is expected to display semiconducting (sc) or metallic (m) behavior, which for a rectangular superlattice depends solely on the value of X.

The band gaps for spin polarized zz triangles are shown for a range of geometries in Fig. 8, where we note a decrease of approximately one order of magnitude compared to the unpolarized cases. In fact, the gaps of semiconducting ac triangles are larger than those for polarized zz triangles. However, spin polarized zz-edged antidots display another interesting feature. The dispersive states surrounding the band gap are completely spin polarized, so that a spin-selective half-metallicity can be induced by small E_F shifts applied using a back gate. This suggests that such geometries may be employed in a range of spintronic components to filter spins of different orientations.

Many of the features we have described in both unpolarized and polarized zz triangles depend on the inhomogeneous electron distributions and in particular the localization on the edge sublattice and near zz edges. It is important to determine if such features are artifacts of the NN model we employ for our calculations and whether they are robust in the face of disorder. The latter point is of interest as many effects induced by superlattices tend to vanish at any realistic disorder [23]. We now briefly address both issues.

C. Effect of higher order hopping terms

Within the NN model, states which occupy only a single sublattice appear completely dispersionless. In comparison, a 3NN model enables intrasublattice coupling by the inclusion of the 2NN terms, and the parametrization we use has been shown to accurately describe zz nanoribbons [46]. For the unpolarized case, we note that the introduction of these additional hopping terms leads to an energy splitting of the previously degenerate midgap states, see Figs. 9(a) and 9(b). This leads to a shift of the Fermi energy relative to the bulk valence and conduction bands in order to satisfy half-filling, increasing the electron-hole asymmetry already introduced by the 2NN hoppings. The NN-model band gap can be identified in the 3NN band structure between the energies $E = -0.025|t|$ and $E = 0.1|t|$ but is now slightly smaller and more importantly contains multiple midgap states. In particular a dispersive channel opens at $E \sim 0.05|t|$, similar to that seen near zz-ribbon edges when a 3NN model is employed [53]. Disregarding these midgap states, the 3NN band gap between $E = -0.025|t|$ and $E = 0.1|t|$ scales similarly to the NN model when varying the system dimensions. The emergence of dispersive states
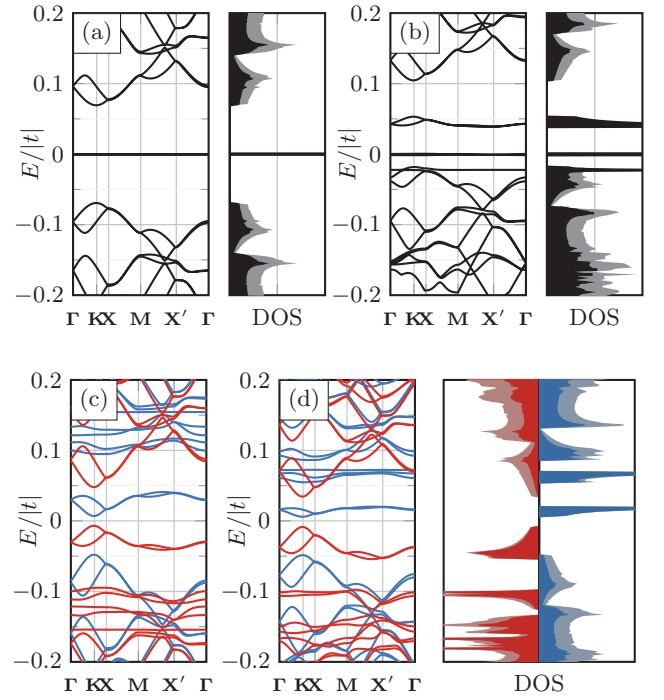
FIG. 9. Band structures for the $\{25,15,5zz\}$ geometry within first (NN) and third (3NN) nearest-neighbor tight-binding models. For NN and 3NN spin unpolarized as well as the 3NN spin polarized band structures, the DOS is also shown. (a) NN and (b) 3NN without spin polarization, (c) NN and (d) 3NN with spin polarization. (a) and (c) are reproduced from, respectively, Figs. 2(b) and 6(a). The DOS projected onto the edge sublattice B (*darker* shading, ↑: *red*, ↓: *blue*) is shown together with the total DOS (*lighter* shading, ↑: *red*, ↓: *blue*).

in the band gap could of course limit the applicability of these systems. However we note that in many cases they have either very little dispersion, or are spaced far enough apart in energy, so as to still offer reasonable band gap or transport gap behaviors.

Considering the polarized case, the band structures and DOS in Figs. 9(c) and 9(d) are remarkably similar despite the large changes we have discussed in their associated unpolarized versions. The most significant change now between NN and 3NN models is the expected (minor) electron-hole asymmetry. Notably the system remains half metallic with spin-dependent dispersive states close to the Fermi level. The excellent agreement between NN and 3NN models in this case can be understood by the fact that the features introduced by the additional 3NN terms in the unpolarized case, namely dispersion and splitting of the midgap states, also result independently from the inclusion of the spin-dependent potentials. We note that the 3NN model, both with and without spin polarization, also agrees qualitatively with previous *ab initio* calculations, which display similar band structures [38]. Although the 3NN model serves to correct the missing intersublattice interaction, it appears that the most important behavior in polarized systems is captured by the lower order NN model.

D. Robustness against disorder

One of the major obstacles in inducing band gaps using graphene antidots is that the large gaps predicted in atomically precise systems are extremely fragile in the presence of even mild geometrical disorders [23]. The gap mechanism for usual antidot arrays, namely the periodicity selection rules, relies on pristine conditions and regular antidot spacing. We have shown that zz-edged triangular antidots behave very differently from other antidots and that their behavior arises from the breaking of sublattice symmetries around individual antidots. We further demonstrated that these effects were independent of the superlattice geometry, which suggests also that they should be more stable than, for example, ac-edged antidots, in the face of disorder. While a full-fledged disorder analysis is beyond the scope of the present paper, we highlight the essential effects by examining a 4×4 geometrically disordered array of antidots in a repeated superlattice. We present one particular random configuration but also note that an additional 10 different configurations have been examined all showing qualitatively the same behavior. The triangle centers are randomly shifted by $\Delta \boldsymbol{r} = \{\delta x a, \delta y (\sqrt{3} a)\}$ with $\delta x = \delta y \leqslant 3$, as shown for zz triangles in Fig. 10(a) and ac triangles in Fig. 11(a). The same size triangles as before are considered, but for computational efficiency we use smaller $\{X = 15, Y = 9\}$ "blocks" to compose the supercell, essentially cutting down on the amount of pristine graphene between perforations. Note that according to the periodicity selection rules these superlattice geometries are predicted to form band gaps [44].

FIG. 11. (a) Schematic of a disordered 4×4 array of $\{15,9,3ac\}$ triangular antidots. (b) Band structure for a pristine system, $U = 0$. (c) Band structure for a disordered system, $U = 0$.

FIG. 10. (a) Schematic of a disordered 4×4 array of $\{15,9,5zz\}$ triangular antidots. (b) Pristine band structure. (c) Disordered system for $U = 0$. (d) Pristine system for $U = 1.33|t|$. (e) Disordered system for $U = 1.33|t|$.

Pristine band structures calculated within the 4×4 framework are shown for unpolarized and polarized $\{15,9,5zz\}$ systems in Figs. 10(b) and 10(d), respectively, and for the (unpolarized) $\{15,9,3ac\}$ system in Fig. 11(b). All calculations here were performed within the 3NN model. We note that larger gaps are present in all cases due to the reduced X and Y values and that significant folding of the bands has occurred due to the larger supercell. However the same qualitative behavior for zz edges from Fig. 9(b) and ac edges from Fig. 2(c) is evident. The gapped region in the disordered unpolarized zz-edged antidot case, Fig. 10(c), is partially quenched due to a small energy spreading of states. The polarized bands, Fig. 10(e), show even less variance relative to the ordered case. In contrast, similar levels of disorder quench the gap almost entirely for ac-edged triangles, as demonstrated in Fig. 11(c), consistent with results for other disordered antidot systems whose band gap emerges from periodicity selection rules. [23] Despite the same level of geometrical disorder, zz-edged triangles appear far more robust compared to ac-edged triangles. In comparison, the spin polarized band structure of the $\{25,15,5zz\}$ geometry, which displays smaller band gaps in Figs. 9(c) and 9(d), might in the presence disorder significantly reduce the spin polarized band gap. Nevertheless, even with reduced band gaps in the spin polarized case we expect the band gap of the unpolarized bands and the half-metallicity of the polarized bands to remain at these levels of disorder. Two additional types of disorder could have a significantly larger effect: orientation angle disorder and edge disorder. The former has the effect of dividing the triangles into smaller regions of zz edges connected by kinks. Reducing the length of the zz-edged regions will in turn reduce the sublattice symmetry breaking and the band gap formed in the superlattice. The latter type of disorder has the same effect of reducing the length of the zz-edged regions but additionally can introduce localized scatterers which could induce additional states within the previous band gap, severely reducing the final band gap of such a superlattice. What is truly different for zz-edged triangular antidots compared to, for example ac-edged antidots, is that while intra-antidot disorder like angle and edge disorder might quench the band gap of both shapes, interantidot disorder will have a much larger effect on the ac-edged antidots.

IV. CONCLUSION

We have discussed the electronic properties of triangular antidots systems in graphene sheets, with a particular focus on zigzag edged geometries whose geometry breaks the symmetry between graphene's two sublattices. In order to shed light on the possibility of magnetic states at such edges, we have analyzed systems in both the spin polarized and the unpolarized cases. We further have illustrated the robustness against disorder by individually displacing the antidots of a 4×4 array unit cell. Spin unpolarized superlattices of triangular zz-edged antidots form band gaps significantly larger than similarly sized ac-edged counterparts. Gap opening occurs irrespective of conventional rules governing the formation of band gaps in, for example, ac-edged triangular antidots and scales with the triangular antidot side length. Furthermore zz- as opposed to ac-edged triangles are far more robust against geometric disorders. We conclude that these unique features are caused by a gap-opening mechanism related to sublattice-symmetry breaking. In contrast to conventional graphene antidot lattices, this mechanism is less sensitive to experimentally unavoidable imperfections in lattice spacings. The zz-edged triangular antidots become half-metallic over a wide range of energies when spin polarization is included, with a high degree of spin selectivity achievable by gating. Spin splitting of the unpolarized band structure leads to the emergence of dispersive spin-dependent states and subsequent reduction of the band gaps compared to the unpolarized cases. The half-metallic behavior of zz-edged triangles also appears more robust against geometric disorder compared to ac-edged counterparts. These findings suggest a robust path to realize devices based on nanostructured graphene with robust band gaps. Further, devices with half-metallic and spin-selective properties appear feasible.

[1] K. S. Novoselov, V. I. Fal'ko, L. Colombo, P. R. Gellert, M. G. Schwab, and K. Kim, Nature (London) **490**, 192 (2012).

[2] A. S. Mayorov, R. V. Gorbachev, S. V. Morozov, L. Britnell, R. Jalil, L. A. Ponomarenko, P. Blake, K. S. Novoselov, K. Watanabe, T. Taniguchi, and A. K. Geim, Nano Lett. **11**, 2396 (2011).

[3] A. H. Castro Neto, N. M. R. Peres, K. S. Novoselov, and A. K. Geim, Rev. Mod. Phys. **81**, 109 (2009).

[4] W. Han, R. K. Kawakami, M. Gmitra, and J. Fabian, Nat. Nanotechnol. **9**, 794 (2014).

[5] L. Wang, I. Meric, P. Y. Huang, Q. Gao, Y. Gao, H. Tran, T. Taniguchi, K. Watanabe, L. M. Campos, D. A. Muller, J. Guo, P. Kim, J. Hone, K. L. Shepard, and C. R. Dean, Science **342**, 614 (2013).

[6] F. Oberhuber, S. Blien, S. Heydrich, F. Yaghobian, T. Korn, C. Schüller, C. Strunk, D. Weiss, and J. Eroms, Appl. Phys. Lett. **103**, 143111 (2013).

[7] Q. Xu, M.-Y. Wu, G. F. Schneider, L. Houben, S. K. Malladi, C. Dekker, E. Yucelen, R. E. Dunin-Borkowski, and H. W. Zandbergen, ACS Nano **7**, 1566 (2013).

[8] M. Y. Han, B. Özyilmaz, Y. Zhang, and P. Kim, Phys. Rev. Lett. **98**, 206805 (2007).

[9] J. G. Pedersen and T. G. Pedersen, Phys. Rev. B **85**, 235432 (2012).

[10] T. Low, F. Guinea, and M. I. Katsnelson, Phys. Rev. B **83**, 195436 (2011).

[11] V. M. Pereira and A. H. Castro Neto, Phys. Rev. Lett. **103**, 046801 (2009).

[12] V. M. Pereira, A. H. Castro Neto, and N. M. R. Peres, Phys. Rev. B **80**, 045401 (2009).

[13] R. Balog, B. Jørgensen, L. Nilsson, M. Andersen, E. Rienks, M. Bianchi, M. Fanetti, E. Laegsgaard, A. Baraldi, S. Lizzit, Z. Sljivancanin, F. Besenbacher, B. Hammer, T. G. Pedersen, P. Hofmann, and L. Hornekaer, Nat. Mater. **9**, 315 (2010).

[14] P. A. Denis, Chem. Phys. Lett. **492**, 251 (2010).

[15] A. Lherbier, A. R. Botello-Méndez, and J.-C. Charlier, Nano Lett. **13**, 1446 (2013).

[16] T. Aktor, A.-P. Jauho, and S. R. Power, Phys. Rev. B **93**, 035446 (2016).

[17] T. G. Pedersen, C. Flindt, J. G. Pedersen, N. A. Mortensen, A.-P. Jauho, and K. Pedersen, Phys. Rev. Lett. **100**, 136804 (2008).

[18] F. Ouyang, S. Peng, Z. Liu, and Z. Liu, ACS nano **5**, 4023 (2011).

[19] J. Eroms and D. Weiss, New J. Phys. **11**, 095021 (2009).

[20] J. Bai, X. Zhong, S. Jiang, Y. Huang, and X. Duan, Nat. Nanotechnol. **5**, 190 (2010).

[21] M. Kim, N. S. Safron, E. Han, M. S. Arnold, and P. Gopalan, Nano Lett. **10**, 1125 (2010).

[22] A. J. M. Giesbers, E. C. Peters, M. Burghard, and K. Kern, Phys. Rev. B **86**, 045445 (2012).

[23] S. R. Power and A.-P. Jauho, Phys. Rev. B **90**, 115408 (2014).

[24] N. Tombros, C. Jozsa, M. Popinciuc, H. T. Jonkman, and B. J. van Wees, Nature (London) **448**, 571 (2007).

[25] W. Han, K. Pi, K. M. McCreary, Y. Li, J. J. I. Wong, A. G. Swartz, and R. K. Kawakami, Phys. Rev. Lett. **105**, 167202 (2010).

[26] M. V. Kamalakar, C. Groenveld, A. Dankert, and S. P. Dash, Nat. Commun. **6**, 6766 (2015).

[27] O. V. Yazyev and L. Helm, Phys. Rev. B **75**, 125408 (2007).

[28] J. J. Palacios, J. Fernández-Rossier, and L. Brey, Phys. Rev. B **77**, 195428 (2008).

[29] R. R. Nair, M. Sepioni, I.-L. Tsai, O. Lehtinen, J. Keinonen, A. V. Krasheninnikov, T. Thomson, A. K. Geim, and I. V. Grigorieva, Nat. Phys. **8**, 199 (2012).

[30] K. M. McCreary, A. G. Swartz, W. Han, J. Fabian, and R. K. Kawakami, Phys. Rev. Lett. **109**, 186604 (2012).

[31] S. R. Power, V. M. de Menezes, S. B. Fagan, and M. S. Ferreira, Phys. Rev. B **84**, 195431 (2011).

[32] J. Hong, E. Bekyarova, P. Liang, W. A. de Heer, R. C. Haddon, and S. Khizroev, Sci. Rep. **2**, 624 (2012).

[33] Y.-W. Son, M. L. Cohen, and S. G. Louie, Nature (London) **444**, 347 (2006).

[34] D. Yu, E. M. Lupton, H. J. Gao, C. Zhang, and F. Liu, Nano Research **1**, 497 (2008).

[35] C. Tao, L. Jiao, O. V. Yazyev, Y.-C. Chen, J. Feng, X. Zhang, R. B. Capaz, J. M. Tour, A. Zettl, S. G. Louie, H. Dai, and M. F. Crommie, Nat. Phys. **7**, 616 (2011).

[36] T. Hashimoto, S. Kamikawa, D. Soriano, J. G. Pedersen, S. Roche, and J. Haruyama, Appl. Phys. Lett. **105**, 183111 (2014).

[37] G. Z. Magda, X. Jin, I. Hagymási, P. Vancsó, Z. Osváth, P. Nemes-Incze, C. Hwang, L. P. Biró, and L. Tapasztó, Nature (London) **514**, 608 (2014).

[38] J. A. Fürst, T. G. Pedersen, M. Brandbyge, and A.-P. Jauho, Phys. Rev. B **80**, 115117 (2009).

[39] X. H. Zheng, G. R. Zhang, Z. Zeng, V. M. García-Suárez, and C. J. Lambert, Phys. Rev. B **80**, 075413 (2009).

[40] M. L. Trolle, U. S. Møller, and T. G. Pedersen, Phys. Rev. B **88**, 195418 (2013).

[41] C. Jin, F. Lin, K. Suenaga, and S. Iijima, Phys. Rev. Lett. **102**, 195505 (2009).

[42] O. V. Yazyev, R. B. Capaz, and S. G. Louie, Phys. Rev. B **84**, 115406 (2011).

[43] R. Petersen, T. G. Pedersen, and A.-P. Jauho, ACS Nano **5**, 523 (2011).

[44] M. Dvorak, W. Oswald, and Z. Wu, Sci. Rep. **3**, 2289 (2013).

[45] E. Lieb, Phys. Rev. Lett. **62**, 1201 (1989).

[46] Y. Hancock, A. Uppstu, K. Saloriutta, A. Harju, and M. J. Puska, Phys. Rev. B **81**, 245402 (2010).

[47] O. V. Yazyev, Phys. Rev. Lett. **101**, 037203 (2008).

[48] O. V. Yazyev, Rep. Prog. Phys. **73**, 056501 (2010).

[49] W. Jaskólski, A. Ayuela, M. Pelc, H. Santos, and L. Chico, Phys. Rev. B **83**, 235424 (2011).

[50] A. D. Güçlü, P. Potasz, and P. Hawrylak, Phys. Rev. B **82**, 155445 (2010).

[51] W.-d. Sheng, M. Korkusinski, A. D. Güçlü, M. Zielinski, P. Potasz, E. S. Kadantsev, O. Voznyy, and P. Hawrylak, Frontiers of Physics **7**, 328 (2012).

[52] K. Nakada, M. Fujita, G. Dresselhaus, and M. S. Dresselhaus, Phys. Rev. B **54**, 17954 (1996).

[53] P.-H. Chang and B. K. Nikolić, Phys. Rev. B **86**, 041406 (2012).

Paper III

Nanostructured graphene for spintronics

Authors:
Søren Schou Gregersen, Stephen R. Power,
and Antti-Pekka Jauho

Nanostructured graphene for spintronics

Søren Schou Gregersen,[1,*] Stephen R. Power,[1,2,3,4] and Antti-Pekka Jauho[1]

[1]*Center for Nanostructured Graphene (CNG), DTU Nanotech, Department of Micro- and Nanotechnology, Technical University of Denmark, DK-2800 Kongens Lyngby, Denmark*
[2]*Department of Physics and Nanotechnology, Aalborg University, Skjernvej 4A, DK-9220 Aalborg East, Denmark*
[3]*Catalan Institute of Nanoscience and Nanotechnology (ICN2), CSIC and The Barcelona Institute of Science and Technology, Campus UAB, Bellaterra, E-08193 Barcelona, Spain*
[4]*Universitat Autnoma de Barcelona, E-08193 Bellaterra (Cerdanyola del Valls), Spain*

Zigzag edges of the honeycomb structure of graphene exhibit magnetic polarization, making them attractive as building blocks for spintronic devices. Here, we show that devices with zigzag-edged triangular antidots perform essential spintronic functionalities, such as spatial spin splitting or spin filtering of unpolarized incoming currents. Near-perfect performance can be obtained with optimized structures. The device performance is robust against substantial disorder. The gate-voltage dependence of transverse resistance is qualitatively different for spin-polarized and spin-unpolarized devices, and can be used as a diagnostic tool. Importantly, the suggested devices are feasible within current technologies.

Introduction. The weak intrinsic spin-orbit coupling and long spin diffusion lengths suggest graphene as an ideal spintronic material [1–10]. Spin splitting or filtering in graphene is predicted for half-metallic nanoribbons [2,11–13], modulated Rashba fields [14], flakes [15], chains [16], or via the spin Hall effect (SHE) [17–21]. Half-metallic systems are excellent platforms for manipulating spin due to their inherent spin filtering behavior. Self-assembled organometallic frameworks [22] and graphene-boron-nitride structures [23], point defects and hydrogenation [24–26], and, in particular, nanostructured zigzag (zz)-edged devices [11–13,15,16,27–33] are among the proposed graphene-based half metals. Spin filters have been proposed using triangular dots [15,31] or perforations [29] with many similarities, e.g., low-energy localized magnetic states and a net sublattice imbalance. However, perforations, or antidots [34–36], have the advantage over dots of being embedded in the graphene sheet which allows a wide range of spin-dependent transport properties. Although signatures of localized magnetic states have been detected [37–39], spin manipulation in graphene-based half metals has yet to be realized in experiments.

In this Rapid Communication, we investigate the transport properties of graphene devices with embedded zz-edged triangular antidots. Such devices are within the reach of state-of-the-art lithographic methods: Triangular holes in graphene have recently been fabricated [40], and experiments suggest the possibility of zz-etched nanostructures [41,42]. Another possibility is to employ a lithographic mask of patterned hexagonal boron nitride, which naturally etches into zz-edged triangular holes [43,44]. The zz-edged structures support local ferromagnetic moments [3], however, global ferromagnetism is induced when the overall sublattice symmetry of the edges is broken [11–13,16,27,28,45]. This occurs for zz-edged triangles [15,29–33]. We have recently discussed the electronic structure of triangular graphene antidot *lattices* (GALs) [33]—here, we focus on transport through devices

containing a small number of antidots. Our calculations show that large spin-polarized currents are generated by the device illustrated in Fig. 1(a). An unpolarized current incident from the left is funneled *below* the triangle if the electron spin is up (↑, red) and *above* if the spin is down (↓, blue), resulting in spin-polarized currents at contacts top (T) and bottom (B), respectively.

The sixfold symmetry of the graphene lattice allows only two orientations for zz-edged triangles. A 180° rotation exposes zz edges with magnetic moments of opposite sign. In turn, this inverts *both* the scattering directions and spin polarization simultaneously. An independent inversion of either scattering direction or spin polarization would change the direction of spin current flow, but inverting both restores the spin current flow pattern [Fig. 1(b)]. This results in robust spin behavior over a wide range of superlattice geometries. The zz-edged triangular GALs have magnetic moment distributions as shown in Fig. 1(c), and display half-metallic behavior over a wide range of energies near the Dirac point. The roles of the two spin orientations can be interchanged by gating, as shown in Fig. 1(d). The magnetic profile remains qualitatively similar when the side length is varied [insets of Fig. 1(c)], changes sign under a 180° rotation, and magnetism vanishes for the 90° rotated (armchair-edged) triangular antidot.

In analogy to (inverse) spin Hall measurements [21], we study the transverse resistance generated by a longitudinal current. Using a spin-polarized left contact we suggest a method to distinguish between magnetic or nonmagnetic antidots in such devices: The transverse resistance has a characteristic antisymmetric behavior with respect to the Fermi level only for spin-polarized antidots.

Geometry and model. The device in Fig. 1(a) consists of a central graphene region with a single triangular antidot. (Below we also consider a larger central region with an array of triangles.) The device has four arms which terminate at metallic contacts—left (L), right (R), top (T), and bottom (B)—which act as sources of either unpolarized or single spin-orientation electrons. The triangular antidots here have a side length $L_\triangle = 5a$, where the lattice constant $a = 2.46$Å. The remaining
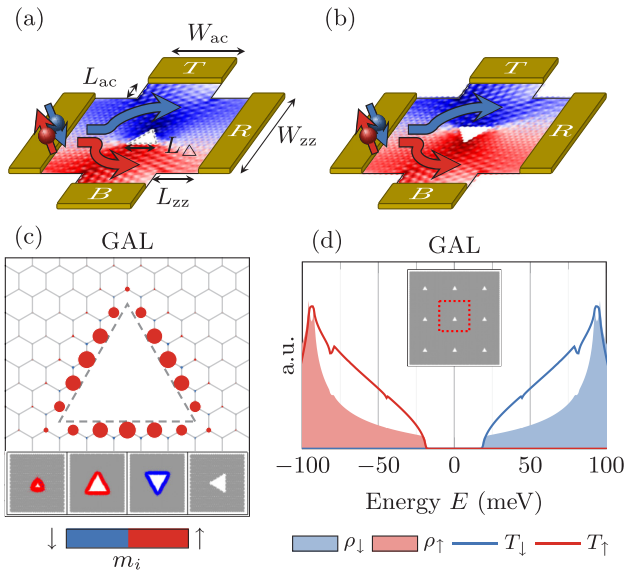
---
*sorgre@nanotech.dtu.dk

FIG. 1. Device geometry (above) and infinite antidot lattice results (below). Spin up (down) is denoted red (blue) throughout. (a) Device geometry, with $W_{ac} \approx 6$ nm, $W_{ac} \approx 4$ nm, $L_{\triangle} \approx 1$ nm, $L_{zz} \approx L_{ac} \approx 2$ nm, and spin-splitting effect with color map displaying the local spin-dependent current magnitude for spin-unpolarized injection through the left electrode (L) J_L^s. (b) Same as (a) but with a 180° rotated antidot. (c) Magnetic moment profile of the antidot lattice: Moments are represented by circles with radii $\propto |m_i|$. The inset illustrates magnetic moment profiles for, from left to right, $L_{\triangle} = 1$ nm, $L_{\triangle} = 4$ nm, rotated $L_{\triangle} = 4$ nm, and armchair-edged $L_{\triangle} = 1$ nm. (d) Spin-dependent transmissions (T_σ) and density of states (ρ_σ) of the antidot lattice. The lattice geometry is shown in the inset and has a $\sim 6 \times 6$ nm square unit cell (dotted box).

dimensions in Fig. 1(a) are given in the caption. Our previous work [33] validates the use of a nearest-neighbor tight-binding Hamiltonian $\mathcal{H}_\sigma = \sum_i \epsilon_{i\sigma} \mathbf{c}_{i\sigma}^\dagger \mathbf{c}_{i\sigma} + \sum_{ij} t_{ij} \mathbf{c}_{i\sigma}^\dagger \mathbf{c}_{j\sigma}$, to describe the electronic structure of such systems, where $\mathbf{c}_{i\sigma}^\dagger$ ($\mathbf{c}_{i\sigma}$) is a creation (annihilation) operator for an electron with spin σ on site i. The hopping parameter t_{ij} is $t = -2.7$ eV for neighbors i and j, and zero otherwise. The T and B arm widths are chosen to yield metallic behavior near the Fermi level $E = 0$.

Local magnetic moments are included via spin-dependent on-site energy terms $\epsilon_{i\sigma} = \pm \frac{U}{2} m_i$, with $-$ for $\sigma = \uparrow$ and $+$ for $\sigma = \downarrow$. The on-site magnetic moments $m_i = \langle \mathbf{n}_{i\uparrow} \rangle - \langle \mathbf{n}_{i\downarrow} \rangle$, where $\mathbf{n}_{i\sigma}$ is the number operator, are calculated from a self-consistent solution of the Hubbard model within the mean-field approximation. This is performed for the corresponding extended GAL, displayed in the inset of Fig. 1(d), which is an approximately square lattice with a $25a \times 15\sqrt{3}a$ (~ 6 nm $\times$ 6 nm) unit cell. The four short graphene arm segments are assumed to be nonmagnetic in order to isolate the magnetic influence of the antidots. An on-site Hubbard parameter $U = 1.33|t|$ gives results in good agreement with *ab initio* calculations in the case of graphene nanoribbons [3]. The sublattice-dependent alignment of moments agrees with Ruderman-Kittel-Kasuya-Yosida (RKKY) theory predictions [46,47]. Our calculations assume that this extends to
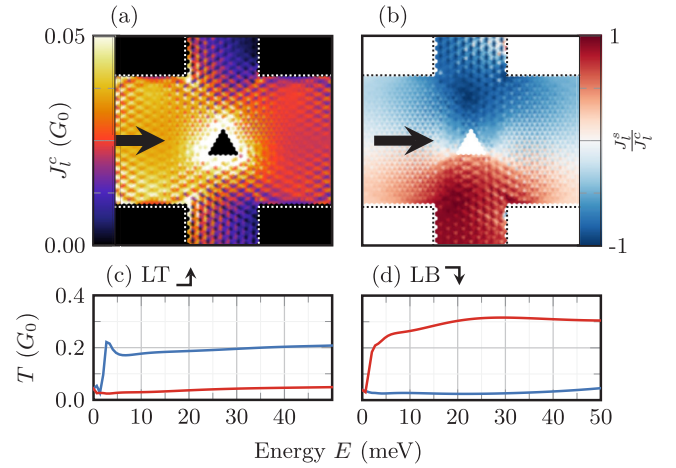
FIG. 2. (a) Local current magnitude through a device with a single triangular antidot at $E = 20$ meV. (b) Spin polarization of currents in the same system (red: spin up; blue: spin down). Bottom: Spin-dependent transmissions left top [LT, (c)] and left bottom [LB, (d)].

intertriangle alignments also. Due to the large total moment at each triangle, the intertriangle couplings should be stronger than those between, e.g., vacancy defects with similar separations.

The transmission $T_{\alpha\beta}^\sigma$ for spin σ between two leads α and β and local (bond) currents $\mathbf{J}_\alpha^\sigma$ from lead α are calculated using recursive Green's function techniques [48]. They are $T_{\alpha\beta}^\sigma(E) = \mathrm{Tr}[\mathbf{\Gamma}_\alpha \mathbf{G}_\sigma^r \mathbf{\Gamma}_\beta \mathbf{G}_\sigma^a]$ and $[\mathbf{J}_\alpha^\sigma]_{ij} = [\mathbf{H}^\sigma]_{ji} \mathrm{Im}[\mathbf{G}_\sigma^r \mathbf{\Gamma}_\alpha \mathbf{G}_\sigma^a]_{ij}$, respectively. $\mathbf{G}_\sigma^r$ ($\mathbf{G}_\sigma^a$) is the retarded (advanced) Green's function, $\mathbf{\Gamma}_\alpha = -2 \mathrm{Im}[\mathbf{\Sigma}_\alpha]$ is the broadening for lead α, $\mathbf{\Sigma}_\alpha$ is the self-energy, and i and j are indices of neighboring sites. The spin and charge transmissions and local currents are defined for independent spin channels as $T_{\alpha\beta}^s(E) = T_{\alpha\beta}^\uparrow(E) - T_{\alpha\beta}^\downarrow(E)$, $T_{\alpha\beta}^c(E) = T_{\alpha\beta}^\uparrow(E) + T_{\alpha\beta}^\downarrow(E)$, $\mathbf{J}_\alpha^s(E) = \mathbf{J}_\alpha^\uparrow(E) - \mathbf{J}_\alpha^\downarrow(E)$, and $\mathbf{J}_\alpha^c(E) = \mathbf{J}_\alpha^\uparrow(E) + \mathbf{J}_\alpha^\downarrow(E)$, respectively. The metallic leads are included via an effective self-energy $\mathbf{\Sigma}_{\mathrm{metal}} = -i|t|$ added to the edge sites of the metal/graphene interfaces [49]. For spin-polarized contacts, the self-energy for one spin channel is set to zero. The four-terminal transverse resistance R_{xy} is determined using L and R as the source and drain and T and B as voltage probes,

$$R_{xy} = V_{TB}/I_L^c. \tag{1}$$

where the transverse potential drop $eV_{TB} = \mu_T - \mu_B$. Using the Landauer-Büttiker relation, the charge currents through lead α are $I_\alpha^c = \sum_{\beta\sigma} T_{\beta\alpha}^\sigma(\mu_\alpha - \mu_\beta)$. It is assumed that spin mixing occurs in the T and B leads, yielding spin-unpolarized potentials $\mu_T^\uparrow = \mu_T^\downarrow$ and $\mu_B^\uparrow = \mu_B^\downarrow$. We apply source and drain potentials $\mu_L = eV_{LR}$ and $\mu_R = 0$, while T and B probes carry zero current, $I_T^c = I_B^c = 0$. The resistance is then determined by solving for μ_T, μ_B, and the longitudinal current.

Results and discussion. Transport properties of the system in Fig. 1(a) are presented in Fig. 2. The spatial spin separation is illustrated by the magnitude of the local charge current $J_{L,i}^c = [\mathbf{J}_L^c]_i$ and its spin polarization $J_{L,i}^s/J_{L,i}^c = [\mathbf{J}_L^s]_i/[\mathbf{J}_L^c]_i$ at $E = 20$ meV, in Figs. 2(a) and 2(b), respectively. At this energy, $\downarrow$ electrons are channeled above the antidot and $\uparrow$ electrons below it. Incoming $\uparrow$ electrons are backscattered
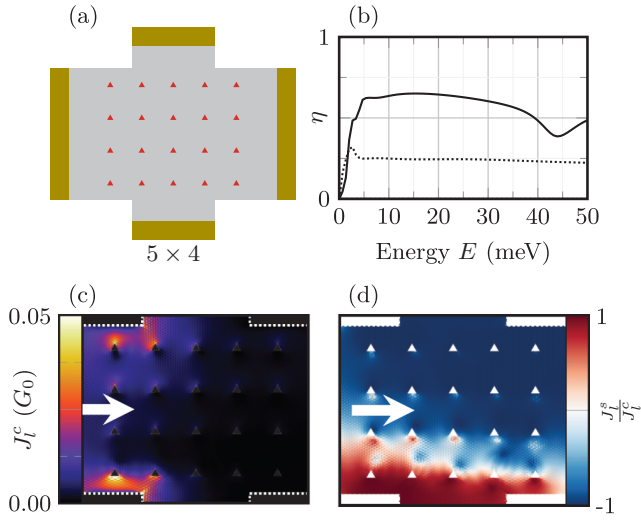
FIG. 3. (a) Schematic of the graphene cross device with a 5×4 array of triangular antidots. All triangles are oriented in the same direction with same magnetic moment profile, i.e., as in Fig. 1(c) (red triangles). $W_{zz} = 60\sqrt{3}a \approx 26$ nm and $W_{ac} = 131a/2 \approx 16$ nm. (b) The splitting efficiency, as defined in main text, of the 5×4 array (solid) and the single-antidot (dotted) devices. (c) The local charge currents and (d) spin polarization for injection from the left electrode for $E = 20$ meV (red: spin up; blue: spin down).

near the top vertex of the triangular antidot. This $\uparrow$-electron behavior is also seen for both spins in the unpolarized system, i.e., letting all $m_i \to 0$ (not shown), and is due to geometrical factors: The jagged top half of the device is a more effective backscatterer in general than the nanoribbonlike bottom half. Conversely, the $\downarrow$ behavior is the opposite: Backscattering occurs in the lower half of the device. This behavior is indicative of scattering near the bottom edge of the triangle which only occurs for $\downarrow$ electrons. This is supported by the presence of strong $\downarrow$ local density of states (DOS) features at the middle of each edge in the corresponding bulk lattice [33]. Therefore, the scattering of $\uparrow$ electrons is dictated mainly by the triangular shape of the antidot, whereas $\downarrow$ electrons are more sensitive to the magnetic profile. The L-T and L-B transmissions shown in Figs. 2(c) and 2(d) reveal that the spin polarization occurs for a broad range of energies. Thus, a single-antidot device can partially split or filter incoming currents into either T or B with a large degree of polarizations $T^s/T^c \sim 70\%-90\%$.

A 5×4 array of triangular antidots is shown in Fig. 3(a). We first assume that the magnetic moment profile is the same for each antidot [illustrated in Fig. 3(a) by red triangles] but below we relax this assumption. The electronic splitting of the spin currents can be quantified by an effective figure of merit

$$\eta = \frac{T_{LT}^{\downarrow} - T_{LT}^{\uparrow} + T_{LB}^{\uparrow} - T_{LB}^{\downarrow}}{\sum_{\sigma\alpha \neq L} T_{L\alpha}^{\sigma}}, \qquad (2)$$

where $\eta \to 1$ for perfect spatial spin splitting into T and B. The figure of merit in Fig. 3(b) is larger for the array (solid line) than for the single-antidot device (dotted line), further illustrated by the charge and spin currents at $E = 20$ meV in Figs. 3(c) and 3(d). The $\uparrow$ electrons are effectively blocked
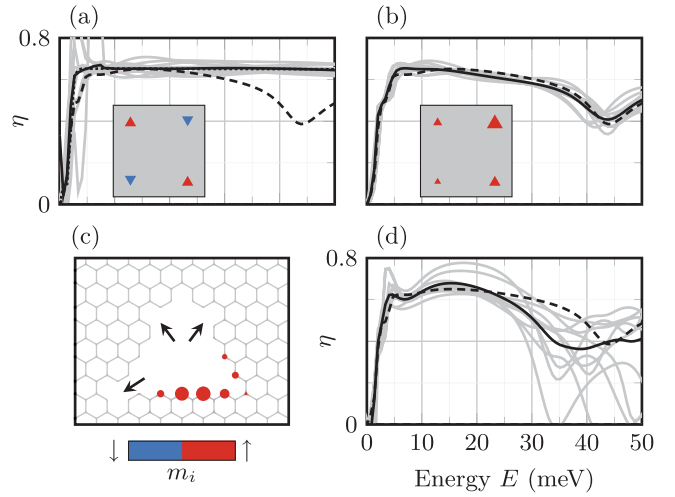
FIG. 4. (a), (b), (d) Transport splitting efficiency of 5×4 antidot arrays with different disorder. The splitting efficiency of ten disordered device realizations is shown in gray, the configurational average for each type in black, and the pristine 5×4 array in black dashed [reproduced from Fig. 3(b)]. (a) Random flipping of antidots and reversal of spin polarization (see inset). An additional array realization with every second antidot flipped ($5 \times 4_R$) is shown by the black dotted curve. (b) Random variation of side length, as in the inset. (c) Realization of an antidot with removed atoms (black arrows) and the corresponding magnetic moment profile. The moment profile here and in Fig. 1(c) are scaled equally. (d) Splitting efficiencies for antidot edge atom disorder [see (c)].

away from the array because of half metallicity at this energy, and are either backscattered, or directed towards the B contact. The $\downarrow$ electrons, on the other hand, may enter the array, but have a large probability of deflection towards the T contact due to repeated scattering of the type discussed for the single-antidot case. Thus, a large imbalance between the spin-resolved transmissions develops, with T and B polarizations $T^s/T^c \sim 99\%$ around $E = 20$ meV, and η is enhanced.

The $\downarrow$ behavior is similar to the ratchet effect previously noted for triangular perturbations in graphene [50]. The spatial spin splitting shown here is somewhat analogous to the SHE [17–21], where currents of opposite spin are pushed to the opposite edges of the device. A key distinction is that our device does not require spin-orbit coupling, or topologically protected transport channels. Even though the antidots share many similarities with regular dots, the enhanced spin splitting by repeated scattering from different antidots is difficult to envision in a dot-based system.

In experiments, disorder severely degrades properties of atomically precise antidot lattices [51]. The half metallicity of triangular GALs is unusually robust against lattice disorder [33]. In Fig. 4, we study the effect of disorder in a 5×4 antidot array using three different methods and ten realizations of each disorder type.

The first disorder type is a random flip of individual antidots, as illustrated in the inset of Fig. 4(a). The individual (gray solid) and averaged (black solid) figures of merit for this disorder [Fig. 4(a)] are of the same order as the pristine 5×4 array (black dashed). This is expected as the standard and
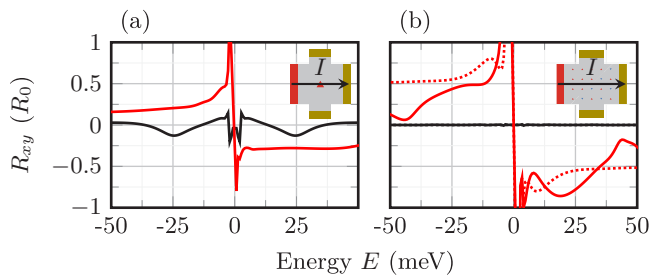
FIG. 5. Transverse resistance R in units of $R_0 = h/e^2$ for a single-antidot device and two 5×4 array devices when injecting only $\uparrow$ electrons into the L lead (shown in red). The resistances of spin-unpolarized ($m_i = 0$) and spin-polarized ($M = \sum m_i \neq 0$) antidot devices are shown in black and red, respectively. (a) Single-antidot device, with the inset showing a schematic of $\uparrow$-polarized electron injection. (b) 5×4 array devices with aligned (solid) and the alternatingly flipped triangles (dotted). The inset shows the schematic of a 5×4 array device with $\uparrow$-polarized electron injection).

flipped single-triangle devices display very similar behavior [Figs. 1(a) and 1(b)]. For comparison, for the case where every second antidot has been flipped [$5 \times 4_R$ (black dotted)], the efficiency is almost exactly identical to the disordered average. The spread of the different disorder realizations (gray curves) is very small, suggesting that the orientation of the individual antidots plays only a very minor role in these devices, and may even improve the figure of merit compared to the lattice of aligned antidots.

The second disorder type [inset of Fig. 4(b)] randomly varies the triangle side lengths $L \to L \pm \delta L$, where $\delta L \in \{0, a, 2a\}$. The individual and the averaged splitting efficiencies are shown in Fig. 4(b). The effect of this disorder is minimal, suggesting that it is the presence of multiple spin-dependent scatterers with similar qualitative behavior and not their exact positioning or size, which enhances the spin-splitting effect. Enlarging or shrinking a triangle changes the length of the spin-polarized zz edge, and thus the total magnetic moment of an individual triangle [see the inset of Fig. 1(c), and the Supplemental Material [52]]. However, the qualitative scattering processes are unchanged.

The third type of disorder, in Fig. 4(c), randomly removes $N_{rem} \leqslant 3$ edge atoms. Removing an edge atom splits the zz edges into smaller segments and significantly influences the magnetic moment profile (see also the Supplemental Material [52]). Random flipping of local moments should play a similar role. Each device realization comprises several antidots with a randomly chosen $N_{rem} \in \{0, 1, 2, 3\}$. The splitting efficiencies shown in Fig. 4(d) show some deviations from pristine behavior. This can be attributed to the reduction of

the total magnetic moment as well as the random introduction of scattering centers at each of the antidots. Edge disorder is particularly severe for small antidots and is capable of quenching magnetism entirely at some edges. The longer edge lengths likely in experiment will be more robust against this type of disorder.

Finally, we consider the transverse resistance in a four-terminal device. The resistances R_{xy} of the single-antidot device and the 5×4 and $5 \times 4_R$ devices are shown in Figs. 5(a) and 5(b), respectively. The difference between the top and bottom chemical potentials is $\mu_T - \mu_B \propto T_{LT}^c T_{RB}^c - T_{RT}^c T_{LB}^c$, and vanishes in the case of complete left-right symmetry. For spin-unpolarized electrons the system is exactly L/R symmetric and the resistance is zero (not shown). Figure 5 shows cases with a $\uparrow$-polarized L lead. The transverse resistances in Fig. 5(a) through a single magnetic antidot (red) show clear antisymmetry with respect to energy. At positive energies, the fact that the $\downarrow$ electrons are now *not* flowing between L and T has the effect of shifting the potential at T closer to that at the R lead, i.e., $\mu_T < eV_{LR}/2$. Simultaneously, the potential at B remains close to midway between the L and R potential, i.e., $\mu_B \sim eV_{LR}/2$. This yields a negative transverse potential drop $\mu_T - \mu_B < 0$ and in turn a negative resistance $R_{xy} < 0$. For $E < 0$ the spins are flipped and the sign of both the potential drop and the resistance is inverted. When the antidot is unpolarized, positive and negative energies behave similarly, and the resistance is symmetric across the Fermi level, as shown in Fig. 5 (black). The same is seen for the both the 5×4 array and the $5 \times 4_R$ array devices in Fig. 5(b). This clear distinction between magnetic and nonmagnetic antidots provides an excellent measure of whether the device actually splits spin currents, and can, in general, be used to detect magnetism in other nanostructured devices.

Summary. We have demonstrated that magnetic triangular antidots in graphene provide an efficient platform for spatial spin-splitting devices. The incoming current is split into output leads according to spin orientation, analogous to the spin Hall effect, but without relying on spin-orbit effects. The outgoing spin polarizations can be flipped using a gate potential. The predicted performance is robust against typical disorders present in realistic devices. The transverse resistance yields a clear signal distinguishing the magnetic nature of the perforations.

[1] A. H. Castro Neto, N. M. R. Peres, K. S. Novoselov, and A. K. Geim, Rev. Mod. Phys. **81**, 109 (2009).

[2] W. Han, K. Pi, K. M. McCreary, Y. Li, J. J. I. Wong, A. G. Swartz, and R. K. Kawakami, Phys. Rev. Lett. **105**, 167202 (2010).

[3] O. V. Yazyev, Rep. Prog. Phys. **73**, 056501 (2010).

[4] R. R. Nair, M. Sepioni, I.-L. Tsai, O. Lehtinen, J. Keinonen, A. V. Krasheninnikov, T. Thomson, A. K. Geim, and I. V. Grigorieva, Nat. Phys. **8**, 199 (2012).

[5] K. M. McCreary, A. G. Swartz, W. Han, J. Fabian, and R. K. Kawakami, Phys. Rev. Lett. **109**, 186604 (2012).

[6] J. Hong, E. Bekyarova, P. Liang, W. A. de Heer, R. C. Haddon, and S. Khizroev, Sci. Rep. **2**, 624 (2012).

[7] R. R. Nair, I.-L. Tsai, M. Sepioni, O. Lehtinen, J. Keinonen, A. V. Krasheninnikov, A. H. Castro Neto, M. I. Katsnelson, A. K. Geim, and I. V. Grigorieva, Nat. Commun. **4**, 2010 (2013).

[8] W. Han, R. K. Kawakami, M. Gmitra, and J. Fabian, Nat. Nanotechnol. **9**, 794 (2014).

[9] D. V. Tuan, F. Ortmann, D. Soriano, S. O. Valenzuela, and S. Roche, Nat. Phys. **10**, 857 (2014).

[10] M. V. Kamalakar, C. Groenveld, A. Dankert, and S. P. Dash, Nat. Commun. **6**, 6766 (2015).

[11] Y.-W. Son, M. L. Cohen, and S. G. Louie, Nature (London) **444**, 347 (2006).

[12] T. Ozaki, K. Nishio, H. Weng, and H. Kino, Phys. Rev. B **81**, 075422 (2010).

[13] A. Saffarzadeh and R. Farghadan, Appl. Phys. Lett. **98**, 023106 (2011).

[14] G. S. Diniz, E. Vernek, and F. M. Souza, Physica E **85**, 264 (2017).

[15] W. Sheng, Z. Y. Ning, Z. Q. Yang, and H. Guo, Nanotechnology **21**, 385201 (2010).

[16] M. G. Zeng, L. Shen, Y. Q. Cai, Z. D. Sha, and Y. Feng, Appl. Phys. Lett. **96**, 042104 (2010).

[17] C. L. Kane and E. J. Mele, Phys. Rev. Lett. **95**, 226801 (2005).

[18] D. A. Abanin, P. A. Lee, and L. S. Levitov, Phys. Rev. Lett. **96**, 176803 (2006).

[19] J. Balakrishnan, G. K. W. Koon, A. Avsar, Y. Ho, J. H. Lee, M. Jaiswal, S.-J. Baeck, J.-H. Ahn, A. Ferreira, M. A. Cazalilla, A. H. Castro Neto, and B. Özyilmaz, Nat. Commun. **5**, 4748 (2014).

[20] A. Cresti, D. Van Tuan, D. Soriano, A. W. Cummings, and S. Roche, Phys. Rev. Lett. **113**, 246603 (2014).

[21] J. Sinova, S. O. Valenzuela, J. Wunderlich, C. H. Back, and T. Jungwirth, Rev. Mod. Phys. **87**, 1213 (2015).

[22] H. Hu, Z. Wang, and F. Liu, Nanoscale Res. Lett. **9**, 690 (2014).

[23] J. M. Pruneda, Phys. Rev. B **81**, 161409 (2010).

[24] O. V. Yazyev and L. Helm, Phys. Rev. B **75**, 125408 (2007).

[25] J. J. Palacios, J. Fernández-Rossier, and L. Brey, Phys. Rev. B **77**, 195428 (2008).

[26] N. Leconte, D. Soriano, S. Roche, P. Ordejón, J.-C. Charlier, and J. J. Palacios, ACS Nano **5**, 3987 (2011).

[27] M. Wimmer, İ. Adagideli, S. Berber, D. Tománek, and K. Richter, Phys. Rev. Lett. **100**, 177207 (2008).

[28] B. Wang, J. Wang, and H. Guo, Phys. Rev. B **79**, 165417 (2009).

[29] X. H. Zheng, G. R. Zhang, Z. Zeng, V. M. García-Suárez, and C. J. Lambert, Phys. Rev. B **80**, 075413 (2009).

[30] P. Potasz, A. D. Güçlü, A. Wójs, and P. Hawrylak, Phys. Rev. B **85**, 075431 (2012).

[31] X. K. Hong, Y. W. Kuang, C. Qian, Y. M. Tao, H. L. Yu, D. B. Zhang, Y. S. Liu, J. F. Feng, X. F. Yang, and X. F. Wang, J. Phys. Chem. C **120**, 668 (2016).

[32] M. E. Khan, P. Zhang, Y.-Y. Sun, S. B. Zhang, and Y.-H. Kim, AIP Adv. **6**, 035023 (2016).

[33] S. S. Gregersen, S. R. Power, and A.-P. Jauho, Phys. Rev. B **93**, 245429 (2016).

[34] T. G. Pedersen, C. Flindt, J. G. Pedersen, N. A. Mortensen, A.-P. Jauho, and K. Pedersen, Phys. Rev. Lett. **100**, 136804 (2008).

[35] R. Petersen, T. G. Pedersen, and A.-P. Jauho, ACS Nano **5**, 523 (2011).

[36] F. Ouyang, S. Peng, Z. Liu, and Z. Liu, ACS Nano **5**, 4023 (2011).

[37] C. Tao, L. Jiao, O. V. Yazyev, Y.-C. Chen, J. Feng, X. Zhang, R. B. Capaz, J. M. Tour, A. Zettl, S. G. Louie, H. Dai, and M. F. Crommie, Nat. Phys. **7**, 616 (2011).

[38] T. Hashimoto, S. Kamikawa, D. Soriano, J. G. Pedersen, S. Roche, and J. Haruyama, Appl. Phys. Lett. **105**, 183111 (2014).

[39] G. Z. Magda, X. Jin, I. Hagymási, P. Vancsó, Z. Osváth, P. Nemes-Incze, C. Hwang, L. P. Biró, and L. Tapasztó, Nature (London) **514**, 608 (2014).

[40] G. Auton, R. K. Kumar, E. Hill, and A. Song, J. Electron. Mater. (2016), doi:10.1007/s11664-016-4938-y.

[41] Z. Shi, R. Yang, L. Zhang, Y. Wang, D. Liu, D. Shi, E. Wang, and G. Zhang, Adv. Mater. **23**, 3061 (2011).

[42] F. Oberhuber, S. Blien, S. Heydrich, F. Yaghobian, T. Korn, C. Schuller, C. Strunk, D. Weiss, and J. Eroms, Appl. Phys. Lett. **103**, 143111 (2013).

[43] C. Jin, F. Lin, K. Suenaga, and S. Iijima, Phys. Rev. Lett. **102**, 195505 (2009).

[44] S. M. Gilbert, G. Dunn, T. Pham, B. Shevitski, E. Dimitrov, S. Aloni, and A. Zettl, arXiv:1702.01220.

[45] A. D. Güçlü, P. Potasz, and P. Hawrylak, Phys. Rev. B **82**, 155445 (2010).

[46] S. Saremi, Phys. Rev. B **76**, 184430 (2007).

[47] S. Power and M. Ferreira, Crystals **3**, 49 (2013).

[48] C. H. Lewenkopf and E. R. Mucciolo, J. Comput. Electron. **12**, 203 (2013).

[49] D. A. Bahamon, A. H. Castro Neto, and V. M. Pereira, Phys. Rev. B **88**, 235433 (2013).

[50] S. V. Koniakhin, Eur. Phys. J. B **87**, 216 (2014).

[51] S. R. Power and A.-P. Jauho, Phys. Rev. B **90**, 115408 (2014).

[52] See Supplemental Material at http://link.aps.org/supplemental/10.1103/PhysRevB.95.121406 for magnetic and transport properties of triangular antidots when varying side length and introducing edge disorder.

List of Figures

Chapter 6   Robust band gaps and half-metallic antidot lattices

Chapter 7   Triangular antidot spin filter

Chapter 8   Large scale triangular antidots

Appendix A   Green's function techniques

Bibliography

[1]   K S Novoselov, D Jiang, F Schedin, *et al.* "Two-dimensional atomic crystals". In: *Proceedings of the National Academy of Sciences* 102.30 (July 2005), pp. 10451–10453 (cit. on p. 1).

[2]   Sheneve Z. Butler, Shawna M. Hollen, Linyou Cao, *et al.* "Progress, challenges, and opportunities in two-dimensional materials beyond graphene." In: *ACS nano* 7.4 (Apr. 2013), pp. 2898–926 (cit. on p. 1).

[3]   Ganesh R. Bhimanapati, Zhong Lin, Vincent Meunier, *et al.* "Recent Advances in Two-Dimensional Materials beyond Graphene". In: *ACS Nano* 9.12 (Dec. 2015), pp. 11509–11539 (cit. on p. 1).

[4]   Kostya S. Novoselov, Andrei K. Geim, Sergey V. Morozov, *et al.* "Electric field effect in atomically thin carbon films." In: *Science (New York, N.Y.)* 306.5696 (Oct. 2004), pp. 666–9 (cit. on p. 1).

[5]   Antonio H. Castro Neto, N. M. R. Peres, Kostya S. Novoselov, and Andrei K. Geim. "The electronic properties of graphene". In: *Reviews of Modern Physics* 81.1 (Jan. 2009), pp. 109–162 (cit. on pp. 1, 2, 7, 17, 18).

[6]   Alexander S. Mayorov, Roman V. Gorbachev, Sergey V. Morozov, *et al.* "Micrometer-Scale Ballistic Transport in Encapsulated Graphene at Room Temperature". In: *Nano Letters* 11.6 (June 2011), pp. 2396–2399 (cit. on p. 1).

[7]   Qing Hua Wang, Kourosh Kalantar-Zadeh, Andras Kis, Jonathan N Coleman, and Michael S Strano. "Electronics and optoelectronics of two-dimensional transition metal dichalcogenides". In: *Nature Nanotechnology* 7.11 (Nov. 2012), pp. 699–712 (cit. on p. 1).

[8]   Patrick Vogt, Paola De Padova, Claudio Quaresima, *et al.* "Silicene: Compelling Experimental Evidence for Graphenelike Two-Dimensional Silicon". In: *Physical Review Letters* 108.15 (Apr. 2012), p. 155501 (cit. on p. 1).

[9]   M E Dávila, L. Xian, S. Cahangirov, A. Rubio, and G. Le Lay. "Germanene: a novel two-dimensional germanium allotrope akin to graphene and silicene". In: *New Journal of Physics* 16.9 (Sept. 2014), p. 095002 (cit. on p. 1).

[10]   Han Liu, Adam T Neal, Zhen Zhu, *et al.* "Phosphorene: An Unexplored 2D Semiconductor with a High Hole Mobility". In: *ACS Nano* 8.4 (Apr. 2014), pp. 4033–4041 (cit. on p. 1).

[11]   Andrei K. Geim and I. V. Grigorieva. "Van der Waals heterostructures." In: *Nature (London)* 499.7459 (July 2013), pp. 419–25 (cit. on pp. 1, 2, 21).

[12]   Filippo Pizzocchero, Lene Gammelgaard, Bjarke Sørensen Jessen, *et al.* "The hot pick-up technique for batch assembly of van der Waals heterostructures". In: *Nature Communications* 7.05 (June 2016), p. 11894 (cit. on pp. 1, 2, 21).

[13]   Robert J. Young, Ian A. Kinloch, Lei Gong, and Kostya S. Novoselov. "The mechanics of graphene nanocomposites: A review". In: *Composites Science and Technology* 72.12 (July 2012), pp. 1459–1476 (cit. on p. 1).

[14]   Kostya S. Novoselov, V. I. Fal'ko, L. Colombo, *et al.* "A roadmap for graphene". In: *Nature (London)* 490.7419 (Oct. 2012), pp. 192–200 (cit. on p. 1).

[15] Marc Drögeler, Christopher Franzen, Frank Volmer, *et al.* "Spin Lifetimes Exceeding 12 ns in Graphene Nonlocal Spin Valve Devices". In: *Nano Letters* 16.6 (June 2016), pp. 3533–3539 (cit. on p. 2).

[16] Igor Žutić, Jaroslav Fabian, and S. Das Sarma. "Spintronics: Fundamentals and applications". In: *Reviews of Modern Physics* 76.2 (Apr. 2004), pp. 323–410 (cit. on p. 2).

[17] H. Dery, P. Dalal, L. Cywiński, and Lu J. Sham. "Spin-based logic in semi-conductors for reconfigurable large-scale circuits". In: *Nature* 447.7144 (May 2007), pp. 573–576 (cit. on p. 2).

[18] Hanan Dery, Hui Wu, Berkehan Ciftcioglu, *et al.* "Nanospintronics Based on Magnetologic Gates". In: *IEEE Transactions on Electron Devices* 59.1 (Jan. 2012), pp. 259–262 (cit. on p. 2).

[19] Wei Han, K. Pi, Kathleen M. McCreary, *et al.* "Tunneling Spin Injection into Single Layer Graphene". In: *Physical Review Letters* 105.16 (Oct. 2010), p. 167202 (cit. on p. 2).

[20] Adam L. Friedman, Olaf M. J. van 't Erve, Connie H. Li, Jeremy T. Robinson, and Berend T. Jonker. "Homoepitaxial tunnel barriers with functionalized graphene-on-graphene for charge and spin transport". In: *Nature Communications* 5 (Jan. 2014), p. 3161 (cit. on p. 2).

[21] R. R. Nair, M. Sepioni, I.-Ling Tsai, *et al.* "Spin-half paramagnetism in graphene induced by point defects". In: *Nature Physics* 8.3 (Jan. 2012), pp. 199–202 (cit. on pp. 2, 3).

[22] Kathleen M. McCreary, Adrian G. Swartz, Wei Han, Jaroslav Fabian, and Roland K. Kawakami. "Magnetic Moment Formation in Graphene Detected by Scattering of Pure Spin Currents". In: *Physical Review Letters* 109.18 (Nov. 2012), p. 186604 (cit. on pp. 2, 3, 33).

[23] Jeongmin Hong, Elena Bekyarova, Ping Liang, *et al.* "Room-temperature Magnetic Ordering in Functionalized Graphene". In: *Scientific Reports* 2 (Sept. 2012), p. 624 (cit. on p. 2).

[24] R. R. Nair, I.-Ling Tsai, M. Sepioni, *et al.* "Dual origin of defect magnetism in graphene and its reversible switching by molecular doping". In: *Nature Communications* 4.05 (June 2013), p. 2010 (cit. on p. 2).

[25] Wei Han and Roland K. Kawakami. "Spin Relaxation in Single-Layer and Bilayer Graphene". In: *Physical Review Letters* 107.4 (July 2011), p. 047207 (cit. on p. 2).

[26] Dinh Van Tuan, Frank Ortmann, David Soriano, Sergio O. Valenzuela, and Stephan Roche. "Pseudospin-driven spin relaxation mechanism in graphene". In: *Nature Physics* 10.09 (2014), pp. 857–863 (cit. on p. 2).

[27] Wei Han, Roland K. Kawakami, Martin Gmitra, and Jaroslav Fabian. "Graphene spintronics". In: *Nature Nanotechnology* 9.10 (Oct. 2014), pp. 794–807 (cit. on pp. 3, 4, 33, 52).

[28] Oleg V. Yazyev and Lothar Helm. "Defect-induced magnetism in graphene". In: *Physical Review B* 75.12 (Mar. 2007), p. 125408 (cit. on p. 2).

[29] Juan Jose Palacios, J. Fernández-Rossier, and Luis Brey. "Vacancy-induced magnetism in graphene and graphene ribbons". In: *Physical Review B* 77.19 (May 2008), p. 195428 (cit. on p. 2).

[30] Stephen R. Power, V. M. de Menezes, S. B. Fagan, and M. S. Ferreira. "Magnetization profile for impurities in graphene nanoribbons". In: *Physical Review B* 84.19 (Nov. 2011), p. 195431 (cit. on p. 2).

[31] Elliott Lieb. "Two theorems on the Hubbard model". In: *Physical Review Letters* 62.10 (Mar. 1989), pp. 1201–1204 (cit. on pp. 2, 33, 37).

[32] Young-Woo Son, Marvin L. Cohen, and Steven G. Louie. "Half-metallic graphene nanoribbons". In: *Nature (London)* 444.7117 (Nov. 2006), pp. 347–349 (cit. on pp. 3, 33, 43).

[33] Gábor Zsolt Magda, Xiaozhan Jin, Imre Hagymási, *et al.* "Room-temperature magnetic order on zigzag edges of narrow graphene nanoribbons". In: *Nature (London)* 514.7524 (Oct. 2014), pp. 608–611 (cit. on pp. 3, 33).

[34] Shiyong Wang, Leopold Talirz, Carlo A. Pignedoli, *et al.* "Giant edge state splitting at atomically precise graphene zigzag edges". In: *Nature Communications* 7.05 (May 2016), p. 11507 (cit. on p. 3).

[35] Taijyu Hashimoto, Syota Kamikawa, David Soriano, *et al.* "Tunneling magnetoresistance phenomenon utilizing graphene magnet electrode". In: *Applied Physics Letters* 105.18 (Nov. 2014), p. 183111 (cit. on pp. 3, 33).

[36] Robert Drost, Andreas Uppstu, Fabian Schulz, *et al.* "Electronic States at the Graphene–Hexagonal Boron Nitride Zigzag Interface". In: *Nano Letters* 14.9 (Sept. 2014), pp. 5128–5132 (cit. on p. 3).

[37] Jayakumar Balakrishnan, Gavin Kok Wai Koon, Manu Jaiswal, A. H. Castro Neto, and Barbaros Özyilmaz. "Colossal enhancement of spin–orbit coupling in weakly hydrogenated graphene". In: *Nature Physics* 9.5 (Mar. 2013), pp. 284–287 (cit. on pp. 3, 4).

[38] Jairo Sinova, Sergio O. Valenzuela, J. Wunderlich, C. H. Back, and T. Jungwirth. "Spin Hall effects". In: *Reviews of Modern Physics* 87.4 (Oct. 2015), pp. 1213–1260 (cit. on pp. 3, 44).

[39] A. H. Castro Neto and F. Guinea. "Impurity-Induced Spin-Orbit Coupling in Graphene". In: *Physical Review Letters* 103.2 (July 2009), p. 026804 (cit. on p. 4).

[40] Thomas Garm Pedersen, Christian Flindt, Jesper Goor Pedersen, *et al.* "Graphene Antidot Lattices: Designed Defects and Spin Qubits". In: *Physical Review Letters* 100.13 (Apr. 2008), p. 136804 (cit. on pp. 4, 18, 19, 22, 23, 34, 36).

[41] Fangping Ouyang, Shenglin Peng, Zhongfan Liu, and Zhirong Liu. "Bandgap opening in graphene antidot lattices: the missing half." In: *ACS Nano* 5.5 (May 2011), pp. 4023–30 (cit. on pp. 4, 19, 36).

[42] René Petersen, Thomas Garm Pedersen, and Antti-Pekka Jauho. "Clar sextet analysis of triangular, rectangular, and honeycomb graphene antidot lattices." In: *ACS Nano* 5.1 (Jan. 2011), pp. 523–9 (cit. on pp. 4, 19, 34).

[43] Marc Dvorak, William Oswald, and Zhigang Wu. "Bandgap opening by patterning graphene." In: *Scientific reports* 3 (2013), p. 2289 (cit. on pp. 4, 19, 20).

[44] Stephen R. Power and Antti-Pekka Jauho. "Electronic transport in disordered graphene antidot lattice devices". In: *Physical Review B* 90.11 (Sept. 2014), p. 115408 (cit. on pp. 4, 36, 40).

[45] A. J. M. Giesbers, E. C. Peters, M. Burghard, and K. Kern. "Charge transport gap in graphene antidot lattices". In: *Physical Review B* 86.4 (July 2012), p. 045445 (cit. on p. 4).

[46] Haijing Zhang, Jianming Lu, Wu Shi, *et al.* "Large-scale Mesoscopic Transport in Nanostructured Graphene". In: *Physical Review Letters* 110.6 (Feb. 2013), p. 066805 (cit. on p. 4).

[47] Zheyong Fan, Andreas Uppstu, and Ari Harju. "Electronic and transport properties in geometrically disordered graphene antidot lattices". In: *Physical Review B* 91.12 (Mar. 2015), p. 125434 (cit. on p. 4).

[48] Tue Gunst, Troels Markussen, Antti-Pekka Jauho, and Mads Brandbyge. "Thermoelectric properties of finite graphene antidot lattices". In: *Physical Review B* 84.15 (Oct. 2011), p. 155449 (cit. on pp. 4, 23, 28).

[49] Shengjun Yuan, Rafael Roldán, Antti-Pekka Jauho, and Mikhail I. Katsnelson. "Electronic properties of disordered graphene antidot lattices". In: *Physical Review B* 87.8 (Feb. 2013), p. 085430 (cit. on pp. 4, 36, 40).

[50] Zhiwen Shi, Rong Yang, Lianchang Zhang, *et al.* "Patterning Graphene with Zigzag Edges by Self-Aligned Anisotropic Etching". In: *Advanced Materials* 23.27 (July 2011), pp. 3061–3065 (cit. on pp. 4, 5).

[51] Gregory Auton, Roshan Krishna Kumar, Ernie Hill, and Aimin Song. "Graphene Triangular Ballistic Rectifier: Fabrication and Characterisation". In: *Journal of Electronic Materials* (Sept. 2016), pp. 1–7 (cit. on pp. 4, 5, 55).

[52] Andreas Sandner, Tobias Preis, Christian Schell, *et al.* "Ballistic Transport in Graphene Antidot Lattices". In: *Nano Letters* 15.12 (Dec. 2015), pp. 8402–8406 (cit. on p. 4).

[53] Florian Oberhuber, Stefan Blien, Stefanie Heydrich, *et al.* "Weak localization and Raman study of anisotropically etched graphene antidots". In: *Applied Physics Letters* 103.14 (2013), p. 143111 (cit. on p. 4).

[54] Qiang Xu, Meng-Yue Wu, Grégory F. Schneider, *et al.* "Controllable Atomic Scale Patterning of Freestanding Monolayer Graphene at Elevated Temperature". In: *ACS Nano* 7.2 (Feb. 2013), pp. 1566–1572 (cit. on p. 4).

[55] Ryuta Yagi, Ryoji Sakakibara, Ryoya Ebisuoka, *et al.* "Ballistic transport in graphene antidot lattices". In: *Physical Review B* 92.19 (Nov. 2015), p. 195406 (cit. on p. 4).

[56] Jeroen B. Oostinga, Hubert B. Heersche, Xinglan Liu, Alberto F. Morpurgo, and Lieven M. K. Vandersypen. "Gate-induced insulating state in bilayer graphene devices." In: *Nature materials* 7.2 (Feb. 2008), pp. 151–7 (cit. on p. 5).

[57] Stephanie Reich, J. Maultzsch, C. Thomsen, and Pablo Ordejón. "Tight-binding description of graphene". In: *Physical Review B* 66.3 (July 2002), p. 35412 (cit. on p. 7).

[58] Eduardo V. Castro, Kostya S. Novoselov, Sergey V. Morozov, *et al.* "Electronic properties of a biased graphene bilayer." In: *Journal of physics. Condensed matter* 22.17 (May 2010), p. 175503 (cit. on p. 7).

[59] Edward McCann and Mikito Koshino. "The electronic properties of bilayer graphene." In: *Reports on Progress in Physics* 76.5 (May 2013), p. 56503 (cit. on pp. 7, 21, 25).

[60] Supriyo Datta. *Electronic Transport in Mesoscopic Systems*. 3rd ed. Cambridge: Cambridge University Press, 1995 (cit. on pp. 7, 9).

[61] Supriyo Datta. *Quantum Transport: Atom to Transistor*. Cambridge: Cambridge University Press, 2005, p. 419 (cit. on pp. 7–9).

[62] Henrik Bruus and Karsten Flensberg. *Many-Body Quantum Theory in Condensed Matter Physics—An Introduction*. Oxford University Press, 2004 (cit. on p. 7).

[63] Caio H. Lewenkopf and Eduardo R. Mucciolo. "The recursive Green's function method for graphene". In: *Journal of Computational Electronics* 12.2 (May 2013), pp. 203–231 (cit. on pp. 7–9).

[64] Luis E. F. Foa Torres, Stephan Roche, and Jean-christophe Charlier. *Introduction to graphene-based nanomaterials: from electronic structure to quantum transport*. 1st ed. New York: Cambridge University Press, 2014, p. 421 (cit. on pp. 8, 13, 55).

[65] Daniel S. Fisher and Patrick A. Lee. "Relation between conductivity and transmission matrix". In: *Physical Review B* 23.12 (June 1981), pp. 6851–6854 (cit. on p. 9).

[66] Y. Hancock, Andreas Uppstu, K. Saloriutta, Ari Harju, and M. J. Puska. "Generalized tight-binding transport model for graphene nanoribbon-based systems". In: *Physical Review B* 81.24 (June 2010), p. 245402 (cit. on pp. 9, 36).

[67] Oleg V. Yazyev. "Emergence of magnetism in graphene materials and nanostructures". In: *Reports on Progress in Physics* 73.5 (May 2010), p. 056501 (cit. on p. 9).

[68] Alexander Weiße, Gerhard Wellein, Andreas Alvermann, and Holger Fehske. "The kernel polynomial method". In: *Reviews of Modern Physics* 78.1 (Mar. 2006), pp. 275–306 (cit. on pp. 11, 12, 14, 55, 81).

[69] Jose H. García, Lucian Covaci, and Tatiana G. Rappoport. "Real-Space Calculation of the Conductivity Tensor for Disordered Topological Matter". In: *Physical Review Letters* 114.11 (Mar. 2015), p. 116602 (cit. on pp. 11, 55, 57, 63).

[70] D A Greenwood. "The Boltzmann Equation in the Theory of Electrical Conduction in Metals". In: *Proceedings of the Physical Society* 71.4 (Apr. 1958), pp. 585–596 (cit. on p. 13).

[71] R Kubo. "The fluctuation-dissipation theorem". In: *Reports on Progress in Physics* 29.1 (Jan. 1966), p. 306 (cit. on p. 13).

[72] Stephan Roche and Didier Mayou. "Conductivity in 3D quasiperiodic systems". In: *Physical Review Letters* 79.13 (Sept. 1997), pp. 2518–2521 (cit. on pp. 13, 55, 82).

[73] Aurélien Lherbier, X. Blase, Yann-Michel Niquet, Franccois Triozon, and Stephan Roche. "Charge Transport in Chemically Doped 2D Graphene". In: *Physical Review Letters* 101.3 (July 2008), p. 036808 (cit. on pp. 13, 55).

[74] Hiroyuki Ishii, Franccois Triozon, Nobuhiko Kobayashi, Kenji Hirose, and Stephan Roche. "Charge transport in carbon nanotubes based materials: a Kubo–Greenwood computational approach". In: *Comptes Rendus Physique* 10.4 (May 2009), pp. 283–296 (cit. on pp. 13, 55).

[75] Zheyong Fan, Andreas Uppstu, Topi Siro, and Ari Harju. "Efficient linear-scaling quantum transport calculations on graphics processing units and applications on electron transport in graphene". In: *Computer Physics Communications* 185.1 (Jan. 2014), pp. 28–39 (cit. on p. 13).

[76] J. M. B. Lopes dos Santos, N. M. R. Peres, and Antonio H. Castro Neto. "Graphene Bilayer with a Twist: Electronic Structure". In: *Physical Review Letters* 99.25 (Dec. 2007), p. 256802 (cit. on p. 22).

[77] J. M. B. Lopes dos Santos, N. M. R. Peres, and Antonio H. Castro Neto. "Continuum model of the twisted graphene bilayer". In: *Physical Review B* 86.15 (Oct. 2012), p. 155449 (cit. on p. 22).

[78] Martin Dienwiebel, Gertjan S. Verhoeven, Namboodiri Pradeep, *et al.* "Superlubricity of Graphite". In: *Physical Review Letters* 92.12 (Mar. 2004), p. 126101 (cit. on p. 22).

[79] Søren J. Brun, M. R. Thomsen, and Thomas Garm Pedersen. "Electronic and optical properties of graphene antidot lattices: comparison of Dirac and tight-binding models." In: *Journal of physics. Condensed matter : an Institute of Physics journal* 26.26 (July 2014), p. 265301 (cit. on p. 23).

[80] Johan Nilsson, Antonio H. Castro Neto, F. Guinea, and N. M. R. Peres. "Transmission through a biased graphene bilayer barrier". In: *Physical Review B* 76.16 (Oct. 2007), p. 165416 (cit. on p. 23).

[81] J. W. González, H. Santos, M. Pacheco, L. Chico, and Luis Brey. "Electronic transport through bilayer graphene flakes". In: *Physical Review B* 81.19 (May 2010), p. 195406 (cit. on p. 28).

[82] J. W. González, H. Santos, E. Prada, Luis Brey, and L. Chico. "Gate-controlled conductance through bilayer graphene ribbons". In: *Physical Review B* 83.20 (May 2011), p. 205402 (cit. on p. 28).

[83] Ashwin Ramasubramaniam, Doron Naveh, and Elias Towe. "Tunable band gaps in bilayer graphene-BN heterostructures." In: *Nano letters* 11.3 (Mar. 2011), pp. 1070–5 (cit. on p. 31).

[84] Søren Schou Gregersen, Jesper Goor Pedersen, Stephen R. Power, and Antti-pekka Jauho. "Graphene on graphene antidot lattices: Electronic and transport properties". In: *Physical Review B* 91.11 (Mar. 2015), p. 115424 (cit. on p. 31).

[85] Taisuke Ozaki, Kengo Nishio, Hongming Weng, and Hiori Kino. "Dual spin filter effect in a zigzag graphene nanoribbon". In: *Physical Review B* 81.7 (Feb. 2010), p. 075422 (cit. on p. 33).

[86] W. Sheng, Z. Y. Ning, Z. Q. Yang, and H. Guo. "Magnetism and perfect spin filtering effect in graphene nanoflakes". In: *Nanotechnology* 21.38 (Sept. 2010), p. 385201 (cit. on pp. 33, 43).

[87] A. Saffarzadeh and R. Farghadan. "A spin-filter device based on armchair graphene nanoribbons". In: *Applied Physics Letters* 98.2 (2011), p. 023106 (cit. on pp. 33, 43).

[88] X. K. Hong, Y. W. Kuang, C. Qian, *et al.* "Axisymmetric All-Carbon Devices with High-Spin Filter Efficiency, Large-Spin Rectifying, and Strong-Spin Negative Differential Resistance Properties". In: *The Journal of Physical Chemistry C* 120.1 (Jan. 2016), pp. 668–676 (cit. on pp. 33, 43).

[89] Oded Hod, Verónica Barone, and Gustavo E. Scuseria. "Half-metallic graphene nanodots: A comprehensive first-principles theoretical study". In: *Physical Review B* 77.3 (Jan. 2008), p. 035411 (cit. on p. 33).

[90] Søren Schou Gregersen, Stephen R. Power, and Antti-Pekka Jauho. "Robust band gap and half-metallicity in graphene with triangular perforations". In: *Physical Review B* 93.24 (June 2016), p. 245429 (cit. on pp. 34, 37, 43, 55).

[91] Kyoko Nakada, Mitsutaka Fujita, Gene Dresselhaus, and Mildred S. Dresselhaus. "Edge state in graphene ribbons: Nanometer size effect and edge shape dependence". In: *Physical Review B* 54.24 (Dec. 1996), pp. 17954–17961 (cit. on p. 36).

[92] Alev Devrim Güçclü, Pawel Potasz, and Pawel Hawrylak. "Excitonic absorption in gate-controlled graphene quantum dots". In: *Physical Review B* 82.15 (Oct. 2010), p. 155445 (cit. on p. 36).

[93] W. Jaskólski, A. Ayuela, M. Pelc, H. Santos, and L. Chico. "Edge states and flat bands in graphene nanoribbons with arbitrary geometries". In: *Physical Review B* 83.23 (June 2011), p. 235424 (cit. on p. 36).

[94] Wei-dong Sheng, Marek Korkusinski, Alev Devrim Güçclü, *et al.* "Electronic and optical properties of semiconductor and graphene quantum dots". In: *Frontiers of Physics* 7.3 (June 2012), pp. 328–352 (cit. on p. 36).

[95] Aurélien Lherbier, Andrés Rafael Botello-Méndez, and Jean-Christophe Charlier. "Electronic and transport properties of unbalanced sublattice N-doping in graphene." In: *Nano letters* 13.4 (Apr. 2013), pp. 1446–50 (cit. on p. 36).

[96] Thomas Aktor, Antti-Pekka Jauho, and Stephen R. Power. "Electronic transport in graphene nanoribbons with sublattice-asymmetric doping". In: *Physical Review B* 93.3 (Jan. 2016), p. 035446 (cit. on p. 36).

[97] Oleg V. Yazyev, Rodrigo B. Capaz, and Steven G. Louie. "Theory of magnetic edge states in chiral graphene nanoribbons". In: *Physical Review B* 84.11 (Sept. 2011), p. 115406 (cit. on p. 37).

[98] Joachim Alexander Fürst, Thomas Garm Pedersen, Mads Brandbyge, and Antti-Pekka Jauho. "Density functional study of graphene antidot lattices: Roles of geometrical relaxation and spin". In: *Physical Review B* 80.11 (Sept. 2009), p. 115117 (cit. on p. 42).

[99] Saeed Saremi. "RKKY in half-filled bipartite lattices: Graphene as an example". In: *Physical Review B* 76.18 (Nov. 2007), p. 184430 (cit. on p. 42).

[100] Stephen Power and Mauro Ferreira. "Indirect Exchange and Ruderman–Kittel–Kasuya–Yosida (RKKY) Interactions in Magnetically-Doped Graphene". In: *Crystals* 3.1 (Jan. 2013), pp. 49–78 (cit. on p. 42).

[101] Michael Wimmer, {\.{I}}nancc Adagideli, Savaş Berber, David Tománek, and Klaus Richter. "Spin Currents in Rough Graphene Nanoribbons: Universal Fluctuations and Spin Injection". In: *Physical Review Letters* 100.17 (May 2008), p. 177207 (cit. on p. 43).

[102] X. H. Zheng, G. R. Zhang, Z. Zeng, Víctor M. García-Suárez, and Colin J. Lambert. "Effects of antidots on the transport properties of graphene nanoribbons". In: *Physical Review B* 80.7 (Aug. 2009), p. 075413 (cit. on p. 43).

[103] P. Potasz, A. D. Güçclü, A. Wójs, and P. Hawrylak. "Electronic properties of gated triangular graphene quantum dots: Magnetism, correlations, and geometrical effects". In: *Physical Review B* 85.7 (Feb. 2012), p. 075431 (cit. on p. 43).

[104] Muhammad Ejaz Khan, P. Zhang, Yi-Yang Sun, S. B. Zhang, and Yong-Hyun Kim. "Tailoring graphene magnetism by zigzag triangular holes: A first-principles thermodynamics study". In: *AIP Advances* 6.3 (Mar. 2016), p. 035023 (cit. on p. 43).

[105] D. A. Bahamon, Antonio H. Castro Neto, and Vitor M. Pereira. "Effective contact model for geometry-independent conductance calculations in graphene". In: *Physical Review B* 88.23 (Dec. 2013), p. 235433 (cit. on p. 44).

[106] Sergei V. Koniakhin. "Ratchet effect in graphene with trigonal clusters". In: *The European Physical Journal B* 87.9 (Sept. 2014), p. 216 (cit. on p. 48).

[107] Søren Schou Gregersen, Stephen R. Power, and Antti-Pekka Jauho. "Nanostructured graphene for spintronics". In: *Physical Review B* 95.12 (Mar. 2017), p. 121406 (cit. on p. 55).

[108] S Matt Gilbert, Gabriel Dunn, Thang Pham, *et al.* "Fabrication of Atomically Precise Nanopores in Hexagonal Boron Nitride". In: 1 (Feb. 2017), pp. 4–8 (cit. on p. 55).

[109] M. Olle, G. Ceballos, D. Serrate, and P. Gambardella. "Yield and Shape Selection of Graphene Nanoislands Grown on Ni(111)". In: *Nano Letters* 12.9 (Sept. 2012), pp. 4431–4436 (cit. on p. 55).

[110] A. Garcia-Lekue, M. Ollé, D. Sanchez-Portal, *et al.* "Substrate-Induced Stabilization and Reconstruction of Zigzag Edges in Graphene Nanoislands on Ni(111)". In: *The Journal of Physical Chemistry C* 119.8 (Feb. 2015), pp. 4072–4078 (cit. on p. 55).

[111] Denis A. Areshkin and Carter T. White. "Building Blocks for Integrated Graphene Circuits". In: *Nano Letters* 7.11 (Nov. 2007), pp. 3253–3259 (cit. on p. 56).

[112] Jin Tae Kim and Sung-Yool Choi. "Graphene-based plasmonic waveguides for photonic integrated circuits". In: *Optics Express* 19.24 (Nov. 2011), p. 24557 (cit. on p. 56).

[113] Hugen Yan, Xuesong Li, Bhupesh Chandra, *et al.* "Tunable infrared plasmonic devices using graphene/insulator stacks". In: *Nature Nanotechnology* 7.5 (Apr. 2012), pp. 330–334 (cit. on p. 56).

[114] Vitor M. Pereira, Antonio H. Castro Neto, and N. M. R. Peres. "Tight-binding approach to uniaxial strain in graphene". In: *Physical Review B* 80.4 (July 2009), p. 045401 (cit. on p. 56).

[115] Keun Soo Kim, Yue Zhao, Houk Jang, *et al.* "Large-scale pattern growth of graphene films for stretchable transparent electrodes". In: *Nature* 457.7230 (Feb. 2009), pp. 706–710 (cit. on p. 56).

[116] S. Odaka, H. Miyazaki, S.-L. Li, *et al.* "Anisotropic transport in graphene on SiC substrate with periodic nanofacets". In: *Applied Physics Letters* 96.6 (Feb. 2010), p. 062111 (cit. on p. 56).

[117] Jesper Goor Pedersen, Aron W. Cummings, and Stephan Roche. "Anisotropic behavior of quantum transport in graphene superlattices: Coexistence of ballistic conduction with Anderson insulating regime". In: *Physical Review B* 89.16 (Apr. 2014), p. 165401 (cit. on p. 56).

[118] Zheyong Fan, Andreas Uppstu, and Ari Harju. "Anderson localization in two-dimensional graphene with short-range disorder: One-parameter scaling and finite-size effects". In: *Physical Review B* 89.24 (June 2014), p. 245422 (cit. on p. 61).

[119] H. X. Yang, A. Hallal, D. Terrade, *et al.* "Proximity Effects Induced in Graphene by Magnetic Insulators: First-Principles Calculations on Spin Filtering and Exchange-Splitting Gaps". In: *Physical Review Letters* 110.4 (Jan. 2013), p. 046603 (cit. on p. 67).

[120] Aijun Du, Ying Chen, Zhonghua Zhu, *et al.* "Dots versus Antidots: Computational Exploration of Structure, Magnetism, and Half-Metallicity in Boron–Nitride Nanostructures". In: *Journal of the American Chemical Society* 131.47 (Dec. 2009), pp. 17354–17359 (cit. on p. 67).

DTU Nanotech
Department of Micro- and Nanotechnology